Gas flow pattern in the freeboard above a bubbling fluidised bed

María Isabel Yórquez Ramírez

Ph.D. thesis, 1999

The University of Edinburgh

(School of Chemical Engineering)

Abstract

At present, a thermal cracking process is being developed at pilot plant scale at BP's research facilities in Scotland. The process converts a mixture of waste plastic into a hydrocarbon intermediate, which can be used for petrochemical or refinery processes. A problem of the process is the formation and growth of small amount of fibrous carbon in the freeboard space of the fluidized bed, used as the main reactor. The fibres are believed to form on active metallic sites, detach and grow in the recirculating areas in the freeboard. This can be tolerated but there are economic advantages in their reduction.

The aim of the research undertaken is to characterise the hydrodynamics of the flow in the freeboard to understand and control the growth of the fibres. A cold model of the fluidised bed used in the pilot plant have been constructed, following scaling laws that allow similar hydrodynamic behaviour of the two beds.

Particle Image Velocimetry, PIV, a full-field non-intrusive optical velocity measurement technique is used to analyse the gas pattern in the freeboard. Due to the complexity of the flow and the limitations of the technique PIV was implemented using image shifting.

The gas flow in the freeboard of a fluidised bed is strongly dependent on bubble eruption at the bed surface. Here, the gas flow above an erupting bubble has been studied by the injection of single bubbles in an incipiently fluidised bed. Gas velocity vector maps of the vertical central plane above the bed surface, i.e. a plane parallel to the direction of the overall flow, have been determined using image shifting. A mechanism has been proposed to describe the process of single bubble eruption.

The gas flow pattern above the bubbling fluidising bed has been elucidated by analysing vector maps of vertical planes across the expanded freeboard in terms of instantaneous coherent structures and statistical aggregates. The influence of

other parameters, such as superficial velocity and geometry of the freeboard, on the freeboard hydrodynamics, have also been determined, to find the conditions that minimise the growth of the fibres.

Acknowledgements

I would like to thank everybody that help me in the course of this work, especially my friends for making my time in Edinburgh so enjoyable.

I would also like to express my gratitude to the Birse Family Trust and B.P. Chemicals for the financial support of this project.

Contents

List of Figures

List of Tables

Chapter 1

Introduction

1.1 Motivation for this work

In Europe, 4% of all natural oil is used to produce plastics. Twenty-four million tonnes of plastic are produced every year of which 15 million tonnes become waste (7% of all household waste is plastic). Plastic is not biodegradable and the waste can only by treated by landfill, incineration and recycling.

Plastic accounts for about 25% of the volume of landfill. Public pressure and new legislation, manifested in the landfill tax, are encouraging a reduction in the number of landfill sites. Although incineration can reduce the volume of waste by up to 90% [1] and there is a guaranteed market for the energy recovered from the plants, it is not a very attractive solution for waste plastic because of the emissions. For example, approximately 71% of the lead emission and 88% of cadmium emission in the incineration of household waste are derived from plastics. On the other hand, PVC (polyvinyl chloride), a commonly used plastic, produces organochlorines that are one of the most toxic chemicals known. A large amount of plastic is used in the food industry; however, due to the organic composition

of the plastic it is very difficult to obtain satisfactory sterilisation. Therefore, it seems that the recycling of plastic is an attractive alternative. Recycling reduces the consumption of non-renewable petroleum sources and reduces the pollution involved in the production process.

There are two different methods of recycling waste plastic. The first method (mechanical treatment) is to reprocess it and to give it other forms and other uses. For example, waste PET (polyethylene terephthalate) used in beverage containers is recycled into insulation boards [2]. The second method transforms waste plastic into lighter hydrocarbons by chemical or thermal treatment.

A promising plastic recycling process, using this second method, is being undertaken by a consortium of five European chemical companies: B.P. Chemicals, D.S.M., Elf Atochem, Enichem and Petrofina. The process involving thermal cracking transforms a mixture of waste plastic into an intermediate hydrocarbon stream that can be used as a feed-stock for petrochemical or refinery processes. The fact that the process can treat a mixture of plastic avoids the cost of sorting. Only a crude sorting by density is needed to separate the bulk contaminants.

The diagram of the polymer cracking process is shown in Figure 1.1. The plastic mixture is fed to the process in the form of pellets. These pellets are fed to the main reactor, a fluidised bed in which the fluidisation gas is a mixture of hydrocarbons at about 500^oC. The product mixture has a lower molecular weight than the initial feed. The product leaves the bed and this outlet gas goes to a second fluidised bed. In this second bed the chlorine, from the PVC, reacts with the calcium oxide to give calcium chloride. The outlet gas goes into a distillation column where the heavy fraction is recirculated to the main reactor and the lighter fraction is split. One fraction is condensed as a wax and removed for storage and the other is recycled to the bed as fluidising gas. The condensed wax can be utilised to produce gasoline and light olefins in a fluidised catalytic cracker unit. It can also produce ethylene and other light olefins using a steam cracker.

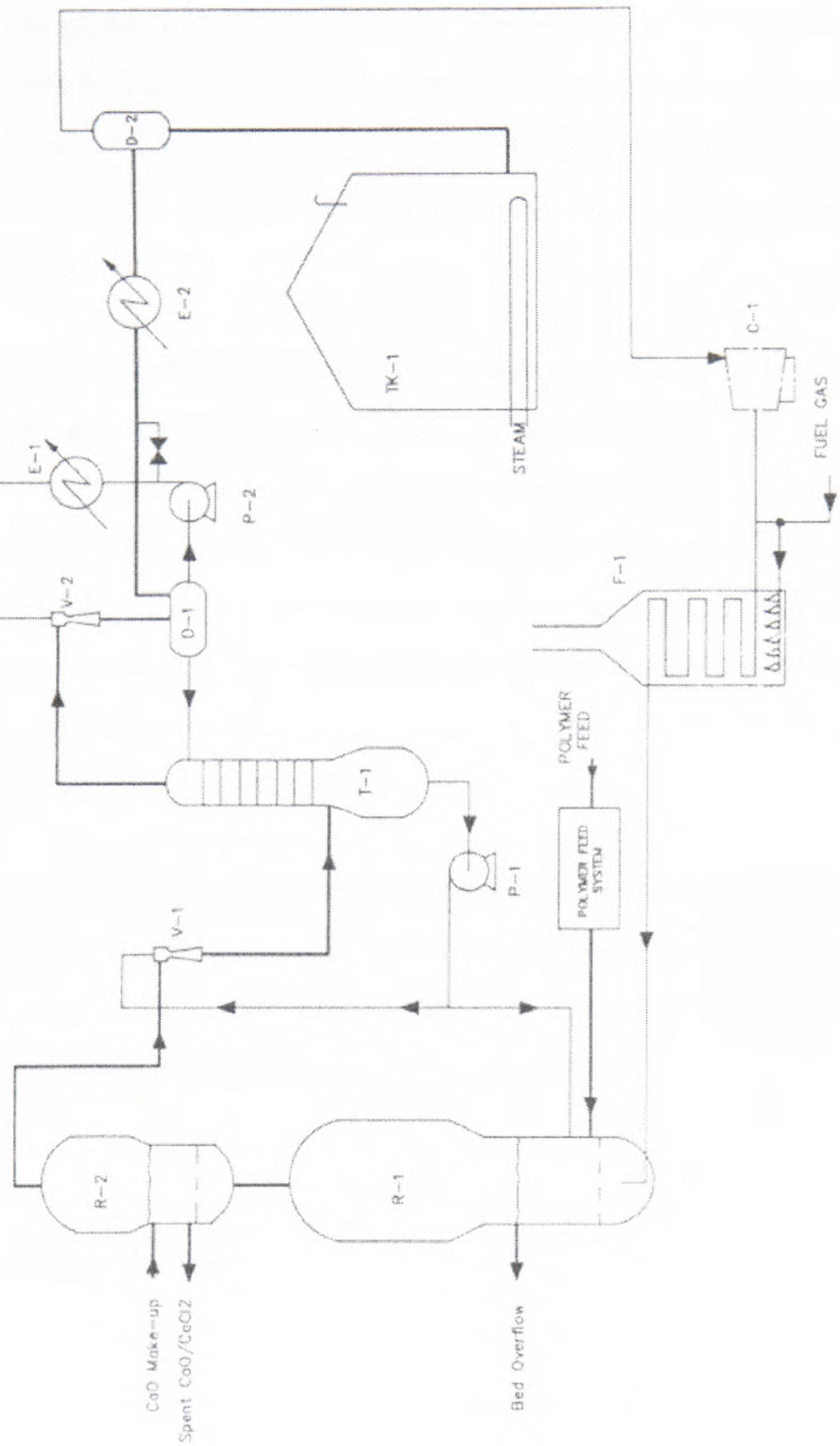

Figure 1.1: Diagram of the polymer cracking process

B.P. Chemicals, at Grangemouth (UK), is carrying out this process using a pilot scale plant. Three different product fractions are produced: a liquid product (80-90%), a gas fraction (10-20%) and a solid fraction of mostly carbon fibres (0-2%). One of the problems found is the carry-over of fibrous carbon from the main fluidised bed, where the cracking of the waste polymer is undertaken. These fibres have a very loose reticular structure and deposit downstream in the pipe work, in the calcium oxide fluidised bed and in the cyclones, producing an increase in the pressure drop.

The mechanism of formation of the fibres is not very clear. It is thought that their precursors are formed on active metal sites in the bed wall or associated with metallic contaminants present in the feed. After desorption from these active sites the fibre precursors travel to the freeboard where there may be recirculation zones that allow fibre growth. The present project is an attempt to elucidate the hydrodynamic behaviour of the gas in the freeboard of the fluidised bed, in order to detect turbulent structures, vortices and dead zones that are believed to be responsible for the growth of the fibres.

Rix [3] proved that particle image velocimetry (PIV), an optical flow measurement and visualisation technique, is very powerful for studying the flow in the freeboard of a fluidised bed. PIV is therefore a very convenient technique to tackle the present research (See Chapter 4).

1.2 Background

When a gas passes upward through a bed of particles and the flowrate is enough to freely support the particles, the bed is said to be fluidised [1]. If the flowrate is increased above the minimum required to produced a fluidised bed (minimum

[1] In the present work only gas fluidised beds with particles of narrow size distribution are considered.

fluidisation velocity, u_{mf}), the gas in excess will pass through the bed in the form of bubbles. The presence of bubbles in fluidised beds is advantageous as it leads to rapid mixing of the solids in the bed and high heat transfer rates between the bed and the heat exchange surfaces. On the other hand, in the case of a catalytic fluidised bed reactor, bubble formation causes bypassing of the reaction gas, reducing the yield of the reactor. The presence of bubbles determines the behaviour of a fluidised bed. For this reason, a large number of studies have been carried out on this topic.

Fluidised beds have a number of advantages over most other methods of gas-solid contacting. There are high rates of heat transfer, between a heat transfer surface and the bed and between the particles and the gas of the bed. This leads to temperature uniformity. The rates of mass transfer are also very high. The solid mobility is an advantage, mixing is very thorough and the bed is practically isothermal. Therefore, fluidised beds have been utilised in many process industries (including chemicals, petroleum, metallurgy, food and pharmaceuticals). Many fluidised bed operations are physical, as for example drying, coating, classification, granulation, and utilise rapid heat transfer as in quenching or annealing. Other operations involve chemical reactions including the catalytic or thermal cracking of hydrocarbons, the synthesis of acrylonitrile, phthalic anhydride and polyethylene, the roasting of metallurgical ores and the regeneration of spent catalysts. In recent years fluidised beds have been of special interest because of their use in coal combustion, gasification processes and clean fossil fuel technology. A new application of fluidised beds is in material processing (silicone and particles with metallic coating).

A fluidised bed reactor has two main parts: the fluidised bed and the freeboard. The freeboard is the region above the bed material where the particles ejected by the bubbles can disengage from the gas. The freeboard of a fluidised bed is one of the important parameters that must be considered when designing a fluidised bed. In a fluidised bed reactor, the freeboard could provide a region where additional

reaction could take place. An undersized freeboard will decrease the conversion and an oversized freeboard will cause a rise in the capital and operating cost. Furthermore, in some cases the entrainment of solid is disadvantageous, because it can contribute to loss of solids; this could imply a high cost (for example in a catalytic process) or a pollution problem (for example in a coal combustion process). The freeboard could also be a region of high attrition. An understanding of the hydrodynamics of the freeboard is essential for design of the fluidised bed as well as the solids recovery equipment downstream.

1.3 Scope of thesis

The aim of the present work is to increase the understanding of the physics of the gas freeboard flow. It is intended to apply this understanding to improve the design of the fluidised bed freeboard, used for the cracking polymer process, to reduce the growth of carbon fibres. In order to achieve this, the effect of different factors influencing the flow in the freeboard, such as the mechanism of bubble eruption, the superficial gas velocity and the freeboard geometry, will be analysed. In particular a freeboard with an expansion section will be studied, as this is the geometry used by B.P. Grangemouth.

1.4 Structure of thesis

Firstly, in Chapter 2, a brief review of bubbling beds, including bubble characteristics, is presented. Once the hydrodynamics of the dense bed is understood, the phenomena occurring at the bed surface, such as bubble eruption and particle ejection into the freeboard, are considered. After this, previous experimental investigations of freeboard flow are summarised and the most important models of entrainment and elutriation are described. This knowledge is important when

attempting to interpret the PIV results.

Chapter 3 describes the experimental equipment. The arguments and calculations considered to scale-down the pilot plant to the bench-scale apparatus are included here. The fluidised bed, the fluidised material and the device utilised to inject single bubbles are explained. A section is dedicated to the choice of the material to construct the bed, since this is of vital importance for the experimental technique.

The principles of particle image velocimetry (PIV) are explained in Chapter 4. PIV is a whole flow field analysis technique based on: i) the seeding of the gas, ii) the illumination of a plane of the flow with a pulsed light source and iii) the measurement of the displacement of seeding particles between pulses and from this the gas velocity at each point. The implementation used in this study and the analysis of the possible errors are also addressed.

The expanded freeboard is divided into three different parts: i) the region directly above the bed surface, ii) the expansion section and iii) the expanded section. Each part is independently studied and the results are described in Chapter 5. Before undertaking the analysis of the freeboard flow at plant operation conditions, the single bubble eruption mechanism is studied. The flow in the expansion section could not be measured due to particle deposition on the wall. Velocity vector maps of the expanded section of the freeboard are presented and analysed.

The influence of some parameters (such as bed outlet location, superficial gas velocity and freeboard geometry) on the freeboard flow is also analysed in Chapter 6. This work is concluded with the discussion of the results (Chapter 7), their implication in fibre growth and conclusions and suggestions for further work (Chapter 8).

Chapter 2

Literature survey

The freeboard above a bubbling fluidised bed has been extensively studied due to its importance in fluidised bed design. The flow pattern in the freeboard is mainly determined by bubble eruption at the bed surface. Therefore, this review first looks at the principles of bubbling fluidised beds and bubble characteristics, including shape, size, distribution, velocity, frequency and number of bubbles erupting simultaneously. The similarity between single injected bubbles and bubbles in freely bubbling beds is also included. The starting point of the freeboard review will be the study of the flow above single injected bubbles. Maxworthy's vortex ring theory [4] is included in this section, since it has been applied to some of the freeboard flow models. The origin of ejected particles into the freeboard, experimental investigations of particles and gas flow are also reviewed.

Some of the correlations proposed to account for the particle flow (entrainment and elutriation) are presented. However, most of them are empirical or semi-empirical (the parameters included in these models need to be determined for each system) and only applicable to the experimental conditions for which they were calculated. This study is mainly concerned with the gas flow in the free-

board (since the gas superficial velocity is not high enough to remove a significant amount of solids from the bed); however, as particle motion may provide information on bubble eruption mechanisms, it is relevant to this work. Finally, the very few studies about expanded freeboards are considered.

2.1 Principles of bubbling fluidised beds

When a fluidised bed is operated in the bubbling regime (i.e. the superficial gas velocity is above minimum fluidization velocity and below particle terminal velocity) the bed can be considered as formed by two phases: i) a continuous phase (also termed dense, particulate or emulsion phase) in which the particles are suspended by the fluidising gas and ii) a discontinuous phase (also termed lean, bubble or visible phase) formed by voids significantly larger than the particles.

The two phase theory [5], that proposes that the gas in excess over that necessary to fluidised the bed (Q) passes through the bed in the form of bubbles, has been widely accepted:

$$Q = (u - u_{mf})\, A \tag{2.1}$$

where u is the superficial velocity, u_{mf} minimal fluidisation velocity and A the bed surface area.

Davidson [6] using the two-phase theory and assuming that the bubble is a circular void free of solid and the emulsion phase behaves as an incompressible fluid of constant velocity, far from the bubble, deduced the nature of flow through the bubble. According to Davidson's model the through-flow or "invisible" flow through a bubble is $2 \times u_{mf}$ for a two-dimensional bubble and $3 \times u_{mf}$ for a three-dimensional one. Depending on the bubble velocity the gas processed through a bubble can be: i) fresh, for a stationary bubble, ii) partially recirculated, for a

slow bubble (cloudless) and iii) totally recirculated, for a fast bubble (clouded).

It has been found experimentally that the amount of gas in the form of visible bubbles is less than that expected from Equation 2.2 [7, 8, 9, 10, 11, 12, 13, 14, 15, 16, 17, 18, 19, 20, 21, 22, 23, 24]. Three possible causes have been reported in the literature to account for the difference between the theory and the experimental results:

- Gas flow through the bubbles, as supported by Davidson and Harrison [11] and Lockett *et al.* [12]. They improved Equation (2.1) introducing a constant, k, the value of which is usually between 0.7 and 27, that accounted for the varied through-flow.

$$Q = (u - k\, u_{mf})\, A \tag{2.2}$$

- Increase in the interstitial gas flow above that required to fluidize the bed, for example due to the presence of fines in the bed. This explanation is supported by Rowe *et al.* [13] and Pyle and Harrison [14]. Clift and Grace [7] found that the discrepancy between the two phase model and the experimental observations was due to the two previous reasons, the through flow and the extra flow though the emulsion phase.

- A "shell" surrounding the bubbles, in which the permeability is higher than in the emulsion phase [25].

The dynamics at the bed surface determine the inlet conditions of the freeboard. The mean gas freeboard velocity depends on the superficial velocity. This is a fixed parameter determined by the operating conditions. The bubble behaviour is of extreme importance in determining the freeboard flow. It can be characterised by: the bubble shape, size, rise velocity, distribution, number and frequency. All of them will be briefly reviewed.

Before looking at the bubble features in a bubbling bed, the properties of single

bubbles and the possibility of inferring information from them about spontaneously rising bubbles will be presented.

There is enough evidence to say that a fluidised bed behaves like a liquid (objects sink or float on it, depending on the relative density, and the surface remains horizontal if the vessel is tilted). Thus, the first attempts to understand the nature of bubbles in fluidised beds were made by studying large bubbles (velocities are sufficiently high for viscous and surface tension forces to be negligible compared with inertia and gravitational forces in determining the shape and velocity of the bubble) in "infinite" liquids (the wall is far enough away and it does not interfere with the bubble).

A more realistic method to study the nature of bubbles in bubbling beds is studying single injected bubbles in an incipiently fluidised bed. Rowe [26] carried out an investigation to determine if injected bubbles are similar to spontaneous bubbles formed in freely fluidised beds. He found:

- Bubbles shrink if they are injected in a bed in which the superficial gas velocity is close to minimum fluidisation velocity.
- Bubbles grow when the flow rate is increased above a certain value.
- The shape of injected bubbles is similar to those in a bubbling bed.
- The rise velocity is slightly higher in spontaneous bubbles than in injected bubbles.

He concluded that injected bubbles have a very similar behaviour to spontaneously formed bubbles.

Bubbles inside fluidised beds have been studied using probes, sensors (optical, capacitance and pressure) and image techniques (X-ray, γ-ray and capacitance tomography). Another very useful way to investigate bubbles characteristics is

to study the bed surface. Among others, Hepbasli [27] measured the bubble size and frequency, at the surface, using frame by frame video analysis.

Bubble shape and size

X-ray visualisations have shown that bubbles in three-dimensional bubbling beds have "spherical-cap" shape, i.e., spherical on the front surface with an indentation at the rear. Two diameters can be defined :

- D_e, the equivalent bubble diameter, defined as the diameter of a sphere having a volume equal to the actual bubble.
- D_f, the frontal diameter at bubble eruption.

Bubbles in beds of coarse particles are bigger than bubbles in beds of fine particles. A number of semi-empirical correlations for bubble growth have been proposed in the literature (based on the equivalent diameter being proportional to the excess of gas velocity and height $D_e = f((u - u_{mf})$, H), of which Darton's [28] is one of the most generally accepted, for its underlying principles [29, 30, 31]. Darton's model is based on bubble growth by coalescence. Coalescence takes place between neighbouring bubbles. The distance travelled by the bubbles before they coalesce is proportional to their horizontal separation. Bubbles grow by coalescence in beds of group B or D particles (according to Geldart's classification [32]). However, in beds of fine particles (group A particles) bubbles coalesce and split, therefore the bubble size is determined by a balance between these two mechanisms. Horio [33] proposed an equation that can be applied for the whole range of non-cohesive particles (A, B and D) and for particles B and D. This equation converges towards the traditional equations ($D_e = f((u - u_{mf})$, H). A good review of bubble size correlations is given by Davidson *et al* [34].

Bubble distribution

The flow pattern in a bubbling bed depends on the gas flow rate, particle characteristics and the height of the bed. In general, the bubbles tend to concentrate near the walls close to the distributor. They tend to coalesce and move towards the centre while they are rising upwards, producing a central bubble-preferred region (due to constraints in bubble coalescence imposed by the wall [35, 36, 34]) if the bed is deep or the flow rate is high enough. The bubble flow generates a solid circulation pattern; at the same time, the solids flow reinforces the bubble pattern. Broadly speaking, it can be said that the particles follow an "ascendant path near the wall, descendent in the centre" model at low fluidising velocity or in a shallow bed; in contrast, the particles follow an "ascendant by the centre, descendent near the wall" model at high fluidising velocity or in a deep bed.

Bubble velocity

The most accepted equation for bubble velocity (u_b) is given by Davidson and Harrison [18] according to the two-phase theory. The absolute bubble velocity is the bubble rise velocity through an infinite stagnant medium ($u_{b\infty}$) plus the upward velocity of the particulate phase between bubbles ($u - u_{mf}$):

$$u_b = u - u_{mf} + u_{b\infty} \tag{2.3}$$

where $u_{b\infty}$ can be estimated using the Davies-Taylor equation:

$$u_{b\infty} = 0.711\sqrt{D_e g} \tag{2.4}$$

Hilligardt and Werther [37] modified the equation:

$$u_b = \phi(u - u_{mf}) + \theta u_{b\infty} \tag{2.5}$$

where ϕ accounts for the deviation of the visible bubble flow rate from the two phase theory and θ for the deviation from the behaviour of a single bubble (bubbles in bubbling beds are affected by neighbouring bubbles and the wall). As in the case of bubble size, many correlations have been proposed, depending of the fluidising system and conditions; a good review of them can be found in

the book by Davidson's *et al* [34].

Frequency and number of bubbles erupting simultaneously

Levy *et al.* [38], using continuity considerations, determined theoretically the number of bubbles erupting simultaneously. This can be expressed as:

$$N = \frac{\delta A}{\frac{\pi}{4}(\Phi_f D_e)^2} \tag{2.6}$$

where δ is the fraction of surface area occupied by bubbles:

$$\delta = \frac{u - u_e}{u_b + mu^* - u_e} \tag{2.7}$$

where m is a through-flow coefficient that relates to k according to the following equation:

$$k = 1 + (m - 1)\delta \tag{2.8}$$

u_e is the gas velocity in the emulsion phase, u^* the gas velocity at minimum fluidisation velocity or at minimum bubbling velocity and Φ_f is a bubble flow area shape factor.

$$\Phi_f = \frac{D_f}{D_e} \tag{2.9}$$

According to Verloop [39] the eruption starts a bit earlier than the actual bubble eruption and finishes a bit later than the bubble has passed, due to the through-flow.

Levy *et al.* [38] proposed an equation for the number of bubble eruptions at the bed surface in unit time and hence the bubble eruption frequency (f):

$$f = \frac{Au_b(u - u_e)}{(u_b + mu^* - u_e)(\frac{\pi D_e^3}{6})} \tag{2.10}$$

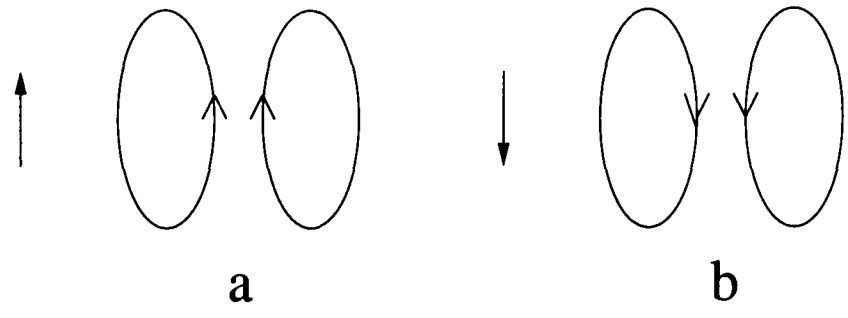

Figure 2.1: Direction of the translational displacement of vortex rings in a stagnant fluid

2.2 Vortex rings

A brief description of Maxworthy's vortex ring theory [4] will be presented before reviewing single erupting bubbles, as some authors [40, 41] have applied Maxworthy's theory [4] to the vortex rings found in the freeboard. Maxworthy studied the growth and velocity of vortex rings (a core surrounded by a circulating toroidal ring) in a stagnant fluid. The vortex rings were generated by the injection of a mass of fluid through a sharp-edged orifice into a stagnant fluid. The vorticity created by viscous forces as a result of separation in the sharp edges rolls up to give rise to a stable vortex ring. The vortex ring has a translational velocity as consequence of the impulse (I) generated by the vorticity:

$$I = \frac{1}{2} \int x \times \omega dV \tag{2.11}$$

x being the position, ω being the vorticity and dV being an element of volume. The direction of movement of the vortex ring is given by the direction of rotation. If the vortex ring is rotating upwards at the centre and downwards at the sides the translational movement is upwards (Figure 2.1a). On the contrary, the vortex ring moves downwards if it rotates downwards at the centre and upwards at the sides (Figure 2.1b).

Vorticity is transmitted to the fluid surrounding the vortex ring and dissipation occurs. This fluid does not have enough vorticity to flow around the vortex and it is entrained into the rear of the vortex. Further away from the vortex,

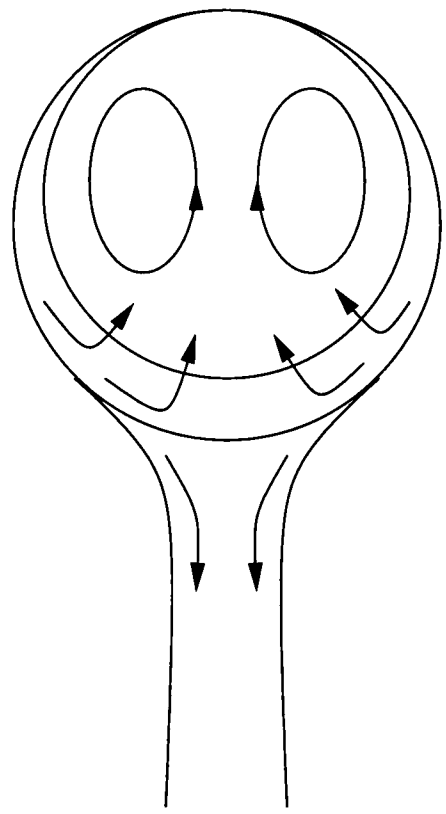

Figure 2.2: Entrainment model of a vortex ring as postulated by Maxwrothy

where the vorticity reaches smaller values, the fluid particles traverse the vortex without being entrained and form a wake (Figure 2.2 shows a diagram of the entrainment process). The thickness of the fluid layer entrained is $\delta_1 = C_1(\upsilon t')^{1/2}$ and the velocity C_2U, being $t' = C_3a/U$ the time for a fluid particle to traverse the distance around the bubble and υ the kinematic viscosity of the fluid. The circumference of the entrained region is C_4a. The growth rate of the volume V of the vortex ring is:

$$dV/dt = C_1C_2C_3aU_{vr}(\upsilon t')^{1/2} \tag{2.12}$$

with $C = C_1C_2C_3C_4^{1/2}$ Equation 2.12 becomes:

$$dV/dt = C\upsilon^{1/2}a^{3/2}U_{vr}^{1/2} \tag{2.13}$$

Equation 2.13 is used by Pemberton and Davidson [40] to deduce the ghost bubble velocity as function of the height above the bed surface(Section 2.3).

The translational velocity due to the self-induced movement generated by the

vorticity is given by:

$$U_{vr} \propto (I/\upsilon)^{1/2} t^{-1} \tag{2.14}$$

υ being the kinematic viscosity and I the impulse responsible for the vortex ring movement:

$$I \propto K a^2 \tag{2.15}$$

where K is the circulation and a a characteristic dimension of the vortex ring:

$$a \propto (I/\upsilon)^{1/6} t^{1/3} \tag{2.16}$$

Caram *et al.* [41] used Equation 2.14 to compare with the measured translational velocity of the vortex ring generated after bubble eruption (Section 2.3).

2.3 Single erupting bubbles

Although the flow pattern above an incipiently fluidised bed is not uniform, disturbances of the flow are very small compared with the disturbance due to bubble eruption. The first step in understanding the flow above a bubbling bed is to study the flow pattern due to a single erupting bubble at the bed surface.

Levy and Lockwood [42], using laser Doppler anemometry, measured the gas velocity variations with time and position above the bed surface after the eruption of single injected bubbles. A 0.3×0.6 m sand bed (mean particle diameter 1 or 0.4 mm) was used. They found that after a bubble erupts at the bed surface, the gas velocity is lower than the minimum fluidisation velocity at the bubble centre-line and higher at either side of the eruption. Consequently, they deduced the presence of a vortex ring near the wall. The vortex ring rotated in a clockwise

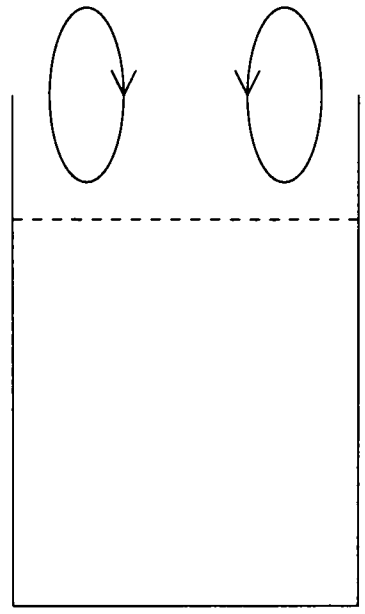

Figure 2.3: Diagram of the vortex ring visualised by Levy and Lockwood

direction at the left of the erupting bubble and an anti-clockwise direction at the right (Figure 2.3). The existence of the vortex was confirmed by the injection of smoke.

It is derived from Davidson's model that when the velocity of a bubble is higher than the velocity in the emulsion phase (u_{mf}/ε_{mf}) gas flows into the bubble from below and leaves the bubble at the top. The gas leaving the bubble is recirculated, since the bubble rises faster than the emulsion phase. This gas circulation (cloud) (See Figure 2.4) is similar to a spherical vortex [6]. In some respects, bubble eruption in liquids provides a point of reference for the behaviour of fluidised beds. Pemberton and Davidson [40] visualised the eruption of a single ammonium chloride bubble from stagnant water into air. The bubble kept its identity after breaking through the surface of the water and was termed a "ghost bubble". The concept of the ghost bubbles was extended to fluidised beds. It was postulated that the ghost bubbles possess a circulating flow, due to the circulating movement that they acquire when travelling in the fluidised bed. If the circulation was laminar Pemberton and Davidson termed the ghost bubbles "vortex rings" and if turbulent the ghost bubbles were termed "puffs" (although turbulent vortex rings would have been a more obvious term). It was suggested that the ghost bubbles rise in the freeboard entraining fluid from the surrounding medium which causes them to decelerate.

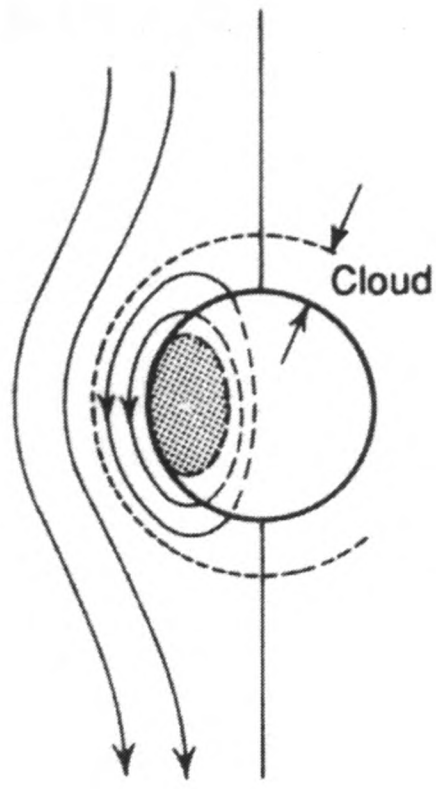

Figure 2.4: Gas streamlines near a single rising bubble (bubble rising faster than the emulsion phase) from Davidson model

Pemberton and Davidson used Maxworthy's theory [4] to estimate the deceleration of a ghost bubble, relative to the bulk fluid, as function of the freeboard height. Assuming that a vortex ring is spherical, the growth rate is given by:

$$\frac{dV}{dt} = \frac{d}{dt}\left(\frac{4\pi a^3}{3}\right) \tag{2.17}$$

Since the vortex ring and the surrounding medium are the same fluid, the conservation of momentum gives:

$$U_{vr}a^3 = U_{vro}a_o^3 \tag{2.18}$$

Differentiating Equation 2.18:

$$3a^2\frac{da}{dt} = -\frac{a^2}{U_{vr}}\frac{dU_{vr}}{dt} \tag{2.19}$$

Since:

$$\frac{dU_{vr}}{dt} = \frac{dU_{vr}}{dz}\frac{dz}{dt} = (U + U_{vr})\frac{dU_{vr}}{dz} \tag{2.20}$$

z being the height above the bed surface. Equating Equation 2.13 to Equation 2.17:

$$\frac{U + U_{vr}}{U_{vr}^2}\frac{dU_{vr}}{dz} = \frac{-3\sqrt{\pi\upsilon}}{4U_{vro}^{1/2}a_o^{3/2}} = \beta_1 \tag{2.21}$$

An equation relating the vortex ring velocity with the height above the bed surface is obtained integrating Equation 2.21 considering $U_{vr} = U_{vro}$ at $z = 0$:

$$ln\frac{U_{vro}}{U_{vr}} + \frac{U}{U_{vro}}\left(\frac{U_{vro}}{U_{vr}} - 1\right) = \beta_1 z \tag{2.22}$$

Velocity fluctuations at different heights above single air bubbles erupting into air, having risen through either a stagnant liquid (water or fluorisol to test the effect of the surface tension) or through an incipiently fluidised bed ($0.6\ m^2 \times 0.4\ m$ bed of 300 μm sand), were measured, using a hot wire anemometer placed vertically in the bubble centreline. Velocity fluctuations decreased with height, consistent with gas entrainment occurring when the ghost bubble rises in the freeboard. However, hot wire anemometry cannot determine the direction of the velocity, making it impossible to know if the fluctuations are due to ghost bubbles rising in the freeboard or to a descendent movement of the gas after bubble eruption. A good agreement between the measured velocity fluctuations, as function of the height above the bed surface, and the rise velocity of vortex rings, deduced from Maxworthy's model, was found, although no other evidence that the fluctuations were due to an identifiable vortex ring existed.

Caram *et al.* [41] visualised a vortex ring after a single smoke-filled bubble erupted above an incipiently fluidised bed. Two different beds were used: i) a semi-cylindrical bed (28.8 cm) and ii) a cylindrical one (19 cm). Five different materials were used: alumina powder (60 μm), glass spheres (255, 300 and 560 μm) and plastic particles (640 μm). The direction of circulation of the vortex ring was clockwise at the left and anti-clockwise at the right, as Levy and Lockwood [42] found, which would be the opposite direction to the circulation inside ghost

bubbles if they existed. They obtained gas velocity measurements along the bubble axis with time using a hot film probe. It was found that after bubble eruption, the velocity at the probe location decreased until a certain critical value and then increased again. The gas velocity measured, using cine-photography, above the erupting bubble was compared with the translational velocity of a vortex ring [4]. This comparison was of limited validity as Maxworthy's model assumes the vortex ring is travelling in stagnant fluid. Furthermore, the self-induction movement of the vortex ring visualised by Caram *et al.* would be expected to produce a downwards translation. However, this translation was of course impeded by the presence of the bed surface, again questioning the relevance of Maxworthy's model to this case. The vortex rings go upwards in the freeboard pushed by the gas velocity leaving the fluidised bed, if it is sufficiently high.

Levy *et al.* [43] calculated the gas flow through an erupting bubble based on a model that combined Davidson's model [6] with kinematic and dynamic boundary conditions for the movement of the free surface. They considered bubbles to be spherical, of fixed size and moving upward with constant velocity. The gas velocity profile obtained had a peak at the bubble centre-line and the velocity decreased with distance from the centre, because the bubble is rising faster than the gas surrounding it, hence any gas leaving the side of the bubble is recirculated. However, the results have not been verified experimentally.

A number of authors have also studied the flow above a single erupting bubble [40, 41, 42, 43]. However, information about the nature of the gas pattern due to the eruption of a bubble is very limited and the mechanism is not well understood.

2.4 Origin of the particles in the freeboard

Levy [44], using Laser Doppler Anemometry, measured particle velocities in the freeboard which were much higher than the superficial gas velocity, especially

near the bed surface. This leads one to think that the particles are ejected into the freeboard by bursting bubbles and carried by the gas flow. The origin of these ejected particles has been a controversial issue. Firstly, there were two different mechanisms proposed for the origin of ejected particles: i) particles coming from the bubble wake and ii) particles coming from the bubble nose.

Do *et al.* [45] used a high speed camera to photograph erupting injected bubbles at the surface of a two-dimensional fluidised bed. The bed particles were glass beads ($177-250\ \mu m$ diameter); the superficial velocity was $(1.5-3) \times u_{mf}$. From the cine film they observed ejected particles which originated at the bed nose. A rising bubble causes a bulge at the bed surface. Particles rain off from the bulge while the bubble is ascending; after the bubble reaches its maximum height, less than a bubble diameter, these particles return to the bed surface.

Saxena and Mathur [46] also found that the ejected particles came from the bubble nose. They used a high speed video camera to film a two-dimensional bed using three different kinds of particles: 265 μm diameter glass beads, 2064 μm diameter millet seeds and 4578 μm diameter green peas. The bed was operated at $1.5 \times u_{mf}$.

Rowe *et al.* [47] utilised dyed particles to analyse the origin of ejected particles in a three-dimensional bed (14 cm diameter). They injected single bubbles in a 250 μm diameter glass ballotini bed. Particles that initially were at the bottom of the bed were carried in the bubble wake and deposited at the bed surface. They also observed bottom particles at the surface of a freely bubbling fluidised bed at $1.5 \times u_{mf}$.

George and Grace [48] used a thin layer of coke particles at the bed surface to see the origin of elutriated particles. They found that less than the 4% of the particles ejected were coke particles. This led them to think that the ejected particles came from the wake rather than from the bubble nose (although this could also be due to the draining of particles when the bulge is rising). They also

observed that the amount of ejected solids increases with the bubble size.

The elutriation rate based on the mechanism of projection from the wake of the bubble over-predicts the experimental results [49]. However, the elutriation rate based on the mechanism of projection from the roof of the bubble under-predicts it. Chen and Saxena [50] tried to overcome this problem by considering the amount of solid ejected as the sum of a fraction of the bulge and the wake solids, but their model still over-predicted the experimental data. Saxena [51] proposed a model in which the bulge is considered to be a concentric circle around the bubble. The solution of this model fits quite well the experimental data obtained in a two dimensional fluidised bed.

Hatano and Ishida [52], using glass beads in a 15 cm diameter bed operated between $1.5 - 5 \times u_{mf}$, observed four different bubble ejection mechanisms which are determined by the kind of bubble arriving at the bed surface. They distinguish between four different kinds of bubble eruption:

- isolated bubbles,
- successive bubbles,
- coalescing bubbles and
- successive coalescing bubbles.

They found that the first two patterns are quite frequent but the ejected particle velocities are lower than the bubble velocity. The opposite occurs in the case of the last two mechanisms, whose contribution to the entrainment mechanism is higher than the first two.

Levy and Lockwood [42] observed bubbles of different natures to determine the particle ejection mechanism. They used two- and three-dimensional beds of different bed materials (125 μm and 450 μm glass beads, 750 μm plastic and 110 μm

catalyst) operating at $1.05-1.08 \times u_{mf}$ with injected bubbles or $3.44 \times u_{mf}$ at free bubbling conditions. They used a high speed video system to obtain information of the eruption process. They found four types of ejection mechanisms:

- Type 1: The bulge bursts. The bulge layer stretches and moves upward when the bubble is approaching the bed surface. After rising a height a little bit smaller than the bubble diameter the bulge particles fall back to the bed surface.

- Type 2: Bubbles coalesce just below the free surface. The roof material of the first bubble is thrown away. The layer of particles between the two bubbles join to the roof layer of the first bubble. The resulting particle cloud expands upwards and outwards and thus comes back to the bed surface.

- Type 3: The wake from the second bubble forms a spike that is ejected higher than the bulge of the middle layer of the preceding bubble.

- Type 4: Jet spray occurs when bubbles coalesce and the trailing bubble elongates. This forms a jet of gas which shoots through the first bubble. The solids of the trailing bubbles are entrained in the bulge of the leading bubble up above the bed surface.

They concluded that in a three-dimensional bed, approximately 90% of the bubbles eject particles according to the first mechanism. Ten per cent of the bubble were double bubbles of which only 3.8% showed a jet and 72.1% showed a wake spike. Something similar was observed in a two-dimensional bed, although the number of jets was smaller than in the case of the three-dimensional bed.

From the above it is concluded that the mechanism of particle ejection depends on the nature of bubble eruption. Pemberton and Davidson [53] observed that bubble coalescence increased with superficial velocity, therefore increasing the number of particles ejected from the bubble wake. The conclusion that can be

obtained from all the studies done to elucidate the origin of the ejected particles, is that the source of the particles is a mixture of both the bulge and the wake of single bubbles, depending on the bubble nature. Usually, the bulge bursting mechanism is more frequent; this mechanism is favoured at low velocity. However, the wake mechanism is more powerful, ejecting particles at higher velocities into the freeboard.

2.5 Particle flow pattern in the freeboard

The particle velocity, the flux and the concentration are the parameters more often measured in the freeboard. In this section, only the findings concerning experimental particle velocity measurements will be considered. This will help to understand the entrainment and elutriation models reviewed later on. A summary of the main works and experimental conditions are presented in Table 2.1. Fibre optic, laser Doppler anemometry (LDA) and laser Doppler velocimetry (LDV) are the experimental techniques used to measure particle velocities, in these studies.

Morooka *et al.* [54] measured the radial velocity profile, at 0.375 m, 0.875 m and 1.375 m above the static bed surface. Upward velocity (higher than superficial velocity) was found at the bed centre and downflow near the wall. The maximum downflow velocity decreased with increasing height. Both ascending and descending velocities increased with superficial velocity.

Horio *et al.* [55], measuring the vertical particle velocity at 0.4, 0.6, 1.0, 1.4 and 1.8 m above the static bed surface and found behaviour similar to Morooka *et al.* Intermittent particle flow, including descending flow was found at the centre of the freeboard; however, the mean velocity was higher than superficial velocity.

Levy and Lockwood [42] were the first to use a non-intrusive technique to meas-

ure the freeboard flow: laser Doppler velocimetry (LDV). The particle velocity was measured above a single injected bubble of 12 *cm* diameter in a bed just above minimum fluidisation velocity. The sand velocity measured at the bubble centreline was lower than the gas velocity at that point. 10 *cm* away from the bed centreline the sand had a descending movement. Very low particle velocities were found when the bed was freely bubbling.

Hamdullahpur and MacKay [56] used LDV implemented by a fluorescence emission technique. The gas seeding particles were coated with a fluorescent substance and an optical filter was used to distinguish between the signal of the gas and particle flow. The bed particles were sand particles with terminal velocity smaller than the fluidizing velocities. It was found that the axial particle velocity profile is a two-stage decay with height, as shown in Figure 2.5. The change of slope is reached when the local mean particle velocity becomes equal to the superficial gas velocity. It was suggested as a possible explanation for this profile that the particles are ejected with ghost bubbles. The ghost bubbles would decelerate while they are going up in the freeboard. When the ghost bubbles reach the average gas velocity the particles would disengage from the ghost bubble and follow the gas.

Berkelmann and Renz [57], used LDV and a particle sizing system, simultaneously, to calculate particle velocity distribution in a commercial combustor. An upward velocity at the bed centre and the downward velocity near the wall were found, at 0.8 and 1.6 m above the bed surface. It was suggested that particles are entrained from the bed by erupting bubbles, hit the wall, lose their momentum and move down near the wall. At 3.6 m above the bed surface only upward flow was measured. It was also found that at different distances from the wall, the velocity of the particles is independent of particle size (0.8 m above the bed surface); this indicates that at that height the particle flow is determined by erupting bubbles which results in the same average velocity for all the particle sizes.

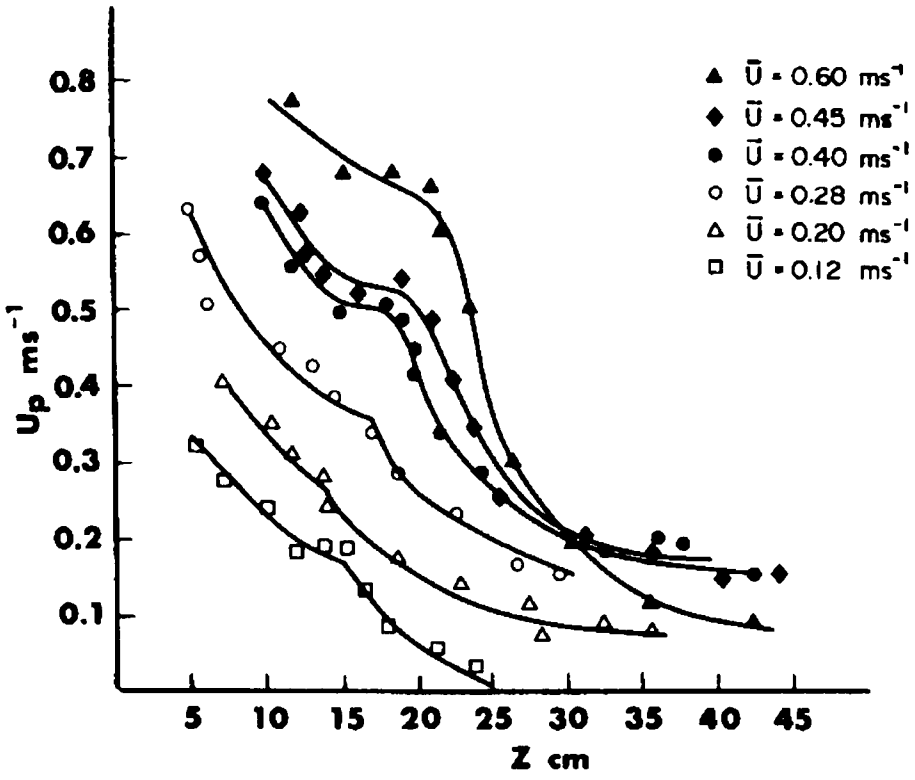

Figure 2.5: Variation of axial particle velocities with position above the bed surface at column centerline. From Hamdullahpur and MacKay (1986)

2.6 Gas flow pattern in the freeboard

A few authors have measured the mean velocity and the fluctuations of the velocity in the freeboard, using either hot wire anemometry or laser Doppler velocimetry. The most significant investigations and the experimental conditions are summarised in Table 2.2.

Horio *et al.* [55], using a hot wire anemometer, measured the radial profile of vertical and horizontal velocity fluctuations (as the fluctuations detected by a horizontally placed or a vertically placed hot wire, although this is questionable, since the single hot wire may register a mixture of both components of the velocity in each position). The measurements were taken at heights between 0.7 and 1.6 m above the bed surface. The vertical component of the fluctuations was higher at the bed centreline and lower near the wall, 0.7 m above the bed surface. The profile reversed with height, presenting a minimum at the bed centreline and a maximum near the wall, at 1.3 m above the bed surface. The horizontal component of the velocity fluctuation did not vary significantly in the radial

Author	Technique	D_b (m)	H_s (m)	u_{mf} (m/s)	u (m/s)	Bed material	d_p (μm)
Morooka *et al.* (1980)	Fibre optic	0.12	1		0.15 0.5	FCC	65
Horio *et al.* (1980)	Fibre optic	0.24	0.2	0.06 0.69	0.3 0.6	glass beads	164 1350
Levy *et al.* (1983)	LDA	0.3× 0.6	0.2 0.36	0.135 0.5	0.4 0.85	sand	400 1000
Hamdullahpur *et al.* (1986)	LDV	0.32× 0.176	0.05 0.12	0.07	0.12 0.60	sand	300
Berkelmann *et al.* (1991)	LDV	2.25× 2.25	1.4		0.95	sand+ ash	100- 5000

Table 2.1: Details about particle measurements in the freeboard

direction.

They also measured the axial profile of the mean vertical component of the velocity fluctuations. They observed an exponential decay of the turbulence with height. It was found that the turbulence intensity increased with gas velocity, bed height and with decreasing particle size. No exponential decay was found when there were no bubbles; therefore, they deduced that the turbulence is induced by erupting bubbles at the bed surface. This was confirmed by the fact that the frequency of the turbulence (calculated as the auto-correlation of the velocity fluctuation) coincided with the bubble frequency.

It was postulated that the decay of turbulence in the freeboard is the result of a decay of the velocity pulsation initiated at the bed surface for the erupting bubbles [55]. It was also assumed that the decay of the turbulence is similar to that of a steady free jet. The relationship for the axial turbulent intensity ($\tilde{u}_v^{'}$) with height (z) given by Abramovich (1963) was used, with the diameter of the erupting bubble (D_b) as duct diameter and the fluctuating vertical component of the velocity at the bed surface as initial jet velocity:

$$\tilde{u}_v^{'} = K_A 0.98(gD_b)^{1/2}(D_b/z)^m + u_{v\infty}^{'} \tag{2.23}$$

$u_{v\infty}^{'}$ being the intensity of fully developed turbulence. It was found that the linear relationship between the average of the fluctuating vertical velocity over

the horizontal cross-section and the erupting bubble diameter divided by the height is better correlated using empirical parameters than using the Abramovich relationship.

Levy and Lockwood [42], measured the mean gas velocity and the velocity fluctuations at 0.3, 0.5 and 0.7 m above the bed surface. A profile with a maximum near the wall and minimum at the centre was found. The velocity fluctuations were very large, especially near the wall. They indicated that erupting bubbles generate vortex rings, that tend to cancel at the bed centre and to combine near the wall, but they could not confirm this experimentally. To check if the freeboard phenomenon was produced by the presence of the wall, a wall was placed in the middle of the dense bed. However, the profile found was very similar, indicating that the wall affects the freeboard profile.

Pemberton and Davidson [40], using a hot wire anemometer, found the same turbulence decay with height as Horio *et al.* [55]. Three different models were proposed to fit the experimental data:

- If the circulating flow within the "ghost bubble" is laminar: vortex ring. The equation of the vortex ring velocity relative to the bulk flow (U_{vr}), deduced from Maxworthy's theory [4], reads:

$$U_{vr} = u_{vro} \exp(-\beta z) \tag{2.24}$$

  where u_{vro} is the bubble velocity at the bed surface and β the decay constant (that it is a measure of the ghost bubble growth).

- If the circulation within the "ghost bubble" is turbulent: Puff. The variation of the ghost bubble velocity is given by:

$$u/u_o = (1 + zna_o)^{-3} \tag{2.25}$$

  a_o being the bubble radius at the bed surface and n was found to be $1.7 < n < 6$ for puffs in water and $3 < n < 5$ for buoyant puffs.

- Decay of isotropic turbulence: it is assumed that the erupting bubbles at

the bed surface generated isotropic turbulence and a power law decay is used to model the decay of the turbulence:

$$1/u^* = 1/u_o^* + 2.45zuD_e \tag{2.26}$$

where u^* and u_o^* are the root mean square (rms) velocity at height z in the freeboard and at the bed surface, respectively and D_e the diameter of a sphere having the bubble volume.

It was found that Horio's data as well as their own were fitted better by the vortex ring model. The ghost bubble growth β is well predicted for small bubbles, but for large bubbles β decreased, with height above the bed surface, slower than predicted by Maxworthy's theory, suggesting that probably turbulence also has a significant contribution in bubble growth.

Hamdullahpur and MacKay [56], using LDV, studied the gas velocity profiles in the freeboard. It was noticed that the vertical gas velocity, measured in the centre of the bed, reduces with increasing height until it reaches the value of superficial gas velocity (Figure 2.6). The radial velocity profile changes with the height (Figure 2.7). There is a maximum in the centre, near the bed surface, due to the migration of bubbles toward the centre to coalesce. This movement of the bubbles to the centre of the bed, because of coalescence, was reported by Grace and Harrison [58] and Werther and Molerus [35]. At greater heights in the freeboard the maximum moves from the centre towards the wall, until the profile becomes flat.

Lang [59], studying a square and a rectangular bed, found that the gas velocity profile depends on the depth of the bed as well as the superficial velocity. The results can be summarised as:

- The shallow bed showed a dip in axial gas velocity profile with a maximum near the walls. The lowest measurement was taken 0.1 m above the bed surface. The profile shifted at 50 cm above the bed surface, presenting

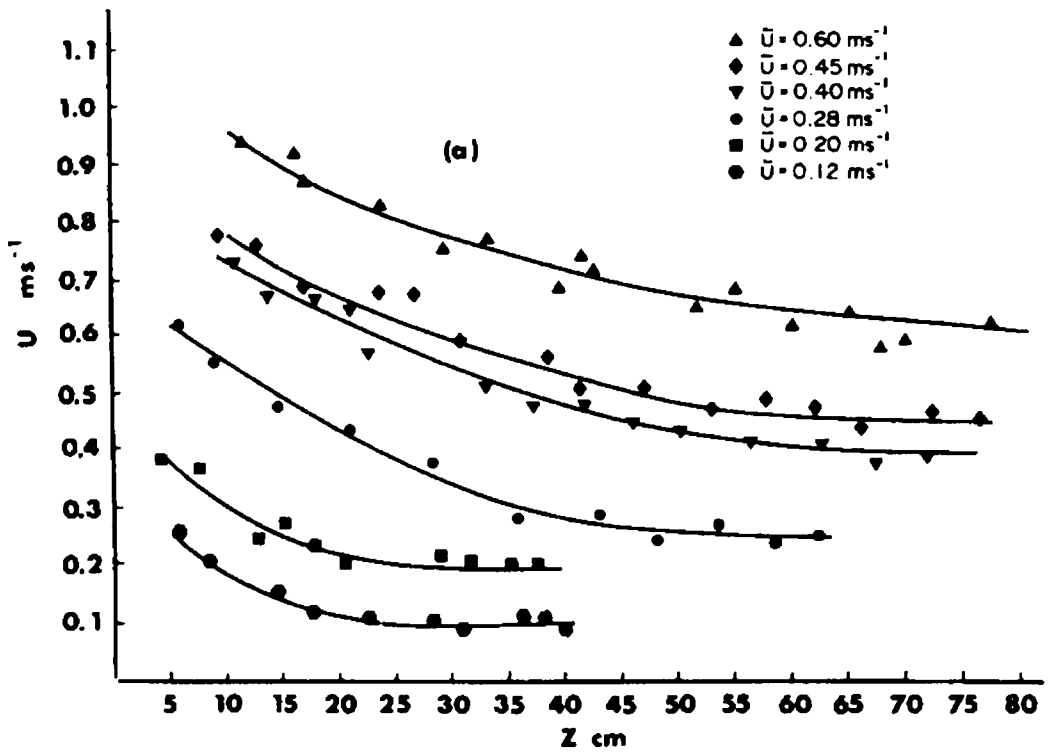

Figure 2.6: Variation of axial local mean velocity with position above the bed surface at column centreline. From Hamdullahpur and MacKay (1986)

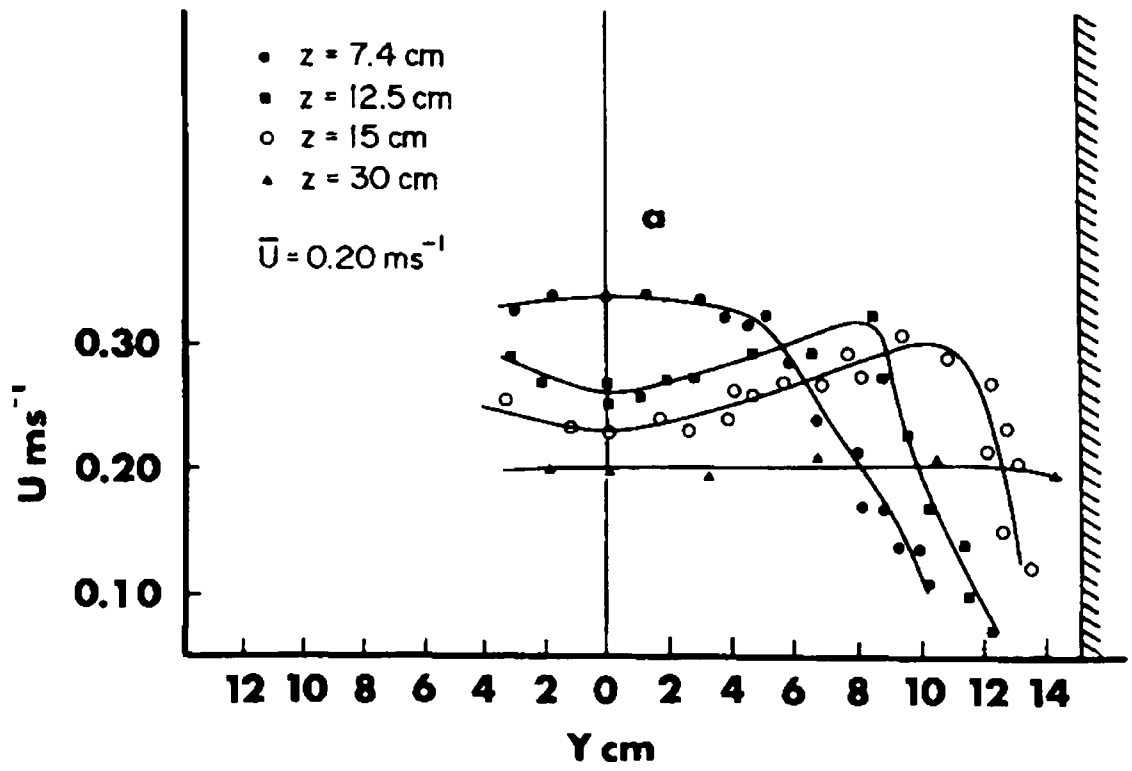

Figure 2.7: Horizontal distribution of local mean gas velocity at different heights above the bed surface z. From Hamdullahpur and MacKay (1986)

a maximum at the centre and minimum near the walls. Lang attributed this behaviour to the bursting bubbles at the surface of the bed, that in a shallow bed move up near the walls [36].

- For deep beds, the profile presented a maximum near the wall and minimum at the bed centre. The lowest measurements were taken 0.9 m above the bed surface and the highest at 1.8 m.

Lang [59] investigated the influence of the bubbling phase on the freeboard flow. The first test was to study the influence of a tube bank, in the bed, on the freeboard behaviour. The general effect of a tube bank on the bubble properties are listed below [60]:

- The bubbles rise velocity decreases.
- The bubble size distribution is not significantly affected.
- The spatial distribution of bubbles is more uniform.

The effect of a tube bank, in the fluidised bed, on the freeboard is:

- Vertical component of the velocity

  -The mean velocity does not change significantly.

  -The fluctuations decrease.

- Horizontal component of the velocity

  -The velocity is modified by the presence of the tube bank, this modification being dependent upon fluidising conditions.

  -The fluctuations are lower.

Lang [59] concluded that the gas flow in the freeboard is not as dependent on bubbling activity at the bed surface as it was believed. He concluded this after

seeing that the vertical velocity profile does not change significantly with the presence of a tube bank in the fluidised bed (although the velocity fluctuations decreased).

Lang's second test was carried out using a distributor plate in which the gas flow was confined to the central region of the bed. Therefore, the maximum bubble activity was in the centre of the bed. He found that in this case the vertical velocity profile in the freeboard was the same as when a homogeneous distributor plate was used. However, the measurements were taken 1.20 m above the bed surface. Thus, it is very difficult to evaluate the effect on the gas close to the bed surface. The results can only be applied in upper regions of the freeboard.

Berkelmann and Renz [57], using LDV, also observed that the gas velocity increases with the distance from the wall, at medium height in the freeboard.

Author	Technique	D_b (m)	H_s (m)	u_{mf} (m/s)	u (m/s)	Bed material	d_p (μm)
Horio *et al.* (1980)	Hot wire	0.24	0.2	0.06 0.69	0.3 0.6	glass beads	164 1350
Levy *et al.* (1983)	LDA	0.3× 0.6	0.2 0.36	0.135 0.5	0.4 0.85	sand	400 1000
Pemberton *et al.* (1984)	Hot wire	0.6 0.3 × 0.3	1-3 0.5-1.5	0.05 0.1	0.3-0.5 0.2-0.4	polymer sand	760 370
Lang 1986	LDA	0.075 ×0.075 0.48 ×0.28	0.03- 0.05 0.6	0.21 0.0095	0.02- 0.04 0.03- 0.04	ballotini sand	440- 530 100
Hamdullahpur *et al.* (1986)	LDV	0.32× 0.176	0.05 0.12	0.07	0.12 0.60	sand	300
Berkelmann *et al.* (1991)	LDV	2.25× 2.25	1.4		0.95	sand+ ash	100- 5000

Table 2.2: Details about gas velocity measurements in the freeboard

2.7 Entrainment and elutriation

The zone above a bubbling fluidised bed has an appreciable particle concentration at high superficial gas velocities. The presence of these particles is mainly due to bubbles bursting at the bed surface. They are subsequently carried with the gas leaving the bed. The density of solids decreases with height in the freeboard until the concentration of solids is constant. The height at which the solid concentration becomes constant is called the *transport disengaging height* (TDH). This is an important parameter in the freeboard design. A freeboard height less than the TDH increases particle loss (not desirable in most of the cases); on the contrary too high freeboard increases the capital cost. Other parameters interesting to define in relation to the freeboard are the entrainment and the elutriation. *Entrainment* is the flux of solids carried by the leaving gas from the bed into the freeboard. *Elutriation* refers to the separation or removal of fines from the bed. Entrainment and elutriation are strongly influenced by the gas flow pattern. Due to the dynamic nature of a fluidised bed the phenomenon of elutriation is likely to happen in most cases. Even if the initial size distribution is uniform, this distribution changes with time as a consequence of attrition (especially in the distributor region, near the wall and internals), chemical reaction (usually producing shrinking of the particles) or agglomeration.

In this section, some models which account for the amount of solid in the freeboard will be reviewed. There are mainly two different approaches to model the particle flow in the freeboard:

- The first approach uses a first order differential equation, the solution of which gives the particle concentration variation with time (as was firstly proposed by Leva [61]):
$$\log \frac{C}{C_0} = -Et \tag{2.27}$$
where C is the concentration of fines after time t, C_0 the initial concentration of fines, and E the elutriation rate constant. The elutriation rate

increases with increasing superficial gas velocity and decreases with height in the freeboard up to the TDH.

Many authors have followed this approach [61, 62, 63, 64, 65, 66, 67, 68, 69, 70, 71, 72, 73] and calculated empirical or semi-empirical correlations for the elutriation rate. The validity of these correlations is not general but only applicable to the specific situations at which they were calculated. Geldart [74] and Kunii and Levenspiel [75] proposed a correlation for the elutriation rate based on dimensionless parameters involving gas and particle properties and operating conditions. Milioli and Foster [76] came up with a phenomenological model, based on experimental evidence. They assumed that the number of particles transferred from the bed surface to the freeboard is the result of two mechanisms: the entrainment of particles whose terminal velocity is smaller than gas superficial velocity and the entrainment of particles from the wake of coalescing bubbles. The proportion in which each mechanism occurs, depends on the conditions of the bed.

- The second approach is a dynamic approach based on momentum balances over each particle entrained in the freeboard. The first dynamic model was proposed by Zenz and Weil [77]. They considered the initial particle velocity in the freeboard as it is ejected from erupting bubbles. However, when the particles reach the bed surface, it was postulated that they enter into a gas stream moving at uniform velocity. A good estimation of the shape of the curve of entrainment versus height above the bed was obtained. However the theory predicted lower TDH values than those determined experimentally. It was proposed that the reason for these low values was that it was considered that the particles move with constant superficial gas velocity once they leave the bed surface. To improve this, the constant flow field velocity was substituted for a "bubble velocity dissipation". This velocity dissipation relationship was established by measuring velocity profiles downstream of pulsating orifice jets or by trial-and-error matching of the theoretical to experimental entrainment curves. The first method is not

very reliable without the presence of a bed of particles and very difficult with the presence of a bed. The second method is easier but it requires data from the considered system.

George and Grace [48] also modelled the freeboard gas flow as a series of decaying jets generated by erupting bubbles at the bed surface. However, their one-dimensional model predicted that the particle concentration in the freeboard should increase with height above the bed surface. There is no experimental evidence to support the model predictions.

Horio *et al* [55] introduced the annulus-core model, in which the particles in the freeboard are divided into two regions: particles ascending in a zone at the centre and particles descending in a zone near the wall. It was further assumed that particles are transported by gas turbulence.

Pemberton and Davidson [78] developed a model very similar to Horio's model. They divided the freeboard flow into three phases: i) particles ejected from erupting bubbles and carried up by the gas flow, ii) particles for which the terminal velocity is higher than gas velocity and consequently they fall back under gravity and iii) particles going downwards near the wall.

Berkelmann and Renz [57] also proposed a model based on a momentum balance for the particles and considering a gas flow with turbulent fluctuations. The model is for a two-dimensional fluidised bed and takes into account the effect of non-spherical particles.

Glicksman and Yule [79] proposed an elutriation model which assumes that the particle acceleration is due to the gas flowing through the bubble at the bed surface. The velocity of the gas is different depending on whether the bubble arrives as a single bubble or coalesces below the bed surface. The bubble voidage and the number of bubbles erupting per unit time were predicted from a modified two-phase flow model. It was postulated that the probability of multi-bubble coalescence at the bed surface is proportional to the bubble voidage. The rate of single and multi-erupting bubbles at the

bed surface was determined statistically.

Any dynamical approach requires the input of the particle velocity at the bed surface and a good knowledge of the gas flow in the freeboard.

2.8 Tronconical fluidised bed

Corella *et al.* [80, 81, 82, 83, 84, 85] have studied a tronconical fluidised bed (a fluidised bed with an expansion section). The enlargement section was part of the bed (in our study it is part of the freeboard). However, the behaviour of this system can give an idea of the behaviour of our system. The main advantages of an enlargement of the upper zone of a fluidised bed are [81]:

- The bubble size decreases.
- The particles have the opportunity to possess the same quality of fluidisation.
- The velocity in the upper zone decreases.

These factors give a better gas-solid contact. However, in the lower zone of the tronconical part there is a dead zone (Figure 2.8), because the expansion angle of the vessel, α, is less than the angle formed by the lines of expansion of the gas ϕ. On increasing the velocity, the fraction of solid in the dead zone decreases slightly. Corella *et al.* [85] suggested that the best fluidisation conditions are achieved with $\alpha < 80^o$ and placing an internal in a "V" shape, as shown in Figure 2.9. They investigated the effects of rows of tubes and inclined plates [82]. The rows of tubes reduced the dead zone more than the inclined plates.

For a bed of the dimensions shown in the Figure 2.9, they analysed the following variables [85]: number of cylinders per row, cylinder diameter, angle of the "V"

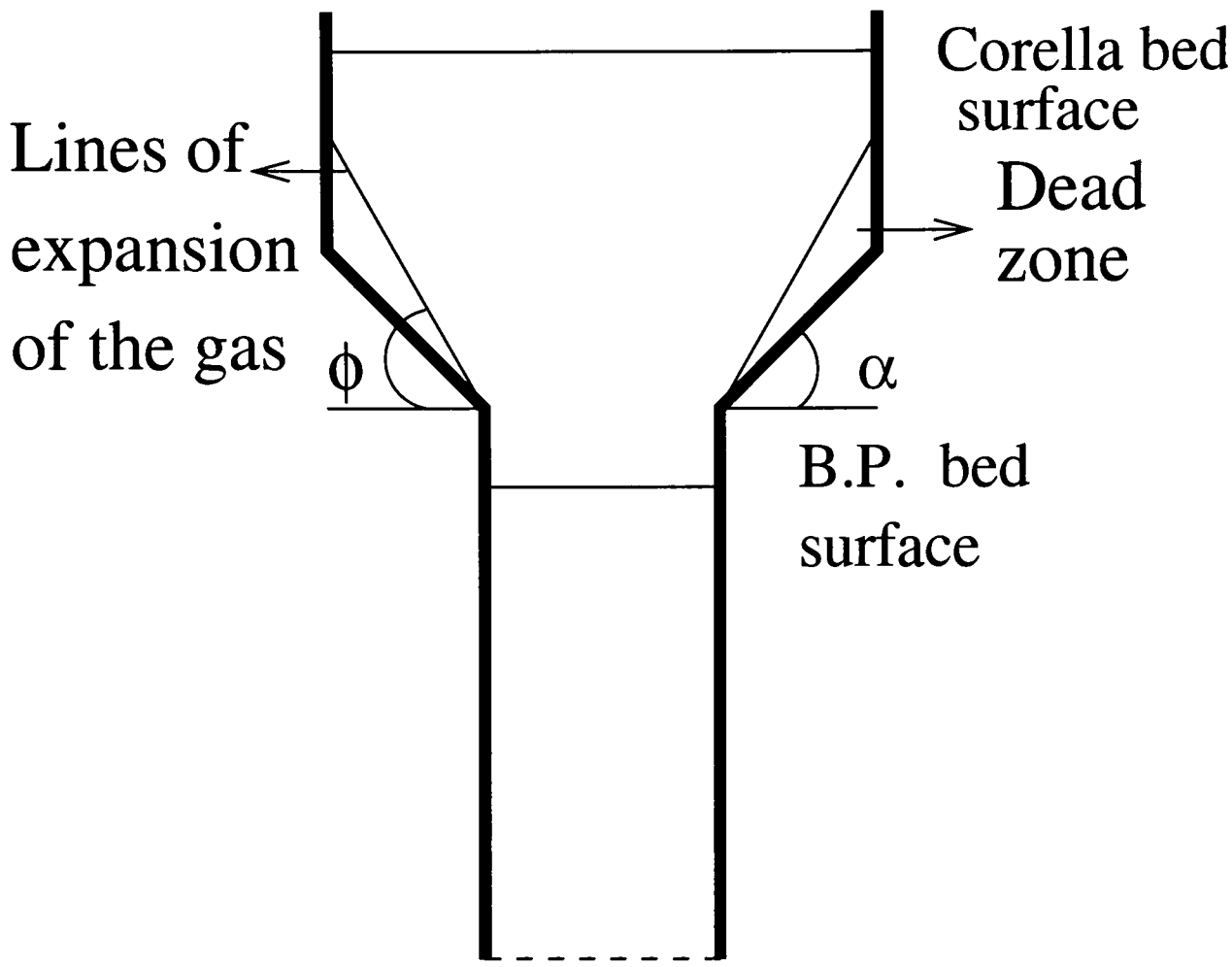

Figure 2.8: Fluidised bed with a tronconical freeboard

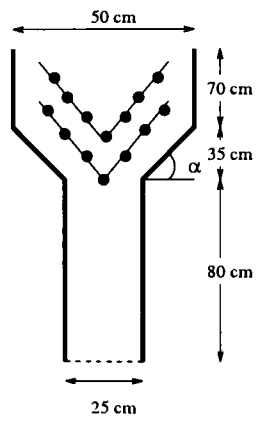

Figure 2.9: Dimensions of Corella *et al.* (1983) fluidised bed

and height at which the lower cylinder of the internal was positioned. They found the best performance with 7-9 cylinders, of 15 mm of diameter, per row, forming a 75^o angle and the lower cylinder positioned at 60 cm above the distributor.

Tasirin and Geldart [86], studied the entrainment of fines from a fluidised bed (0.076 m diameter) with an expanded freeboard (0.152 m diameter). It was found that the total entrainment was reduced to 1% of that measured in the bed without the expansion.

2.9 Conclusions

The flow above a fluidised bed determines the inlet flow in the freeboard. Therefore, it is important to understand the bed behaviour before analysing the freeboard. The flow pattern in the bed as well as the bubble characteristics have been reviewed. The bubble nature is characterised by its shape, size, velocity, frequency and number of simultaneous erupting bubbles, that is mainly determined by coalescence. It can be concluded that the bed flow pattern is mainly determined by the gas flow, the bed height, the bed material and consequently bubble properties.

It has been found that single injected bubbles in incipiently fluidised beds behave in a similar way to single spontaneous bubbles in fluidised beds.

The finding in the freeboard could be summarised as follows:

- Most often the gas above single erupting bubbles has been found to move downwards at the centre and upwards near the wall at the bed surface, after bubble eruption. The main theory proposed to explain the gas flow is the "ghost bubble" theory. Ghost bubbles have not been visualised as such above fluidised beds by previous workers. The technique used in the

present investigation (PIV) will allow visualisation of them if they were present. Thus one of the aims of the undertaken work is to find evidence to support the ghost bubble theory.

- The particles in the freeboard are launched by erupting bubbles. In general, it can be said that the origin of the ejected particles is a combination of two different mechanisms: i) single bubbles, that eject particles coming from the bubble roof and ii) coalescing bubbles that eject particles from the wake of the bubbles. This latter mechanism is usually less frequent and more violent than the former and contributes more to the solid ejection into the freeboard.

- The freeboard particle flow is characterised by particles moving upwards, carried by the gas, and a layer of particles going downwards beside the wall.

- The gas flow is characterised by high velocity fluctuations. The vertical velocity at the bed centreline decreases with height above the surface. The radial vertical velocity profile has a maximum at the centre near the bed surface. This maximum moves towards the wall with height until the profile becomes flat. A clear explanation for this velocity profile has not been found yet. This is probably because the experimental measurement techniques give time-averaged values at certain points and do not allow for the simultaneous analysis of the whole freeboard. A flow visualisation technique will help to provide more details about the flow in the freeboard.

- Many models accounting for entrainment and elutriation in the freeboard have been proposed, but none of them are either accurate or general. The models depend on the size of the bed, size distribution of the particles, kind of distributor and superficial gas velocity. The main factors to be considered when proposing an entrainment or elutriation model are the ejection of particles to the wall, the turbulence at the bed surface, the gas circulation in the freeboard and the complicated velocity profiles in the freeboard [76]. All the models have exponential decay of the particle

concentration with height and consider that some particles with terminal velocity greater than gas flow in the freeboard are elutriated and only a few with terminal velocity lower than the gas velocity are removed from the bed.

- The presence of internals in the fluidised bed reduces the freeboard fluctuations, but they do not have a big influence on the vertical velocity profile.
- The bubble distribution does not have an immediate influence on the flow at high freeboard heights.
- The use of a fluidised bed with an enlargement in the upper bed decreases the number and size of bubbles in the freeboard but introduces a dead zone near the walls. This effect can be reduced by placing internals in the lower zone of the freeboard.

It is not immediately obvious from previous work what to expect in the B.P. polymer bed (due to the interaction of different factors such as bed behaviour at the bed surface and freeboard geometry). In order to understand more about the flow pattern in and above the expansion section of the B.P. polymer fluidised bed, PIV, as a visualisation technique, is used to obtain information about local instantaneous gas velocities. The scaling and the requirements for PIV application dictate the choice of the experimental apparatus.

Chapter 3

Experimental equipment

3.1 Introduction

The principal aim of this project is to try to find the cause of fibrous carbon growth in the process of thermal cracking of waste plastic carried out in the pilot plant of B.P. Chemicals at Grangemouth. The first step in this study is to build a fluidised bed with the same hydrodynamic behaviour as that used in Grangemouth. The dimensions of the bed are given by the scale-down laws.

This chapter describes the scale-down and design of the fluidised bed, the choice of the bed particulate material and the construction material of the bed and the measures adopted to minimise the laser reflection. After that, the experimental conditions used in this work are enumerated. A bubble injector (used to study the eruption of single bubbles) is also described, as well as the operating conditions for this case.

3.2 Scale-down

To obtain a fluidised bed smaller than the bed in the B.P. pilot plant but with similar hydrodynamic behaviour it is necessary to scale-down the pilot plant bed.

The freeboard behaviour depends on the behaviour of the bed, mainly frequency, size, distribution and rise velocity of the bubbles. Therefore, a scale-down of the bed plus geometrical similarity in the freeboard might give rise to the same freeboard behaviour.

Many works have been carried out to find the dimensional and non-dimensional parameters that characterise the dynamics of a fluidised bed [87, 88, 89, 90, 91, 92]. Glicksman *et al.* [92] obtained the dimensionless scaling laws using the equations that govern the process. This method is quite convenient, since the dimensionless parameters obtained are related to physical phenomena. They approached the phenomenon using two equations: the equation of motion for individual particles and the equation of motion for a continuum model of fluid and solid phase. The dimensionless parameter list becomes,

$$\frac{u^2}{gH},\ \frac{\rho_p}{\rho_f},\ \frac{\rho_p u d_p}{\mu},\ \frac{\rho_f u H}{\mu},\ \frac{G_s}{\rho_p u},\ \textit{bed geometry},\ \varphi_p,\ \textit{particle size distribution}$$

where $\frac{u^2}{gH}$ is the Froude number, that is the ratio of inertial to gravitational forces, $\frac{\rho_p}{\rho_f}$ is the ratio of particle to fluid inertial forces, $\frac{\rho_p u d_p}{\mu}$ and $\frac{\rho_f u H}{\mu}$ are the Reynolds numbers representing the ratio of particle inertial to fluid viscous forces and fluid inertial to fluid viscous forces, respectively, $\frac{G_s}{\rho_p u}$ is the ratio to the solid feed to the bed to the particle inertial forces and φ_p is the sphericity.

They obtained the same list for the freeboard of a bubbling bed except for $\frac{G_s}{\rho_p u}$. They used the equation of motion of a particle suspended in unbounded turbulence for particles far from the wall and the equation of motion for a particle near a solid boundary for particles near the wall.

This parameter list is applicable to the general case but it can be reduced in the limits, a fact that allows one to relax the constraints on the dimensions of the model relative to the bed. Glicksman *et al.* [87] found that the number of dimensionless parameters could be reduced if the fluid-particle drag is predominantly viscous or inertial. They proposed the following limits:

Viscous: $Re_p = \frac{\rho_f \ d_p \ u}{\mu} < 4$

Inertial: $Re_p = \frac{\rho_f \ d_p \ u}{\mu} > 400$

At low Reynolds number viscous forces dominate and the inertia of the fluid is negligible. Therefore, the density ratio parameter may be omitted. At high Reynolds number the viscous drag forces between the particles and fluid are negligible compared to inertial forces. In this case the Reynolds numbers may be omitted.

Horio *et al.* [90] deduced scaling laws based on the governing equations of bubble and interstitial gas dynamics. Although the Glicksman *et al.* laws are the most general, Horio's laws are used in this work since the former are too restrictive and do not allow us to do the scale-down. In 1988 Glicksman [89] demonstrated that the parameters deduced by Horio are identical to those developed by him in the viscous limit.

Horio *et al.* [90] started from the following assumptions:

1. The excess of gas over that needed for minimum fluidisation velocity passes through the bed in the form of bubbles, as postulated in the two-phase theory of Toomey and Johnstone [5].

2. The flow of gas and particles is given by Davidson's model [6].

3. The coalescence of bubbles is described by the Clift and Grace model [7], considering the coalescence as the result of the merging of two isolated bubbles.

4. The bubble splitting process can be expressed by Horio and Nonaka's model [93], which proposed that the splitting frequency of a bubble is proportional to $u_{mf}^{-\frac{1}{2}}$.

Geometrical similarity requires that the diameter of the column, the bed height, the distributor orifice diameter, the orifice pitch and other spatial parameters have the same proportionality:

$$m = \frac{D_b}{D_b^o} = \frac{H_b}{H_b^o} = \frac{P_n}{P_n^o} = \frac{d_n}{d_n^o} \tag{3.1}$$

where the superscript o denotes the original scale unit parameters.

The hydrodynamics of a fluidised bed are dominated by the bubble behaviour. Thus, if the two beds have a geometrical similar fluidisation condition, they will also have similar bubble condition. The conditions that they proposed were:

- Identical bubble fraction.
- Geometrically similar bubble size distribution.
- Equivalent splitting frequency.
- Geometrically similar flow field around each bubble.

The length parameters were made dimensionless using the column diameter since this is more relevant for the bubble characteristics than the particle diameter. Thus:

the condition for *geometrically similar bubble coalescence is*:

$$u - u_{mf} = m^{1/2}(u - u_{mf})^o \tag{3.2}$$

and the condition for *geometrically similar flow field around a bubble and for similar bubble splitting* is:

$$u_{mf} = m^{1/2}(u_{mf})^o \tag{3.3}$$

These two conditions are necessary and sufficient to achieve geometrically similar fluidizing conditions. Horio *et al.* checked the theory with previous correlations for bubble diameter and grid zone structure, and also with experiments for Geldart group B particles and found a fairly good agreement.

3.3 Design of the bed

The gas used in the plant is a mixture of ethylene and propylene, although there is a range of other components as well. The available data are shown in table 3.1.

Given	Pilot Plant Bed
$T(^0C)$	510
$d_p(m)$	1.65×10^{-4}
$D(m)$	0.5
$H(m)$	2.9
$P(bar)$	1.5
$Pm(kg/kmol)$	28
$\mu(kg/ms)$	1.8×10^{-5}
$\rho_g(Kg/m^3)$	1.4
$u_{mf}(m/s)$	3.7×10^{-2}
$u(m/s)$	8.95×10^{-2}

Table 3.1: Data of the pilot plant fluidised bed

The first step is to determine the Reynolds number to identify the working regime. If Reynolds number is less that 4, we are in the viscous regime, where Horio's scaling relationships are applicable [89].

The Reynolds number based on the particle diameter is easily calculated with the available data.

$$Re = \frac{\rho_g u d_p}{\mu} = \frac{1.4 \;\; 8.95 \times 10^{-2} \;\; 1.65 \times 10^{-4}}{1.8 \times 10^{-5}} = 1.4$$

This value of Reynolds number demonstrates that we are in the viscous regime. The proportionality between the geometrical dimensions is given by m, with m equal to $1/2$. The condition for similar flow fields and similar splitting gives the value of minimum fluidisation velocity for the model:

$$u_{mf} = \sqrt{m}(u_{mf})_o; \quad u_{mf} = \sqrt{1/2}\ \ 3.7 \times 10^{-2}; \quad u_{mf} = 0.026\ m/s$$

The bed material of the model should have a minimum fluidisation velocity of $0.026\ m/s$. Minimum fluidisation velocity is a function of the size and density of the particles and density and viscosity of the fluid. Air, at room temperature, is the fluid to be used, thus the density and viscosity of the gas are fixed. The same kind of solid as in the pilot plant is to be used, Chelford sand. Thus, it is not necessary to worry about either the mechanical or the electrical properties of the particles related to inter-particle collisions and electrostatic forces, respectively.

Density, minimum fluidisation velocity and size distribution of several Chelford sands have been determined experimentally, to find which sand has minimum fluidisation velocity close to $0.026\ m/s$. The density has been calculated by weighing 50 ml of sand. The sand volume was measured in a 150 ml flask filled with 100 ml of distilled water.

Chelford type	$\rho(\frac{kg}{m^3})$
95	2608
80	2604
50	2620

Table 3.2: Density of the sand

Minimum fluidisation velocity has been calculated in a 16 cm diameter bed, as the intersection point of the pressure drop for a fixed bed and a fluidised bed in the graph of pressure drop *vs* fluid velocity.

The particle size distribution has been measured using a Malvern sizer analyser based on laser diffraction. It is given as mean Sauter diameter (MSD):

$$d = \frac{\sum d_i x_i}{\sum x_i} \tag{3.4}$$

where x_i is the mass fraction of solids with diameter d_i.

$$d_i = \frac{D_{i-1} + D_i}{2} \tag{3.5}$$

D_{i-1} and D_i are the diameters of the ith and the previous size, respectively.

Type	MSD (μm)	$u_{mf(exp)}$	$u_{mf(C-K)}$	$u_{mf(W-Y)}$
Chelford 95	169	2.3	2.27	3.3
$210 < d_p < 250$	249	-	3.62	5.3
$180 < d_p < 210$	217	3.35	2.72	4.03
$150 < d_p < 180$	183	2.53	1.96	2.88
$< d_p$ 150	146	1.99	1.23	1.83
Chelford 80	205	2.75	3.5	3.63

Table 3.3: Minimum fluidisation velocity (cm/s) and Sauter mean diameter of the sand

The table 3.3 shows the mean Sauter diameter (MSD), the minimum fluidisation velocity calculated experimentally ($u_{mf(exp)}$), using the Carman-Kozeny equation ($u_{mf(C-K)}$):

$$u_{mf} = 5.9 \times 10^{-4} \frac{d_p^2(\rho_p - \rho_f)g}{\mu} \tag{3.6}$$

and the Wen-Yen ($u_{mf(W-Y)}$) equation:

$$Re_{mf} = \sqrt{(33.7)^2 + 0.0408Ga} - 33.7 \tag{3.7}$$

where

$$Re = \frac{d_p u \rho_f}{\mu} \tag{3.8}$$

and

$$Ga = \frac{d_p^2 \rho_f (\rho_p - \rho_f) g}{\mu^2} \tag{3.9}$$

for six different size distributions of Chelford sand. It can be seen that the particles with the closest minimum fluidisation velocity to the value determined by Horio's scaling law correspond to the particles with 183 μm Sauter mean diameter. In order to obtain such particles one should sieve them from Chelford 95, and the sieving utility available is very slow. It is more convenient to use Chelford 95 itself because it is already available and because it has a size distribution proportional to the size distribution of the Chelford 80 used in B.P. pilot plant. The minimum fluidisation velocity of Chelford 95 is close enough to that given by Horio's scaling law. Chelford 95 belongs to group B (i.e. minimum

bubbling velocity is approximately equal to minimum fluidisation velocity) in Geldart's classification [32].

Once minimum fluidisation velocity is known, the condition of similar bubble coalescence gives the gas superficial velocity.

$$u - u_{mf} = \sqrt{m}((u)_o - (u_{mf})_o)$$

$$u = [\sqrt{0}.5(8.95 \times 10^{-2} - 3.7 \times 10^{-2})] + 2.3 \times 10^{-2}$$

$$u = 0.06 \ (m/s)$$

The dimensions of the model are calculated using the proportionality given in Equation 3.1. The dimensions of the pilot plant and the model fluidised bed are shown in Figure 3.4. Figure 3.2 is a sketch of the model bed.

The distributor is a perforated plate with a 60^o triangular pitch. It is made up of three plates (of 5 mm thickness), one over another (Figure 3.3). Between the first plate (A) and the second plate (C) there are three meshes (B) with a hole aperture of 50 μm. The plates are shown in Figure 3.4. The diameter of the holes is 1 mm in the first plate (A) and 2 mm in the second (C) and third plate (D). The plates are placed in a way that the centre of the holes of the three plates coincide. They are glued around the edge, with silicone rubber, to avoid air leaks. The plates provide strength and the mesh a controllable pressure drop.

The bed was filled to a height of 4 cm, to check the operation of the distributor. Similar bubbles were observed issuing from all 31 holes of the distributor (Figure 3.5). As the bed height was increased the number of bubbles decreased and their size increased, as can be seen in Figure 3.5. The bed height was 4 cm, 11.5 cm and 14 cm respectively. This fact may indicate that bubble coalescence occurred. There was no region where there were more bubbles than in another. The places where the bubbles appeared changed with time, the bubble pattern was random and the bubbles did not follow preferential paths.

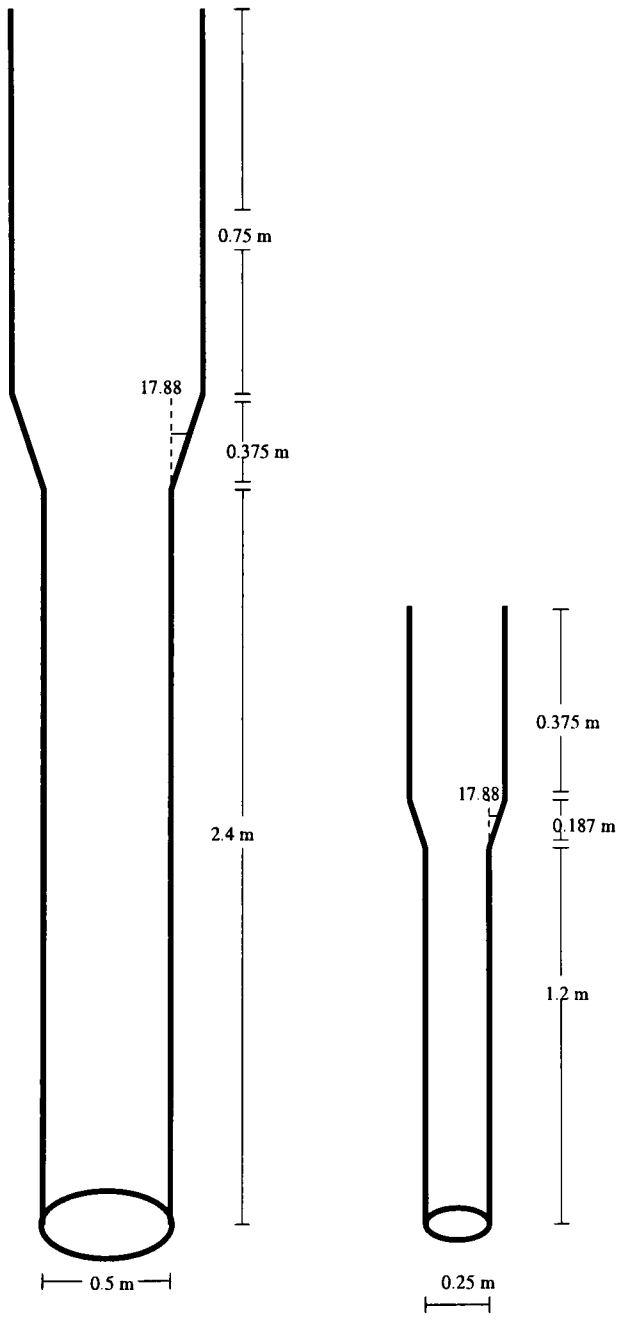

Figure 3.1: Pilot plant and proposed model fluidised beds

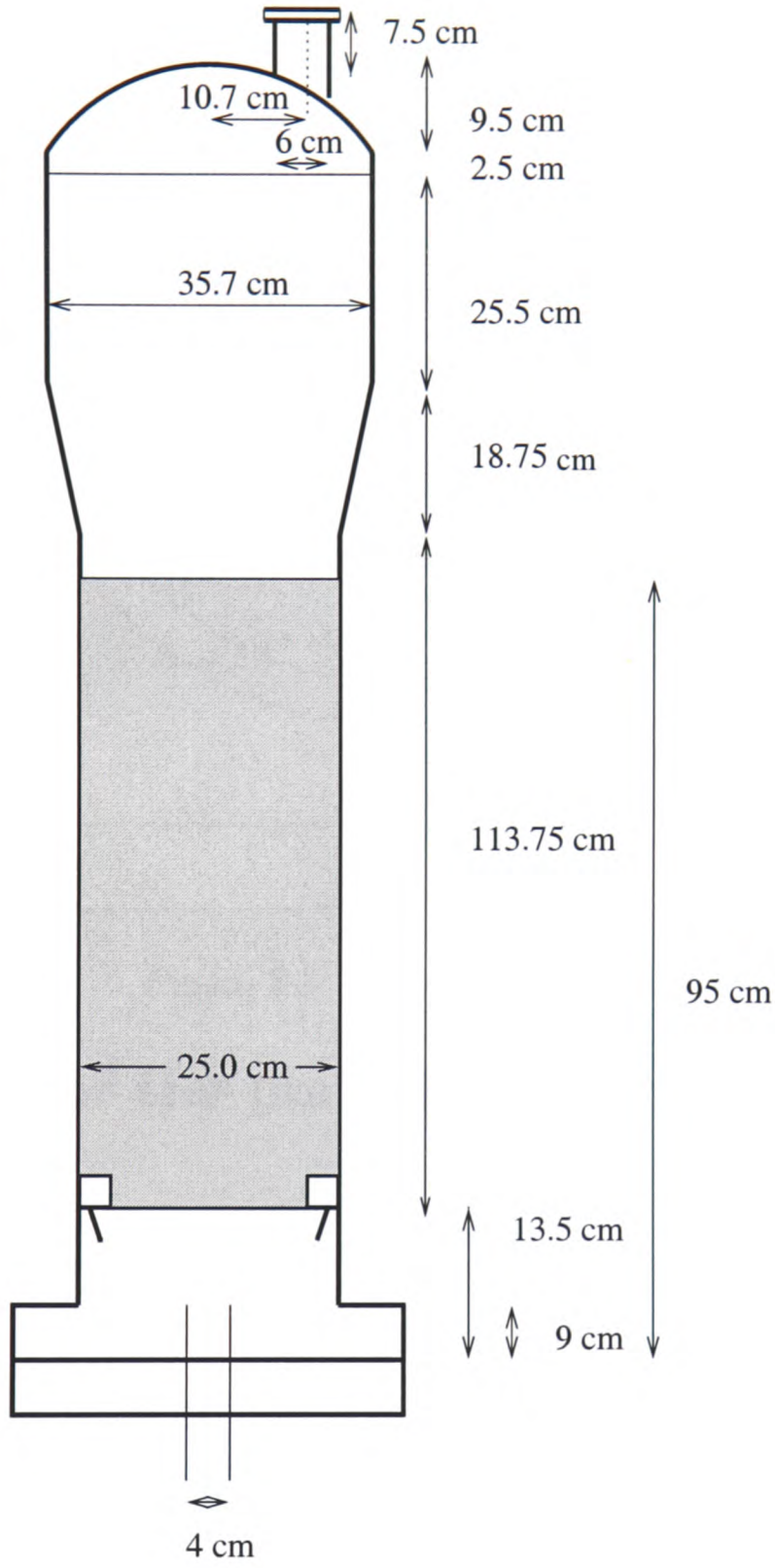

Figure 3.2: Fluidised bed

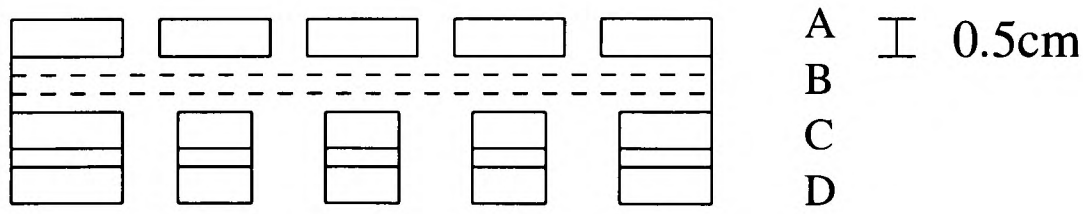

Figure 3.3: Cross section of the distributor

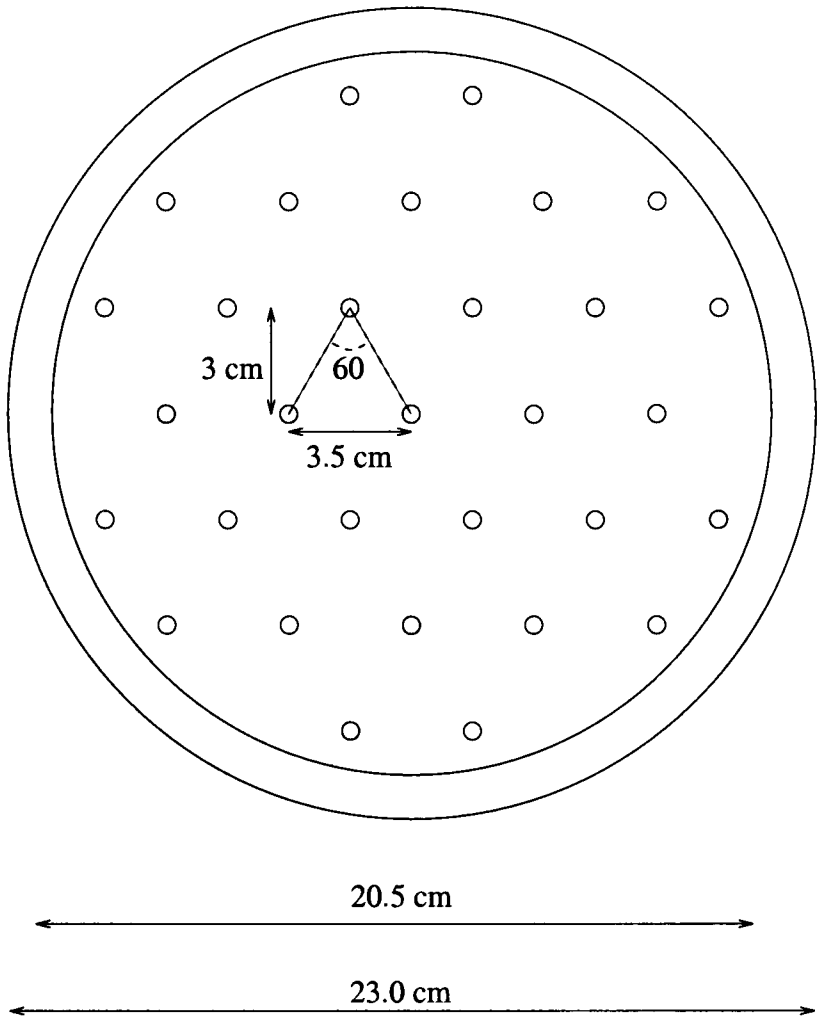

Figure 3.4: Distributor plate

3.4 Choice of the material to construct the bed

For the present application, the material to construct the fluidised bed must have a good optical quality. The material must be highly transparent to visualise and record what happens inside the bed. The refraction must be as low as possible in order to minimise distortion. It is also desirable to have little reflection to avoid the internal reflections of the laser beam.

Two possible materials have been considered: glass and polycarbonate. The latter, a thermoplastic polymer, seems to be very attractive since it is cheaper and easier to handle than glass. To decide which one is more convenient for the research work, the properties of both materials will be reviewed.

The optical behaviour of a material depends on the indices that determine refraction, reflection and transparency. The index of refraction of the glass and polycar-

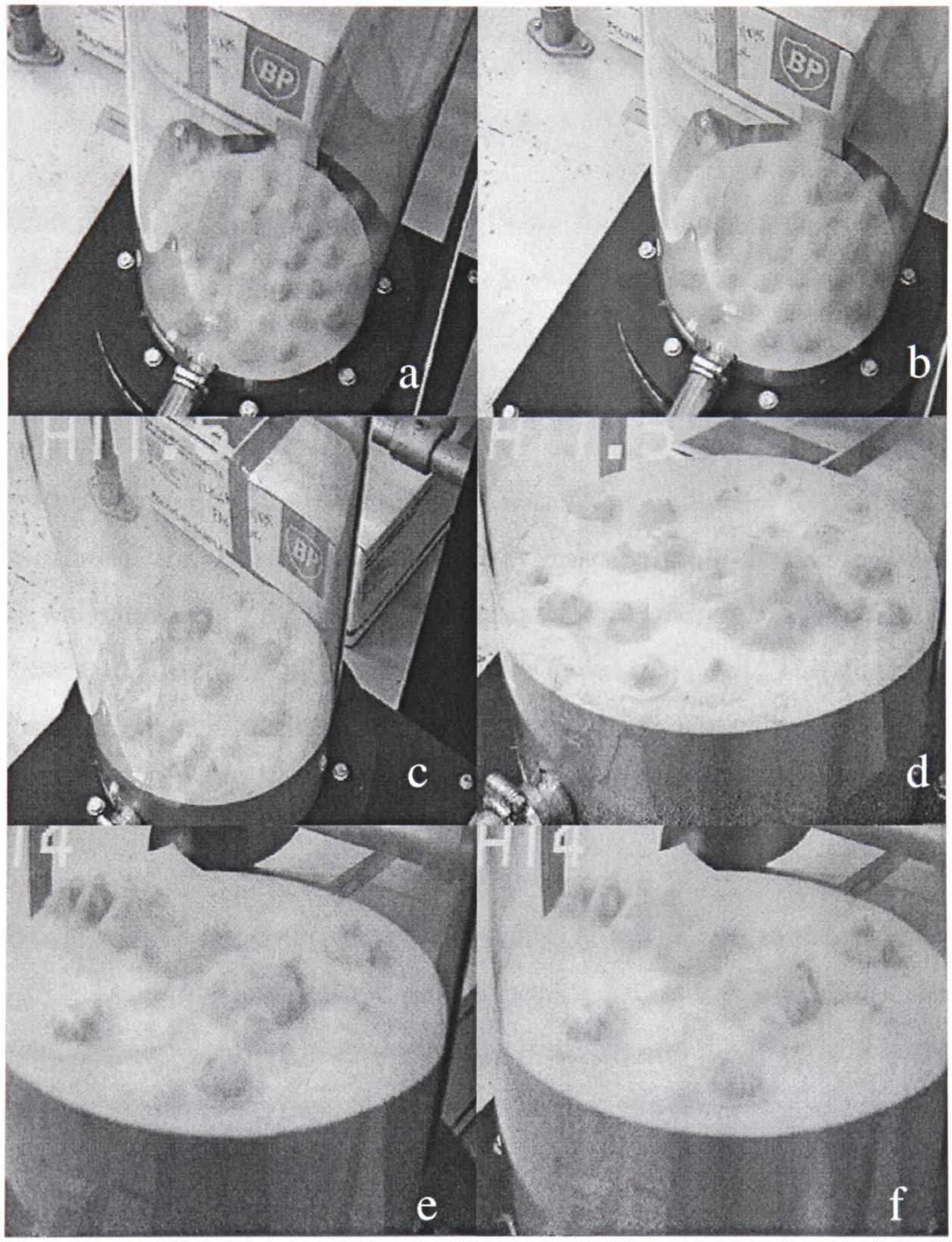

Figure 3.5: Observations concerning the distributor

bonate are 1.5 and 1.6 respectively. This indicates that refraction is slightly less in the glass than in the polycarbonate.

The reflectivity gives the fraction of incident beam that is reflected. Materials with high index of refraction give high reflectivity. High reflectivity implies that the material is opaque. The reflectivity of the glass is 0.04 and of the polycarbonate is 0.05, therefore the glass is less reflective and more transparent.

The difference in the optical properties between the polycarbonate and the glass is not significant. To check the optical behaviour of both materials a glass cylinder and a polycarbonate cylinder were photographed within a square grid (Figure 3.6). Half of the grid was inside and the other half was outside, to compare the distortion due to the wall of the cylinders only and not to the quality of the photographic system. The glass cylinder was 7.9 cm external diameter and the wall thickness 3 mm. The polycarbonate cylinder was 5.9 cm external diameter and the wall thickness 4 mm. The photographs were taking using a Nikon 60 mm lens camera, a f number of 5.6 and a shutter speed of $\frac{1}{30}$ sec. The distortion due to the wall of the cylinder was calculated as the difference between the length of the squares outside and inside the cylinder, to avoid the effect of the camera lens, and are given as a percentage.

The distortion calculated experimentally is higher in the case of the glass cylinder (Figure 3.7) than in the case of the polycarbonate cylinder (Figure 3.8). However, the glass cylinder is more transparent, thus it allows one to see clearly through it. Knowing the exact distortion, this can be subtracted from the image. However the distortion is so little that it can be neglected.

It is not enough to consider the optical behaviour of the material, the mechanical and electrical behaviour must also be take into account, because the constant movement of the particles in the bed might modify the internal surface of the bed.

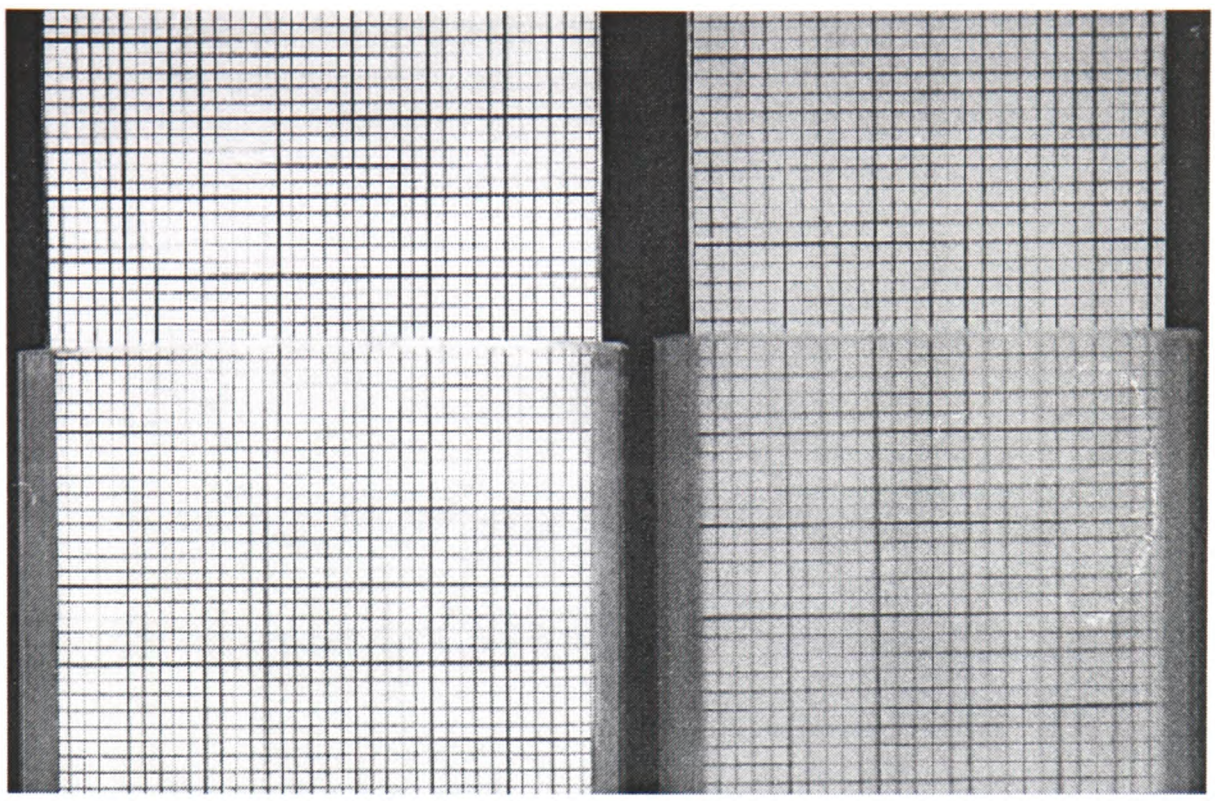

Figure 3.6: Grid inside a glass and a polycarbonate cylinder

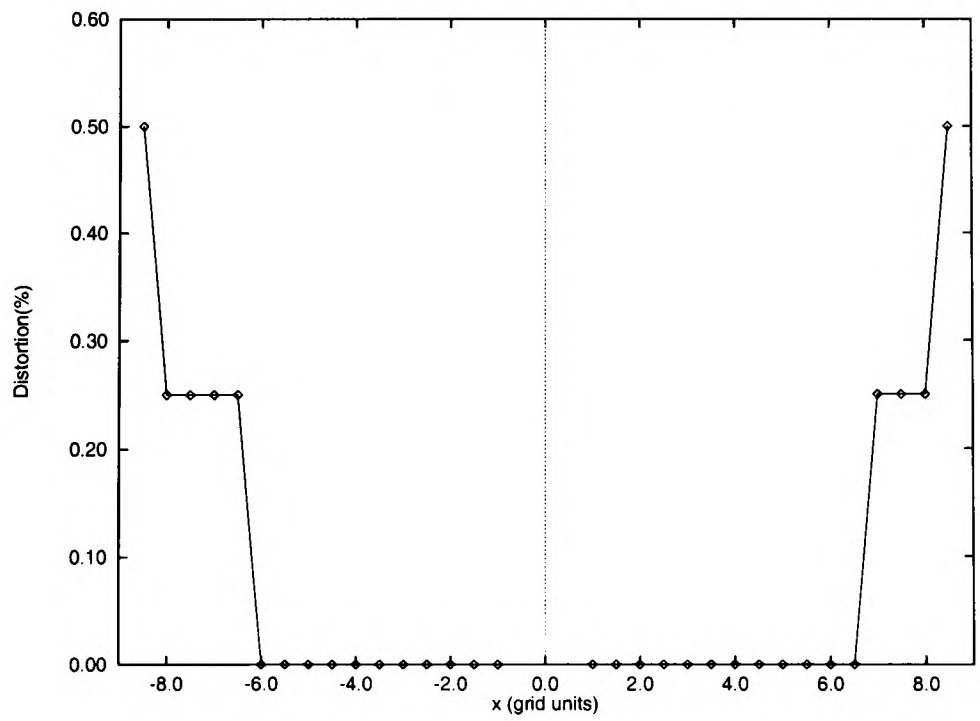

Figure 3.7: Distortion inside a glass cylinder due to the effect of the wall

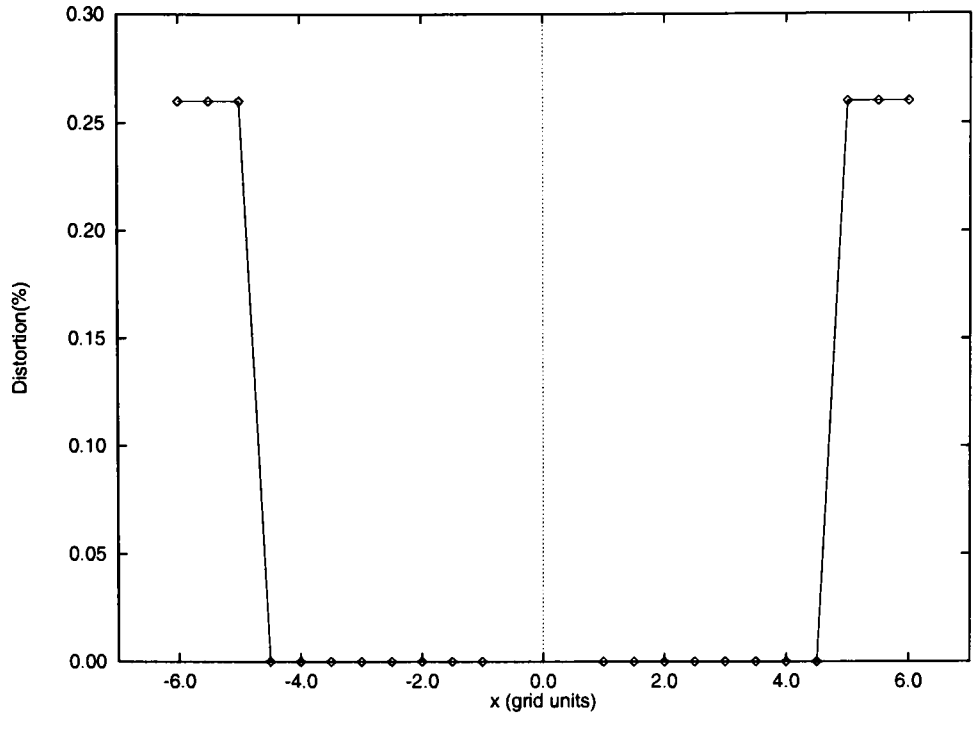

Figure 3.8: Distortion inside a polycarbonate cylinder due to the effect of the wall

The friction of the moving particles against the wall may scratch it, decreasing the visibility through the wall. Polycarbonate is scratched more easily than glass. The polycarbonate is a polymer where the bonding between the atoms is covalent with polymer chains being held to one another by weak Van der Waals secondary bonds, thus they can deform plastically as chains stretch, rotate, slide and disentangle under load to cause permanent deformation. The bonds between the glass atoms are solely covalent therefore a plastic deformation is more difficult.

The measure of hardness is the resistance to penetration of the surface of a material by a hard object, i.e. how difficult it is to scratch a material. On the Mohr's scale of scratch hardness glass lies between apatite (5) and quartz (7). The polycarbonate has a hardness in the Rockwell scale of M70 [94] which means that it is very close to gypsum (2) [95]. In order to use polycarbonate it will be necessary to give it a scratch resistant coating to prevent abrasion.

The static electricity between the seeding particles and the wall is greater in the case of polycarbonate than in the case of glass. The particles stick to the wall, making the visibility through the freeboard more difficult. In theory, it should be necessary to use an anti-static coating for the bed to avoid this. In practice, we

have shown that the use of an anti-static coating seems not to have any effect.

Although the optical, mechanical and electrical properties of the glass are more convenient than those of the polycarbonate, the difficulty of constructing the tronconical shape of the freeboard of glass led to polycarbonate being used which is very easy to handle and cheaper than glass. Thus, the bed was made of glass and the freeboard of polycarbonate. The dome was constructed with glass fibre.

3.5 Freeboard reflections

Figure 3.9 shows the reflections when the laser sheet passed through the freeboard. The white lines in the front were due to internal reflections and they disappeared when the inside surface of the back wall was painted in black. The black background also gives a good contrast and makes it easier to visualise the seeding particles.

The lateral reflections were decreased by placing paper so that it projected shadows over the reflection lines. A vertical slip of paper was located on the left side, just before the freeboard. Another slip of paper was fixed to a metal strip with an inclination angle of 30^o approximately (Figure 3.10). A beam stopper was placed where the laser sheet hits the safety board that encloses the rig.

Even so, there is a reflection region near the wall that impeded visualisation of what occurs there. A possible way to visualise this region could be using phosphorescent particles and filtering the light in order to remove the reflected light.

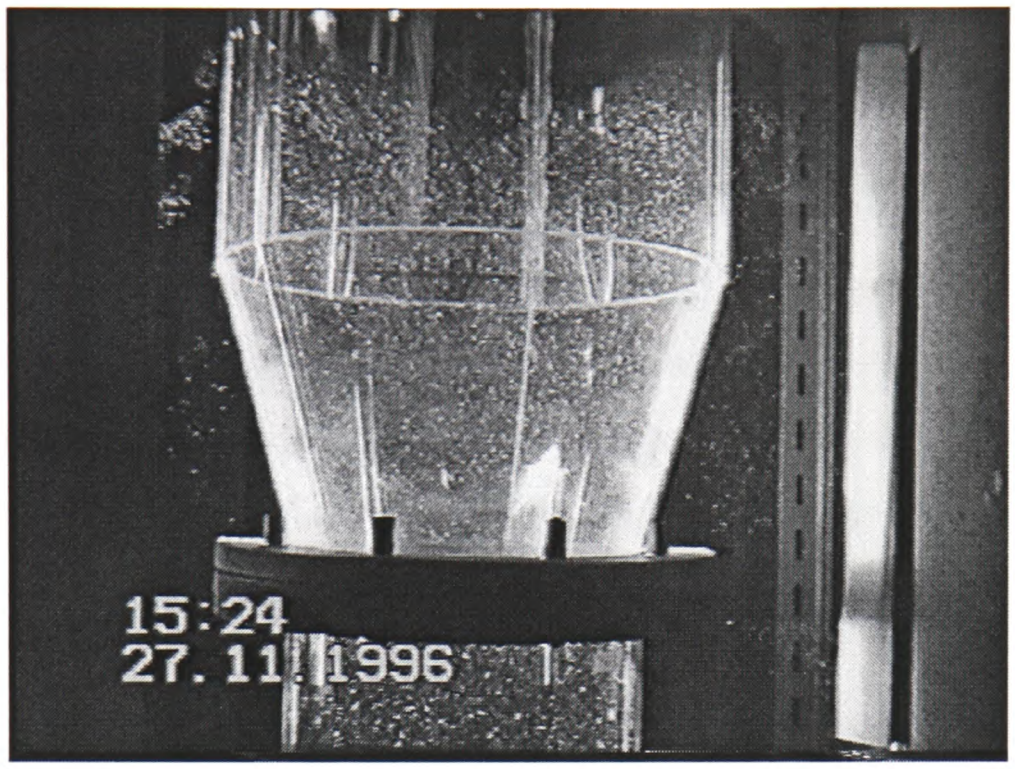

Figure 3.9: Initial freeboard

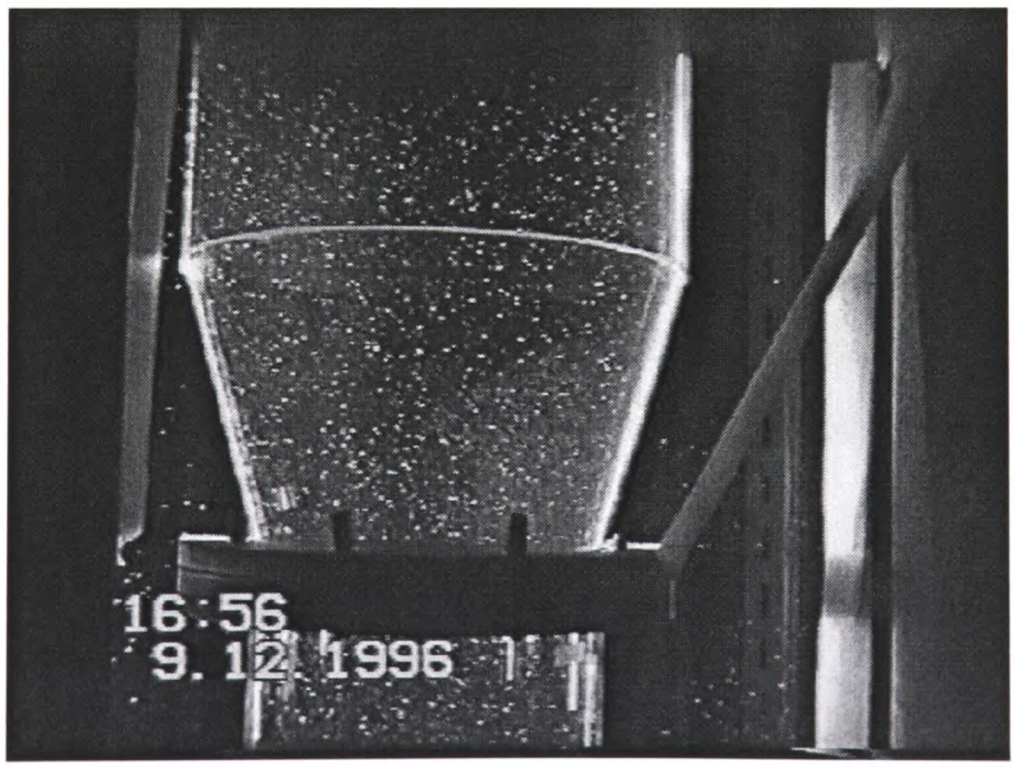

Figure 3.10: Modified freeboard

3.6 Freely bubbling bed operating conditions

Experiments were carried out with air, at room temperature, at a superficial velocity of 6.3 cm/s (as given by the flowrate measured by the rotameter divided by the area of the bed). The static bed height was 90 cm. The average diameter of the single bubbles measured at the bed surface was 14 cm and the average frequency 1.8 Hz. Under these conditions there was no particle loss; the freeboard gas was a single phase flow. Sometimes particles were ejected by erupting bubbles, usually returning to the bed surface before reaching the expanded section of the freeboard and making the freeboard conditions ideal for the study of the gas phase.

Once the scale-down working conditions from the pilot plant were studied, the conditions were varied to determine the influence of some parameters. Experiments were carried out:

- with a central outlet (instead of the off-centre outlet used in the pilot plant),
- at higher superficial velocity 11.5 cm/s (instead of 6.3 cm/s), and
- with a straight-sided freeboard with a central outlet (instead of an expanded freeboard).

Table 3.4 displays the labelling and experimental conditions for each experiment. The superficial velocity u is calculated from the flowrate given by the rotameter.

3.7 The single bubble injector

A sketch of the single bubble injector is depicted in Figure 3.11. Compressed air of controlled pressure was fed through a tube, via a solenoid valve connected to

Experiment number	u (cm/s)	Freeboard geometry	Outlet location
1	6.3	Expanded	Off-centre
2	6.3	Expanded	Off-centre
3	6.3	Expanded	Off-centre
4	6.3	Expanded	Central
5	6.3	Expanded	Central
6	11.5	Expanded	Central
7	11.5	Expanded	Off-centre
8	6.3	Straight	Central
9	6.3	Straight	Central

Table 3.4: Experimental conditions

a timer. The tube was placed 5 cm above the distributor. In order to maintain symmetry and to make the bubble rise in the centre of the bed the tube was placed across the whole diameter of the bed with the opposite side sealed. There was a perpendicular outlet tube in the centre of the feed tube, through which the air necessary to produce the bubble was injected. The diameter of the tube was 6 mm. A very fine mesh was placed on top of the outlet, to stop the sand entering the tube.

Operating conditions

These experiments were carried out using a bronze sinter plate distributor, at superficial velocity of 2.5 cm/s (above minimum fluidisation and below bubbling velocity). This ensured that the only bubble initiation was that from injected gas. The static bed height was 59 cm.

3.8 Execution of research

The gas was seeded, as required by PIV technique (Chapter 4), by mixing the seeding particles with the bed particles just below the bed surface.

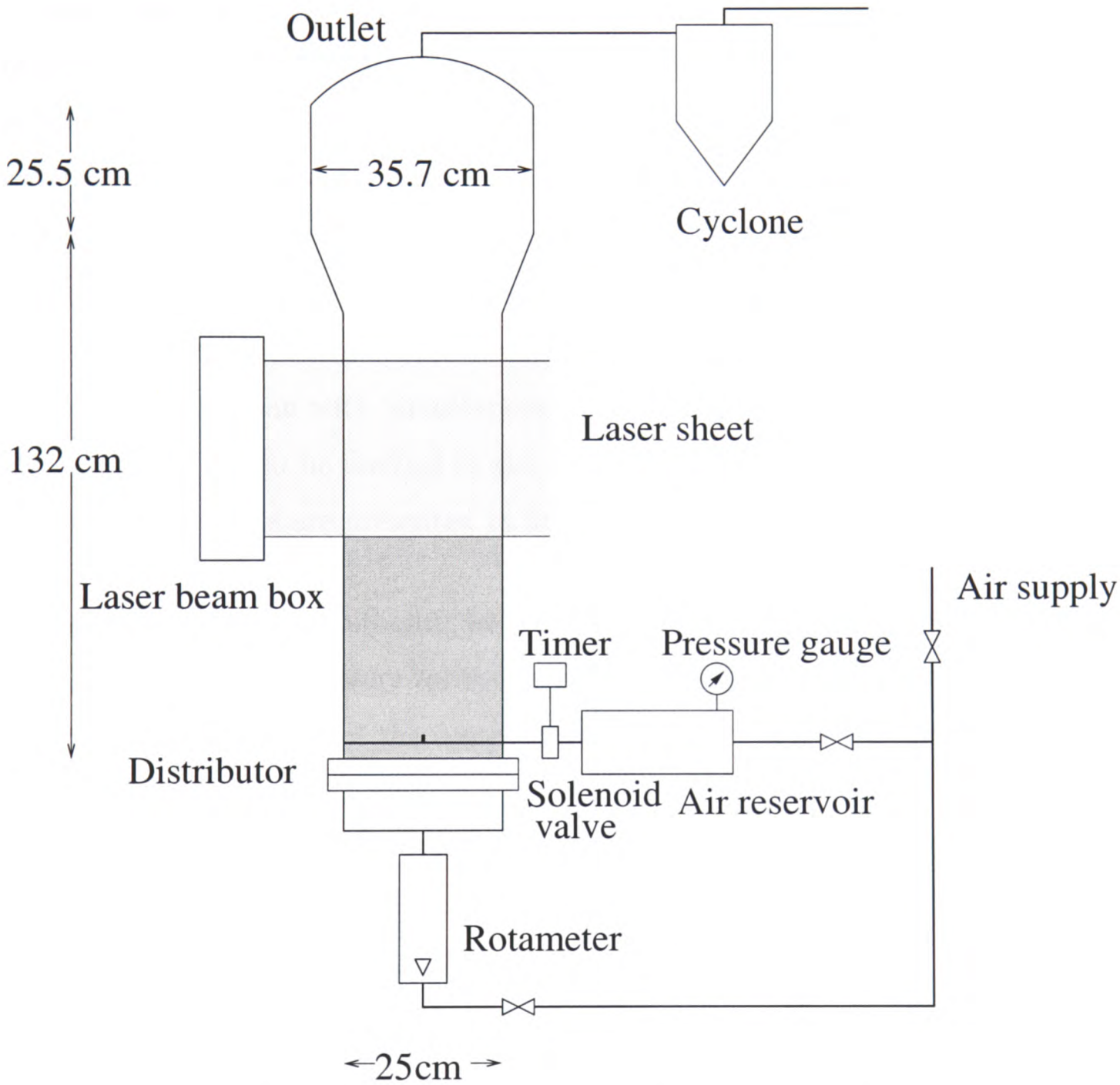

Figure 3.11: Single bubble release device

In order to study the flow above a single injected bubble, the vertical central plane across the bed above the surface was illuminated with the pulsed laser sheet and photographs were taken. Bubbles were released every ten seconds to allow the freeboard gas to settle before the next bubble arrived. Only one image could be taken after the eruption of a single bubble, due to the slowness of image shifting, as explained in Section 4.6. The duration of the bubble eruption, defined as the time between the first disturbance of the surface and the end of this disturbance, is about 0.2 seconds. Consequently, several pictures that cover times from before bubble arrival at the bed surface until the freeboard gas has settled were taken, though obviously each picture is of a different bubble. Although all the bubbles were produced using the same conditions, it was very difficult to form identical bubbles since they are influenced by the bed history. These pictures along with simultaneous video images allowed the behaviour of the freeboard gas to be studied in the presence of a bubble erupting at the bed surface. The results are presented in Section 5.1 and discussed in Section 7.1.

The experiments in the bubbling bed were carried out at the conditions shown in Table 3.4. Photographs were taken above the expansion section of the freeboard. A vertical cross-section of the central plane, 31.5 *cm* by 20.7 *cm*, was analysed. The region near the wall could not be analysed due to the internal reflection of the laser. Photographs were taken one second apart form each other (this is the minimum separation time allowed by image shifting (Section 4.6)). The results are presented in Section 5.3 and discussed in Section 7.3.

Chapter 4

Particle image velocimetry

The advantages of particle image velocimetry (PIV) over other techniques used to measure the gas flow in the freeboard are discussed in this chapter. The technique and the implementations used in this work are also described. Special emphasis is placed on image shifting implementations. The chapter is concluded with a revision of the errors associated with PIV and suggestions for improvements of the technique.

4.1 Introduction

Traditionally, techniques such as hot wire anemometry [40, 55], film wire anemometry [41] and laser Doppler anemometry [42] have been used to determine the gas flow in the freeboard. However, they are point measurement techniques (and in the case of hot and film wire anemometer intrusive techniques that may disturb the flow) which give mean and rms fluctuating velocities. They do not give a whole picture of the flow, i.e. different points are not investigated simultaneously. Furthermore, the velocity at a point is a time-average value. This is not appropriate when the reproducibility of the flow is low. Therefore, a whole field

instantaneous velocity measurement technique is more suitable. Flow visualisation using smoke has also been employed [42] and [41], but it can only provide qualitative information. So far there have been no techniques that allowed flow visualisation and quantification of the velocity over a large area at the same time.

Ideally, the measurement technique required in the undertaken work should be:

- non-intrusive since the insertion of probes would modify the flow;
- full-field since the flow is not homogeneous and the behaviour of the gas in a point does not predict the behaviour in a different point;
- qualitative since fluid flow theory is not completely understood and it has been shown that flow visualisation is a very helpful tool in fluid dynamics;
- quantitative since it is desirable to quantify instantaneous velocities and use them to calculate the statistics of the flow.

PIV seems to fulfil these four objectives. PIV allows one to measure the instantaneous velocity of a fluid throughout an illuminated plane with a pulsed light [1]. The origin of PIV is speckle velocimetry [96] which is based on recording images of highly seeded flows. The random interference of light scatter from the images gives rise to a speckle pattern. Groups of particles produce a nearly constant speckle pattern, allowing the movement of the fluid to be followed. If the density of the seeding material in the flow is low, the individual particles can be followed and the technique is then called particle tracking velocimetry. PIV falls between these two techniques. PIV has also been developed to measure the three components of the velocity (using stereo-graphic, holographic and multi-plane light-sheet methods). However, they have considerable experimental and processing difficulties [97]. There are many articles that contain a good review of PIV [97, 98, 99, 100, 101, 102, 103, 104].

[1] Although flow studied here is three-dimensional and PIV only measures two-dimensional flow fields, this is much better than point measurements.

The basic steps in PIV are as follows:

- **Seeding** of the flow with particles that follow the flow faithfully and scatter enough light to be recorded.
- **Illumination** of a plane with a pulsed light.
- **Recording** of the image with enough resolution to distinguish individual particles.
- **Analysis** of the image by dividing the illuminated plane into very small regions and calculation of the average displacement of the particles in each region.
- **Post-processing** to remove the obviously erroneous vectors.

Each of the above steps as well as the experimental conditions used in this work are discussed in the following sections.

4.2 Seeding of the flow

The seeding particles must follow the flow faithfully, without disturbing it and must scatter enough light. In order to follow the flow faithfully, differences between velocity of the seeding particles and the flow should be small.

Several authors have suggested equations to calculate differences in velocity between the fluid and the particles (slip velocity) [100, 105]. The equation of the relative motion of a sphere in a fluid is given by Melling [106]:

$$\frac{\pi d_p^3}{6}\rho_p\frac{dU_p}{dt} = -3\pi\rho d_p U_{pf} + \frac{\pi d_p^3}{6}\rho_f\frac{dU_f}{dt} - \frac{1}{2}\frac{\pi d_p^3}{6}\frac{dU_{pf}}{dt} - \frac{3}{2}d_p^2\sqrt{\pi\mu\rho_f}\int_{t_o}^{t}\frac{dU_{pf}}{dt'}\frac{dt'}{\sqrt{t-t'}} \tag{4.1}$$

where d_p, ρ_p and U_p are the diameter, density and instantaneous velocity of the particle respectively, ρ_f and U_f are the density and instantaneous velocity of the fluid respectively and $U_{pf} = U_p - U_f$ is the instantaneous relative velocity. The first term represents the force required to accelerate the sphere, the second term the viscous drag according to Stokes' law, the third term the acceleration of the fluid, the fourth term the resistance of the fluid to the acceleration of the sphere and the last term the drag force arising from unsteady flow (Basset term). However, if Equation 4.1 is used for small particles in a gas with low Reynolds number (< 1), based on relative velocity, the equation is simplified to:

$$\frac{dU_p}{dt} = \frac{18\mu}{\rho_p d_p^2}(U_f - U_p) \tag{4.2}$$

However, Stokes' equation (calculated through a balance between the gravitational and resistance force) gives the maximum slip velocity. This equation is easy to handle and adequate to assess whether a particle can be used as a tracer. A particle would move with the fluid when the fluid velocity is bigger than the terminal velocity (u_t) of the particle.

$$\frac{1}{6}\pi d_p^3(\rho_p - \rho_f)g = 3\pi\mu d_p u_t \tag{4.3}$$

$$u_t = \frac{d_p^2 g}{18\mu}(\rho_p - \rho_f) \tag{4.4}$$

Like Equation 4.2, Equation 4.3 is also only valid for low Reynolds numbers.

It is convenient to have particles of very small diameter because they follow the flow more faithfully and they produce a smaller number of overlapping images with higher concentration of seeding particles. This allows an uninterrupted record of the flow and eliminates the drop-out from eddies of small size. Furthermore, the position of smaller images can be measured more accurately than the position of large particles. The optical exposure and resolution of the recording media give the lowest diameter of the particles that can be used (as explained in Section 4.4).

The seeding particles chosen were hollow glass spheres (Sphericel 110P8) of $8\mu m$ mean diameter and $1100\frac{kg}{m^3}$ density. The terminal velocity is $2 \times 10^{-3} m/s$; this velocity is negligible compared with the characteristic velocity of the flow (approximately $2 \times 10^{-2} m/s$) and the Reynolds number at terminal velocity is 3.2×10^{-3}, thus making Sphericel a good seeding material.

The terminal velocity for an isolated particle has been calculated, but the presence of other particles has not been taken into account. The presence of other particles will decrease the sedimentation velocity. The effect will become more marked as the concentration is increased. There are three main factors that contribute to this:

1. When the particles settle, they will displace a volume of fluid that will flow upward.

2. The suspension will have a larger density than the fluid.

3. The flow pattern of the fluid will change as well as the velocity gradient.

Therefore, the terminal falling velocity of the seeding particles may be smaller than that calculated. Once it is known that the particle will be lifted with the flow, it is necessary to assess how long the particles need to react to the changes of the fluid. This is given by the velocity relaxation time. This corresponds to the time required for the particle velocity to acquire the velocity of the fluid. The relaxation time for a spherical particle is given by:

$$\tau_p = \frac{\rho_p d_p^2}{18\mu} \tag{4.5}$$

The relaxation time of the seeding particles used is 2.17×10^{-4} s. This is acceptable as the relaxation time is smaller than the time of duration of a frame (a typical value of which is 33 ms).

It is desirable that the seeding particles do not disturb the flow. Gray [107] determined a formula for the approximate seeding concentration, C_s, to achieve

successful PIV:

$$C_s \approx \frac{24M^2}{\Delta z \pi d_I^2} \tag{4.6}$$

with M being the magnification, Δz the thickness of the light sheet and d_I the length of the interrogation area. The seeding concentration is approximately 10^7 $particles/m^3$, according to Equation 4.6. For this study, 2×10^{-7} of the volume of the flow is taken by the seeding particles. Therefore, it can be expected that the flow will not be influenced by the presence of the seeding material.

As will be seen in Section 4.4 the energy scatter by a particle increases with particle size. Thus, the particle diameter is a compromise between two opposite tendencies. On one hand, large particles scatter more light and are more readily detectable. On the other hand, small particles give more accurate information of the flow, because a lesser time is needed to follow the changes of the flow and they fill more area of the fluid.

4.3 Illumination

It has been seen before that small particles have a number of advantages over large particles. The scattering efficiency of the particles decreases when the diameter decreases. To increase the scattering power it is necessary to use very powerful sources of light. A laser is used as the light source due to its high intensity and easy control. The Argon-ion continuous wave laser and the Nd:YAG pulsed laser are the most frequently used. Both have good beam profiles that are almost Gaussian. The sheet of light is achieved using cylindrical and spherical lenses. The laser must be pulsed to provide precise timing of the images. The duration of the light pulse determines the degree to which an image is frozen during the illumination. The time separation between pulses determines the maximum and minimum displacements that can be measured. The three illumination methods used most often in PIV are: pulsed laser, expanded beam and scanning beam.

1. Pulsed laser: two or more bursts of high energy light are emitted over a short period of time. However, they are difficult to align.

2. Expanded beam: a continuous wave laser is modulated into pulses using a mechanical or electro-optic beam modulator. The resulting beam is expanded by a cylindrical lens arrangement. This sheet is collimated and it illuminates the flow field.

3. Scanning beam: a continuous wave laser is directed into a rotating mirror that has several faces. The beam is projected into a parabolic mirror to produce a sheet of light.

The use of pulsed lasers is limited to the range of pulsed separation that they can produce. They are mainly used for high flow rates and when the cross-correlation analysis method is used. The disadvantage of the expanded beam method is that the Gaussian profile of the laser beam produces an irregular intensity across the light sheet. Furthermore, the modulation of the light means that only a fraction of the initial light is used to illuminate the flow. On the contrary, the scanning beam method produces a light sheet of uniform intensity and does not waste any energy passing through lenses and beam modulators. Moreover, the pulse separation is large and the pulse duration short, giving particle images without blurring. In general, it can be said that the pulsed laser is used to obtain frames of single exposure while the other two methods are suitable to obtain double or multiple exposure frames.

In the present study a Spectra-Physics 171 Argon-Ion continuous wave laser (15 W) was used. The laser was delivered through an optical fibre laser beam system using a Schott (12 W) multi-mode optical length guide as described by Martin [108]. The laser beam was transformed into a pulsed laser sheet using an OFS scanning beam system (Figure 4.1), producing a 0.5 m light sheet length.

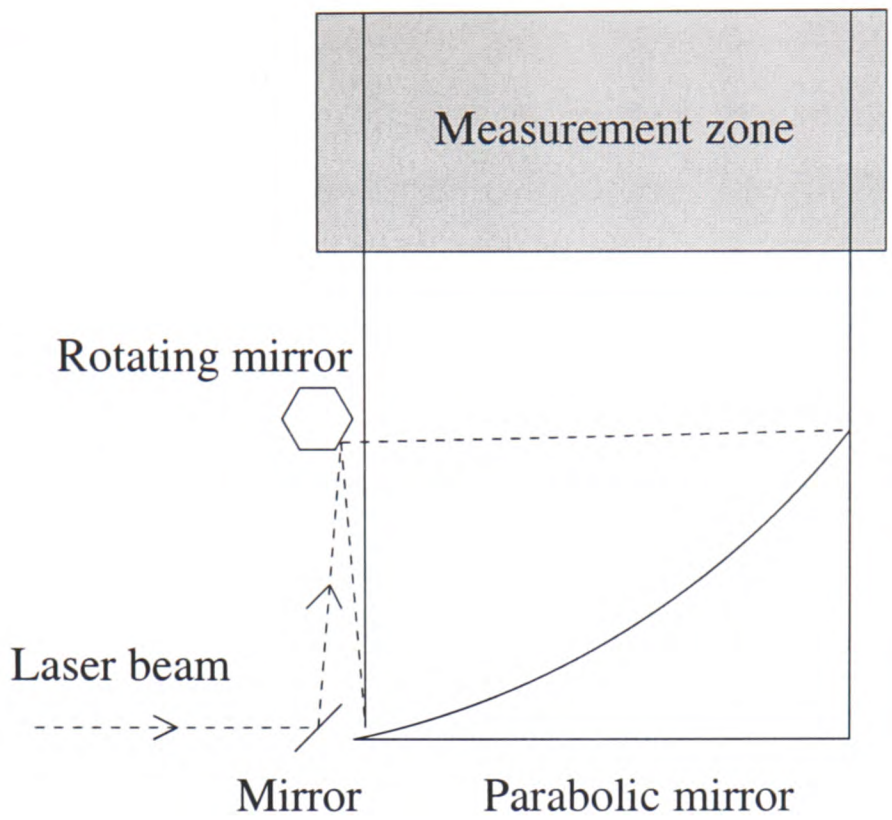

Figure 4.1: Scanning beam illumination method

4.4 Recording the image

In order to record an image onto a recording medium a certain optical exposure must be reached. The optical exposure ($\varepsilon(x)$) is proportional to the response of an optical recording medium (CCD camera, photographic film, or any other). The mean exposure ($\bar{\varepsilon}$) for a single particle image is given by [109]:

$$\bar{\varepsilon} = \frac{4}{\pi k^2 d_i^2} \frac{W}{\Delta y \Delta z} \int_\Omega \sigma^2 d\Omega \tag{4.7}$$

where $k = \frac{2\pi}{\lambda}$, and λ is the wavelength of the light source. Equation 4.7 shows that the optical exposure is a function of the diameter of the image of the particle d_i, the illumination intensity $\frac{W}{\Delta y \Delta z}$ and the scattering power $\int_\Omega \sigma^2 d\Omega$. The largest effect on $\bar{\varepsilon}$ comes from the change in the diameter and in the refractive index of the scattering particles. The diameter of the image of the particle is determined by the magnification M, the diameter of the particle d_p, the point response function of the lens d_s (which accounts for the image blurring) and the resolution of the recording media d_r:

$$d_i = (M^2 d_p^2 + d_s^2 + d_r^2)^{1/2} \tag{4.8}$$

d_s is given by:

$$d_s = 2.44(1 + M) f^\sharp \lambda \tag{4.9}$$

where $f^\sharp$ is the focal number of the lens. These Equations (4.8 and 4.9) are valid when the particle is in the depth of field of the camera (δz), otherwise, the image is blurred by more than 20% of the in-focus diameter. The depth of field is given by:

$$\delta z = 4\left(1 + \frac{1}{M}\right) f^{\sharp 2} \lambda \tag{4.10}$$

The mean scattering energy increases with particle size. In the Rayleigh scattering regime ($d_p \ll \lambda$) the mean scattering power increases proportionally to d_p^4 and the diameter of the image is controlled by the point response function, $d_i = d_s$, and does not depend on the diameter of the particle. In the geometric scattering regime ($d_p \gg \lambda$), the average scattering energy increases proportionally to d_p^2 and d_i is proportional to d_p. Beyond a certain size, of approximately 100 μm, the image intensity becomes independent of the particle diameter because the image area and the scattering light increase with d_p^2. The average optical exposure increases with the particle diameter.

The scattering of light also depends on the ratio of the refractive index of the particle to the refractive index of the fluid. The scattering energy increases with this ratio. The refractive index of the particles could be increased by metallic coating of the particles.

Traditionally, the flow is recorded using a photographic film or a CCD (charged coupled device) sensor. Film recording allows for higher resolution. For example, the 35 mm film used in the present work (Kodak Tmax 400) has a resolution of 125 lines/mm which corresponds to a resolution of 4500×3000 pixels. CCD cameras with resolutions up to 4096×4096 pixels are available but they are extremely expensive; the most common ones are those of 512×512 pixels resolution.

The minimum separation time required between two pictures is smaller in a CCD camera than in a photographic camera, allowing the recording of single frames that can be analysed by cross-correlation. Another advantage of the CCD cameras is that the results can be obtained shortly (i.e. few seconds) after the images

are taken. A photographic film requires a processing time (to develop and dry the film) of about forty minutes. After the film is processed each picture needs to be scanned. This is a very time consuming process, especially because it is very difficult to guarantee that the pictures will be in focus, due to the restrictions of the experimental conditions. The plane of light needs to cross perfectly perpendicularly to the freeboard (to minimise reflections) and perfectly parallel to the camera. Due to the size of the seeding particles a very low $f^\sharp$ number is required, usually 2.8, implying a very small depth of field. However, as resolution was critical in this work, the image was recorded using a Nikon 60 mm lens photographic camera.

4.5 Analysis of the image

Once the particles are recorded the PIV image is divided into small regions called "interrogation areas", where the average displacement of the particles in each of these areas is measured and since the time between illumination pulses is known the velocity can be calculated. There are two main methods to measure the separation between the image of the particles: these are the Young's fringe method and the correlation method.

4.5.1 The Young's fringe method

When the images of the particles within an interrogation area are illuminated by a coherent beam of light, each image of the particles acts as a coherent source of light. The interference of the light transmitted by each particle interacts to produce a Young's fringe pattern. The fringes are perpendicular to the flow direction and the separation between them is proportional to the particle displacement, thus allowing one to calculate the fluid velocity.

4.5.2 Spatial correlation

The most common method used to analyse the PIV image is the spatial correlation of the intensity of the particle images. Correlation processing is the basis for auto-correlation and cross-correlation: it interrogates a local area of flow map and produces a measure of the average local displacement of particles within the region [110]. The general correlation function is given by:

$$C(s_x, s_y) = \sum\sum I(x, y)I(x + s_x, y + s_y)dS_x dS_y \tag{4.11}$$

where $I(x, y)$ and $I(x + s_x, y + s_y)$ are the intensity distribution of a local interrogation area. The output of the function $C(s_x, s_y)$ is the correlation function from which the local displacement is measured. Both auto and cross-correlation methods are described below.

Auto-correlation

The intensity of the image is correlated with itself. Figure 4.2 shows an enlargement of a small region of a PIV image. The image of each seeding particle (a white dot) is repeated six times (the camera was open for 1/30 milliseconds and the time between pulses was 5.5 milliseconds). The auto-correlation process can be thought of as if one had a second copy of the image. The first image is kept in a fixed position; if the second image is superimposed on the first one and their intensities are added a maximum value is obtained (self-correlation peak). The second maximum is obtained when the second image is displaced a distance equal to the distance between particles, thus the image of the second particle of the first image will be superimposed on the image of the first particle of the second image, the third to the second and so forth. The auto-correlation function obtained from Figure 4.2 is presented in Figure 4.3. As can be seen the auto-correlation function presents a strong central self-correlation peak, generated when the image is correlated with itself at zero displacement. The second

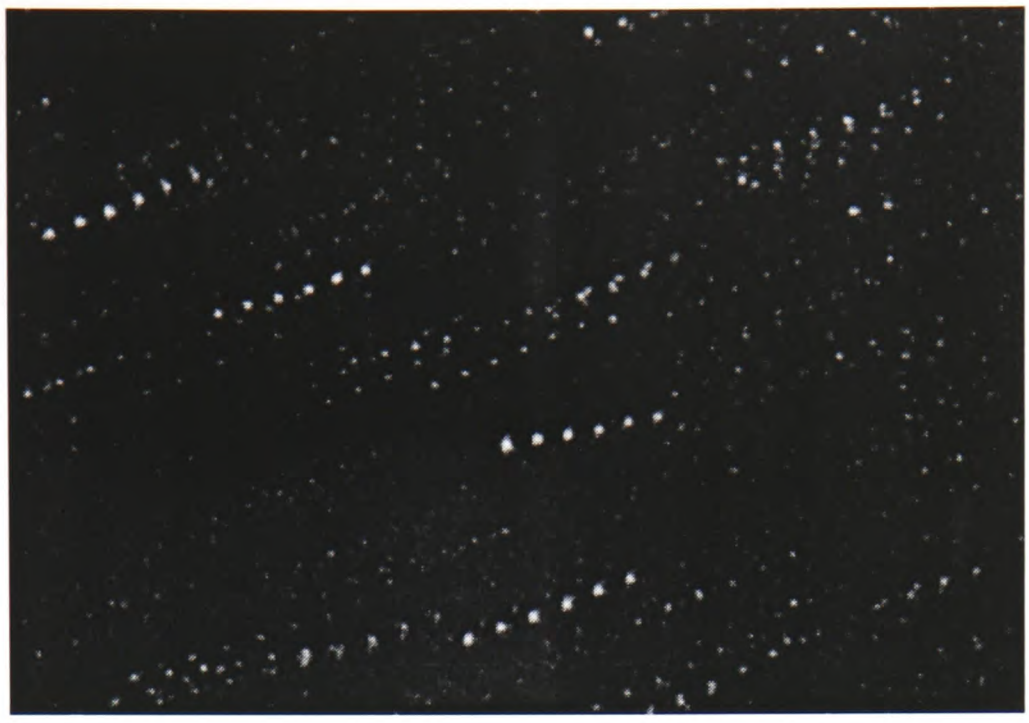

Figure 4.2: Enlargement of a small region of a PIV image

peak occurs when the first images of the particles overlap the second images. The harmonic peaks correspond to the correlation of the second image with the third and so on. The distance from the central correlation peak to either of the displacement correlation peaks is proportional to the average particle displacement within the interrogation area. The autocorrelation function has 180 degree rotational symmetry. For that reason is impossible to say which exposure comes first.

In Young's fringe and autocorrelation techniques, particle images are usually taken on film which enables high resolution measurements [111]. Large velocities can thus be measured if the time interval between two exposures is very small. The associated directional ambiguity [112, 113], however, makes these techniques difficult to apply. A systematic study of these techniques is presented by Keane and Adrian [114].

Cross-correlation

This is used when two different interrogations are correlated with each other [115]. Separated interrogation areas may be sampled from the same image or from sep-

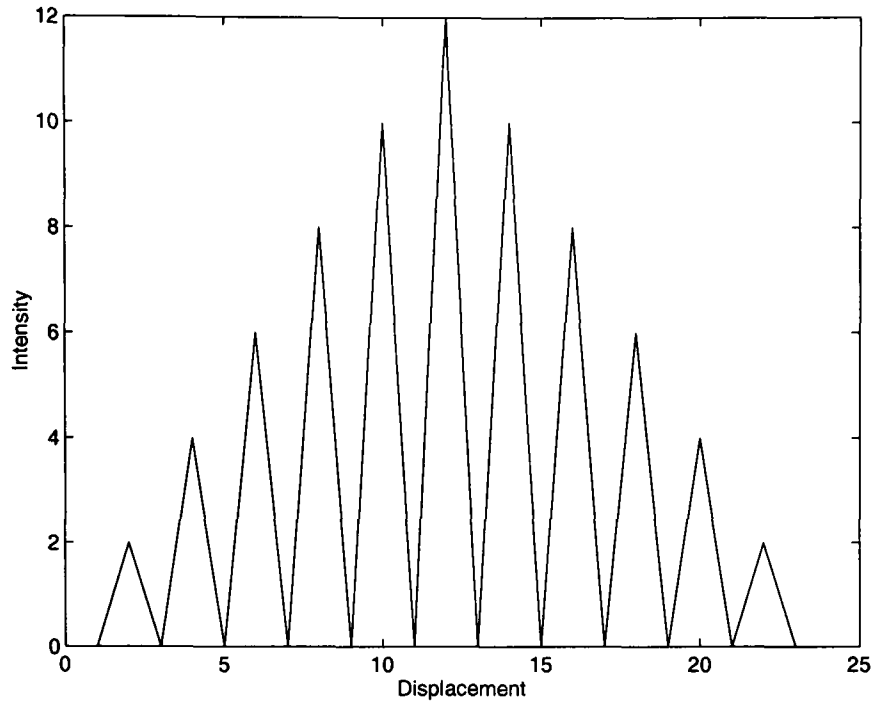

Figure 4.3: Sketch of the auto-correlation function corresponding to Figure 4.2

arate images. When the input intensity distributions $I(x, y)$ and $I(x + s_x, y + s_y)$ are different, but from the same image, they represent two areas displaced by a known distance. This approach is appropriate for measuring small flow fluctuations on top of a known mainstream velocity component. The cross-correlation function is shown in Figure 4.4.

The cross-correlation function is not symmetric. In the case shown, there is still a self-correlation peak, but it is displaced from the centre of the correlation by the distance that separates the interrogation areas. The displacement correlation is visible to one side of the self-correlation. The position of this peak is measured and then adjusted for the displacement of the interrogation areas to give the real displacement value.

In the correlation of separated images, the interrogation areas $I(x, y)$ and $I(x + s_x, y + s_y)$ are obtained from separate images. This approach is the most effective for PIV because the order in which particles are recorded is known and so the direction of the flow is unambiguous [116]. The cross-correlation function resulting from the correlation of a displaced particle distribution between two separately recorded images is shown in Figure 4.5.

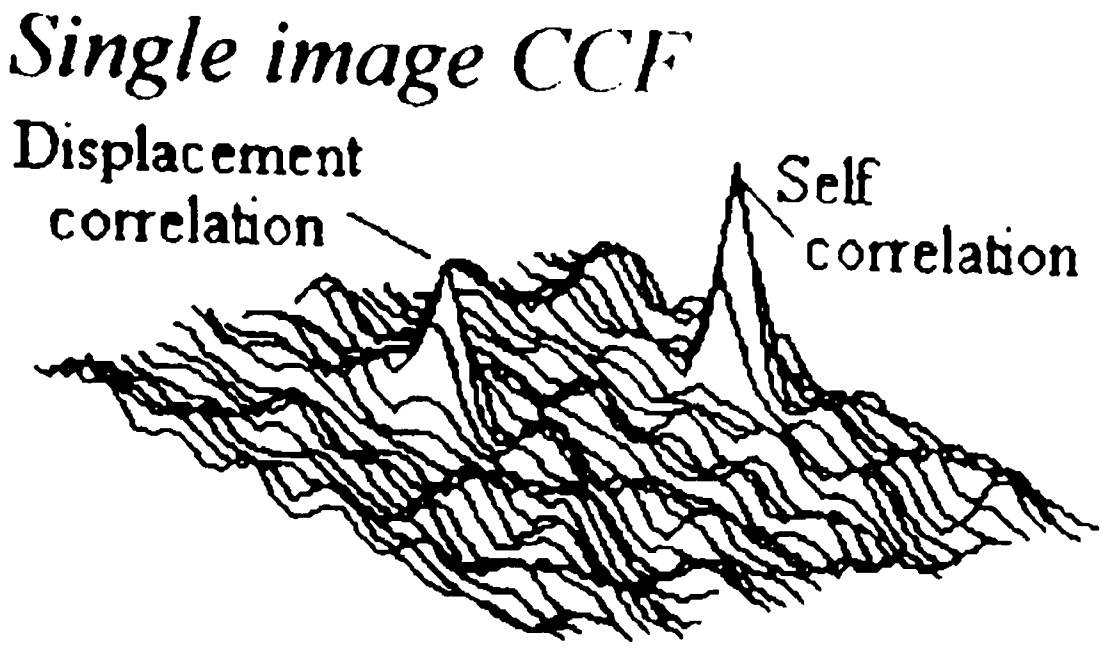

Figure 4.4: Cross-correlation function generated from different interrogation areas from the same image and the displacement relative to each other by the main flow component. From Bruce *et al.* (1993)

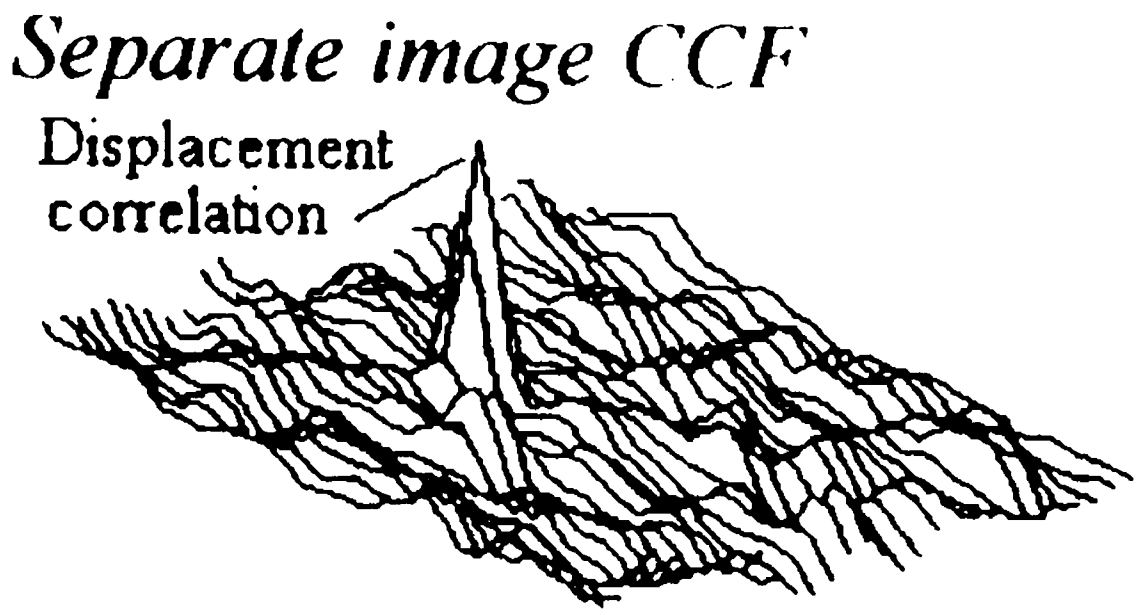

Figure 4.5: Cross-correlation function generated from separately recorded different interrogation areas. From Bruce *et al.* (1993)

There is no self-correlation peak in this case, as there are no identical parts in either interrogation areas. There is no symmetry in the cross-correlation function either, as the directional ambiguity that arises from recording both exposures onto the same image is removed. Additional benefits from recording successive exposures onto separate frames are that zero velocities can be identified and shorter pulse separations used. This improves the spatial resolution and the velocity dynamic range.

In this work, the auto-correlation method was used. In order to cross-correlate different images a CCD camera that rapidly captures successive images would have been required. Fast CCD cameras did not have good resolution (which is fundamental for the understanding of the flow under study) and they were very expensive when this research started.

Once the flow is recorded, the image is digitised using a photographic negative scanner (3600×2500) and then converted into a file that contains the brightness of each pixel in an array. The image is analysed using the in-house PIVANAL software. The image is divided into small "interrogation areas" whose size can be chosen; for the present analysis interrogation areas of 64×64 pixels were chosen since this gave very good results. The auto-correlation of the intensity of the image is calculated, using fast Fourier transforms (FFT) that involve less computing time than using the auto-correlation function directly. The calculation of FFT implies that the analysed data are periodically repeated, with a period equal to the length of the interrogation area. This can generate wrap-around noise (for example, extra correlations will be produced between particles in the "real" interrogation area and particles in the "repeated" interrogation area giving rise to spurious displacement peaks). Zero padding (the interrogation area is placed in the middle of a region with zero brightness) was used to calculate the FFT, so avoiding the wrap-around noise. The location of the auto-correlation peak is found by a Gaussian least squares fit (other popular methods are the volume moment and Whittaker's interpolation) using a 3×3 array with the highest peak

in the centre; this gives sub-pixel accuracy. No validation was applied to the measured data. This means that the second tallest peak (the self-correlation peak is the highest) was chosen to calculate the displacement. Knowing the displacement between particle images, the real displacement can be calculated using the magnification and the velocity can be determined from the known time between pulses.

4.5.3 Limitations of the auto-correlation method

The following drawbacks are usually associated with the use of the auto-correlation method:

- Small dynamic range (ratio between the maximum and minimum velocity). The displacement of the image of the particles needs to be in the range: $1.5\ d_p < d < 0.25\ d_I$. The lower limit is determined by the requirement of the image of each particle to be distinct. The upper limit is given by the size of the interrogation area. Large displacements imply that fewer particles contribute to the auto-correlation function. This results in an auto-correlation that is biased towards smaller displacement.
- Directional ambiguity, due to the symmetry of the auto-correlation function. Therefore, it is not possible to determine the direction of the flow.

Three approaches can be used in order to overcome these limitations:

- Cross-correlation of different images.
- Image encoding techniques, using different colours, pulses of different lengths or holography with beams of different path lengths.
- Image shifting: i.e. imposing a known translation to the real flow.

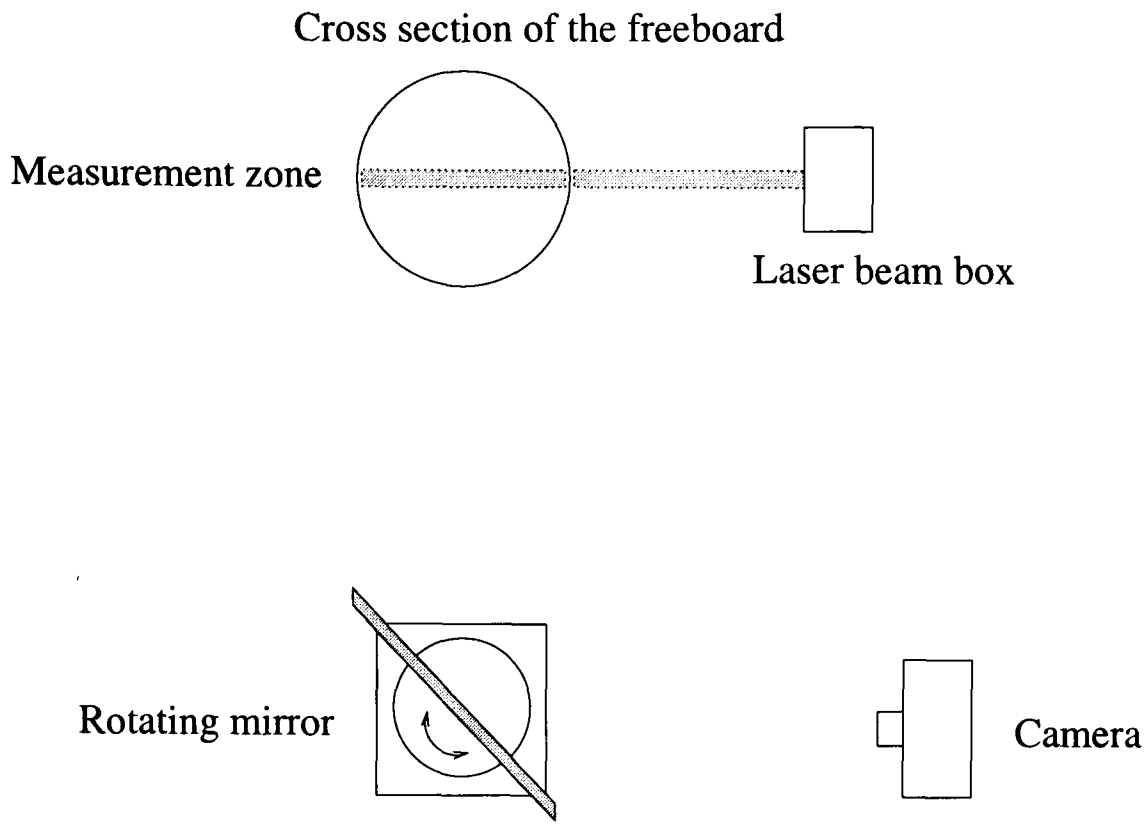

Figure 4.6: Image shifting

4.6 Image shifting

Image shifting is based on the application of a known displacement to the image of the experimental flow. In this work, this is achieved by using a rotating mirror, at 45^o with respect to the flow, to visualise the flow. A sketch of the experimental arrangement is displayed in Figure 4.6. As can be seen the camera does not photograph the illuminated flow directly, instead the image of the flow produced in the rotating mirror is photographed.

Figure 4.7 shows the basic principle of image shifting. The space between the two concentric circles represents the velocity range that can be measured ($1.5\ d_p < d < 0.25\ d_I$). In a real flow with high velocity gradients, some particles have smaller or bigger velocity than those that can be measured. To overcome this, it is needed to: i) decrease the time between pulses, reducing the displacement of the particles (Figure 4.7 b), and ii) add an additional displacement (using a rotating mirror) to the real displacement; this produces a displacement very similar for all the particles (in this case, the shifting adds a displacement bigger than that of the original flow), that can be easily calculated using auto-correlation analysis.

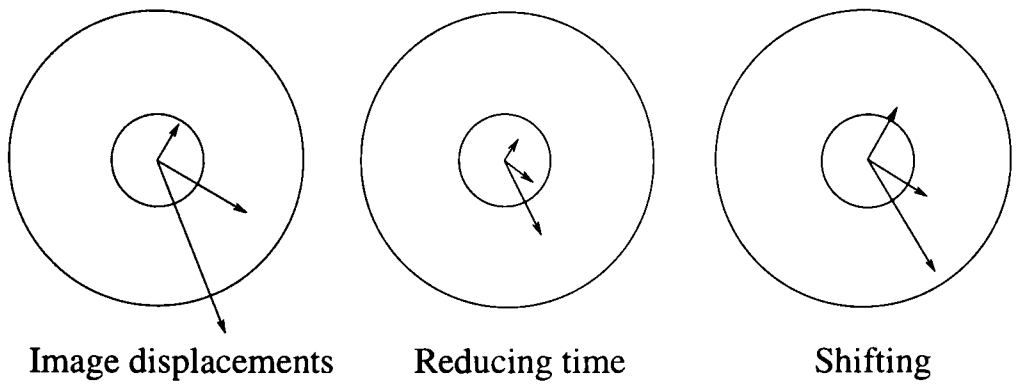

Figure 4.7: Image shifting

Figure 4.8 shows a typical vector map obtained when applying image shifting. The next step is to subtract the imposed displacement (Figure 4.9). Usually, the shifting should be perpendicular to the measured flow to optimise particle displacement. The mean direction of the real flow is upwards. A horizontal displacement has been imposed onto the flow. The ideal [2] horizontal, d_x, and vertical, d_y, shifting added to the real velocity is:

$$d_x = 2\omega RM\Delta t \tag{4.12}$$

$$d_y = 0 \tag{4.13}$$

where w is the rotational velocity of the mirror, R is the distance between the centre of the mirror and the light sheet, M is the magnification and Δt is the time between pulses. After the shifting, all the vectors have the same known direction, thus avoiding the directional ambiguity. The vector map obtained after subtracting the shifting (Figure 4.9) is shown in Figure 4.10. The same scale has been used to plot the three vector maps (shown in Figure 4.8, Figure 4.9 and Figure 4.10). As can be seen the real velocity is smaller than the shifted one. The vector map shown in Figure 4.10 has been plotted in Figure 4.11 using a greater magnification, which allows a better visualisation of the flow. It can be seen that high and low velocities occur in the flow at the same time while the direction of the flow is not constant. This flow could not have been resolved without using image shifting.

Equations 4.12 and 4.13 give the ideal displacement due to the shifting. However,

[2]The effect of mirror rotation is included later.

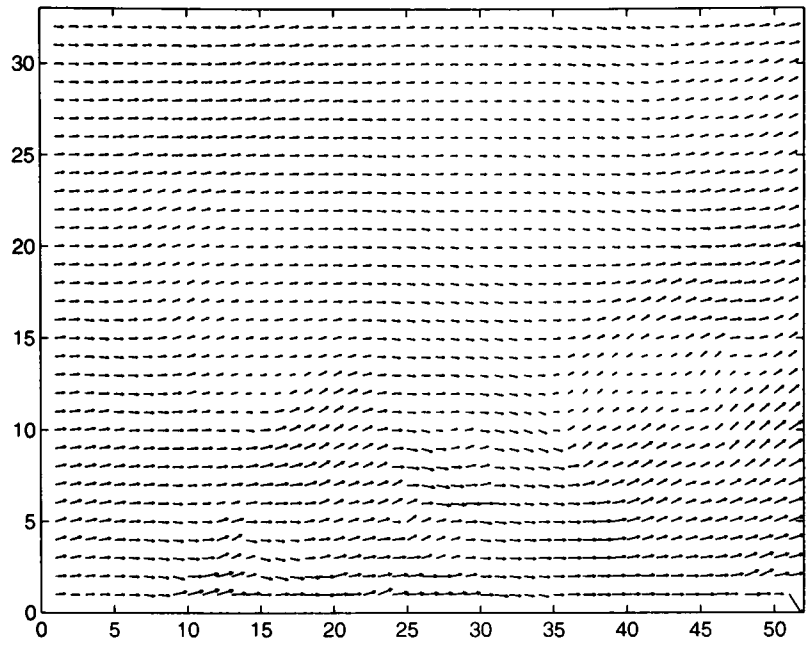

Figure 4.8: Vector map after image shifting

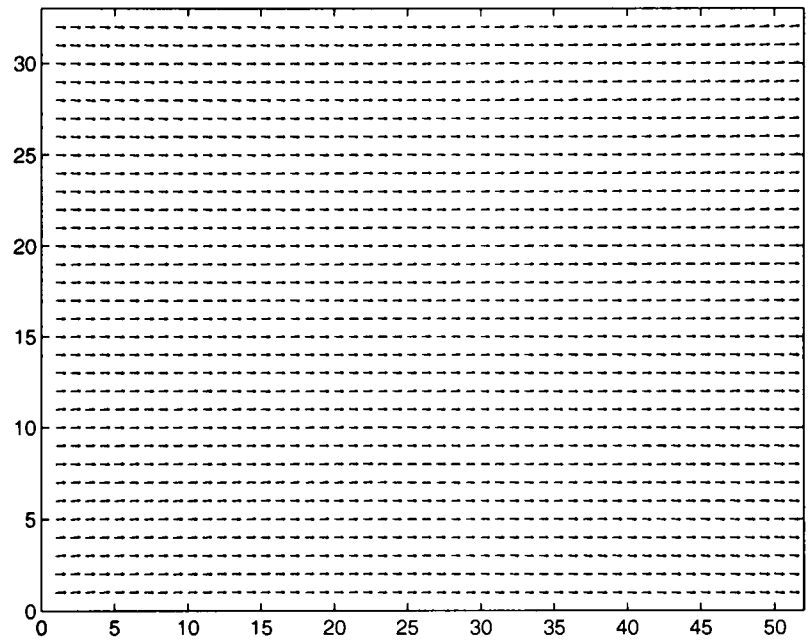

Figure 4.9: Shifting

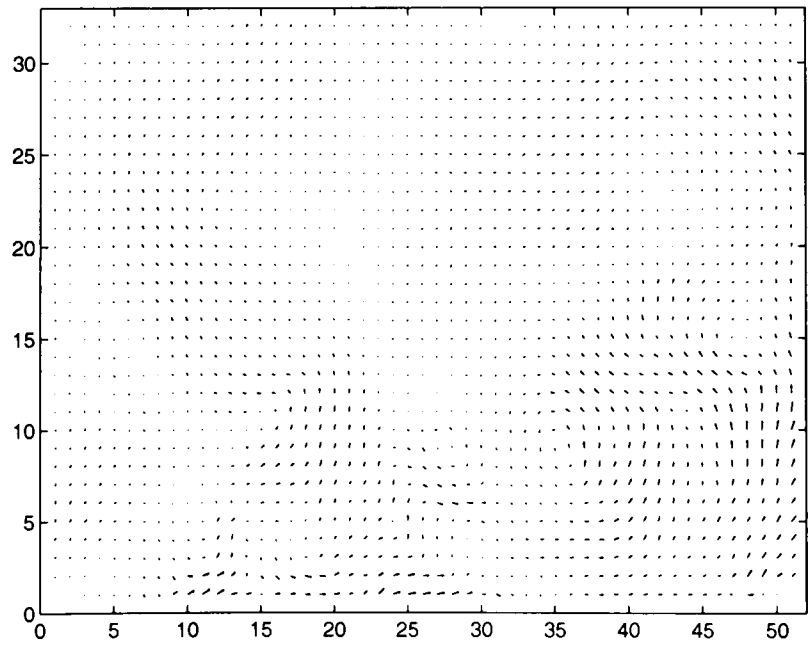

Figure 4.10: Vector map after subtracting the shifting

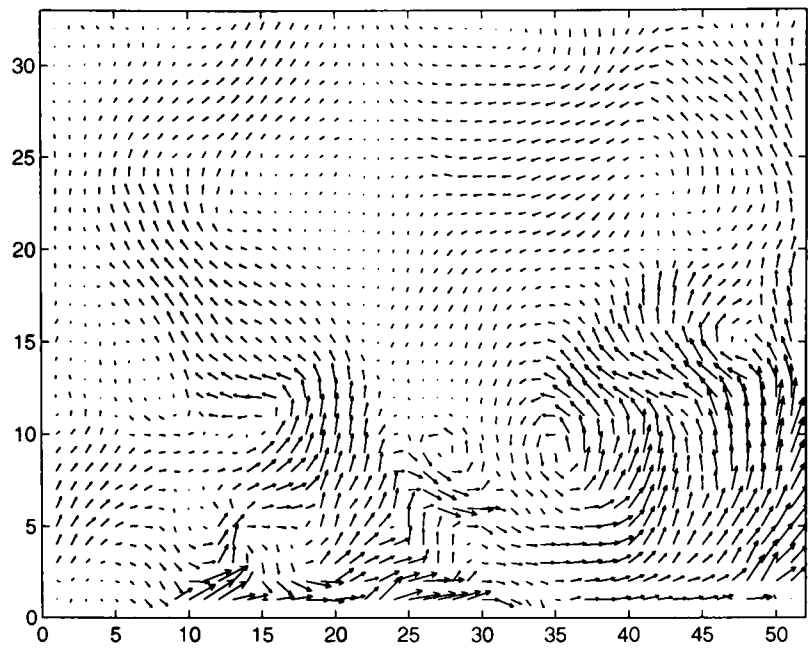

Figure 4.11: Magnification of Figure 4.10

the mirror rotates around its axis rather than moving linearly, thus distorting the measurement region. Raffel and Kompenhaus [117] and Morrison [118] developed equations which account for the shifting:

$$d_x = \frac{x - 2\omega RM\Delta t}{(x + CM)2\omega\Delta t F^{-1}(1+M)^{-1} + 1} - x \tag{4.14}$$

$$d_y = \frac{y}{(x + CM)2\omega\Delta t F^{-1}(1+M)^{-1} + 1} - y \tag{4.15}$$

where C is the distance between the optical axis of the camera and the mirror rotation axis and F is the focal length of the camera lens.

One of the drawbacks of image shifting is that this is a very slow technique. Firstly, the mirror needs to accelerate until a constant velocity is achieved (that is when the picture is taken) then to decelerate and to return to the initial position. The closest that two pictures could be taken using image shifting is just less than one second.

4.7 Errors

The following criteria were found to optimise multiple exposure PIV:

- The mean number of images N_p in the interrogation area is given by: $N_p > 15(n-1)$, n being the number of pulses.

- The separation between two images of the same particle (d) has to be bigger than one and a half diameters of the particle image (d_i) and smaller than a quarter of the length of the interrogation area (d_I): $1.5d_i < d < 0.25d_I$.

- The out-of-plane displacement ($\Delta z_0 = w\Delta t$, with w being the normal component of the velocity and Δt the separation time between pulses) should be less than a quarter of the laser plane width (Δz_0): $w\Delta t < 0.25\Delta z$.

- The detectability (D_o defined as the ratio of the height of signal peak to height of the next highest peak) should be about 1.2: $D_o \simeq 1.2$.

4.7.1 Errors arising from the seeding particles

Due to the nature of turbulent flow preferential concentration of the seeding particles may occur. Turbulence is dominated by coherent structures that can modify particle distribution giving rise to regions of either high or low particle concentration (for example, low particle concentrations may occur in the core of a vortex). Another effect of turbulent flow, especially shear flow, is the lifting experienced by particles due to the velocity gradient induced by the shear flow [119]. The effect of the fluid turbulence on particle motion is determined by the Stokes number (the ratio of the particle aerodynamic time constant to an appropriate turbulence time scale). The time constant for particles with higher density than the flow as is the case of solid particles in a gas, can be calculated using Stokes' equation.

4.7.2 Errors arising from illumination

The **time between pulses** needs to be known very accurately. In the present study it is determined by the frequency of rotation of a quartz crystal and fixed intervals can be chosen.

The **pulse duration** has to be fast enough to freeze the image, otherwise the shape of the particle will be distorted.

The light sheet has to be perfectly **flat**, because otherwise an error in the magnification will be produced. The finite **thickness of the light sheet** may also give rise to a small error.

4.7.3 Errors arising from image recording

The **lens** may distort the image edges (for example a pincushion or barrel effect). This distortion can be measured and subtracted from the image. However, the effect of the distortion in the present study can be considered negligible, since for most of the experiments the edges of the negatives were not analysed.

The **photographic film** may introduce some errors to the image such as: film noise due to the grains and variation of the emulsion thickness. This can be minimised by using a high quality film.

The errors arising from illumination and image recording are systematic. They can be measured and a correction can be applied to the images.

4.7.4 Errors arising from analysis method

Magnification: a careful calibration needs to be done to convert the image from

plane coordinates to real coordinates.

Out of plane movement: PIV assumes that the fluid is moving within the analysed plane. However, some particles can move outside the interrogation plane for two reasons: i) particles have a normal component of the velocity and they move out of the plane of light or ii) particles move too fast and they move out of the interrogation area. The first mechanism of reduction of particle pairs increases the noise to signal ratio. The second one produces a bias towards zero velocity.

Velocity gradient bias: PIV assumes that there is no fluid velocity variation in an interrogation area. A gradient in velocity gives rise to two problems: i) the variation of image separation lowers and broadens the correlation peak, decreasing the ratio of signal to noise and ii) the peak centroid is biased towards lower velocities since the number of particles with small velocity is bigger than those with high velocity in an interrogation area. In a shear flow the peak is broader towards the direction of the shear.

Digitisation process: This introduces an error in the particle location and in the peak location. Willert and Gharib [115] found that when the particle diameter image size is less than about two pixels the particle displacement is biased towards the nearest integer.

Due to the nature of the flow in the present work and the advantages of PIV over other techniques, PIV implemented by image shifting has been used as the measuring technique.

Chapter 5

Gas flow in the freeboard

The gas flow in the freeboard was studied at similar conditions to those used in the B.P. Chemicals pilot plant (See Section 3.2). It would have been ideal to analyse the complete freeboard (from just above the bed surface to the freeboard outlet) simultaneously. However, the spatial resolution of the PIV equipment precluded this. Therefore, it was necessary to divide the freeboard into three parts: above the bed surface, the expansion section and the expanded section. Each of these parts was independently studied and the result will be presented in this chapter.

5.1 Flow above the bed surface

The gas flow pattern in the freeboard above a bubbling bed is believed to be strongly dependent on the bubble behaviour at the bed surface. For this reason, bubble characteristics were studied (using video images), when the bed was operated at its normal bubbling condition, before undertaking the study of the gas flow in the freeboard. The most important characteristics were:

- Bubbles arrived preferentially at the bed surface as a large central bubble, imposing an overall circulation pattern of particles: up at the centre and down near the wall.

- The average bubble size measured was 14 cm. These bubbles are expected to be spherical caps [47], i.e., to be approximately spherical at the front surface with an indentation at the rear, resembling a kidney shape (this is the characteristic shape of bubbles in fluidised beds of group B [34] particles).

- The average bubble frequency, was 1.8 s^{-1}.

- Only 17% of the bubbles exploded violently when they reached the bed surface, ejecting bed material. However, the ejected particles returned to the bed surface and did not leave the bed.

- The most repetitive feature was the continuous presence of a large vortex ring above the bed surface near the wall. The rotation of the vortex ring was upwards nearer the wall and downwards nearer the bed centre.

It was indicated (Section 4.6) that the fastest that two successive images can be taken using image shifting is close to one second; however a new bubble rises to the bed surface every 0.55 s. For this reason PIV, implemented by image shifting, could not follow the development of a bubble at the bubbling bed surface.

A very good way to start studying the influence of the erupting bubbles on the gas flow pattern is to generate single bubbles and study them at known times after injection. This assumes that bubble features are very similar to those of spontaneous bubbles in bubbling fluidised beds, as discussed in Section 2.1. A single bubble injector was devised and constructed as described in Section 3.7 and bubbles were injected in an incipiently fluidised bed.

5.1.1 Single ejected bubbles

Experimental results

The bed was operated just beyond incipient fluidisation; the gas velocity (4.7 cm/s) was slightly below the point of formation of bubbles and above the point of minimum fluidisation velocity. The seeding particles were mixed with the bed particles just below the bed surface. The vertical central plane across the bed above the surface was illuminated with the pulsed laser sheet and photographs were taken at known times, as described in Section 3.7.

The average velocity of the single injected bubbles measured (calculated as the bed height divided by the delay between bubble injection and its arrival to the bed surface) was 66 cm/s. The bubble velocity in an infinite medium ($u_{b\infty}$) is given by:

$$u_{b\infty} = 0.711\sqrt{gD_e} \tag{5.1}$$

Using this equation (where the bubble frontal diameter measured at the bed surface has been used as D_e) a bubble velocity of 83 cm/s was found. However, this equation does not take into account the influence of the presence of the wall. When the bubbles are affected by the presence of the wall, i.e. $0.125 \leq D_e/d_t \leq 0.6$, D_e being the diameter of a sphere having the same volume as the spherical cap and d_t the bed diameter, the rise velocity is reduced [120]. Furthermore, injected bubbles rise slower than spontaneous bubbles [121]. Hence, it is expected that the measured value would be lower than that theoretically calculated.

When a single bubble was injected into the bed, the bed height increased by approximately 2.7 cm. From this, the volume of injected gas was estimated to be 1.4 litres. The bed was operated just below bubbling velocity, hence the extra introduced gas would be expected to form the bubble. The average bubble diameter measured at the bed surface was approximately 14 cm. Assuming that the bubble is spherical (a more realistic shape would be spherical cap, as explained in Section 2.1), a diameter of 14 cm would give a volume of 1.4 litres in good

agreement with the observed height increase.

These bubbles are expected to have thin clouds and the cloud radius is predicted to be 8.1 *cm* [75] for a 7 *cm* radius bubble. A circulation of gas within the bubble would be predicted by Davidson's model [75].

Although this study deals with the gas flow, a brief description of the observed movement of the sand particles at the bed surface due to an injected bubble will be given to clarify the terminology used. When the gas was injected, the level of the bed surface rose. When the bubble approached the surface particles moved upwards to form a bridge-like structure called a "dome". The fraction of the bubble above the bed surface plus the dome will be called the "bulge". When the bulge is rising the voidage of the dome is increasing by stretching. After the bubble reached its maximum height the dome particles were seen to return to the bed surface maintaining a coherent structure.

Vector maps corresponding to four different defined moments after the single bubble was injected into the bed are presented in Figures 5.1, 5.3, 5.6 and 5.8. The photographs were taken 7 *cm* above the static bed surface. The photographed area was 13×25 *cm*. The vector maps show instantaneous velocities in this region. Three vectors have been added to the left upper corner of each vector map to indicate the scale. The areas near the wall could not be analysed due to the multi-surface images generated by the mirror rotation and the internal reflection of the laser. However, seeding particles in a very fine gas layer (estimated to be 1 *cm*) could be seen continuously next to the wall, with the naked eye, going upward faster than the surrounding gas (the estimated velocity is approximately 20 cm/s). This may be due to the fact that the voidage in the bed is higher near the wall and hence the wall itself decreases the local resistance to the flow. The same behaviour is found in packed beds [122].

In the bulk of the bed the gas does not follow a straight trajectory, because a fluidised bed is not a uniform suspension of solid particles. There exist regions

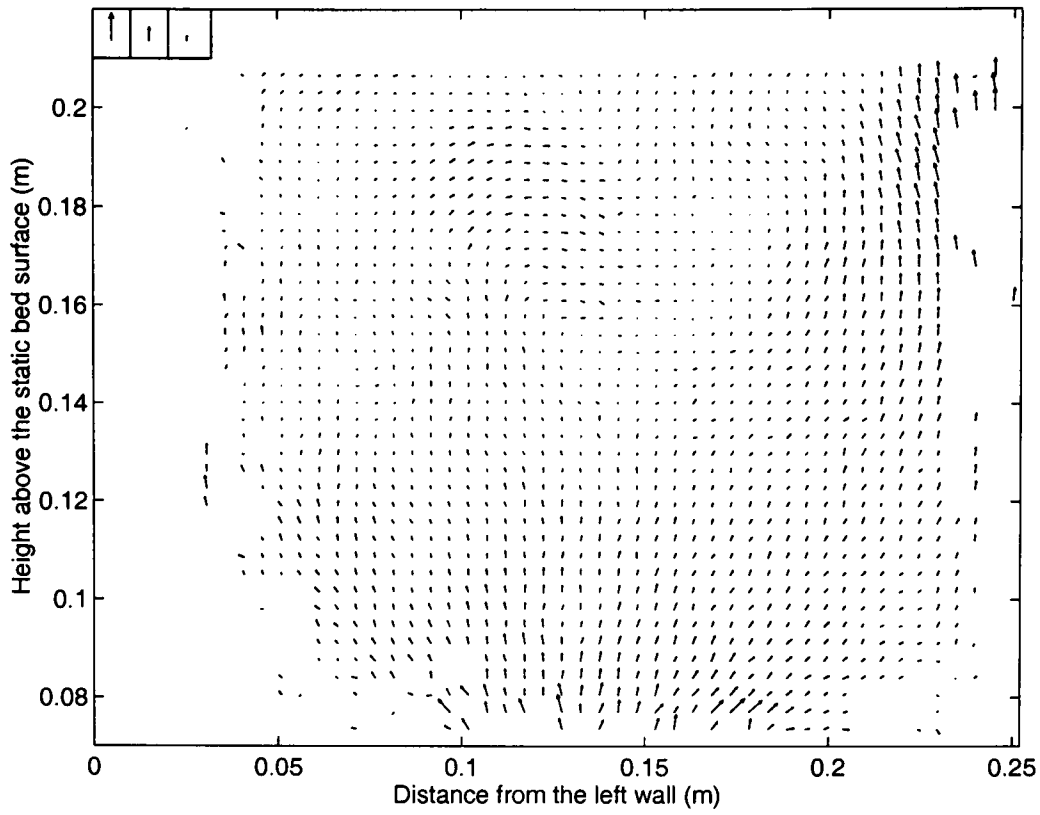

Figure 5.1: Velocity vectors of the vertical cross-sectional central plane 7 cm above the static bed surface of the incipiently fluidised bed just before the bubble reached the bed surface, 0.715 seconds after bubble injection. Vectors in the left upper corner from left to right: 5 cm/s, 2.5 cm/s and 1 cm/s

of different voidage (including a bubble of voidage approximately one) that offer preferential paths to the gas, resulting in a non-uniform gas flow. This non-uniform flow influences the flow pattern in the freeboard.

Figure 5.1 corresponds to 0.715 seconds after the bubble was injected into the bed and just before it reached the bed surface. When the bubble is injected in the fluidised bed the height of the bed increases, pushing the gas above it, acting like a piston. The gas above the bed surface is moving vertically upwards with very small horizontal component velocity. The upwards velocity decreases with height. In the central upper part of Figure 5.1 a region of low velocity can be seen, suggesting, by continuity, that the velocity of the gas in the normal direction to the considered plane may be high, indicating the three-dimensional character of the flow.

Figure 5.2, 0.873 seconds after the bubble is injected, shows the moment after the bubble nose reaches the bed surface and forms the dome. The lighter parts

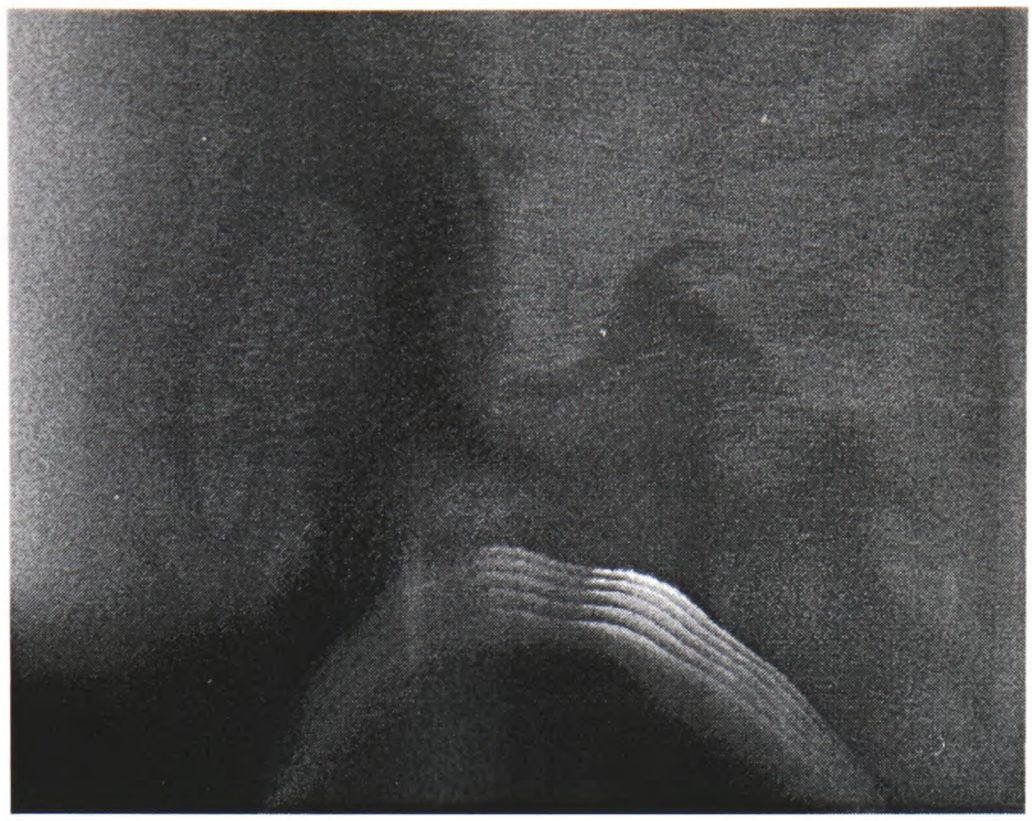

Figure 5.2: Photograph, obtained using image shifting, of the vertical cross-sectional central plane 7 *cm* above the static bed surface of the incipiently fluidised bed when a bubble is rising above the bed surface, 0.873 seconds after bubble injection

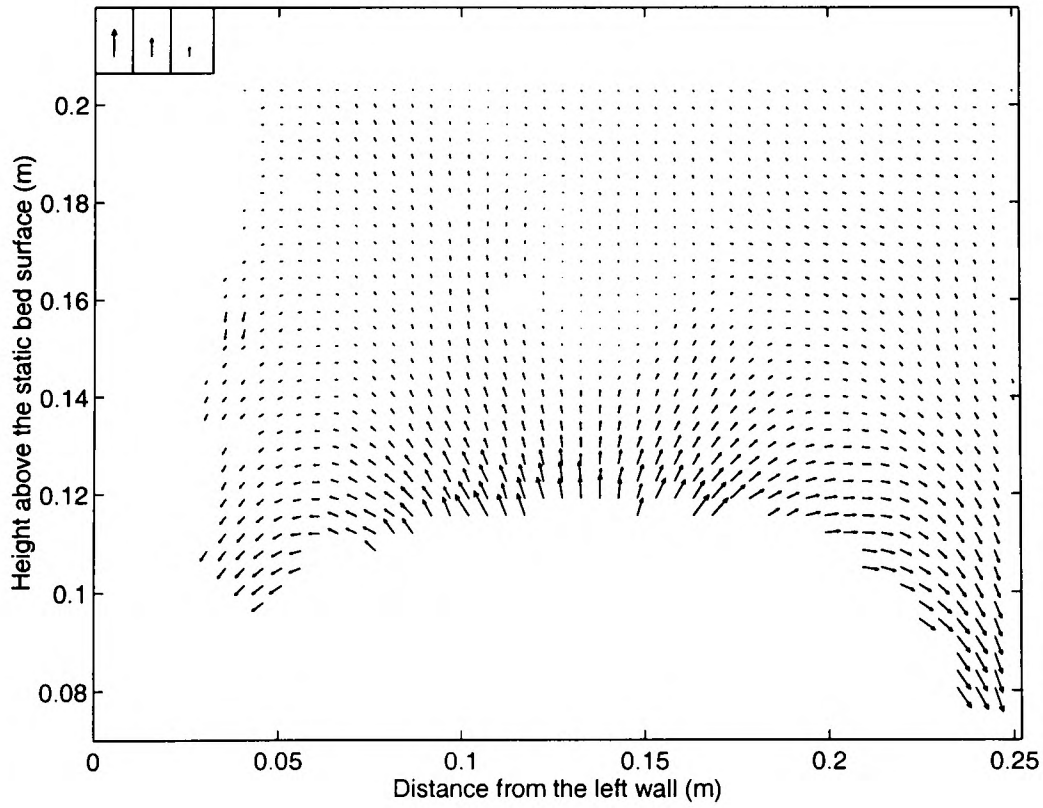

Figure 5.3: Velocity vectors of the vertical cross-sectional central plane 7 *cm* above the static bed surface of the incipiently fluidised bed when a bubble is rising above the bed surface, 0.873 seconds after bubble injection. The empty region corresponds to the region occupied by the rising bulge. Vectors in the left upper corner from left to right: 15 cm/s, 10 cm/s and 5 cm/s

are due to the presence of seeding particles (apart from the bottom part that corresponds to the sand particles forming the bulge) and the darkest part corresponds to regions empty of seeding particles. The dark part on the left hand side is the shadow projected by the bubble, since the plane is illuminated from right to left. The seeding particle distribution is not uniform because the flow is still influenced by the previous bubble. The out of focus appearance of the photograph is due to the movement of the image imposed by the rotating mirror. Figure 5.3 is the vector map calculated from Figure 5.2 (The empty region at the bottom of the vector map is the region occupied by the bulge). The gas velocity is maximum (18.7 cm/s) at the centre of the bubble, having only a vertical component. Towards the sides of the bubble, the gas describes a circular movement, leaving the bubble and tending to return to the surface, maintaining the same circulating movement as a bubble rising in a fluidised bed. This kind of flow pattern is maintained during the time that the bulge is rising.

Bulge height(cm)	Time after injection(sec)	Bulge top velocity(cm/sec)
4.71	0.873	46.7
4.98	0.880	38.7
5.12	0.887	29.9

Table 5.1: Rise velocity of the top of the bulge

Table 5.1 shows the experimental rise velocity of the bulge top, corresponding to Figure 5.2. These velocities have been calculated measuring the increase of height that occurs between each pulse. The experimentally measured bubble velocity through the bed is approximately 66 cm/s. The bubble decelerates after the nose reaches the bed surface. The radial profile of the vertical component of the gas velocity above the rising bulge, corresponding to Figure 5.3, is plotted in Figure 5.4. The vertical gas velocity at the bed surface varies spatially, decreasing from the centre to the sides of the bubble. The vertical profile above the bulge can be divided in two different regions, as predicted by the calculations of Levy *et al.* [43]; a core region, where the upward gas velocity is higher than superficial velocity, and an annular region surrounding the core, where the vertical gas velocity is lower than the superficial velocity. If the radius of the core and the upward

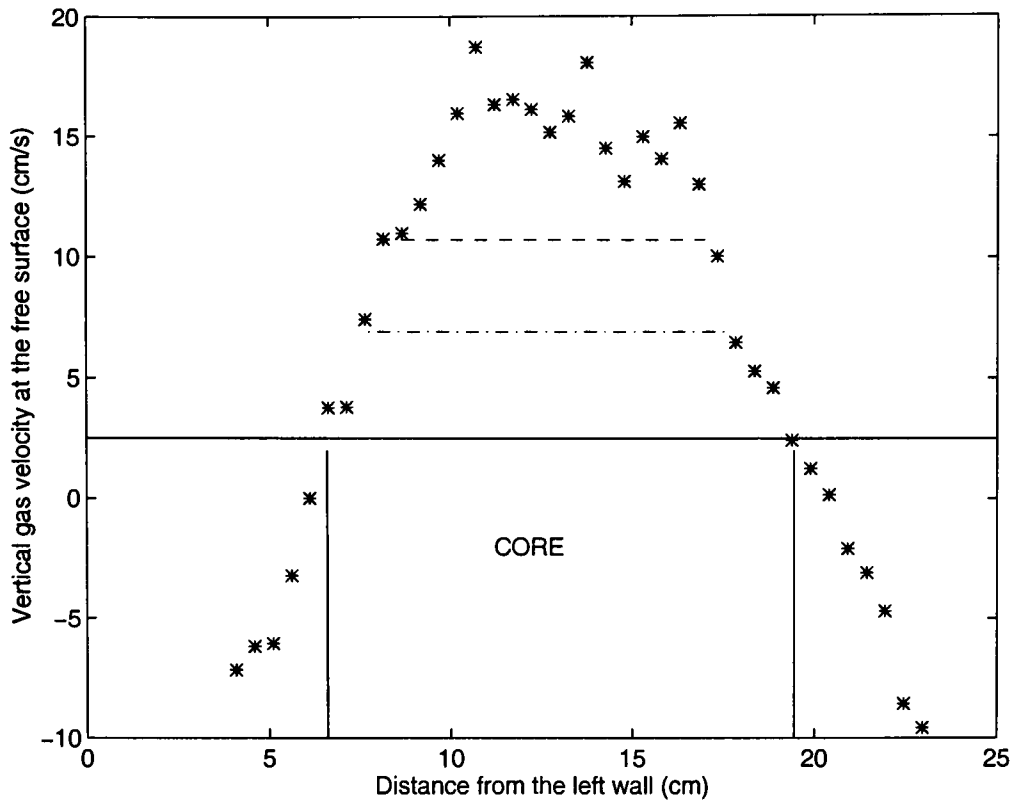

Figure 5.4: Radial profile of the vertical component of the gas velocity above the rising bubble in Figure 5.3 (- Superficial velocity; -. Davidson through-flow for a stationary bubble; – Experimental through-flow)

velocity are known, the flow of gas processed by the bubble can be determined. This is an important parameter for calculating the conversion in a fluidised bed reactor.

In order to compare the experimental results with Davidson's model predictions, the upward flow of gas across the bubble at its maximum cross-section was calculated by averaging the upwards velocities at the free surface. The value of the calculated through-flow was 10.7 cm/s. Davidson's model predicts that for a stationary bubble deep within the bed the through-flow is three times minimum fluidisation velocity ($3 \times 2.3 = 6.9$ cm/s). This seems to indicate that the measured velocity is the result of gas going through the bubble and percolating across the dome. This percolation may be due to the pressure difference and to the fact that the dome may be very thin and of high voidage, therefore easy to cross. The values of the through-flow calculated from the experimental results and from Davidson's model, for a stationary bubble, have been added to Figure 5.4.

After the spherical cap reached its maximum height the particles above the bubble

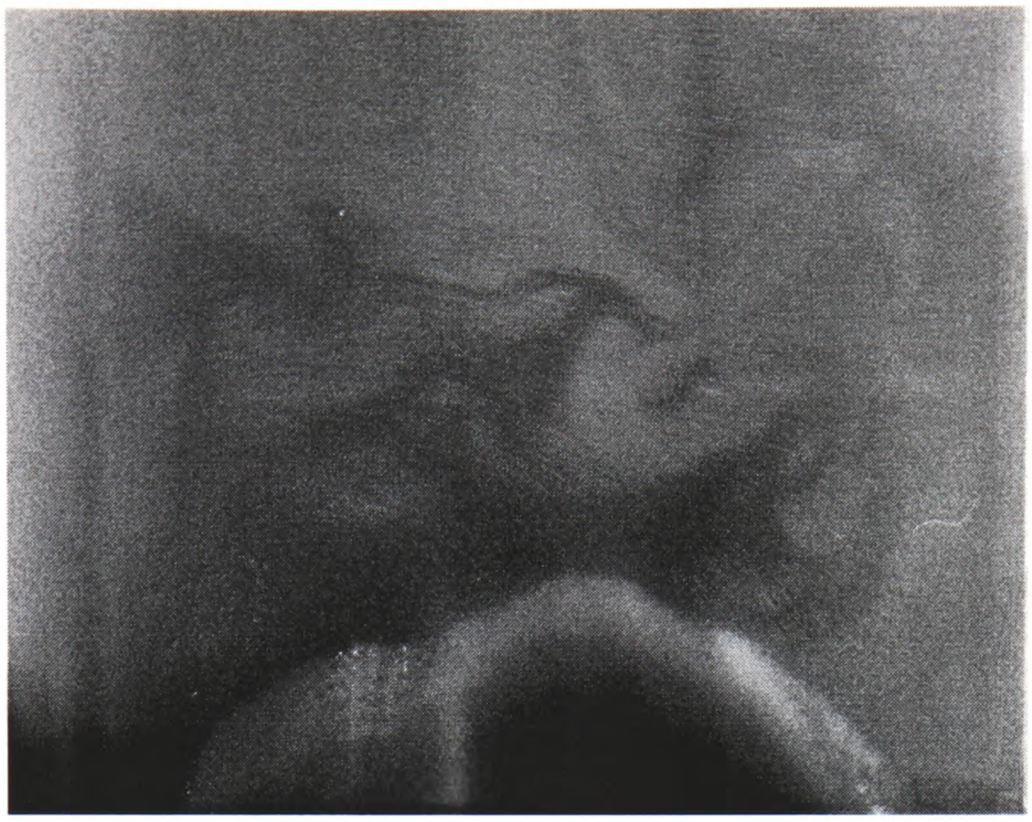

Figure 5.5: Photograph, obtained using image shifting, of the vertical cross-sectional central plane 7 *cm* above the static bed surface of the incipiently fluidised bed just after the bubble reaches its maximum height when the particles above the bubble are returning to the bed surface, 0.961 seconds after bubble injection

were seen to return to the bed surface, due to the insufficient remaining force to support them. They are seen to maintain their bridge-like structure until fully collapsed. No hole in the bubble roof was seen to form which would have allowed a greater leakage of the gas (this is obviously not analogous to air bubble eruption in a liquid).

Figure 5.5, 0.961 seconds after bubble injection, displays the moment when the material of the bubble dome is returning to the bed. As in the case of Figure 5.2 the seeding particles are not distributed homogeneously. The bulge-descending velocity could not be measured because the images of different pulses could not be distinguished. As the sand falls back to the bed surface, it drags gas with it, producing a circulating movement above both sides of the bubble. At this moment the bed height decreases to its initial value. Figure 5.6 is the vector map corresponding to Figure 5.5 (as in Figure 5.3, the empty region at the bottom of the vector map is due to the presence of the bulge). The maximum vertically downward velocity measured was 12.1 cm/s. Figures 5.3 and 5.6 cannot be

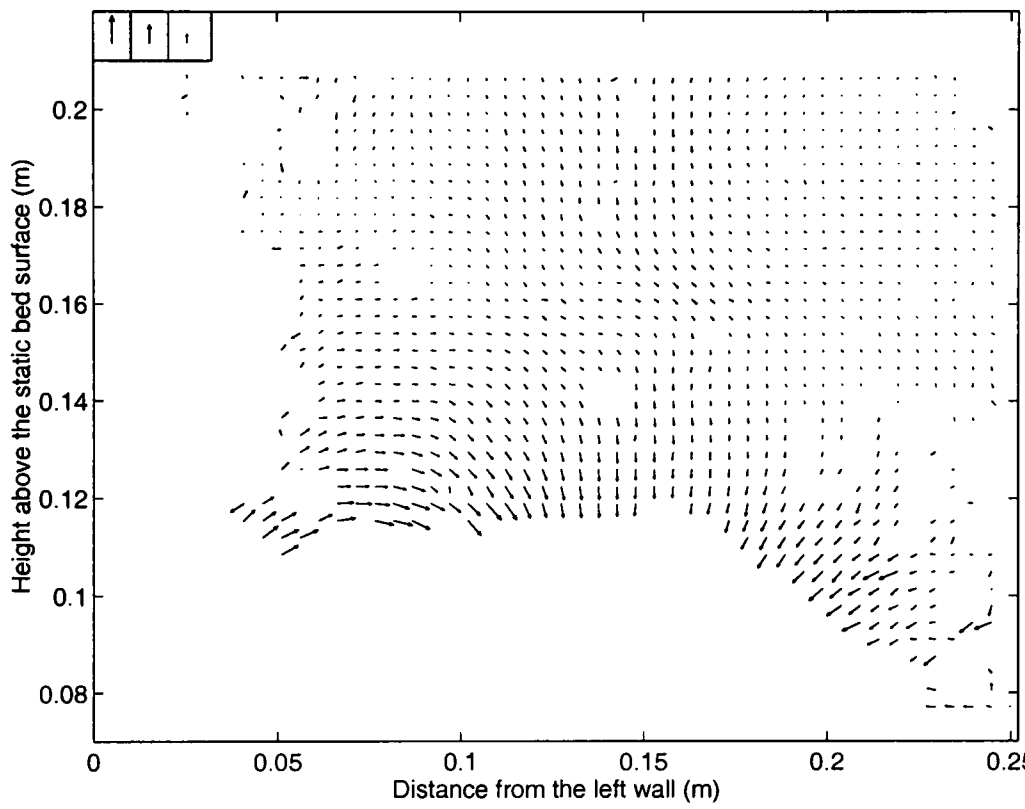

Figure 5.6: Velocity vectors of the vertical cross-sectional central plane 7 cm above the static bed surface of the incipiently fluidised bed just after the bubble reaches its maximum height when the particles above the bubble are returning to the bed surface, 0.961 seconds after bubble injection. The empty region corresponds to the region occupied by the returning bulge.Vectors in the left upper corner from left to right: 15 cm/s, 10 cm/s and 5 cm/s

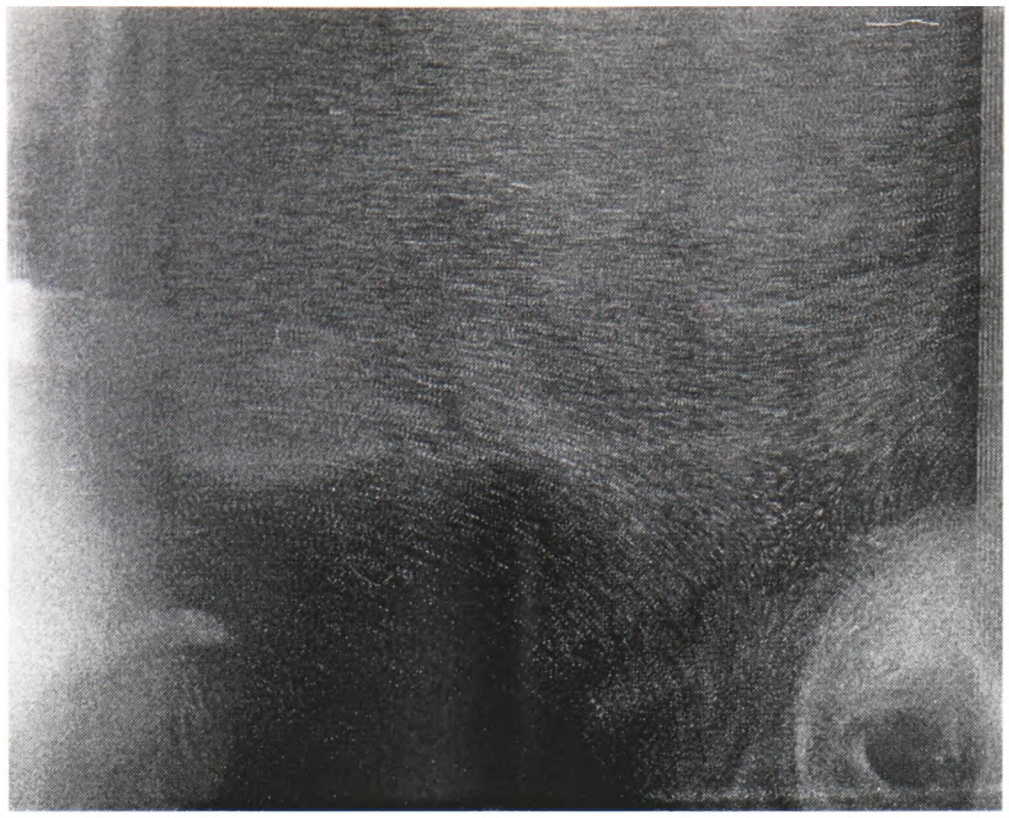

Figure 5.7: Photograph, obtained using image shifting, of the vertical cross-sectional central plane 7 *cm* above the static bed surface of the incipiently fluidised bed after bubble eruption, 1.530 seconds after bubble injection

compared directly, because they correspond to two different bubbles.

When the gas dragged by the sand particles, returning to the bed surface, collides with the surface a circular movement of the gas near the wall was observed, as shown in Figure 5.7, 1.530 seconds after bubble injection. Side vortices are produced, which rotate in a clockwise direction on the left and an anti-clockwise direction on the right. The direction of circulation is the opposite of the predicted gas circulation inside a bubble and same as that observed by Levy and Lockwood [42]. The side vortices have a high internal velocity compared with the external gas. Figure 5.8 has been calculated from Figure 5.7. Unfortunately, the velocity of the vortex ring could not be measured due to the preferential seeding particle concentration.

Figure 5.9 shows four images just after the sand above the bubble returned to the bed surface. The dark spires (1,2) that can be seen in frame (a) are remaining from the previous bubble eruption. After the bubble roof returns to the surface the side vortices are seen as a dense cloud of seeding particles beside the wall (3,4).

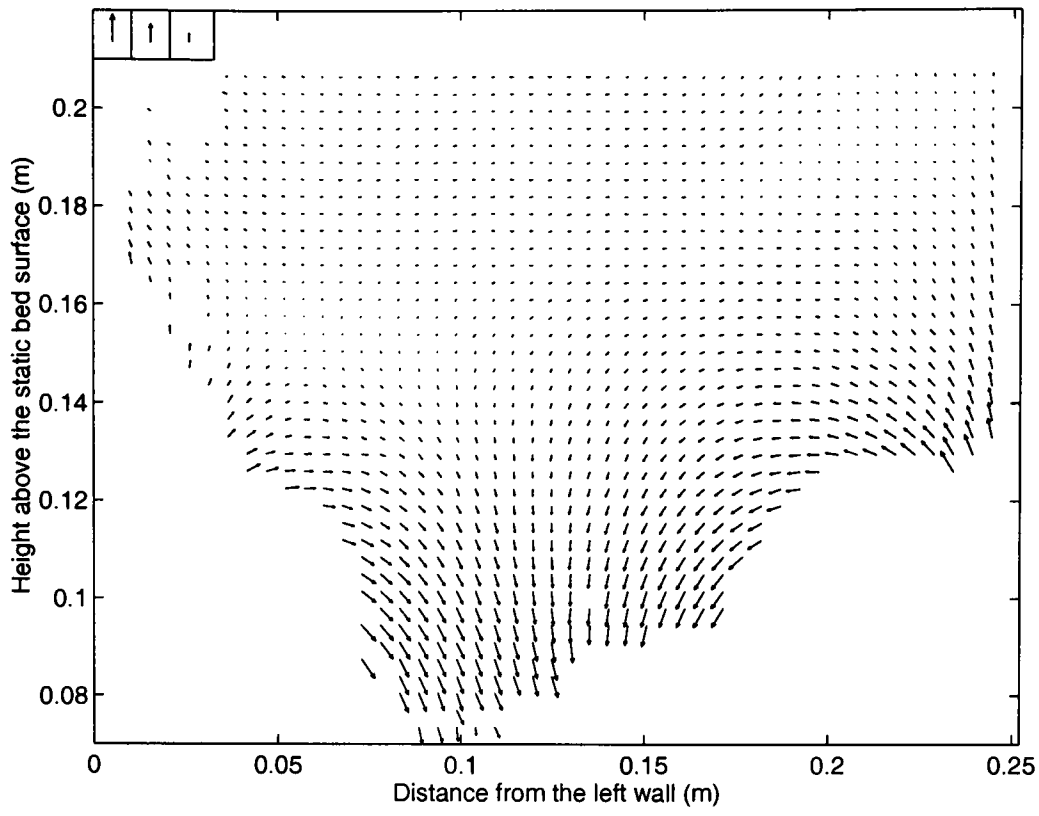

Figure 5.8: Velocity vectors of the vertical cross-sectional central plane 7 *cm* above the static bed surface of the incipiently fluidised bed after bubble eruption, 1.530 seconds after bubble injection. The empty regions on the sides corresponds to the side vortices. Vectors in the left upper corner from left to right: 15 *cm/s*, 10 *cm/s* and 5 *cm/s*

The direction of rotation would be expected to produce a downwards movement relative to the bulk flow and perhaps an overall downwards velocity for the low superficial velocity used here. However, the presence of the bed surface precludes this. The only possibility for the vortex expansion is toward the centre of the bed (5,6) and this can be seen in frame (b) in Figure 5.9. The inner edge of these side vortices seems to generate smaller vortices which interact with each other. When the side vortices are large enough they meet at the bed centre (7), as seen in frame (c) of Figure 5.9, giving rise to a high vorticity structure that expands and loses energy slowly while moving up in the freeboard (frame (d) Figure 5.9).

The gas behaviour described here corresponds to an erupting bubble of considerable size, approximately 14 *cm*, compared with the 25 *cm* diameter of the bed. This is approximately the size of bubble that one would obtain if the bed were operated at bubbling conditions corresponding to twice the minimum fluidisation velocity. If the bubble is smaller, approximately 7 *cm*, the side vortices are

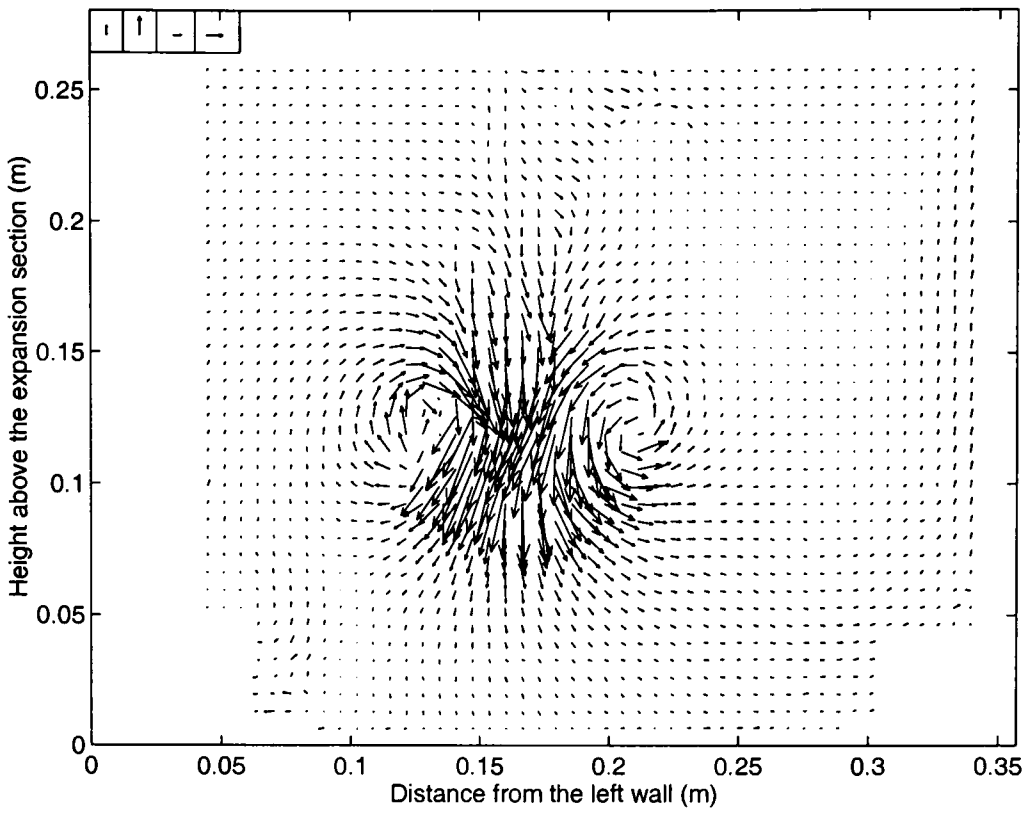

Figure 5.11: Velocity vectors of the vertical cross-sectional central plane of the expanded region. Vectors in the left corner from left to right: 5 cm/s and 10 cm/s vertically and horizontally respectively

formed on both sides of the bubble, but still at some distance from the wall. They then travel towards the wall. Two vortices (1,2) can be seen in frame (a) of Figure 5.10 on the bed surface (the other vortex-like structures present in this figure are due to the previous bubble). The left vortex (1), in frame (a) of Figure 5.10 cannot be seen in frame (b), either because it travelled away from the plane of light or because of disruption. The right vortex moves towards the wall and seems to ascend.

Additional work was performed to observe the gas behaviour in the expanded freeboard after bubble eruption. The light sheet was in the 35.7 cm diameter section shown in Figure 3.2. The bed height was 90 cm, with the bed surface 20 cm below the expansion. The flow pattern was disturbed by a small amount due to bubble injection. Immediately after bubble collapse, vortex ring formation was observed at the outlet of the bed as a result of a puff of gas sucked from the outlet tube due to the pressure gradient produced when the bed material returns to its initial height after bubble eruption. These vortices travelled downwards into the expanded section. The average translational velocity of these vortex

rings measured was 50 cm/s. The formation of these vortex rings was stopped by placing a hinged flange above the outlet to the cyclone. This flange only allowed the gas to flow from the freeboard to the cyclone, impeding the reverse gas flow. A vector map of one of these vortex rings is presented in Figure 5.11. This figure shows the appearance of a true vortex ring, as visualised by PIV. Hence, it is clear that PIV has enough resolution to find such structures. If ghost bubbles existed a similar vortex should have been observed, but travelling upwards from the surface after bubble eruption. The absence of these vortex rings after bubble eruption is clear evidence that coherent **ghost bubbles do not exist**.

5.2 Flow in the expansion section

The increase of the cross-sectional area in the expansion section will produce a reduction in the gas velocity, as governed by the continuity principle. Furthermore, if the loss of mechanical energy is not excessive, the pressure increases in the direction of flow, as given by Bernoulli's principle. The velocity of the fluid flowing near the wall decreases with distance from the entrance. If the flow cannot follow the shape of the expansion, there will be a point where the velocity gradient is zero, called a separation point, where the fluid detaches from the wall. Downstream of this point, as a consequence of the adverse pressure gradient the flow may be reversed, these zones being called stalls. The result will be that these stalls block the region around the wall, reducing the section available for the flow. Thus, a core of higher velocity is expected at the centre of the expanded region. At the top of the expansion section the flow may present high velocity at the centre with a tendency of transferring momentum towards the wall to re-attach the flow.

It would have been very interesting to do PIV in this part of the freeboard to find if a separation region did exist. However, the deposition of seeding particles

on the walls precluded visualisation through the walls. It was thought that the particles stuck at the walls as consequence of electrostatic forces. Three different approaches were tested to try to avoid the presence of the particles on the wall.

- To humidify the air: the air was passed through a water reservoir before it was introduced into the wind-box.
- To earth the bed.
- To spray an anti-static aerosol directly onto the wall before starting each run.

However none of these approaches produced any improvement.

The next test carried out was designed to check the angle of repose of the seeding particles. They were allowed to fall onto a sheet of polycarbonate (to which anti-static spray had been applied) with the same inclination angle as that of the expansion section. The particles did not roll down but stayed on the surface of the polycarbonate sheet.

It was very unfortunate that the flow in the expansion section could not be analysed. On the other hand, the particle deposition on the wall indicated that the expansion angle of the freeboard is greater than the angle of repose of the seeding particles so they will accumulate on the wall. Fibres would stay on a surface that had a very much higher angle than one which retains the more or less spherical seed material. If this result is applied to the freeboard of the polymer cracking bed, it seems to indicate that the carbon fibres would deposit on the wall, giving them enough time to grow to an undesired size.

5.3 Flow in the expanded section

The gas flow above a bubbling bed is a complex phenomenon, resulting from a combination of flow proceeding from single and coalescing bubbles at the bed surface. 83% of the bubbles that arrived at the bed surface, in the bubbling bed used in the present study, have similar behaviour to single injected bubbles. However, the rest explode violently ejecting particles into the freeboard; giving rise to a gas flow pattern very different from that determined by the ejection of single injected bubbles.

PIV images, using image shifting, were taken of a vertical plane across the expanded section when the bed was operated in its normal bubbling condition (see Section 3.2). Figure 5.12 shows two consecutive vector maps, taken one second apart from each other (that is the closest that two images can be taken). As can be seen, the time separation between them is too long (due to the slowness of image shifting) with the consequence that the structure of the flow has changed a lot between the two photographs, precluding one from following the development of the flow with time. However, instantaneous vector maps can give a good insight into the hydrodynamics of the gas. A large collection of instantaneous vector maps has been obtained during the course of this work. In this chapter, a few of them, showing representative flow features, are presented to understand the gas behaviour from a qualitative point of view. A statistical analysis of the flow is also presented to quantify the flow behaviour, including time-averaged velocity, velocity fluctuations, correlation coefficients and time-averaged vorticity.

5.3.1 Instantaneous flow structures

The vector maps (Figure 5.14- Figure 5.24) display instantaneous velocities corresponding to the cross-hatched area in Figure 5.13. Four vectors have been added to the left upper corner to indicate the scale (4.41 cm/s is the superficial

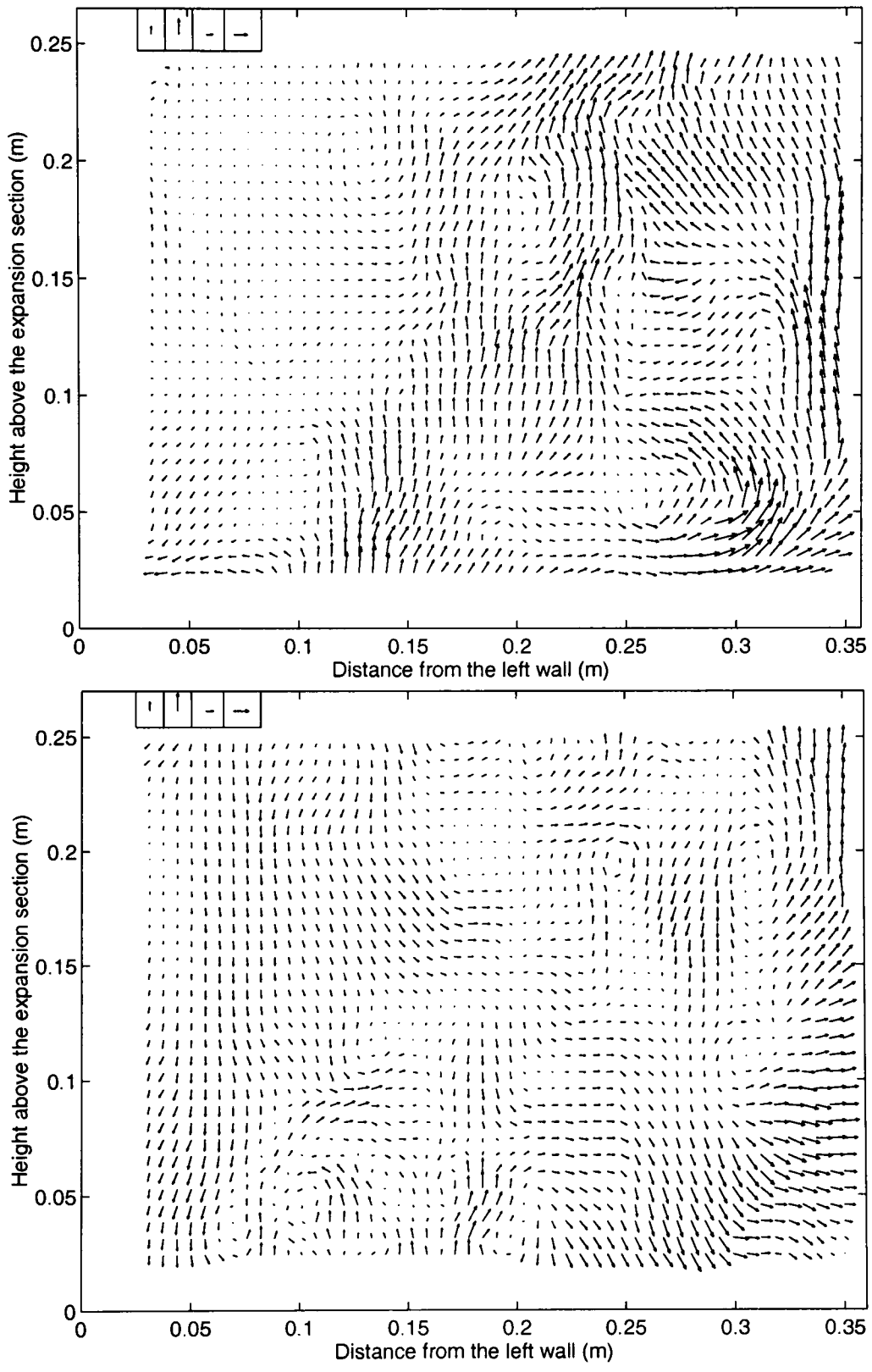

Figure 5.12: Consecutive vector maps (Time separation = 1 s). Velocity vectors in the left upper corner from left to right: 4.41 cm/s, 8.82 cm/s, 4.41 cm/s and 8.82 cm/s

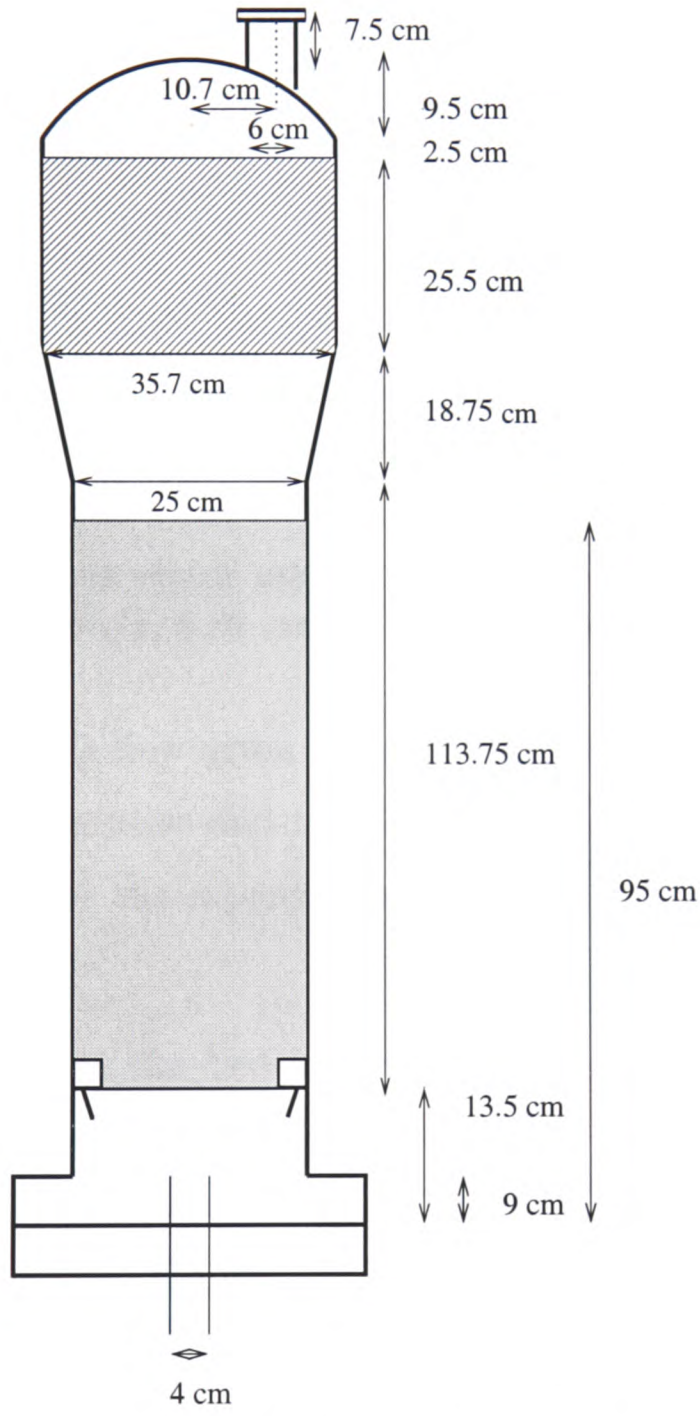

Figure 5.13: Fluidised bed

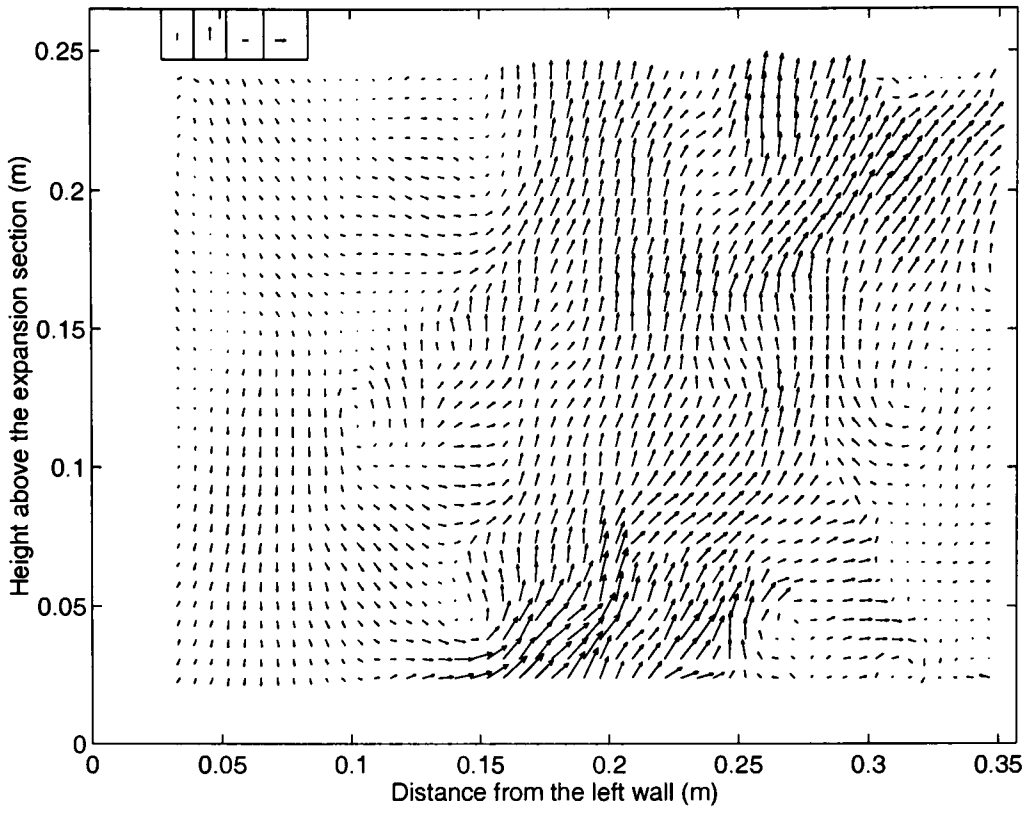

Figure 5.14: Instantaneous vector map. Velocity vectors in the left upper corner from left to right: 4.41 cm/s, 8.82 cm/s, 4.41 cm/s and 8.82 cm/s

velocity calculated by the flow given by the rotameter divided by the freeboard area). The most representative and reproducible characteristics of the flow, due to bubble eruption, above the expansion section are:

1. Bubbles erupting at the bed surface project gas "jets". These gas jets interact with the surrounding gas giving rise to vortical structures and eddies produced by the shear between two layers of different velocity. This can be seen in Figure 5.14. It can be seen that the "jets" are not perfectly vertical; the bubble imposes a horizontal movement to the gas. The velocity of the "jets" is typically four or five times the superficial velocity, hence the gas velocity outside the "jets" is very low. A region of descending flow can be seen on the left hand side.

2. The gas "jets" do not describe a straight path when they rise but rather a tortuous path (Figure 5.15 and Figure 5.16), due to the arrival of the jet into a gas with a non-uniform pressure distribution (resulting from previous

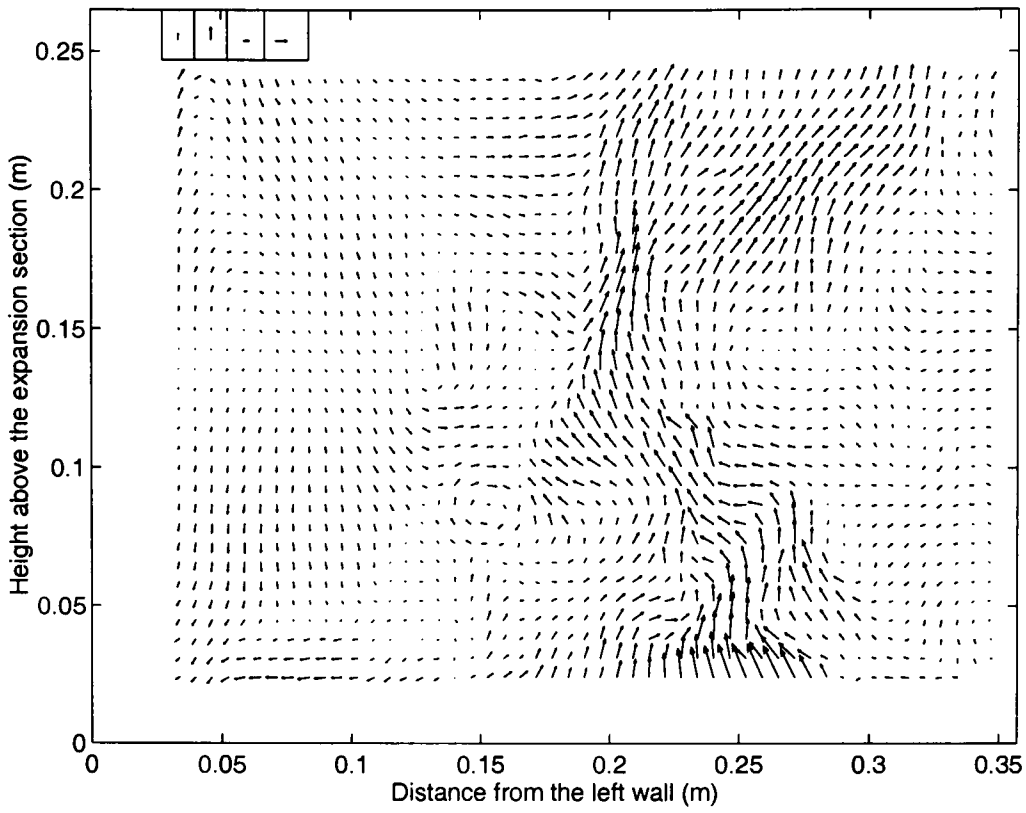

Figure 5.15: Instantaneous vector map. Velocity vectors in the left upper corner from left to right: 4.41 cm/s, 8.82 cm/s, 4.41 cm/s and 8.82 cm/s

bubble eruptions) plus the fact that the movement of the bed surface is imposing an extra non-uniform pressure on the jet.

3. The shape of the "jet" depends on the characteristics of the bubble that generate it. A few examples are presented here:

   - A central "jet" generating vortices on both sides due to the shear stress of layers with different velocities. An example is presented in Figure 5.17. This kind of structure is likely to be generated by a central bubble erupting at the bed surface.
   - A lateral "jet" that has high velocity only on one side while the other side has low velocity, generating a central vortex. Logically, the direction of the vortex depends on the side in which the jet is located. If the jet is on the left, the direction of rotation of the vortex is clockwise (see Figure 5.18). Conversely if the jet is on the right, the central vortex rotates anti-clockwise (see Figure 5.19).

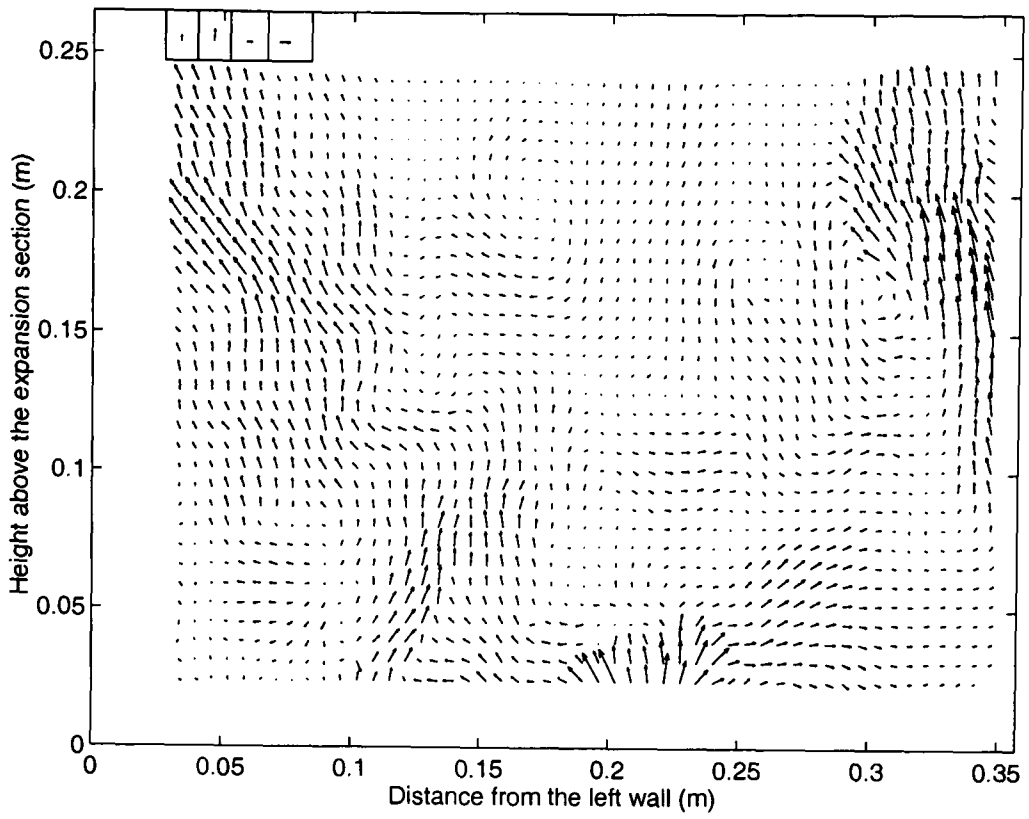

Figure 5.16: Instantaneous vector map. Velocity vectors in the left upper corner from left to right: 4.41 cm/s, 8.82 cm/s, 4.41 cm/s and 8.82 cm/s

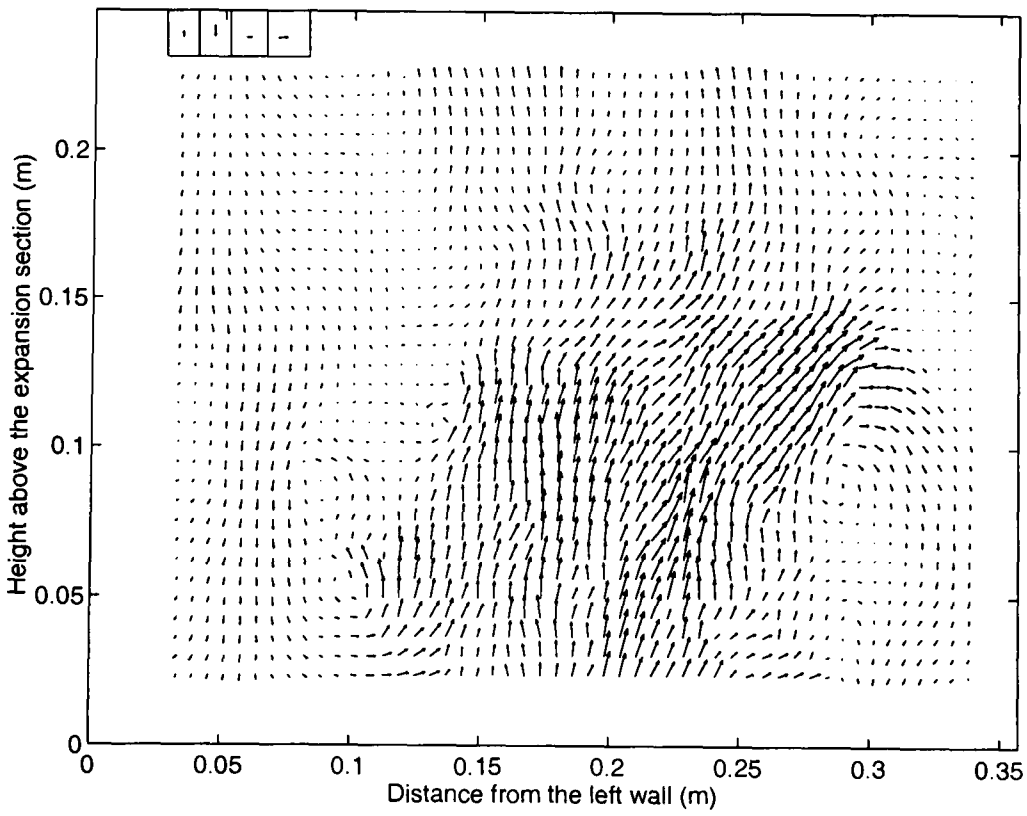

Figure 5.17: Instantaneous vector map. Velocity vectors in the left upper corner from left to right: 4.41 cm/s, 8.82 cm/s, 4.41 cm/s and 8.82 cm/s

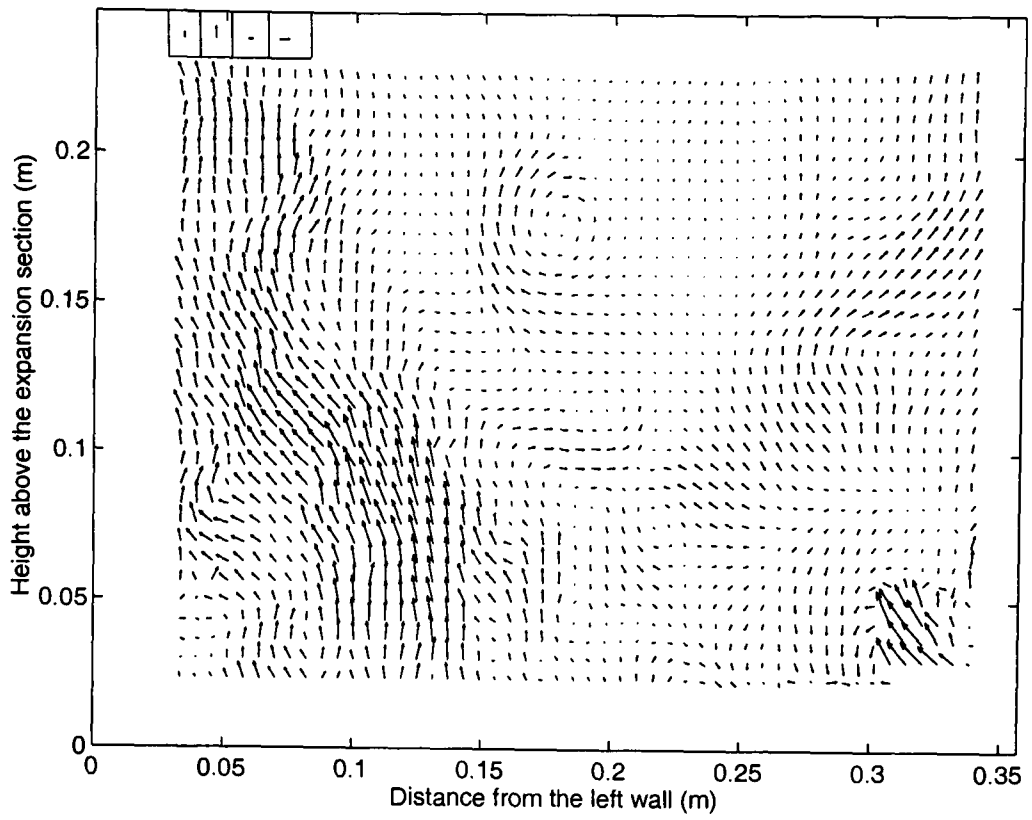

Figure 5.18: Instantaneous vector map. Velocity vectors in the left upper corner from left to right: 4.41 cm/s, 8.82 cm/s, 4.41 cm/s and 8.82 cm/s

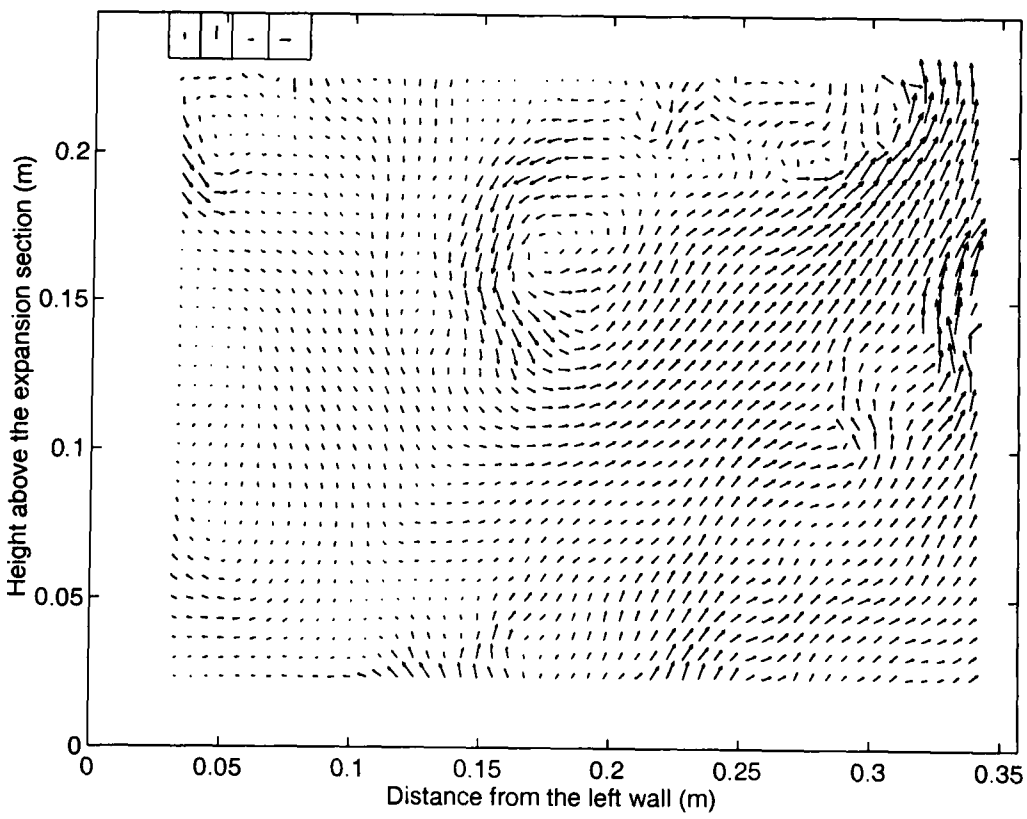

Figure 5.19: Instantaneous vector map. Velocity vectors in the left upper corner from left to right: 4.41 cm/s, 8.82 cm/s, 4.41 cm/s and 8.82 cm/s

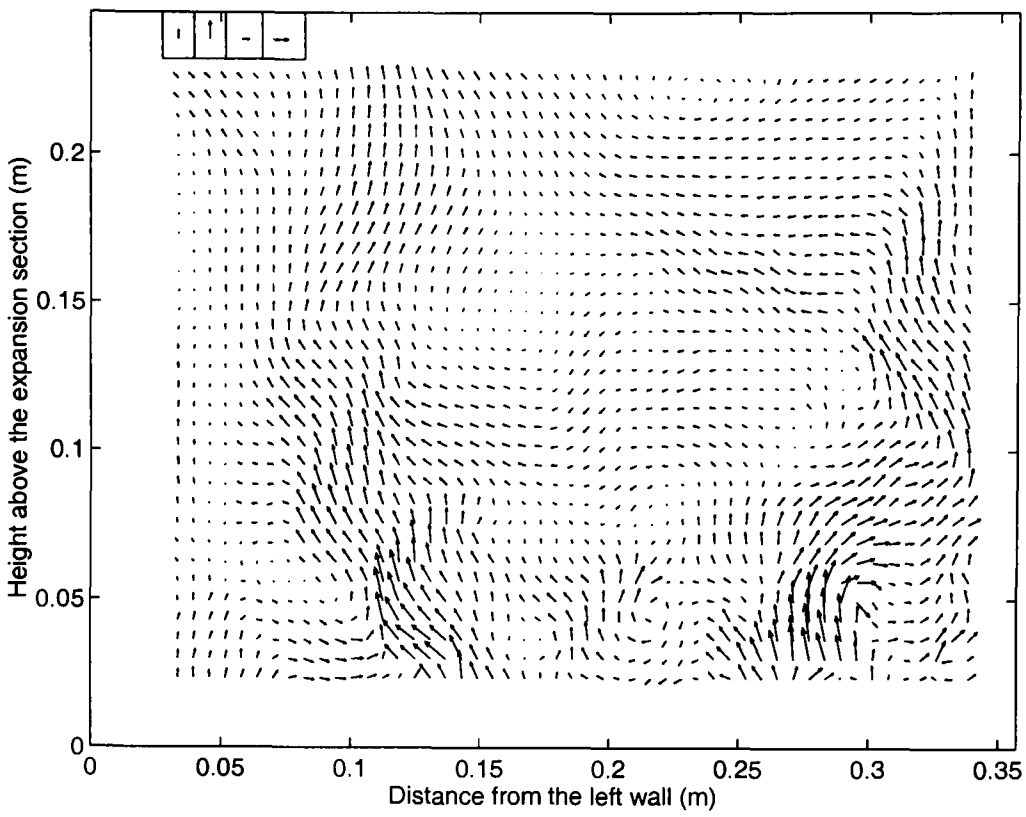

Figure 5.20: Instantaneous vector map. Velocity vectors in the left upper corner from left to right: 4.41 cm/s, 8.82 cm/s, 4.41 cm/s and 8.82 cm/s

- Two "jets" with a central region of low vertical velocity (as shown in Figure 5.20). Continuity considerations imply high horizontal velocity or high out-of-plane velocity. These jets are probably generated by two bubbles arriving at the bed surface simultaneously or two bubbles coalescing laterally just beneath the bed surface.

4. The gas is pulled down when the bed surface comes back to its initial height after bubble eruption (Figure 5.21 and Figure 5.22). The pressure gradient is so strong that the flow direction is completely reversed and the gas travels downwards (The vortices generated by bubble eruption have not yet had enough time yet to reach the expanded section).

5. The flow in the freeboard is a combination of the flow generated from a bubble interacting with the flow remaining from the previous bubble eruption, because the time separation between two bubbles is not long enough to allow the gas to settle. When the gas is still going downwards (dragged by the bed material returning to the bed surface after bubble eruption), a new bubble arrives at the bed surface, projecting a jet of gas. The upward

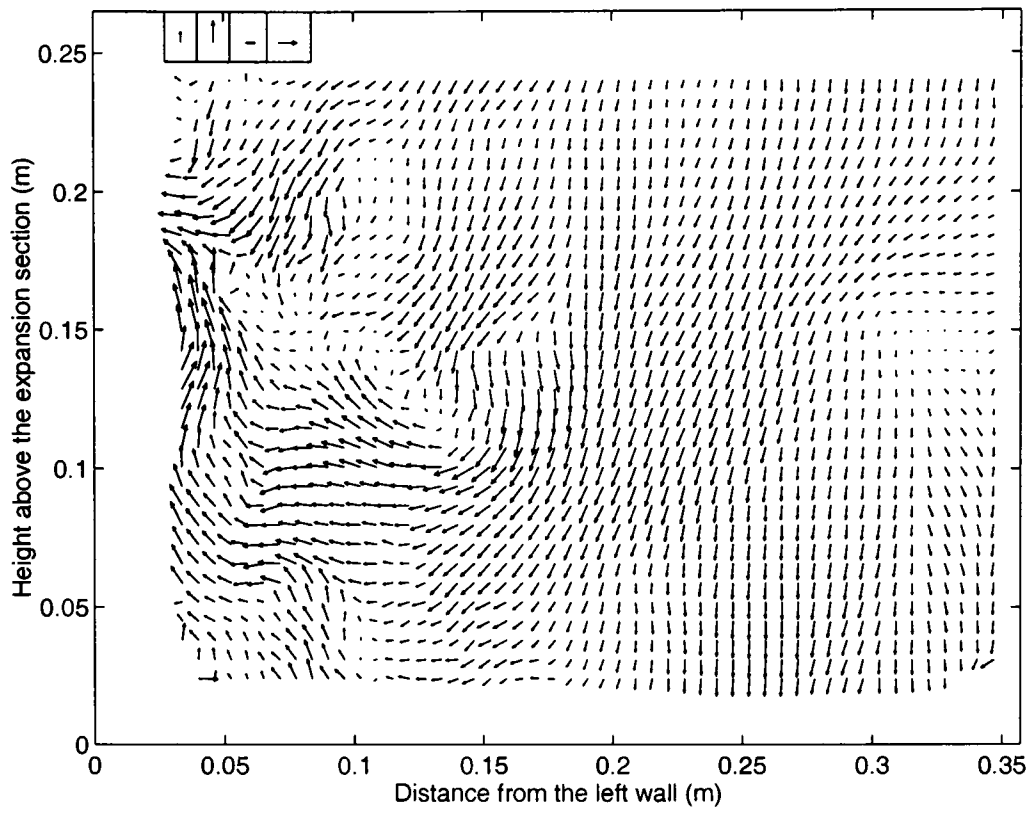

Figure 5.21: Instantaneous vector map. Velocity vectors in the left upper corner from left to right: 4.41 cm/s, 8.82 cm/s, 4.41 cm/s and 8.82 cm/s

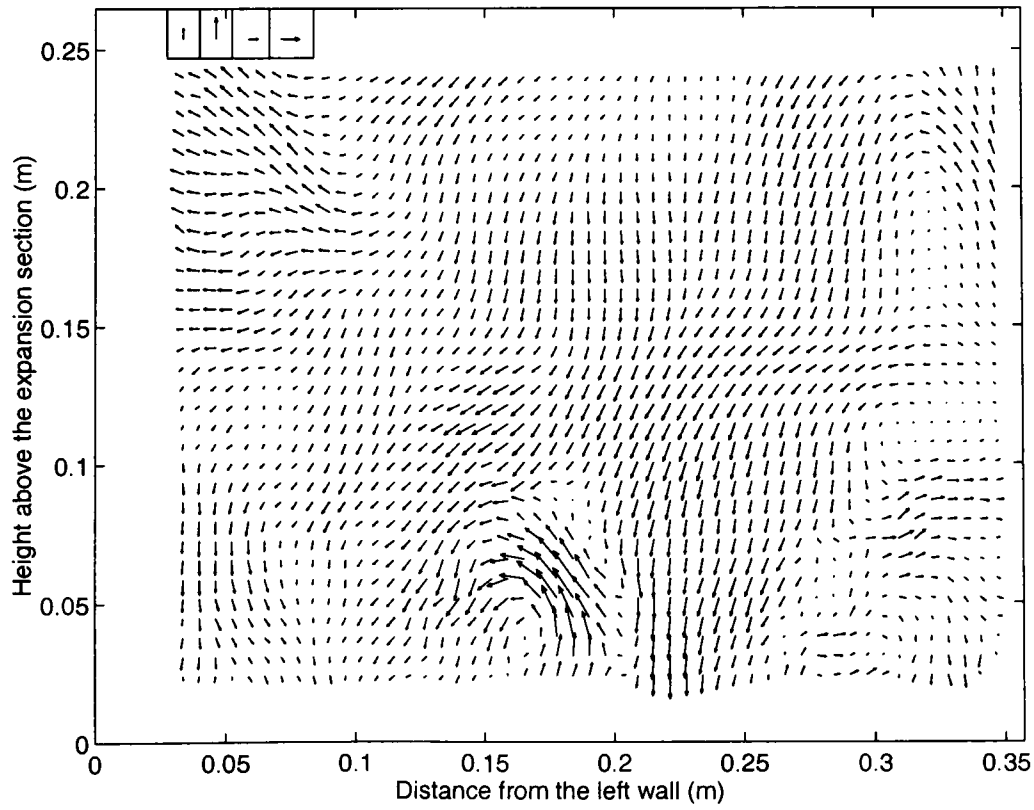

Figure 5.22: Instantaneous vector map. Velocity vectors in the left upper corner from left to right: 4.41 cm/s, 8.82 cm/s, 4.41 cm/s and 8.82 cm/s

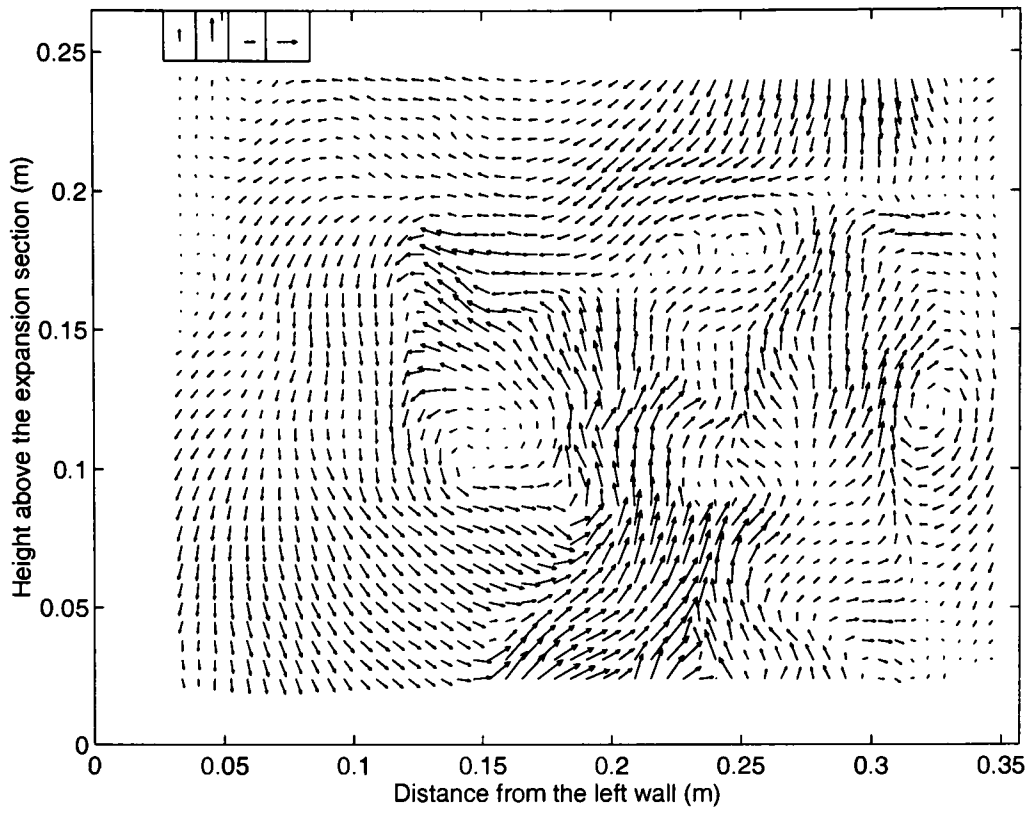

Figure 5.23: Instantaneous vector map. Velocity vectors in the left upper corner from left to right: 4.41 cm/s, 8.82 cm/s, 4.41 cm/s and 8.82 cm/s

jet of gas finds the downward gas and entrains it, giving rise to vortical structures that increase the residence time of the gas in the freeboard (Figure 5.23 and Figure 5.24). It also gives rise to regions of converging flow (characterised by high strain rate and low vorticity. This can be seen in the upper right corner of Figure 5.23, where higher fibre concentration could be expected).

6. Figure 5.25 and 5.26 show the typical flow pattern in the freeboard between two bubble eruptions. The resulting flow is far from being uniform or symmetric. The three-dimensional nature of the flow can also be noticed. These pictures confirm the non-isotropic, turbulent nature of the flow. The main feature is the presence of little vortices remaining from the eruption process. These stay in the freeboard until they are displaced by a new erupting bubble.

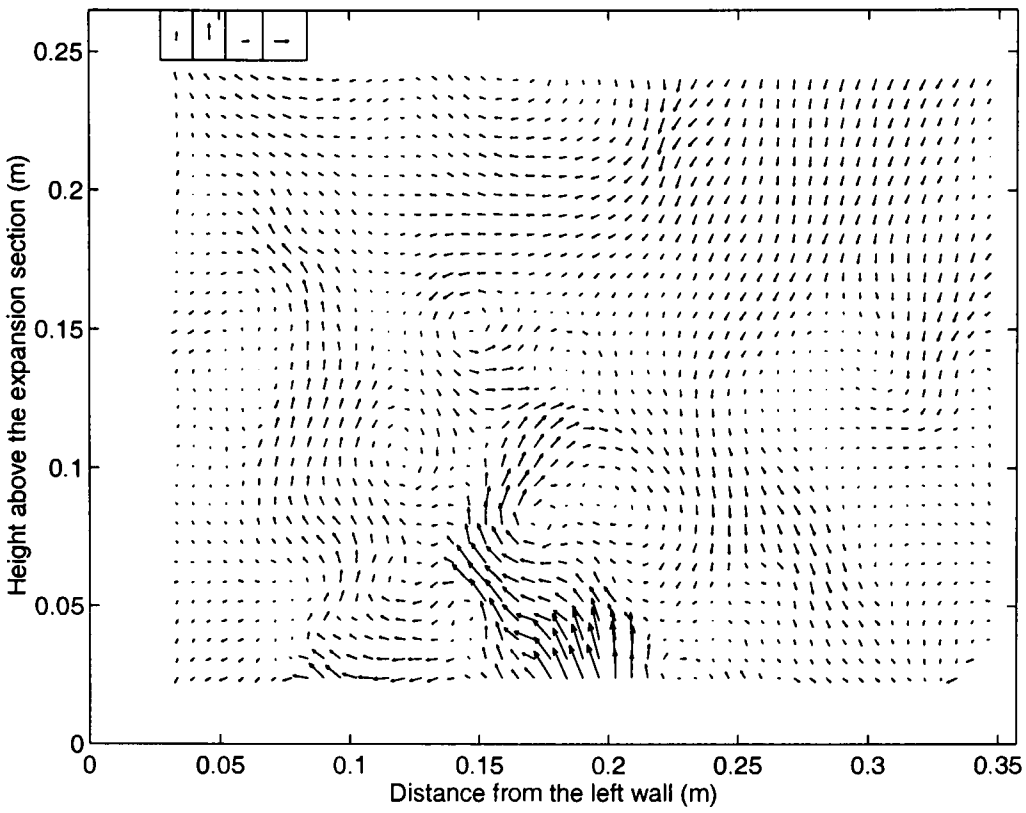

Figure 5.24: Instantaneous vector map. Velocity vectors in the left upper corner from left to right: 4.41 cm/s, 8.82 cm/s, 4.41 cm/s and 8.82 cm/s

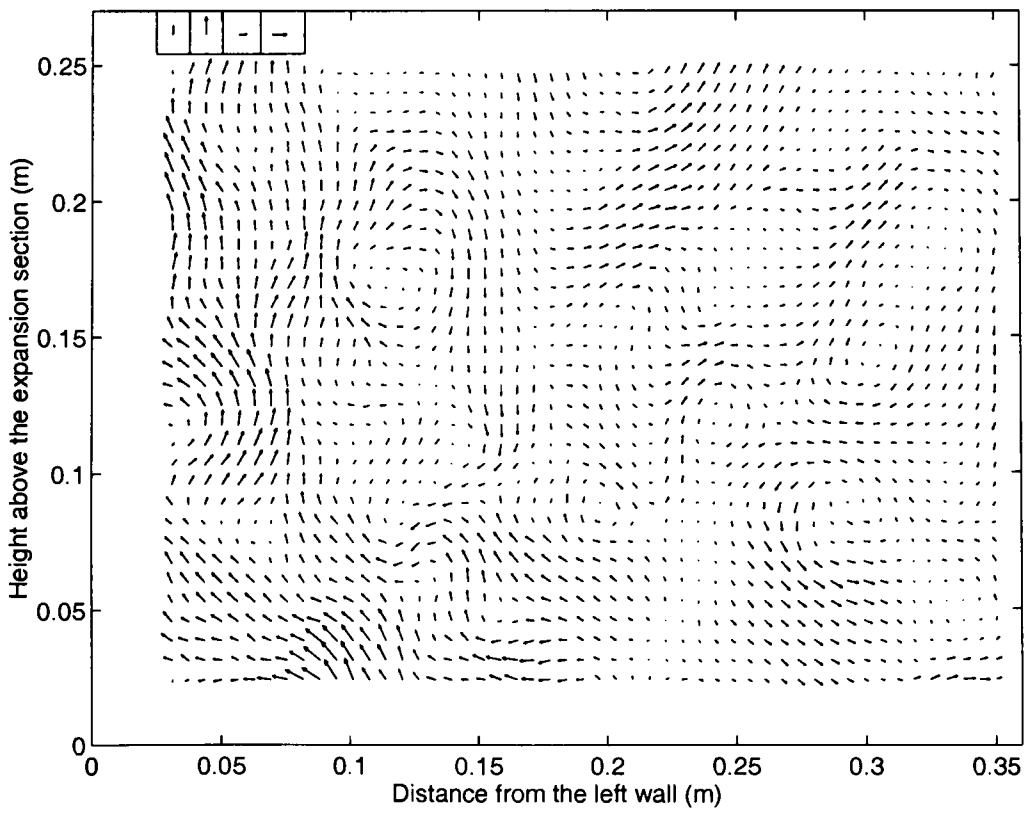

Figure 5.25: Instantaneous vector map. Velocity vectors in the left upper corner from left to right: 4.41 cm/s, 8.82 cm/s, 4.41 cm/s and 8.82 cm/s

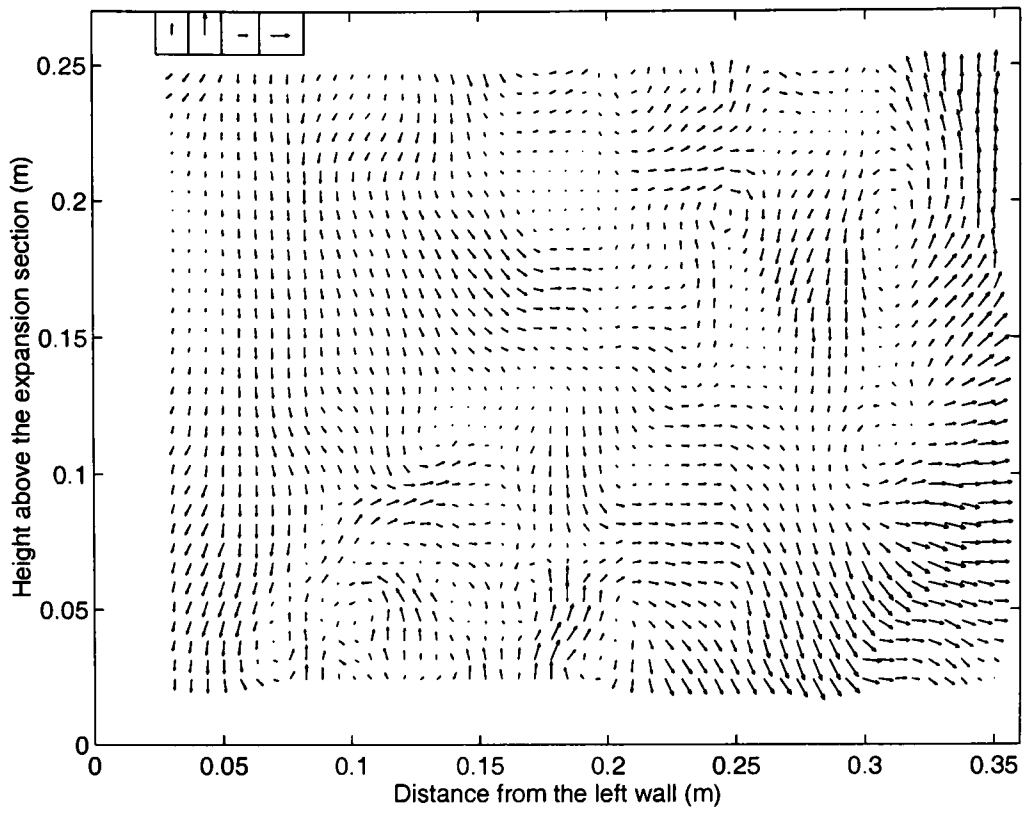

Figure 5.26: Instantaneous vector map. Velocity vectors in the left upper corner from left to right: 4.41 cm/s, 8.82 cm/s, 4.41 cm/s and 8.82 cm/s

No instantaneous characteristics were found in the individual vector maps that could be directly attributed to the presence of the outlet. This is not surprising since the outlet is 10 cm behind the analysed plane (and the outlet plane could not be illuminated because the wall was painted in black). Furthermore, the outlet is approximately 15 cm above the analysed plane. The present finding could have two possible interpretations:

- the outlet position does not have an effect on the gas flow in the freeboard or
- the presence of the outlet only influences the region close to it.

The second possibility seems more likely but so far not enough information is available to fully support either interpretation. Outlet position is further discussed in Section 6.1.

The qualitative behaviour of the flow in the freeboard has been described. The flow is intermittent but non-periodic and there is no clear symmetry. The three-dimensional nature of the flow is an additional complication. The flow is characterised by the presence of eddies and vortices, due to the shear stress between layers of different velocity generated by bubble eruption, that gives rise to a high residence time of the gas in the freeboard.

5.3.2 Statistical description of the flow

Each vector map represents the instantaneous velocity of the flow. Each experiment consisted of 37 vector maps, taken, approximately, one second apart from each other. The description of the flow involves dividing the velocity into a time averaged and a fluctuating component. The time over which the average is calculated (37 seconds) is long compared with the time scale of the fluctuations (0.5 seconds, approximately). The results obtained for two different experiments, under the same experimental conditions (Table 7.4), will be presented to show reproducibility (Experiment 1 and 2, respectively). The time-averaged vector map of an experiment at the same conditions but calculated from photographs taken at random times (Experiment 3) will also be presented to show that the transient features of the flow are random.

Time-averaged velocity

The time-averaged vector map of Experiment 1 is presented in Figure 5.27. The central region just above the expansion is a region of high velocity while the sides have lower velocity, thus the flow goes from the centre to the sides when rising in this section of the freeboard. At the top of this region the high velocity region is near the wall while the central region has a lower velocity.

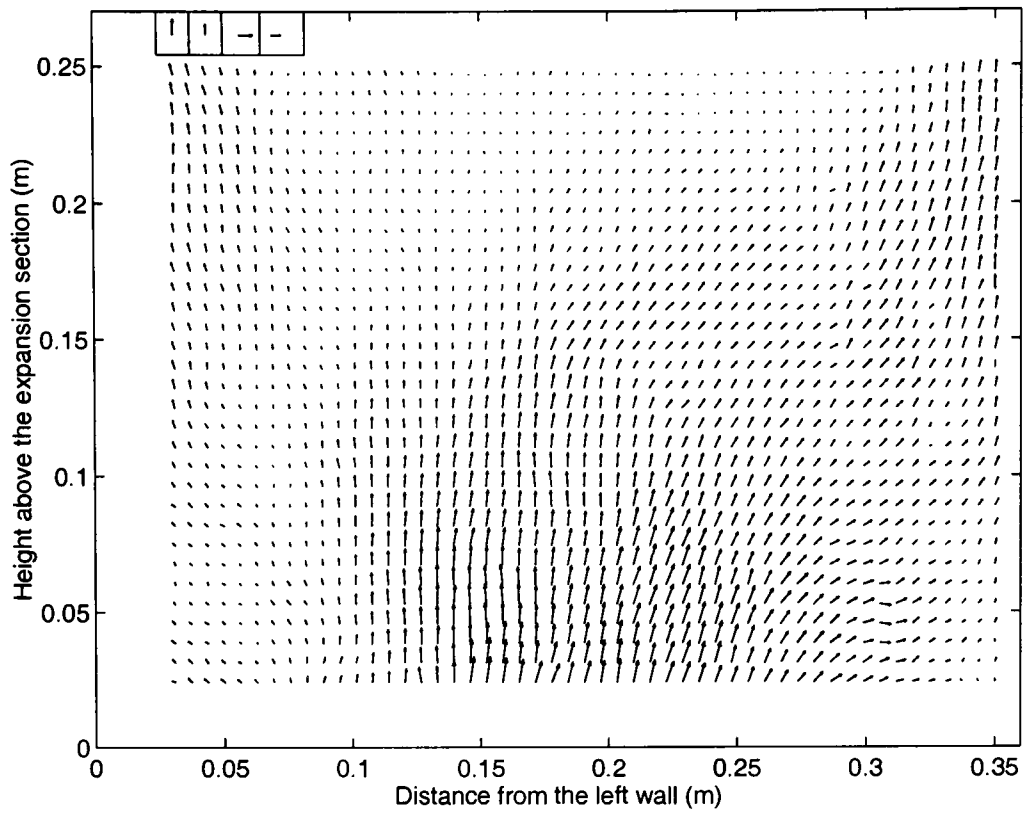

Figure 5.27: Time-averaged vector map over 37 seconds (Experiment 1). Velocity vectors in the left upper corner from left to right: 3 cm/s, 2 cm/s, 3 cm/s and 2 cm/s

A very similar behaviour was found in Experiment 2 (Figure 5.28) and in Experiment 3 (Figure 5.29). Both of them present a high velocity region, in the central part above the bed surface. This region is not necessarily in the exact centre. For example, in Figure 5.28 the region of high velocity is displaced slightly towards the left. In Figure 5.29 the region is also slightly displaced towards the left. This high velocity region is shifted toward the walls when rising in the freeboard. A high velocity region, of a few centimetres wide, was observed with the naked eye, going upwards parallel to the wall. The velocity of this layer was estimated to be about 5 times the velocity of the measured gas. The velocity could not be measured due to the internal reflection of the wall.

Although velocity vectors have been added to the vector maps to show the scale, histograms allow for a clear presentation of the range and distribution of the magnitude of the velocity. Histograms of the statistical distribution of the vertical component of the average velocity are presented in Figures 5.30, 5.31 and 5.32 and the corresponding horizontal component are presented in Figures 5.33, 5.34 and 5.35. Each bin represents 0.2 cm/s.

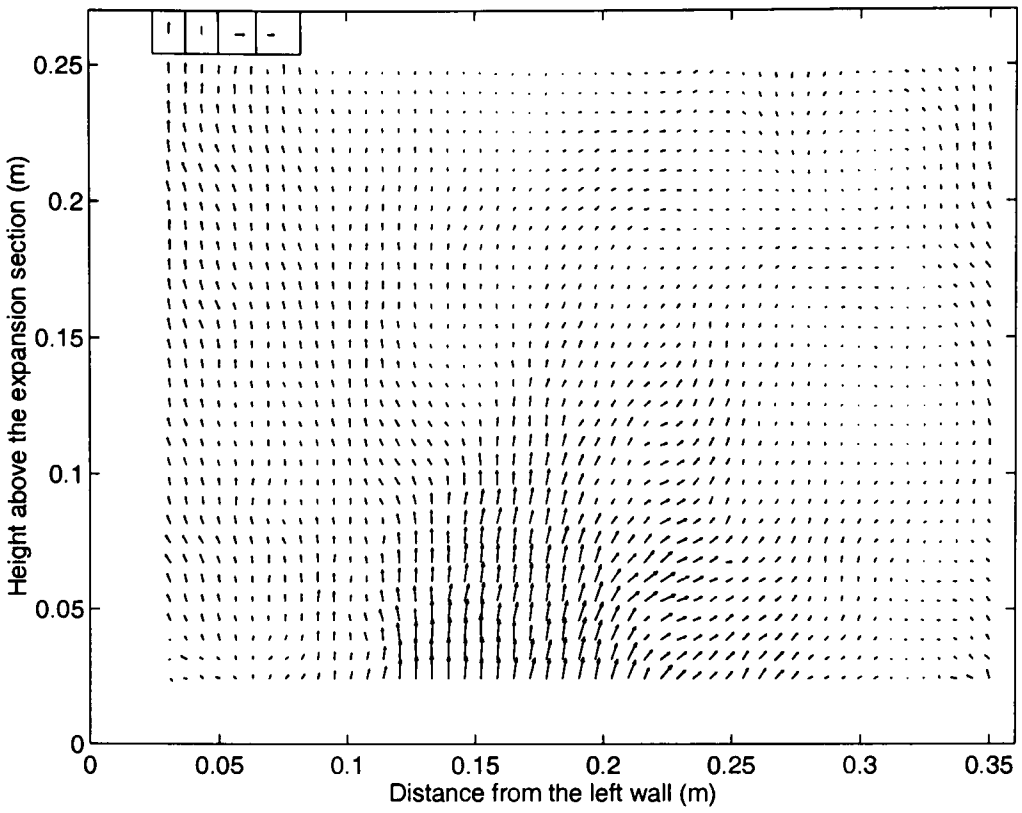

Figure 5.28: Time-averaged vector map over 37 seconds (Experiment 2). Velocity vectors in the left upper corner from left to right: 3 cm/s, 2 cm/s, 3 cm/s and 2 cm/s

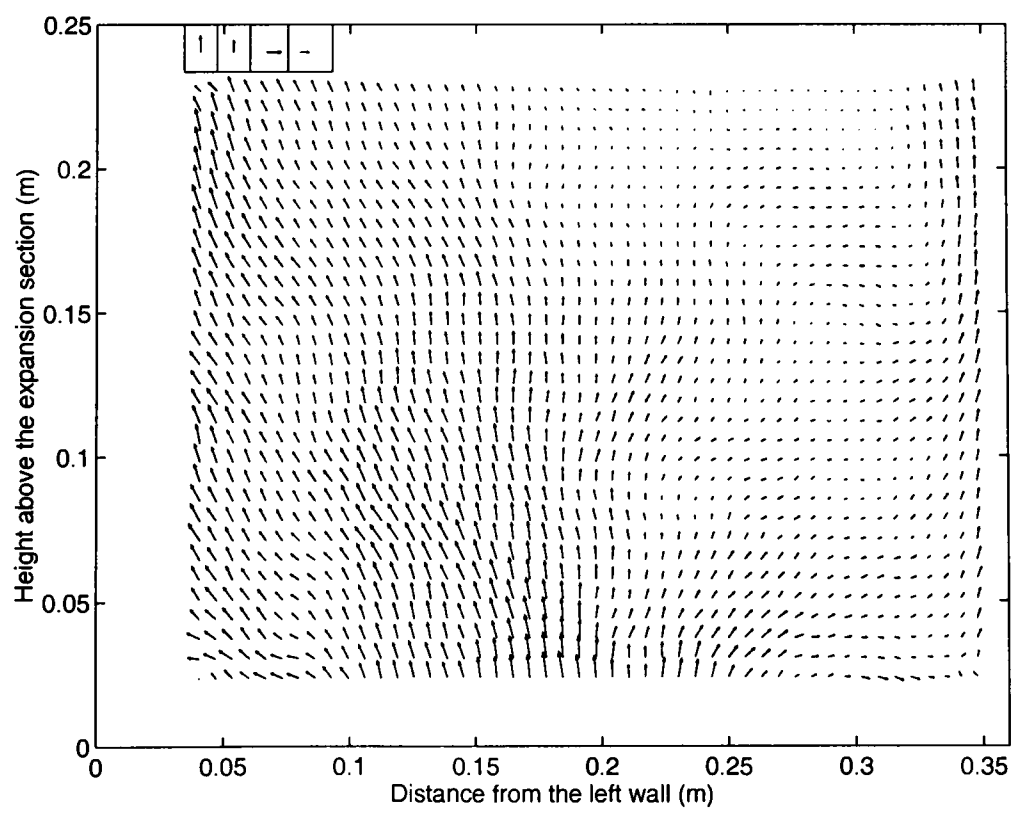

Figure 5.29: Time-averaged vector map over 37 seconds (Experiment 3). Velocity vectors in the left upper corner from left to right: 3 cm/s, 2 cm/s, 3 cm/s and 2 cm/s

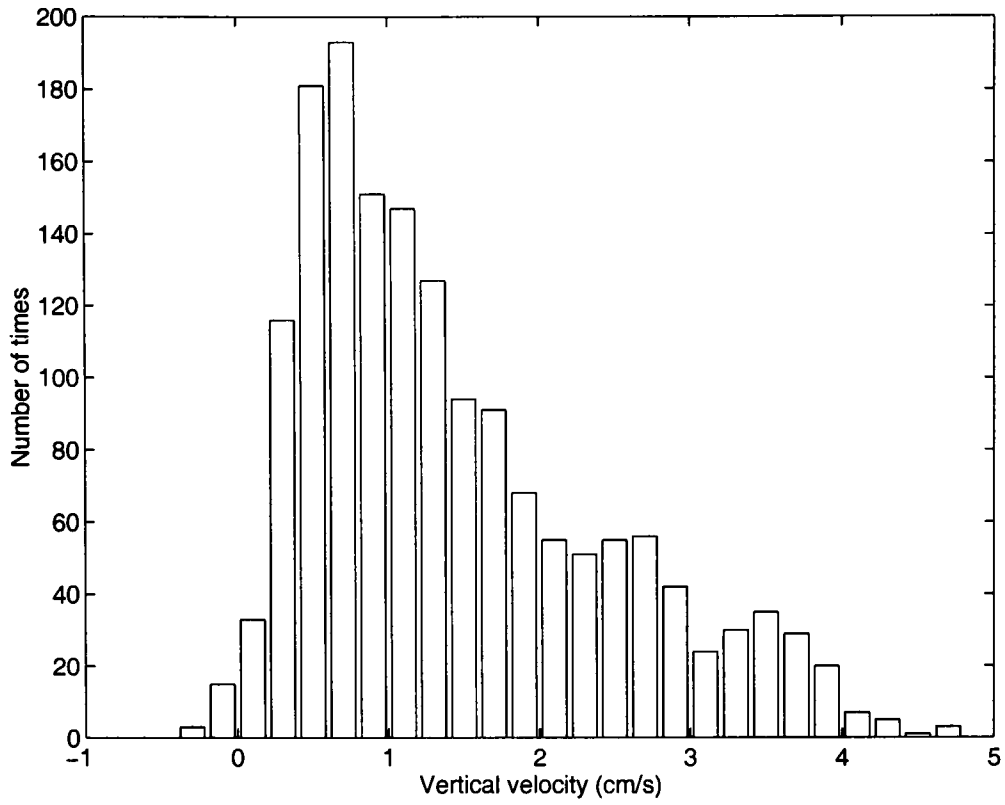

Figure 5.30: Statistical distribution of the vertical component of the velocity (Experiment 1). Each bin represents 0.2 cm/s

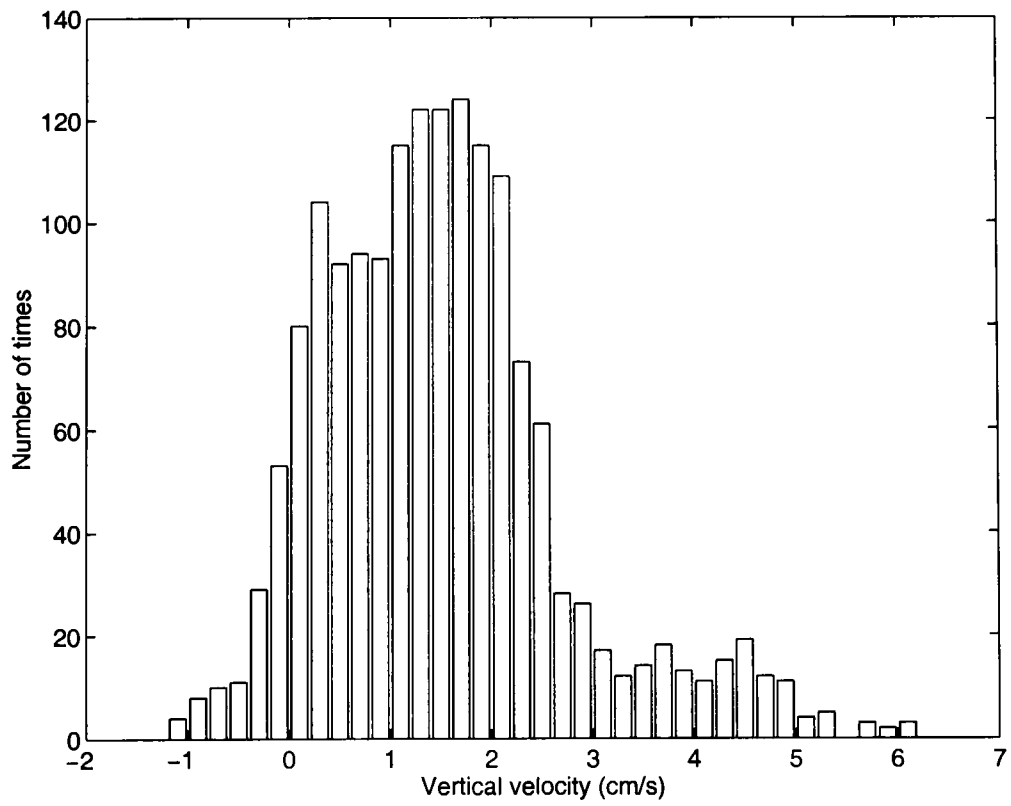

Figure 5.31: Statistical distribution of the vertical component of the velocity (Experiment 2). Each bin represents 0.2 cm/s

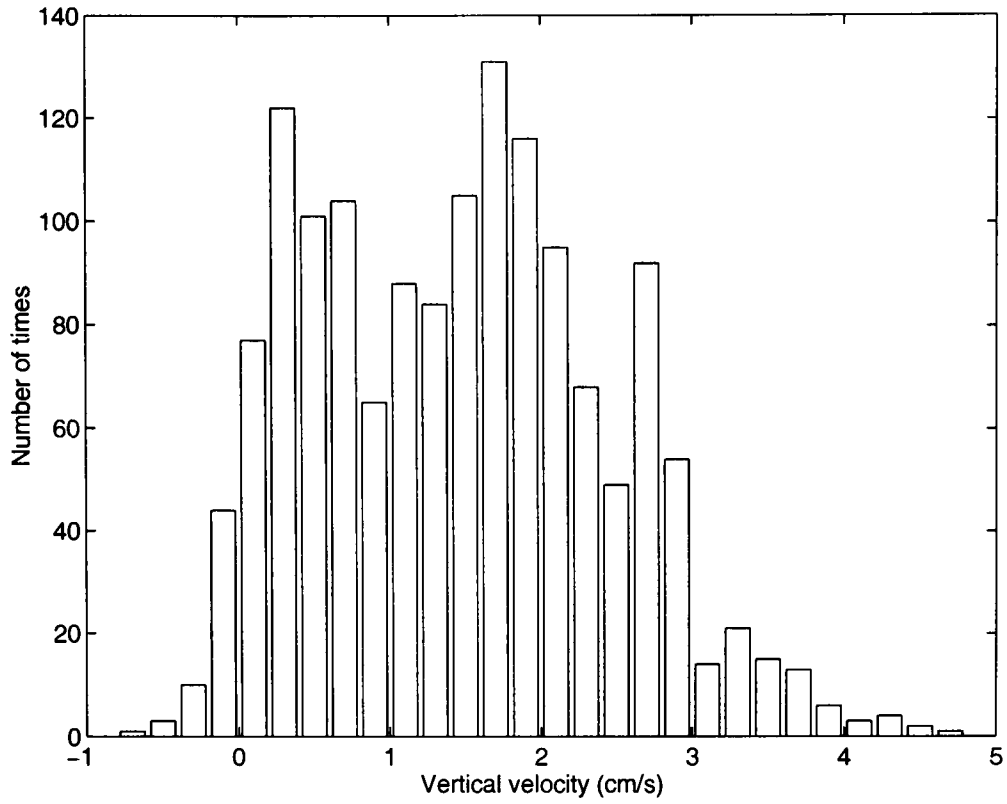

Figure 5.32: Statistical distribution of the vertical component of the velocity (Experiment 3). Each bin represents 0.2 cm/s

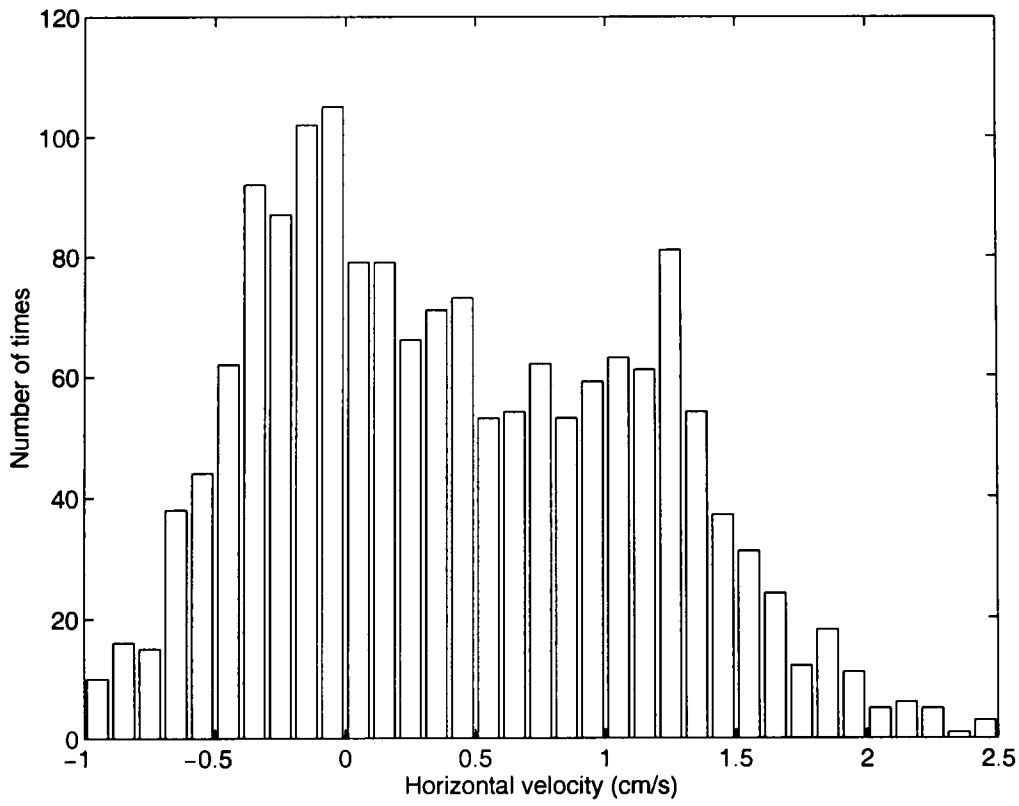

Figure 5.33: Statistical distribution of the horizontal component of the velocity (Experiment 1). Each bin represents 0.2 cm/s

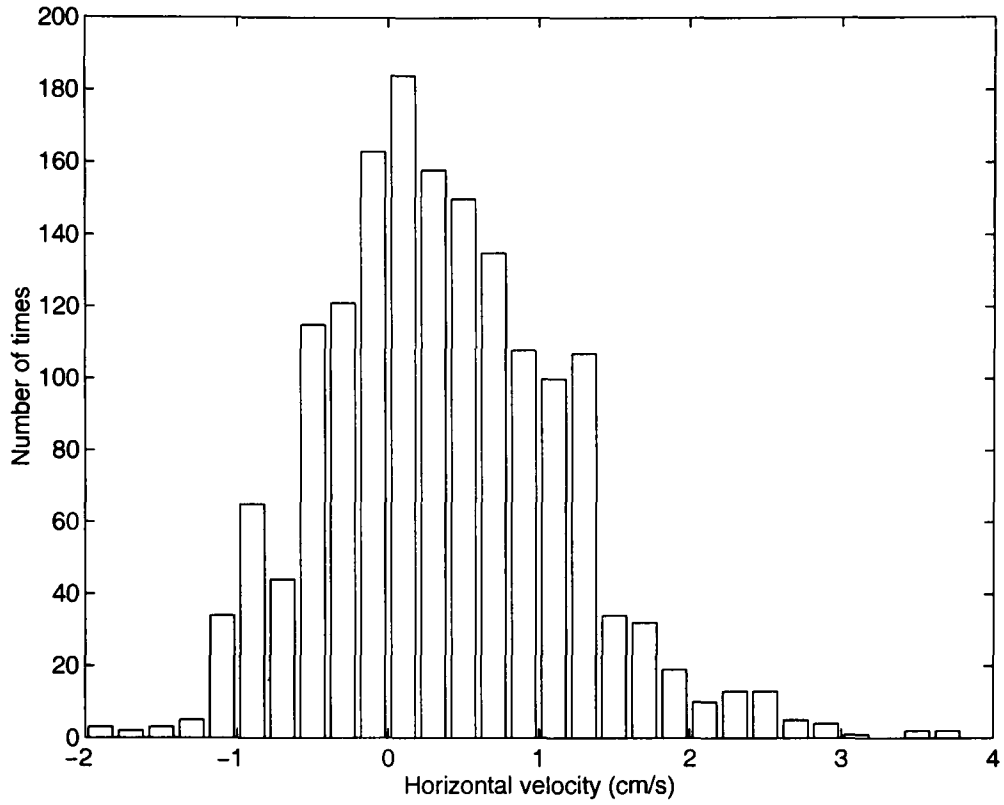

Figure 5.34: Statistical distribution of the horizontal component of the velocity (Experiment 2). Each bin represents 0.2 cm/s

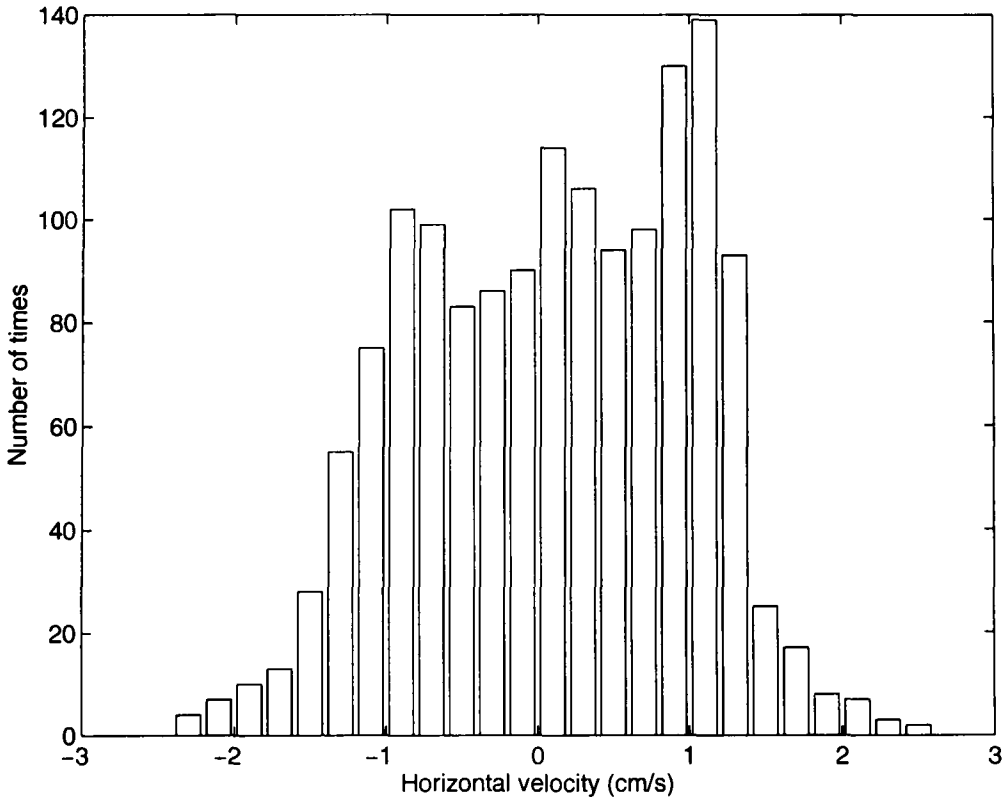

Figure 5.35: Statistical distribution of the horizontal component of the velocity (Experiment 3). Each bin represents 0.2 cm/s

The histograms of the time-averaged vertical component of the velocity can be described as follows:

- Most of the time the velocity is positive; there were very few negative values.
- Most of the velocities are in the range between 0 and 3 cm/s.
- The histograms have a tail of high velocities, usually from 3 cm/s to 6 cm/s.
- The distribution of the velocity is unimodal.

The histograms of the time-averaged horizontal component of the velocity can be described as follows (negative velocity has been assigned to the direction from right to left):

- The maximum magnitude of the horizontal component of the velocity is lower than the maximum magnitude of the vertical component.
- The magnitudes of positive velocities are higher than the magnitudes of negative velocities.
- The distribution is unimodal.

Table 5.2 presents the vertical (v_y) and horizontal (v_x) component of the velocity calculated by spatial averaging over the entire time-averaged vector map. The flow has a small mean horizontal velocity component. This low velocity is the result of averaging velocities in different directions. To show that the flow is characterised by a high magnitude horizontal velocity, the average of the horizontal absolute velocity component ($|v_x|$) is also presented. The standard deviations are also presented to quantify the velocity dispersion. The values obtained for both components of the velocity from the three different experiments are very similar, showing a good reproducibility. The vertical component of the velocity is higher than the horizontal. The horizontal velocity may be imposed by erupting

bubbles and enhanced by the expansion section. The velocity calculated from the flowrate, given by the rotameter, is approximately 4.41 cm/s; the mean vertical velocity calculated using the PIV data is approximately 1.4 cm/s.

Experiment number	v_y (cm/s)	Vertical std (cm/s)	v_x (cm/s)	Horizontal std (cm/s)	$\|v_x\|$ (cm/s)
1	1.48	0.38	0.47	0.15	0.66
2	1.41	0.57	0.28	0.17	0.66
3	1.45	0.27	-0.22	0.05	0.77

Table 5.2: Spatial average velocity and standard deviation of the time-averaged vector maps

In order to check continuity the radial average of the vertical velocity has been calculated at three different heights, for Experiment 1, as:

$$v_{yr} = 2\pi \int_0^r v_y r dr \tag{5.2}$$

The integral:

$$v_{yl} = 2\pi \int_{-r}^0 v_y r dr \tag{5.3}$$

has also being calculated to estimate how good the assumption of axy-symmetry is. Table 5.3 shows the values calculated using Equations 5.2 (corresponding to the right hand side v_{yr}) and 5.3 (corresponding to the left hand side v_{yl}) at three different heights above the bed surface (for Experiment 1). Only a 15 cm radius section could be considered when calculating v_{yr} and v_{yl}. From the data it can be seen that the difference between the average vertical velocity calculated from Equations 5.2 and Equations 5.3 is around 30% of the absolute values of these velocities. This significant difference means that the assumption of axy-symmetry must be questioned.

Since the difference in the average vertical velocity calculated from Equations 5.2 and Equations 5.3 is of the same order as the difference in the average vertical

velocity calculated at different heights, it is difficult to make a definite statement about whether continuity is obeyed or not within this region.

Looking at Table 5.3 it can be seen that the average velocity decreases with height. This is consistent with the fact that the vertical velocity is higher near the walls far from the bed surface. In all the cases the velocity values are lower than expected from continuity (4.41 cm/s). This may be due to the fact that the velocity near the wall could not be measured due to the inevitable internal reflection of the laser. Visual observation confirmed the presence of a layer of high upwards vertical velocity (of a few centimetres thickness and approximately travelling at 10 cm/s) beside the wall.

Height cm	v_{yr} cm/s	v_{yl} cm/s
45	1.35	1.73
53	1.19	1.45
61	1.09	0.78

Table 5.3: Radial average vertical velocity (Experiment 1)

Figures 5.36 - 5.38 show the radial profile [1] of the time-averaged vertical component of the velocity, for the three different experiments, at three different heights above the bed surface (z): (a) just above the expansion section ($z = 45\ cm$), (b) in the middle of the expanded section ($z = 53\ cm$) and (c) near the bed outlet ($z = 61\ cm$). For all the experiments it was found that:

- Just above the expansion section, the velocity is higher at the centre; the shape of the graph resembles an inverted "U".
- The profile becomes flatter with height.
- Near the outlet the profile changes its shape, now resembling an upright "U". [2]

[1] Cartesian coordinates have been used due to the non-symmetric nature of the instantaneous flow.

[2] The instantaneous vector maps are subject to the three-dimensional character of the flow, so it should not be expected to find continuity obeyed for any component of the velocity.

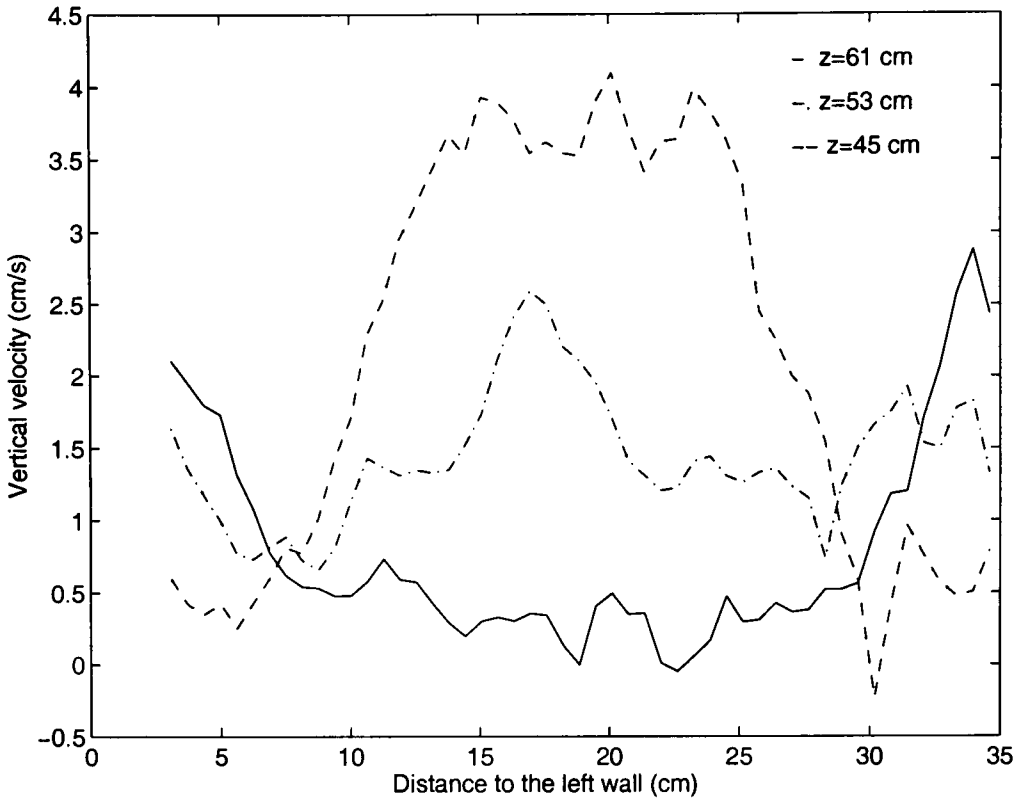

Figure 5.36: Time-averaged vertical velocity profile (Experiment 1)

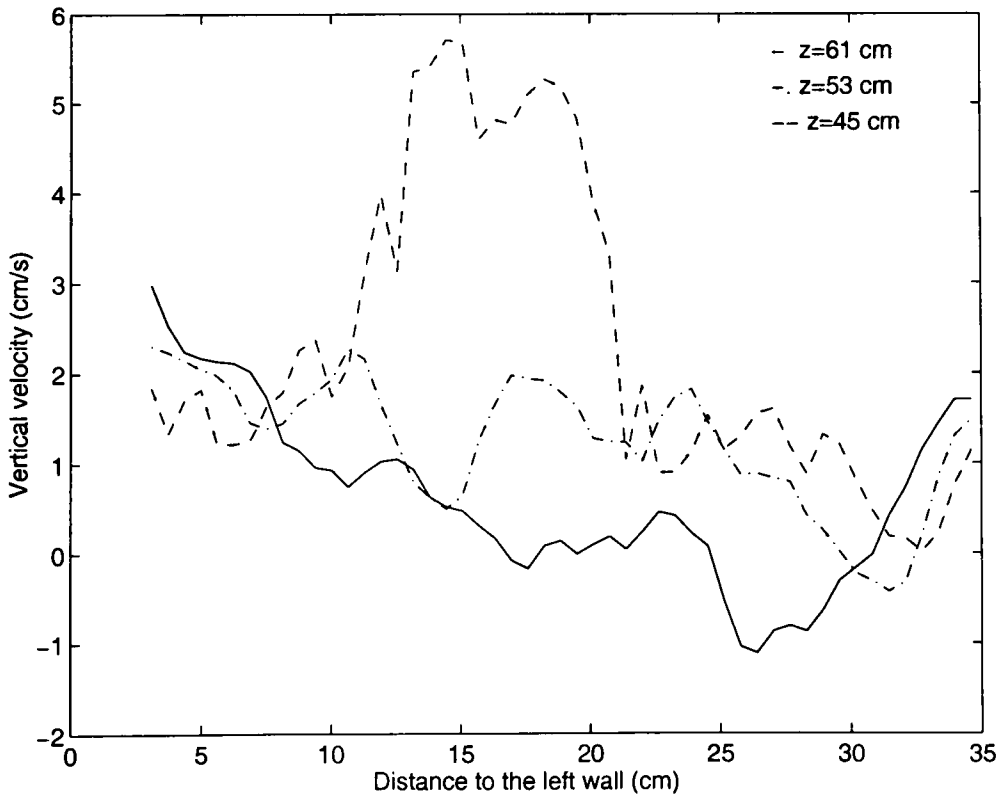

Figure 5.37: Time-averaged vertical velocity profile (Experiment 2)

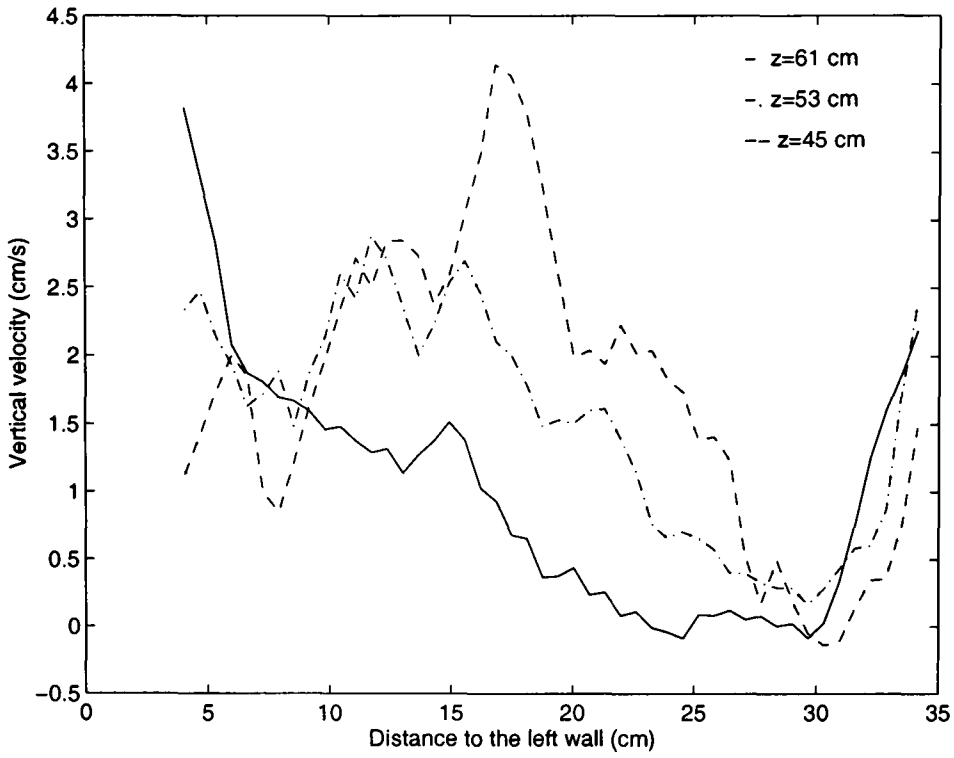

Figure 5.38: Time-averaged vertical velocity profile (Experiment 3)

Figures 5.39 - 5.41 present the error-bars showing the 95% confidence limits associated with the time-averaged process, at $z = 45\ cm$, $z = 53\ cm$ and $z = 61\ cm$ for Experiment 1. The confidence limits have been calculated using a t-distribution because the variance was not known but estimated from the samples. The confidence limits are very similar for the three different heights. It can be seen that the results are still good enough to know the shape of the velocity profile and the range of the velocities. Confidence increases with increasing number of samples (37 samples were used because this is the maximum number of photographs that an easily available photographic film contains; this gives a reasonably good result). The profiles are expected to become smoother increasing the number of vector maps used in the process of averaging.

Figures 5.42 and 5.43 show the 95 % confidence limits for Experiment 2 and 3 at $z = 45\ cm$ above the bed surface. The range of variation of the velocity is very similar to Experiment 1.

The radial profile of the time-averaged horizontal component of the velocity is shown in Figures 5.44-5.46 for the same three experiments and at the same three

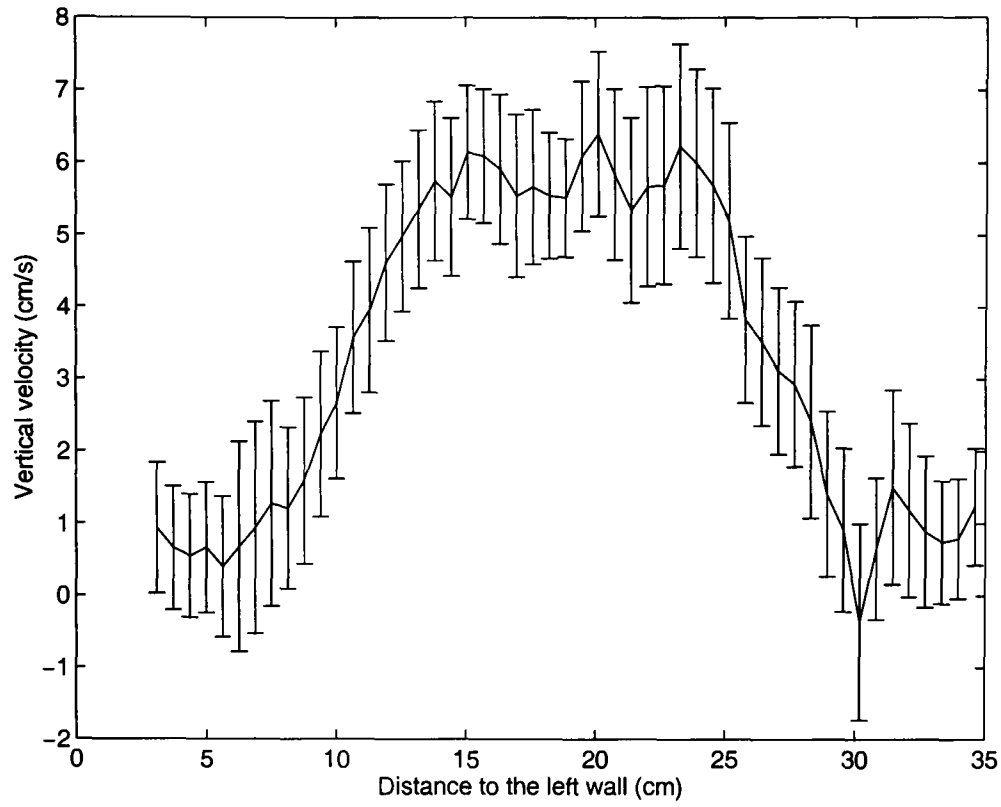

Figure 5.39: 95 % confidence limits for Figure 5.36 at $z = 45\ cm$ (Experiment 1)

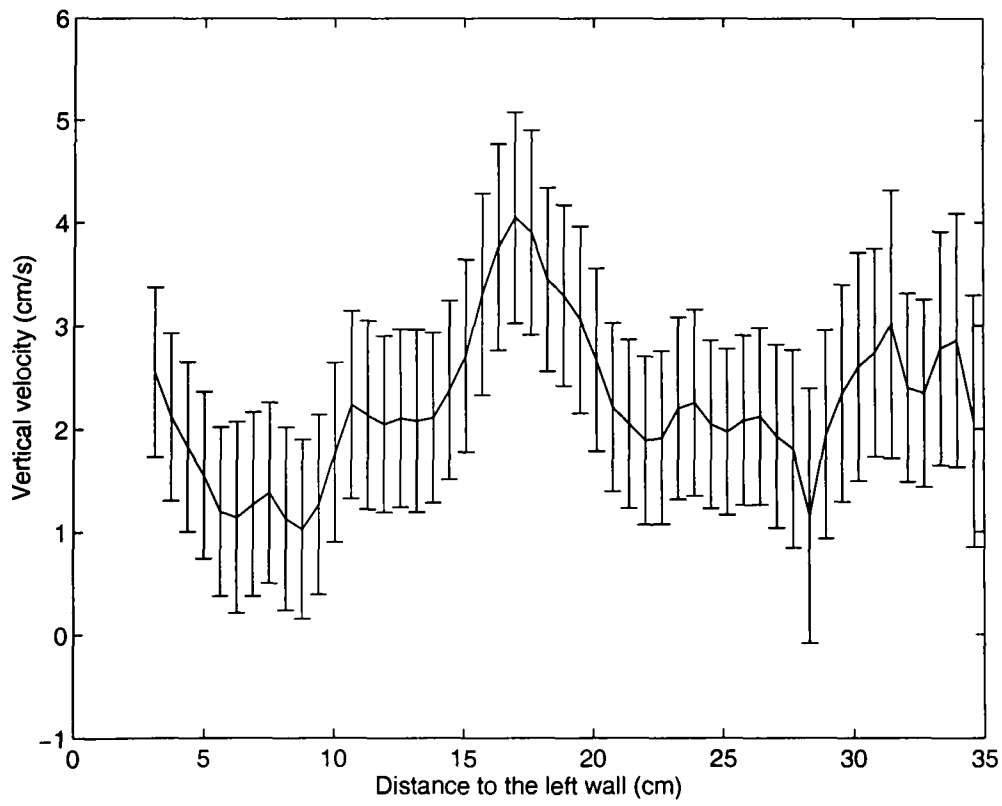

Figure 5.40: 95 % confidence limits for Figure 5.36 at $z = 53\ cm$ (Experiment 1)

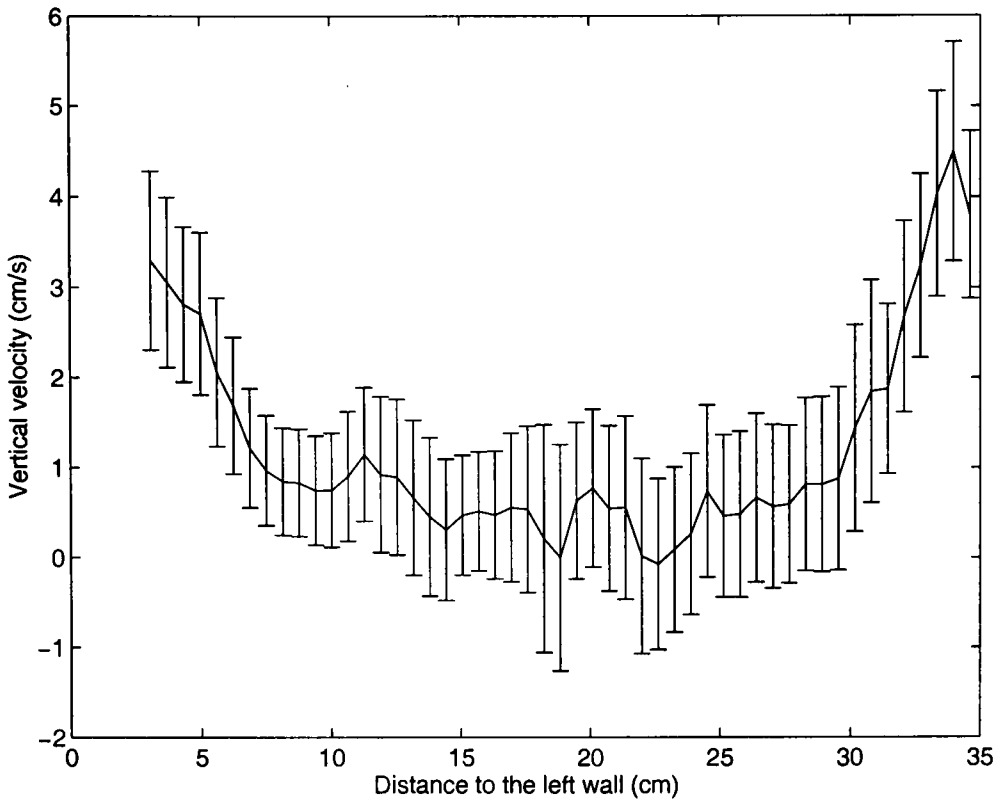

Figure 5.41: 95 % confidence limits for Figure 5.36 at $z = 61\ cm$ (Experiment 1)

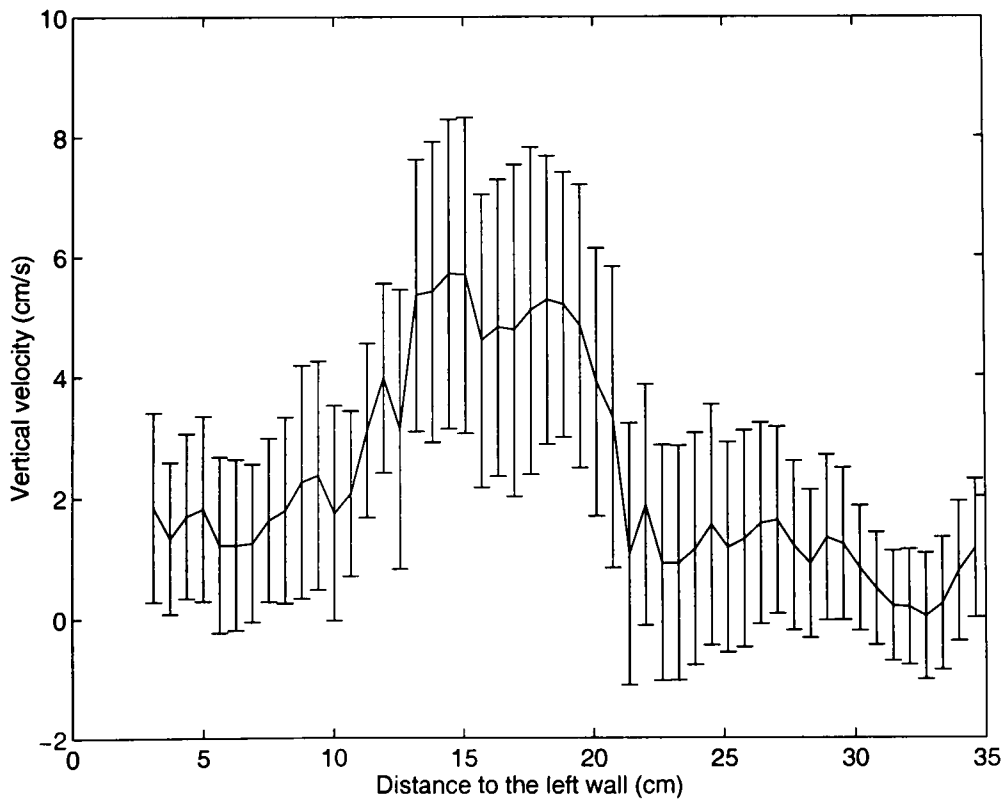

Figure 5.42: 95 % confidence limits for Figure 5.37 at $z = 45\ cm$ (Experiment 2)

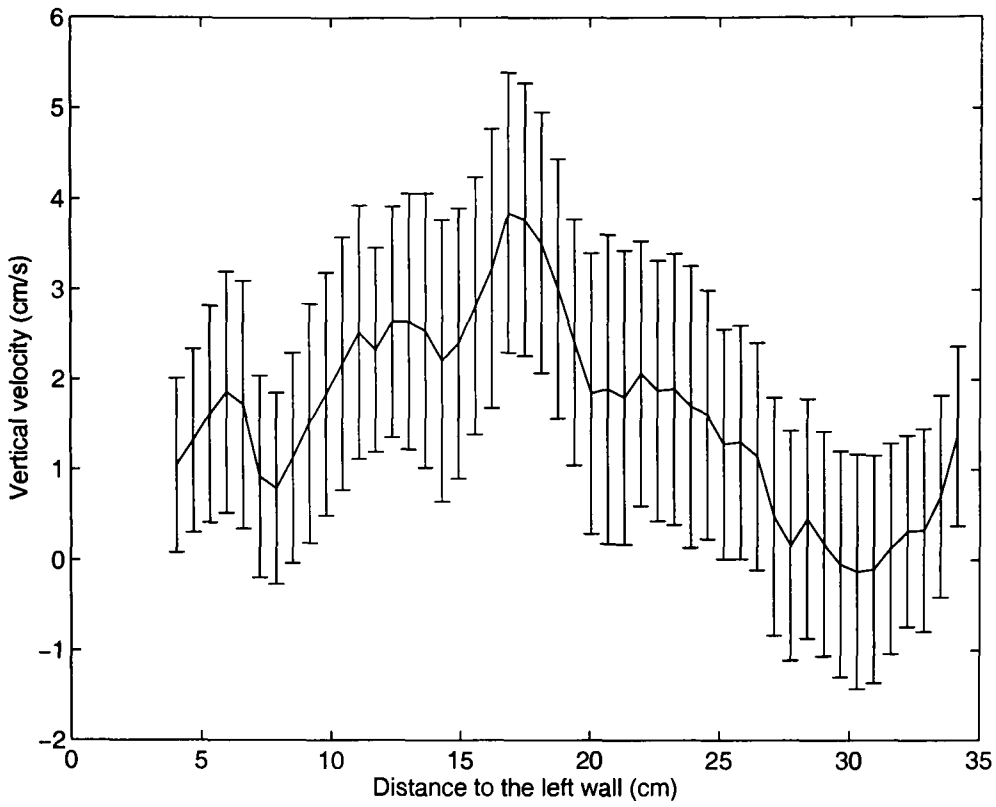

Figure 5.43: 95 % confidence limits for Figure 5.38 at $z = 45$ *cm* (Experiment 3)

heights as for the vertical profile (Figures 5.36-5.38). Again, negative velocity has been assigned to a velocity going from right to left.

- The horizontal velocity is higher closer to the bed surface; this is possibly due to the lateral movement generated by the bursting bubbles in the bed.
- The profile becomes flatter with height.
- The horizontal component of the velocity is also higher on the right side of the freeboard. The bed outlet is on this side, but in a plane behind the analysed plane. It is not clear whether this is the effect of the outlet on the flow. Paradoxically, it seems that the biggest effect of the outlet location is on the profile closer to the bed surface instead of the profile closer to the outlet, as would be expected (the "lid" of the bed could not be rotated, for design reasons, precluding the study of the outlet at different positions).
- The three Figures (5.44-5.46) present similar features, although Figure 5.45 does not seem so similar because the velocity close to the bed surface is higher than in the two other cases so the profile does not develop to the same extent.

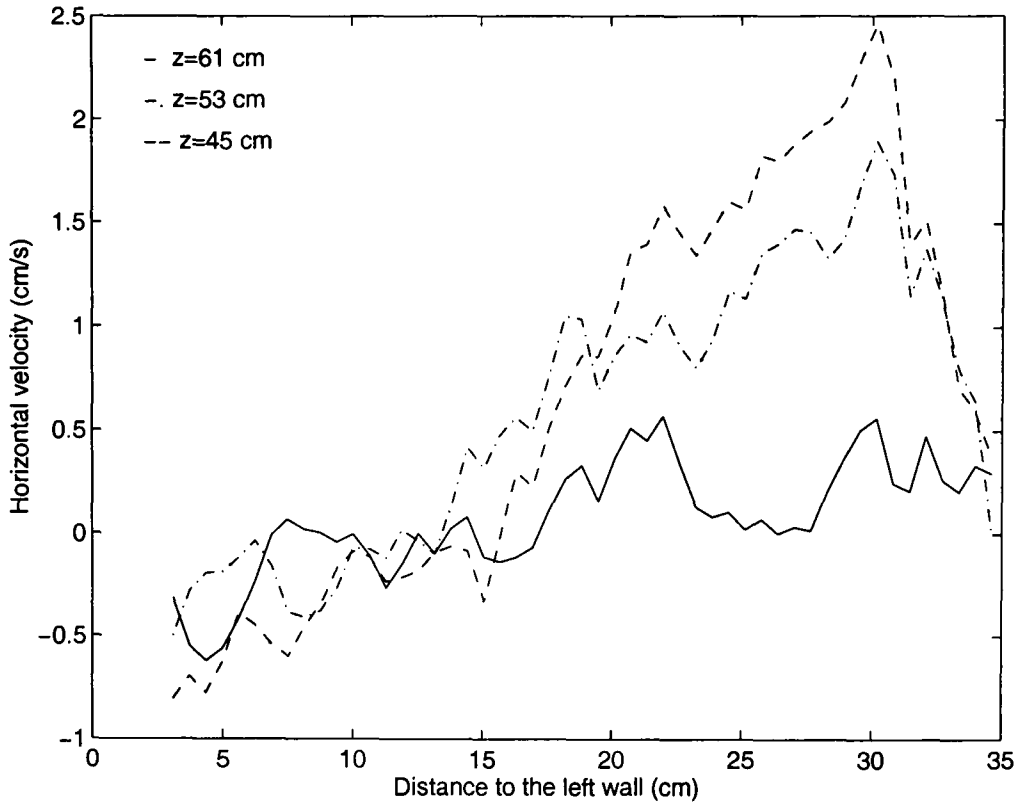

Figure 5.44: Time-averaged horizontal velocity profile (Experiment 1)

By comparing the velocity profiles of the two components of the velocity (Figures 5.36-5.38 and Figures 5.44-5.46) it can be seen that the higher velocities are found closer to the bed surface. Mass conservation requires that the third component of the velocity may be higher far from the bed surface.

Figures 5.47 - 5.49 presents the 95% confidence limits at three different heights in the freeboard, for the horizontal velocity profile, corresponding to Experiment 1. The graphs of Experiments 2 and 3 are very similar and will not be presented here for simplicity. The relative error in the horizontal velocity is higher than that of the vertical velocity, due to the difficulty in measuring low velocities using PIV.

The variation of the time-averaged vertical component of the velocity with height has been plotted at three different radial positions for the three different experiments (Figure 5.50- 5.52). d=0 corresponds to the centre of the bed (17.5 *cm* from the left wall) while, d=-13.9 cm corresponds to the left side (3.6 *cm* from the left wall) and d=13.9 cm corresponds to the right side (31.4 *cm* from the left wall). It can be seen that the mean vertical velocity decreases considerably with

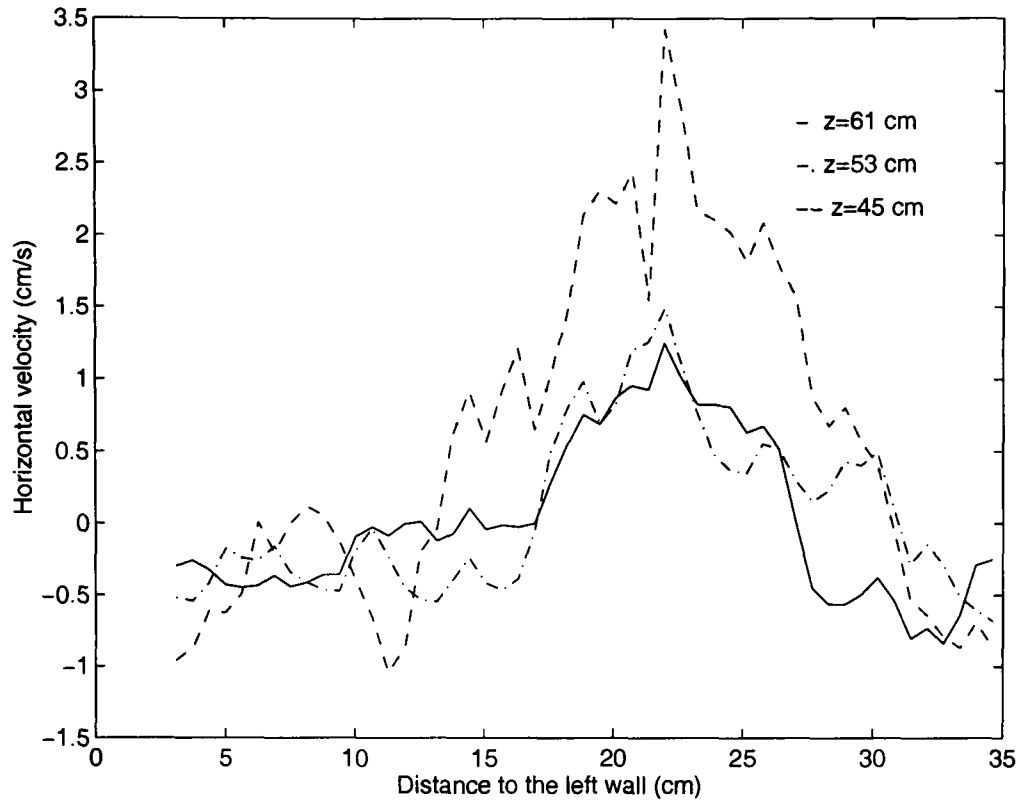

Figure 5.45: Time-averaged horizontal velocity profile (Experiment 2)

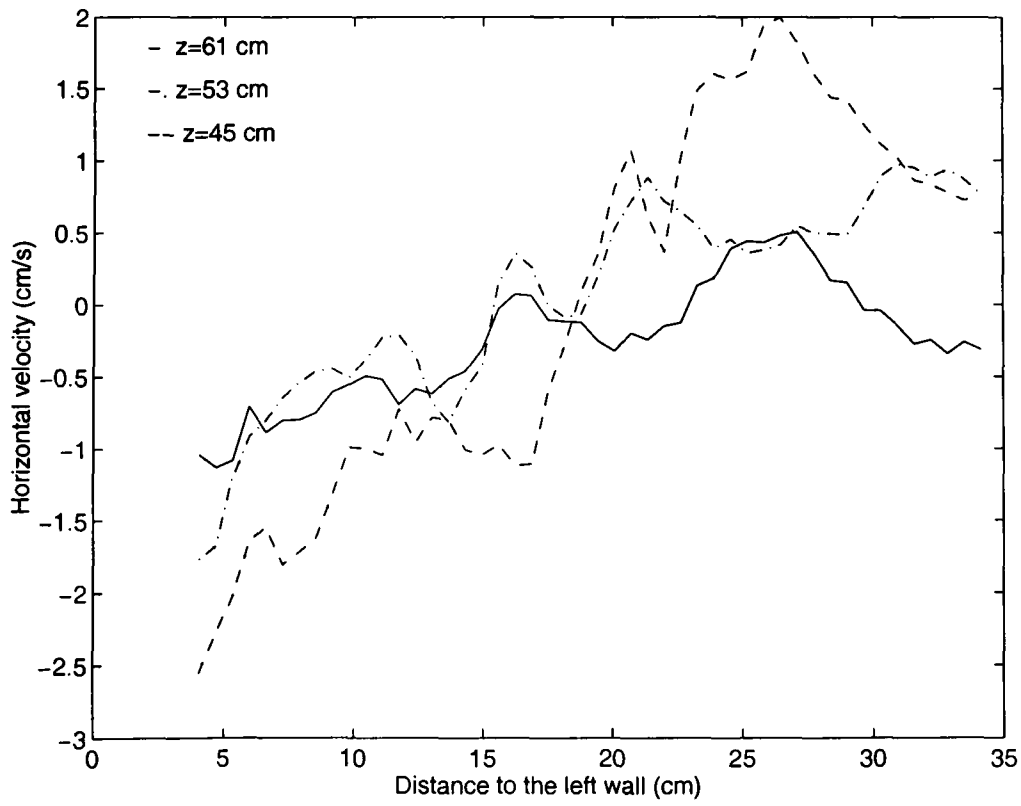

Figure 5.46: Time-averaged horizontal velocity profile (Experiment 3)

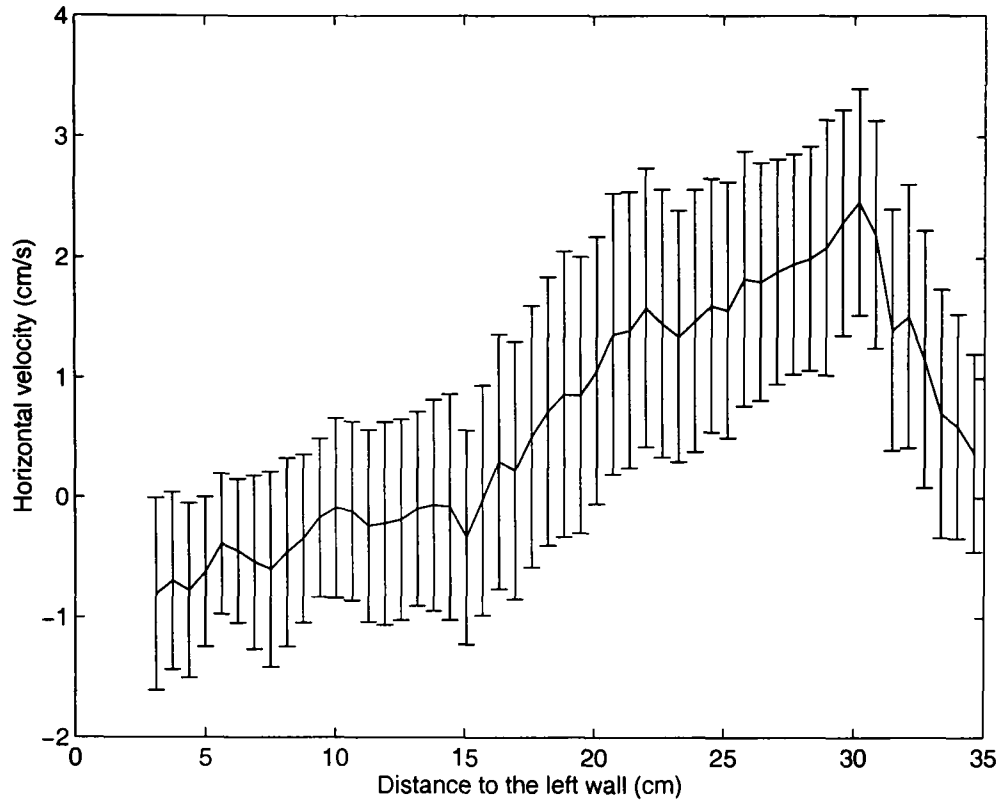

Figure 5.47: 95 % confidence limits for Figure 5.44 at $z = 45\ cm$ (Experiment 1)

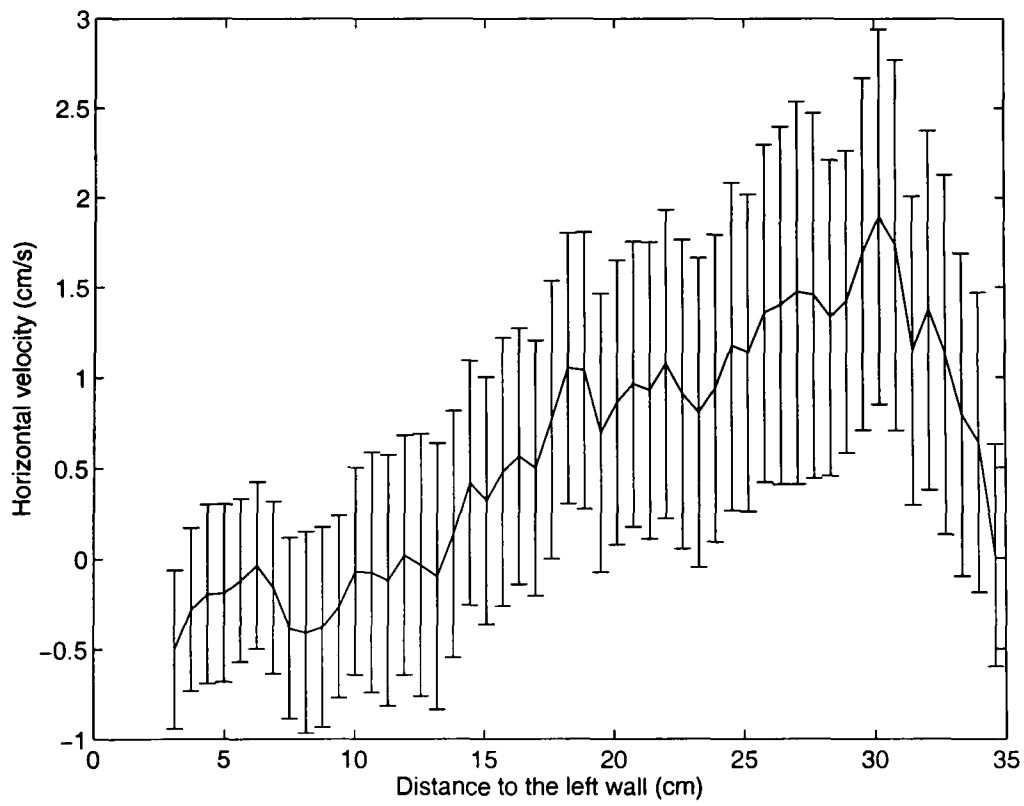

Figure 5.48: 95 % confidence limits for Figure 5.44 at $z = 53\ cm$ (Experiment 1)

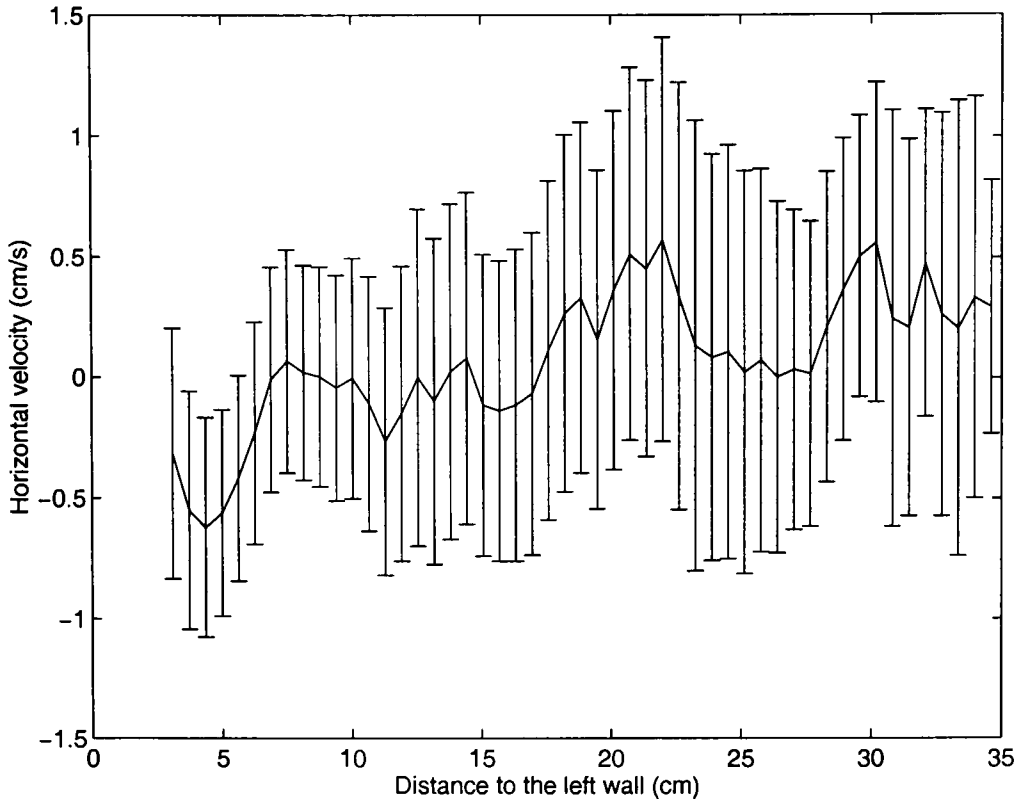

Figure 5.49: 95 % confidence limits for Figure 5.44 at $z = 61\ cm$ (Experiment 1)

height at the centre of the bed. On the contrary, the velocity increases slightly with the height near the wall. It could be thought that the vertical component of the velocity does not present central symmetry (if this were the case the velocity on both sides of the bed would be the same); however the difference between both sides is within the experimental error ($\simeq \pm 1\ cm/s$).

The horizontal component of the velocity stays more or less constant with height for the three positions studied (as it can be seen for the three experiments in Figures 5.53 - 5.55). It is difficult to elucidate the behaviour of the horizontal velocity component due to the fact that the experimental error is of the same order as the value of the velocity itself.

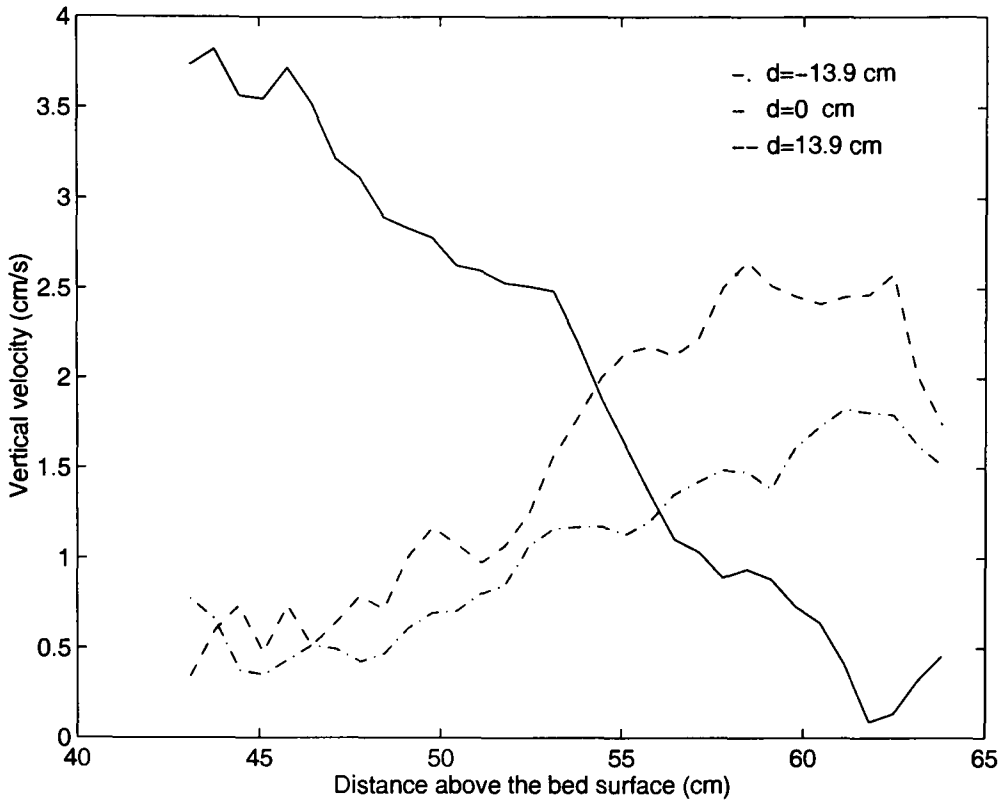

Figure 5.50: Mean vertical velocity vs. height (Experiment 1)

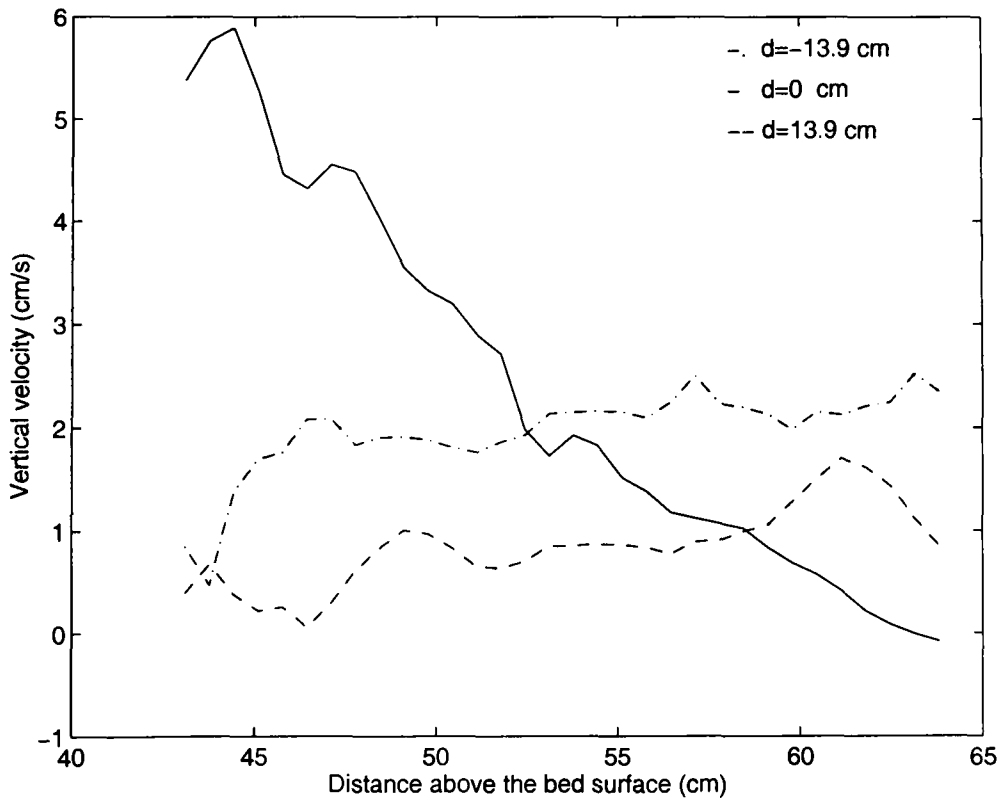

Figure 5.51: Mean vertical velocity vs. height (Experiment 2)

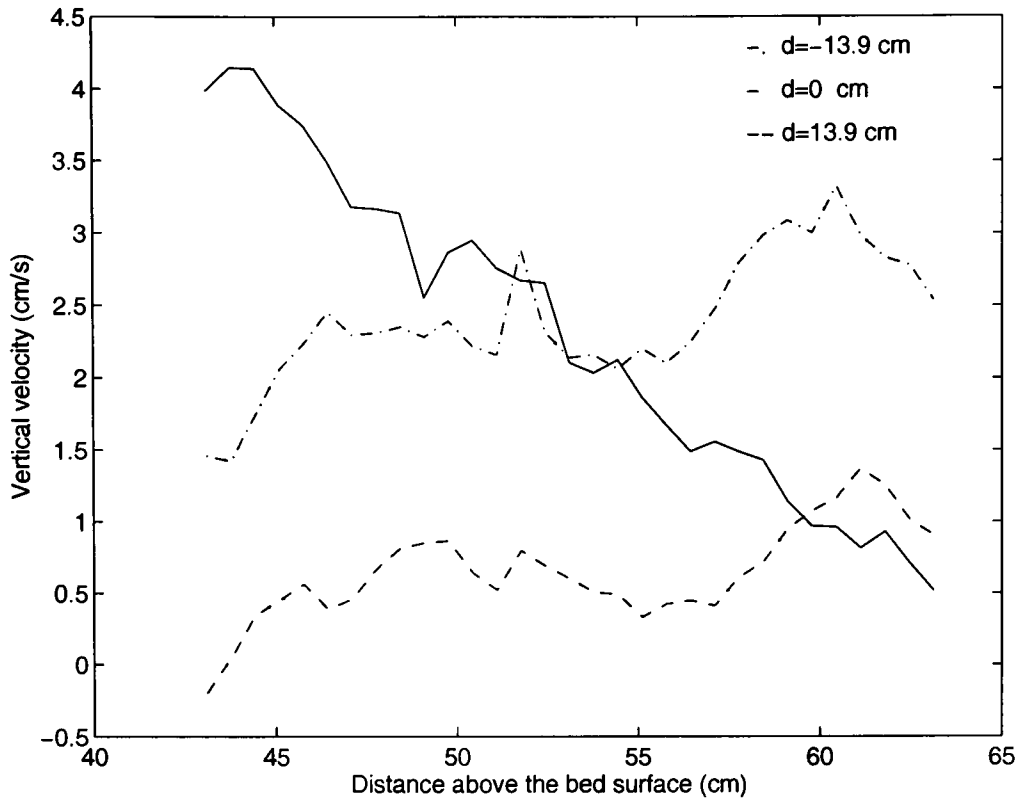

Figure 5.52: Mean vertical velocity vs. height (Experiment 3)

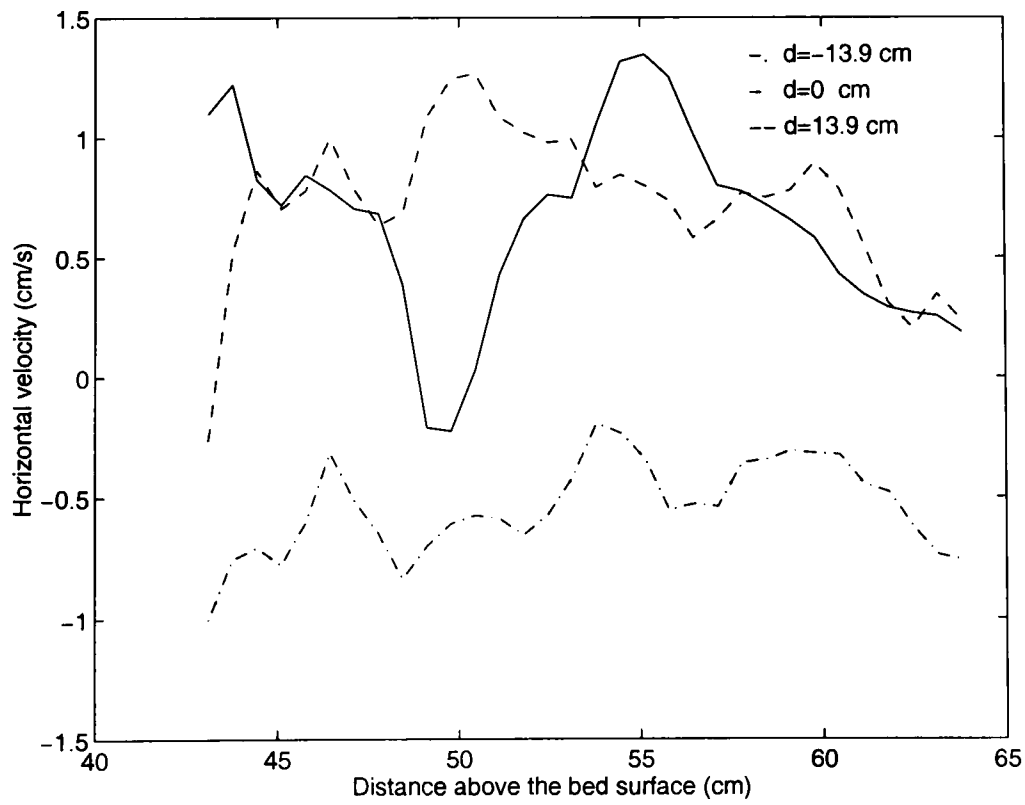

Figure 5.53: Mean horizontal velocity vs. height (Experiment 1)

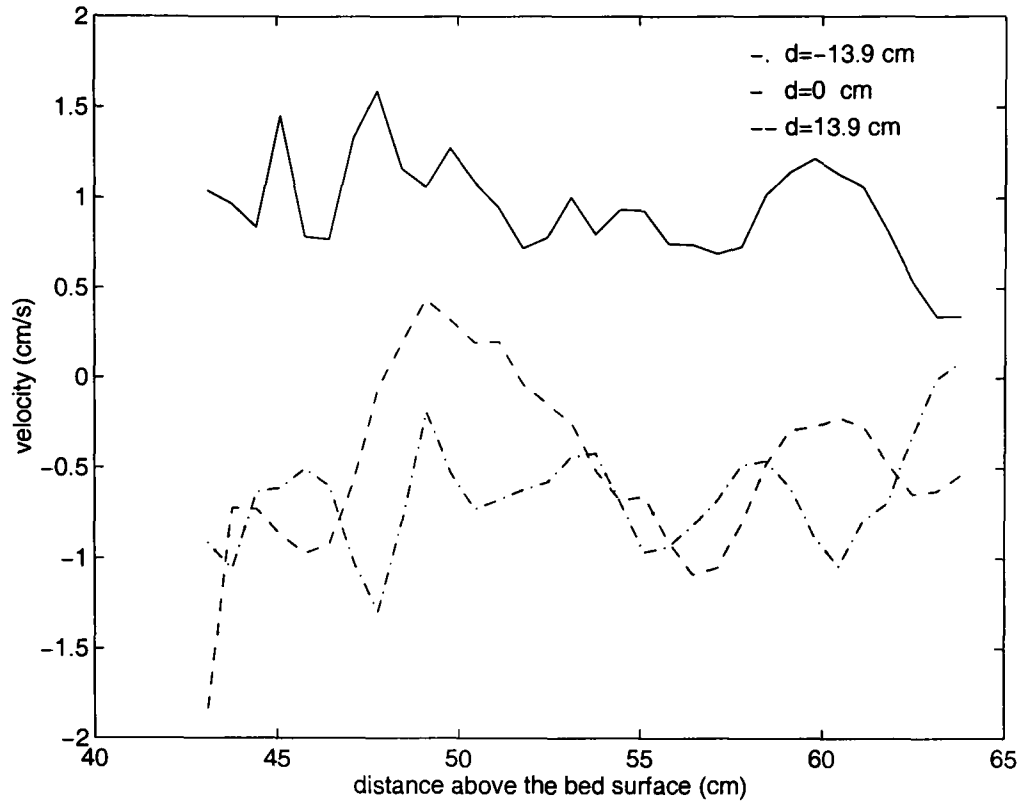

Figure 5.54: Mean horizontal velocity vs. height (Experiment 2)

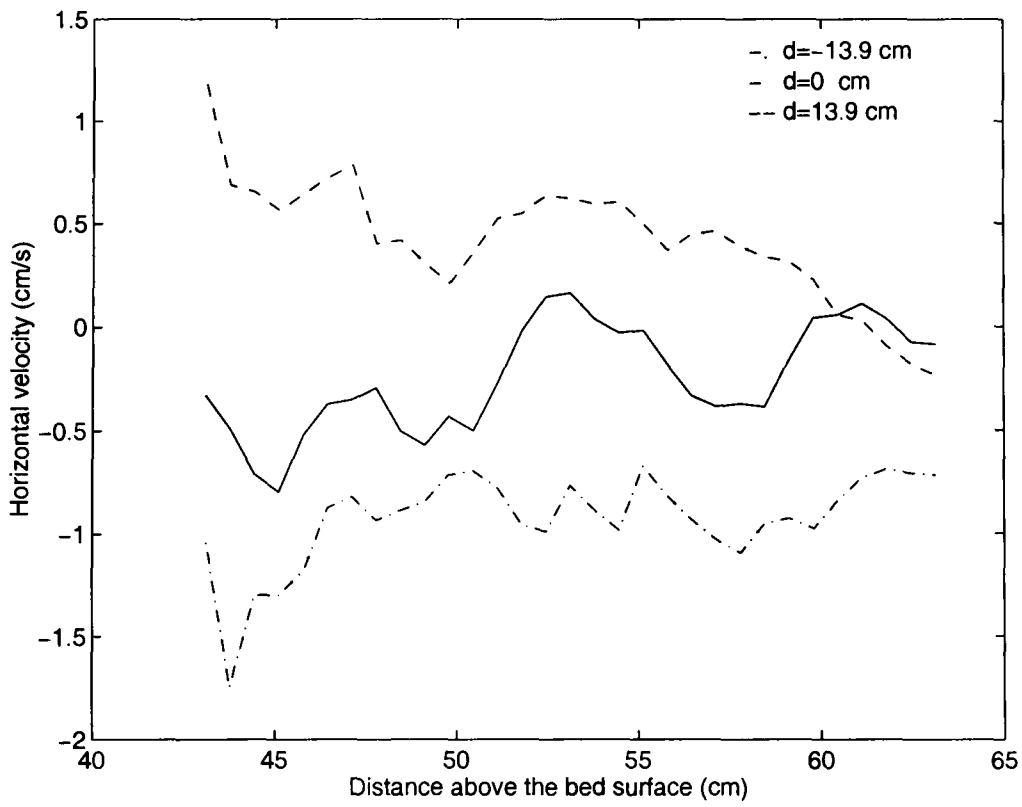

Figure 5.55: Mean horizontal velocity vs. height (Experiment 3)

Fluctuations of the velocity

The root mean square velocity fluctuation (rms) is a measure of the violence or intensity of the turbulence relative to the average flow and it is given by:

$$u' = \frac{\sqrt{\sum_{i=1}^{n}(u_i - \bar{u})^2}}{n-1} \tag{5.4}$$

where u_i is the instantaneous velocity component, $\bar{u}$ the time average of the velocity component and n the number of vector maps. An equivalent equation is applied to each of the velocity components. The vertical and horizontal rms velocities are presented in Figures 5.56 - 5.58 and 5.59 - 5.61, respectively. It can be seen that:

- The magnitude of the fluctuations is higher than the average velocities for both components of the velocity (especially for the horizontal component).
- The intensity of the turbulence decreases with height.
- The fluctuations of the velocity do not present any clear symmetry.
- The graphs corresponding to different experiments do not present much similarity among them.

Spatial correlation coefficients

Although the rms is a measure of "how strong" the turbulence is relative to the average flow, this quantity does not provide any information with respect to the features of the flow. The average structure of the turbulence (length and time scales) can be characterised using spatial and temporal correlation curves [123]. The erupting bubbles at the bed surface are the origin of the freeboard turbulence. Therefore, it seems logical to think that the inverse of the bubble eruption frequency is the characteristic freeboard time scale, which has indeed

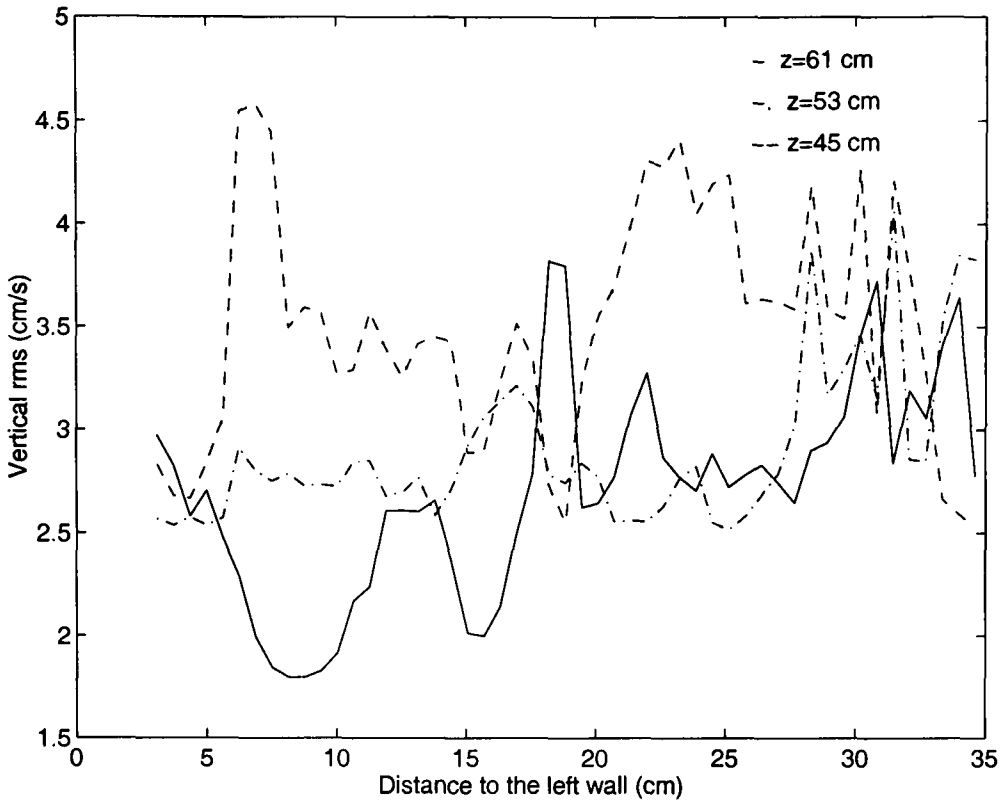

Figure 5.56: Rms vertical velocity profile (Experiment 1)

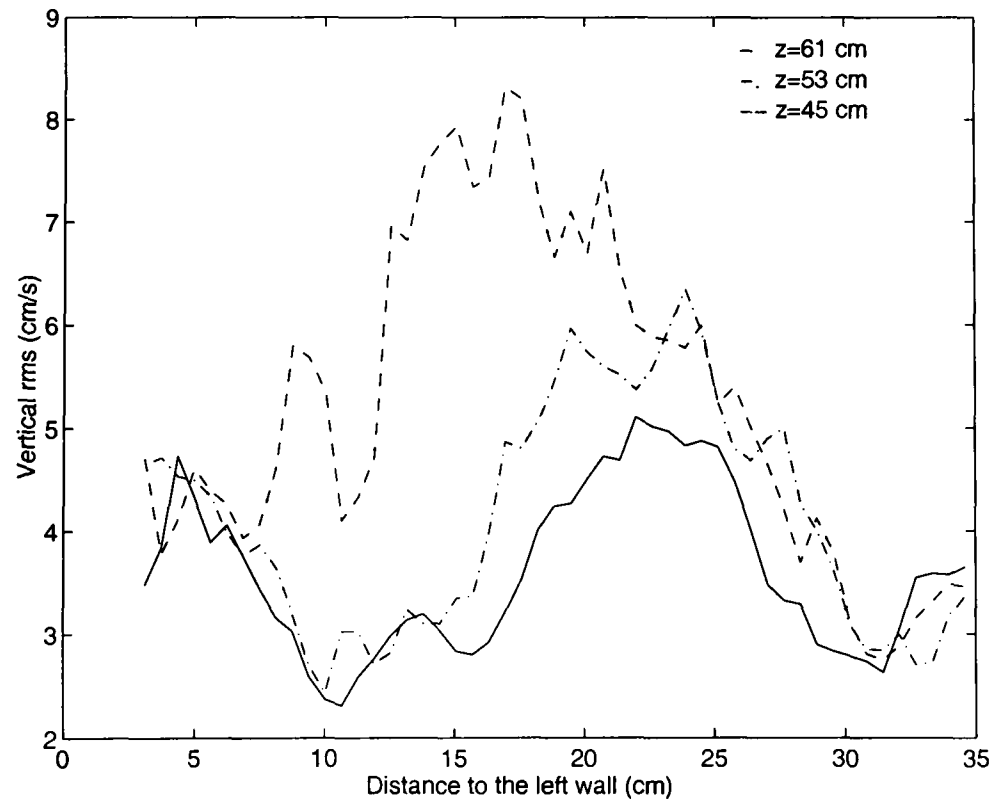

Figure 5.57: Rms vertical velocity profile (Experiment 2)

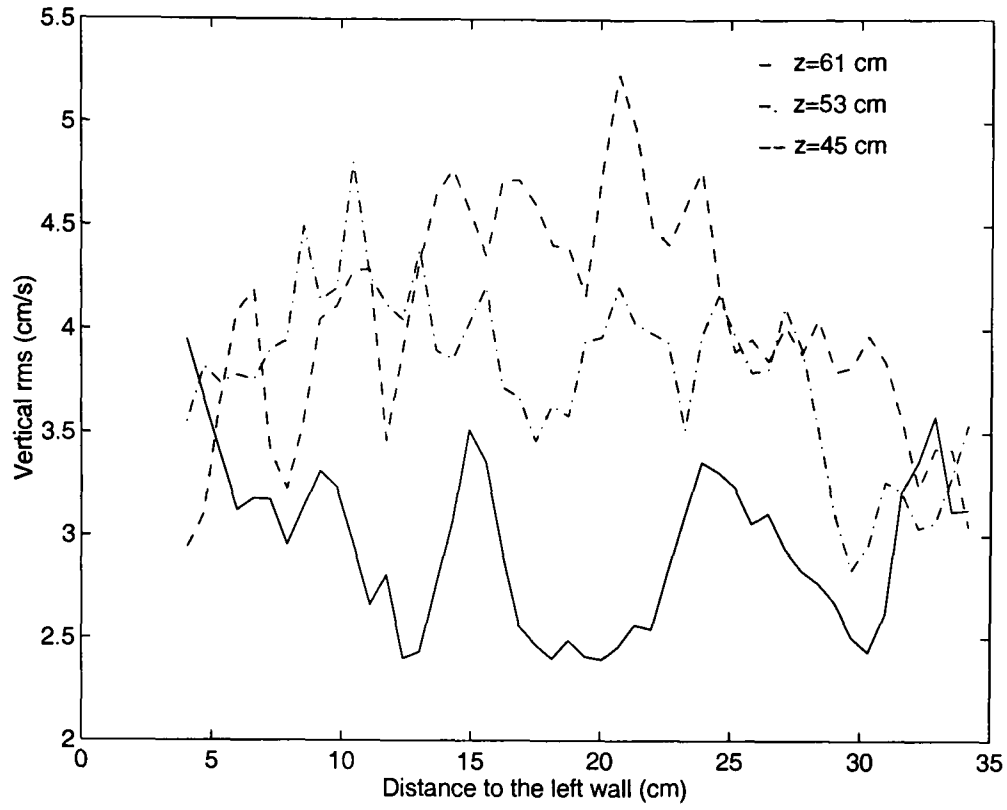

Figure 5.58: Rms vertical velocity profile (Experiment 3)

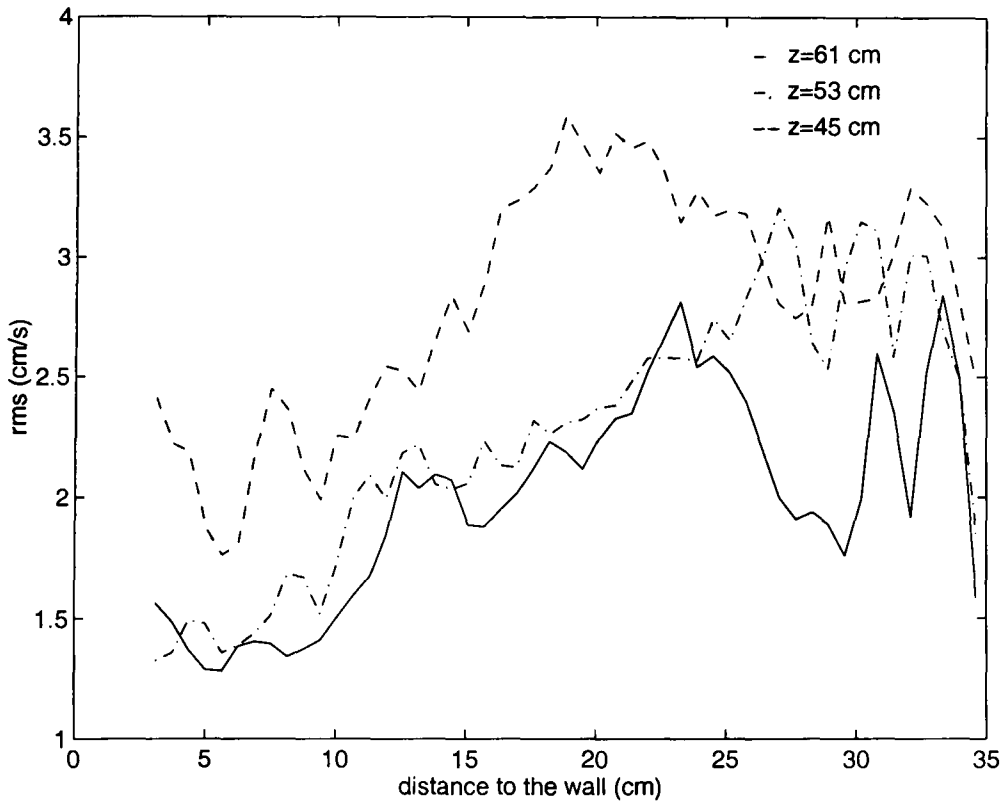

Figure 5.59: Rms horizontal velocity profile (Experiment 1)

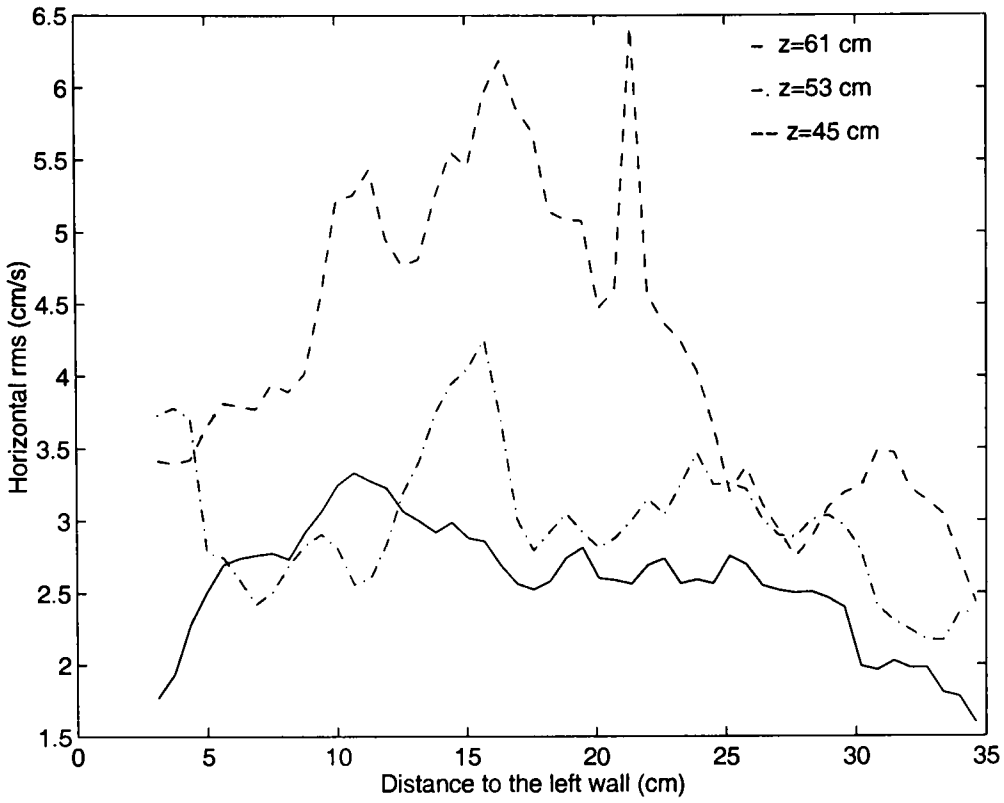

Figure 5.60: Rms horizontal velocity profile (Experiment 2)

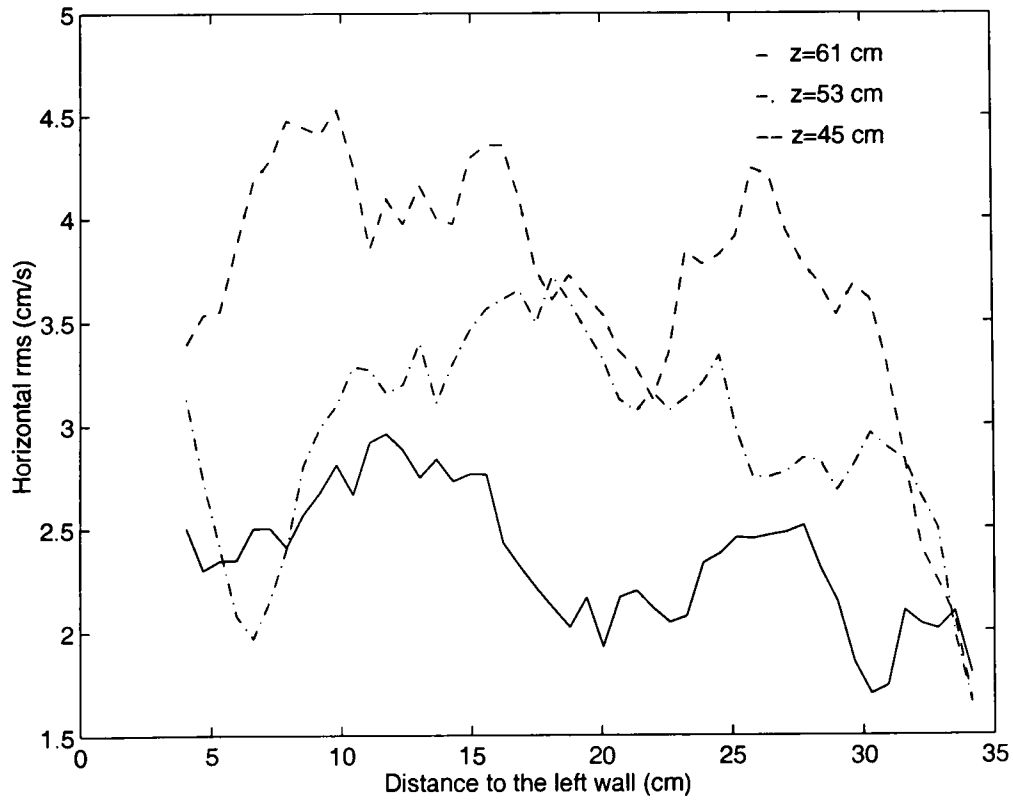

Figure 5.61: Rms horizontal velocity profile (Experiment 3)

been found by Horio *et al.* [55]. Due to the fact that the separation between the vector maps, in time, is too long, the time correlations could not be calculated. Only spatial correlation coefficients could be calculated with the available data. The spatial correlation indicates the distance over which the motion at one point significantly affects that at another and it is a function of each fluctuating velocity component and each position and orientation in the flow, i.e. it is a tensor. The value of the correlation coefficient is 1 or -1 when the fluctuations are perfectly correlated and 0 when they are totally independent. A correlation coefficient is defined by:

$$R_{ij} = \frac{\sum_{t=1}^{t=n} u'_{it} u'_{jt}}{\sqrt{\sum_{t=1}^{t=n} (u'_{it})^2 \sum_{t=1}^{t=n} (u'_{jt})^2}}$$

u'_{it} and u'_{jt} are simultaneous fluctuating components of the velocity at two different points and n the number of vector maps used. The correlation of different components of the velocity gives rise to a cross-correlation function. The correlation of the same components of the velocity give rise to an auto-correlation function. Correlations can be calculated for each component of the velocity in each position of the flow. In the present study, a two-point spatial autocorrelation has been chosen, since published work concerning these parameters can be found [124]. The autocorrelations can be calculated in the flow direction (longitudinal correlation) or in perpendicular direction to the flow (transversal correlation).

It would have been necessary to know all the components of the velocity to calculate the correlation functions since the flow does not present symmetry in any direction. However, a few components of the correlation functions (correlation coefficients) can give indications of the structure of the flow. Figures 5.62-5.64 shows the radial correlation coefficient for the horizontal (longitudinal correlation) and vertical (transversal correlation) component of the velocity. The inhomogeneity of the flow does not allow any kind of spatial average. The radial correlation

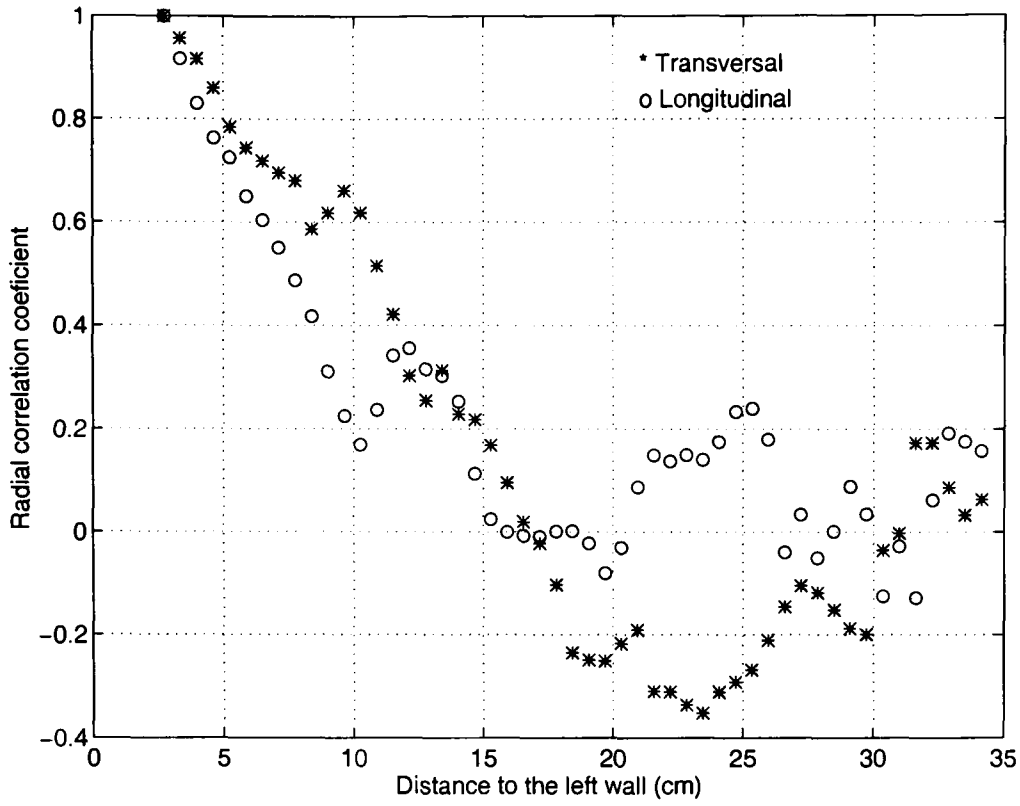

Figure 5.62: Two point radial spatial correlation coefficient in the middle of the expanded region (Experiment 1)

coefficient is given by the correlation of the velocity at the closest point to the left wall with all the velocities along the diameter of the bed, at the mean height of the expansion section ($z = 53\ cm$ above the bed surface). A more complete description would imply calculating correlation functions at each height in the expanded section. The axial correlation coefficient has been calculated by correlating the velocity at a point, 45 *cm* above the bed surface, with all the velocities at the in the centre-line of the expanded section (Figures 5.65-5.67) for the vertical (longitudinal correlation coefficient) and horizontal (transverse correlation coefficient) velocity components.

Transversal correlations have a negative region, due to there being two velocities in opposite directions. Figures 5.62 to 5.67 indicate: i) eddies of different sizes are present in the flow, indicated by the occurrence of high curvature, ii) the flow is inhomogeneous, since the correlations are not symmetric in all the directions, iii) the flow is not isotropic, because the correlations are not the same in all the directions and iv) the *shape* of the correlation curves resembles "free turbulence" rather than "wall turbulence", indicating that turbulence is not produced by

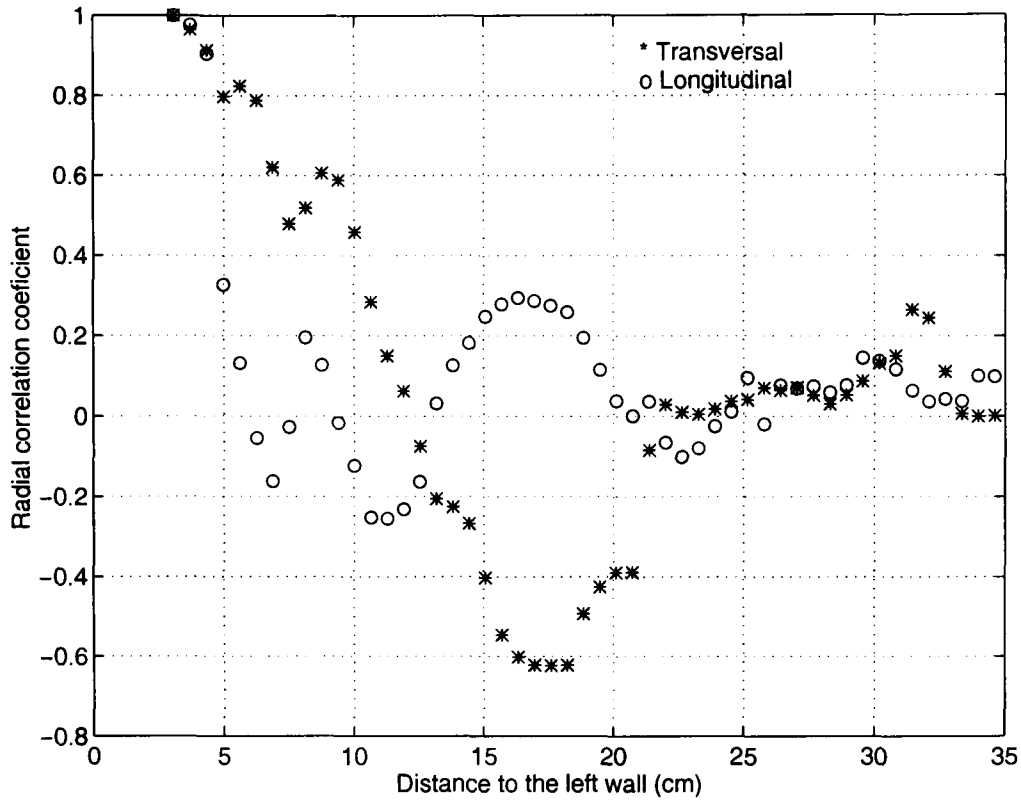

Figure 5.63: Two point radial spatial correlation coefficient in the middle of the expanded region (Experiment 2)

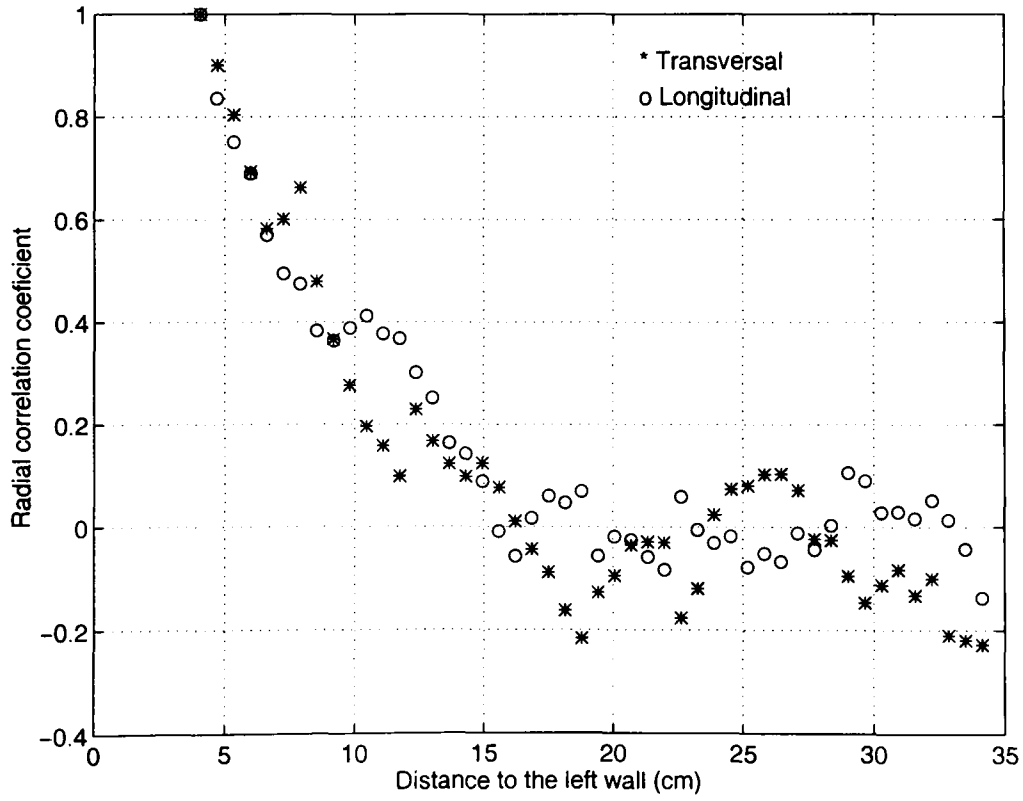

Figure 5.64: Two points radial spatial correlation coefficient in the middle of the expanded region (Experiment 3)

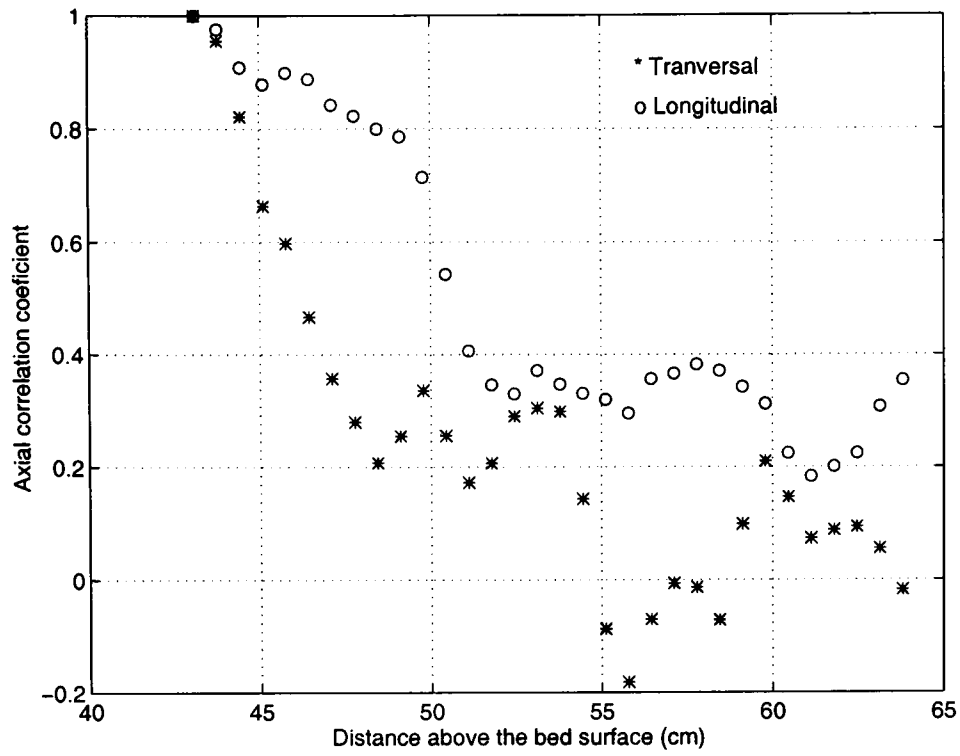

Figure 5.65: Two point axial spatial correlation coefficient at the bed centre-line (Experiment 1)

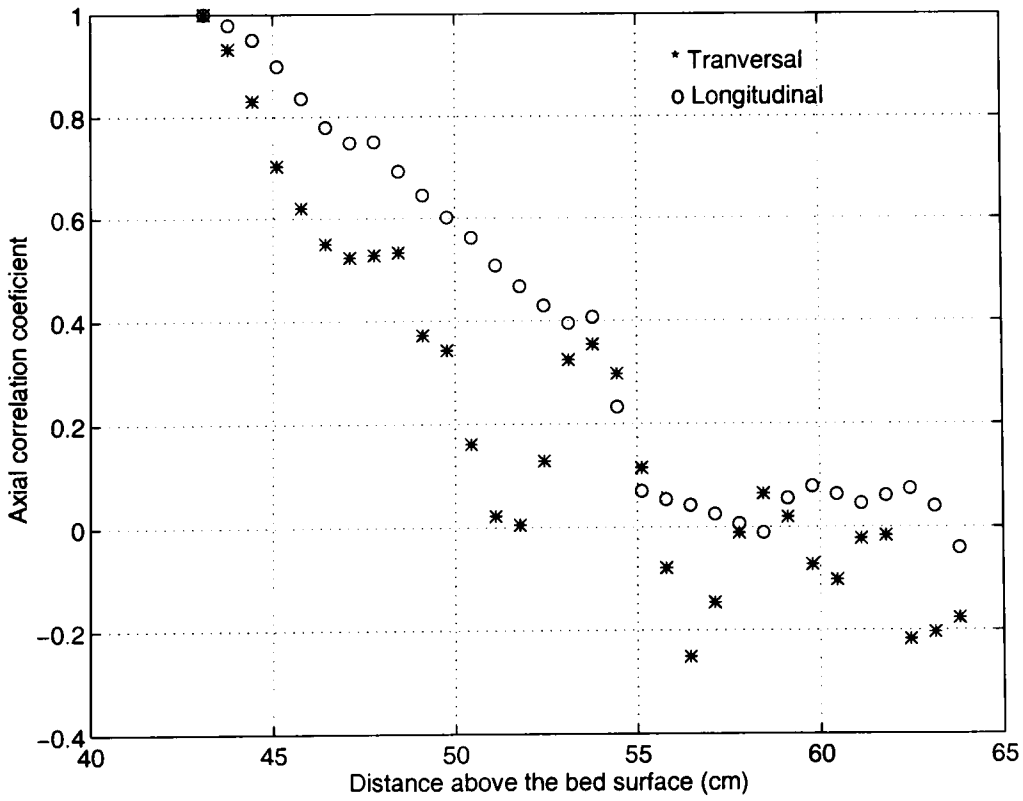

Figure 5.66: Two point axial spatial correlation coefficient at the bed centre-line (Experiment 2)

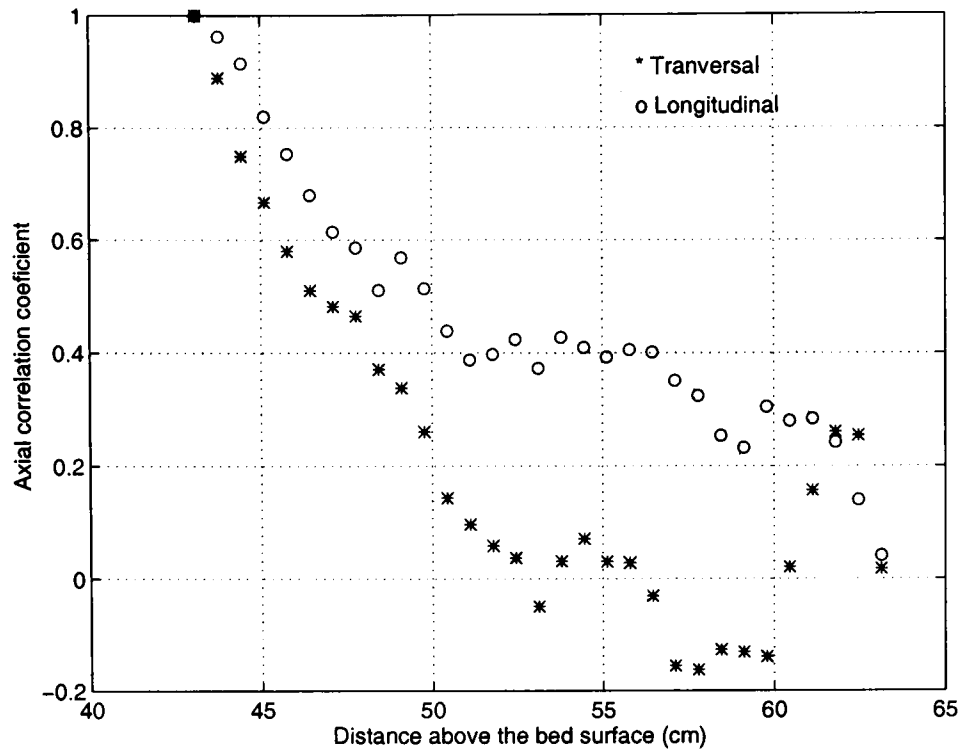

Figure 5.67: Two point axial spatial correlation coefficient at the bed centre-line (Experiment 3)

friction forces at the wall but by the presence of regions of fluid with different velocities originated from bubble eruption at the bed surface.

Time-averaged vorticity

The average component of the vorticity perpendicular to the image plane ($w_z = \delta v/\delta x - \delta u/\delta y$) is plotted in Figures 5.68-5.70 where positive vorticity is assigned to the anti-clockwise direction. The vorticity has been obtained in each point by calculating the circulation along a line that connects the eight neighbours of a point and dividing the result by the enclosed area (as given by Stokes' theorem) [125]. The most remarkable feature shown in these vorticity plots is the presence of four eddies at the corners, rotating in opposite direction to their neighbours as well as the presence of a central vortex. The same behaviour is found in the three cases, although the intensity of the vorticity is not exactly the same.

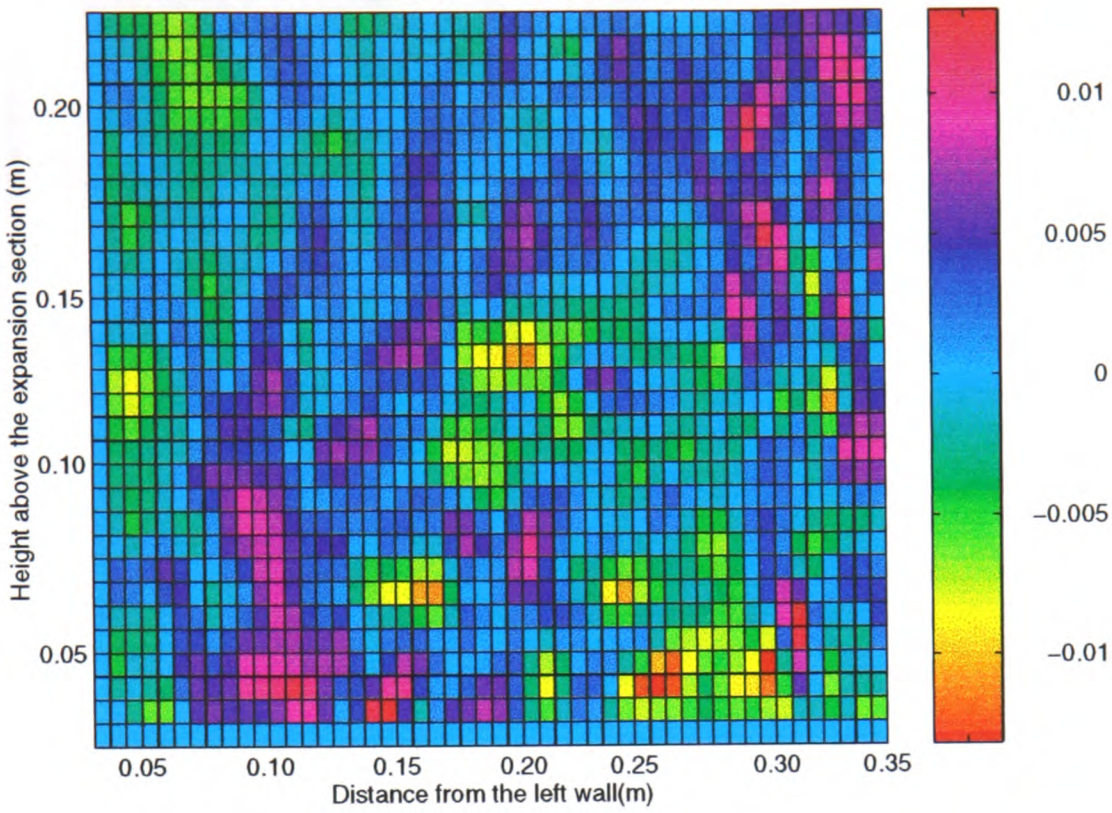

Figure 5.68: Time-averaged vorticity (s^{-1}) (Experiment 1)

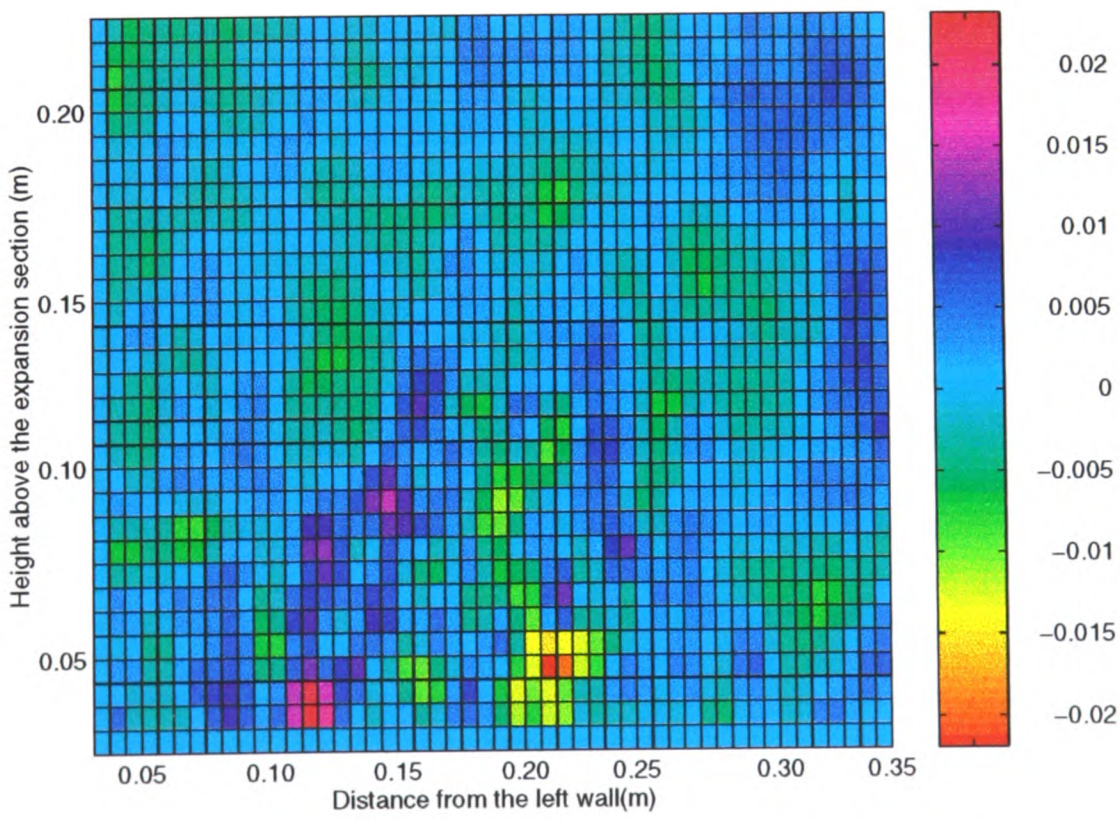

Figure 5.69: Time-averaged vorticity (s^{-1}) (Experiment 2)

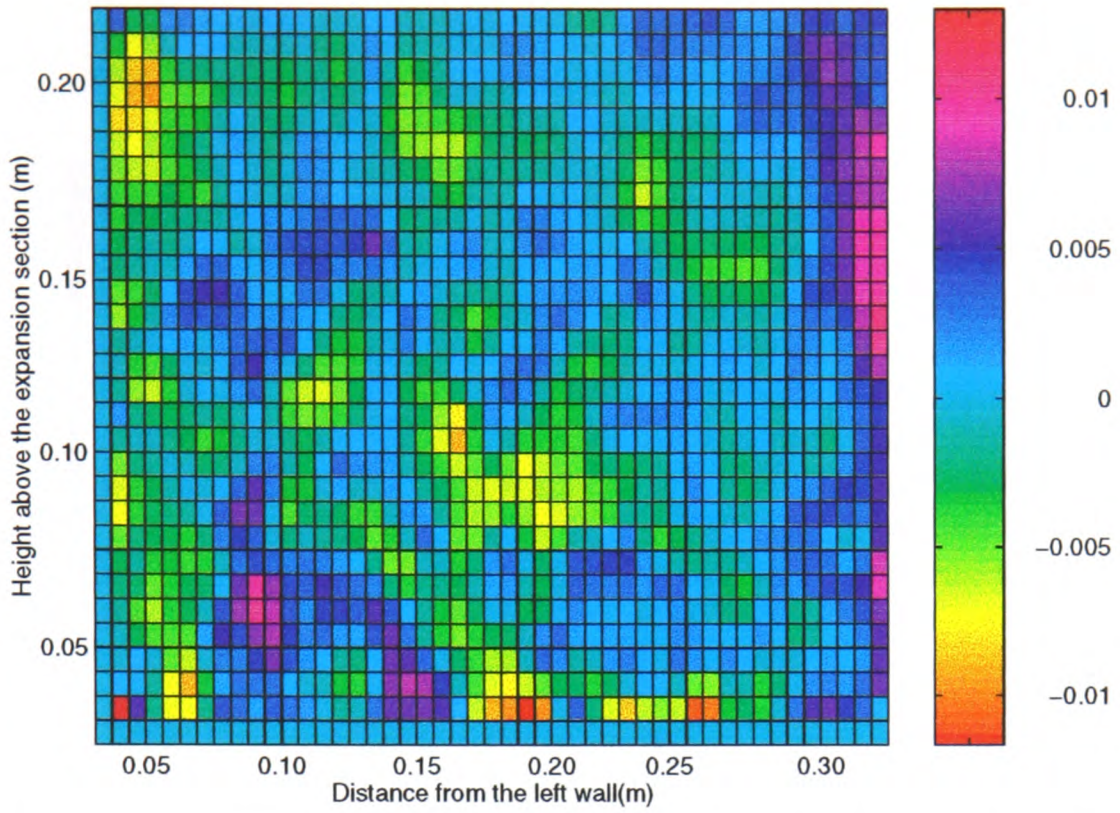

Figure 5.70: Time-averaged vorticity (s^{-1}) (Experiment 3)

Secondary structure of the flow

The mean velocity of the time-averaged vector map (over 37 seconds) is calculated (mean flow velocity) and it is subtracted from the time-averaged vector map (Figure 5.27) to produce Figure 5.71. Thus the mean flow velocity is removed to visualise the turbulent structures. The characteristics of the flow, once the mean velocity has been removed, are:

- Above the bed surface there is upward high central gas velocity region and downward velocity close to the wall.
- In the middle of the expanded section there is a low in-plane velocity region.
- At the top of the expanded section there is downward velocity at the centre and upward velocity near the wall.

These characteristics suggest that the flow is divided into four recirculation areas, as sketched in Figure 5.72. They seem to be elongated, the horizontal diameter being about 10 cm. They may be generated by a combination of the fluctuations

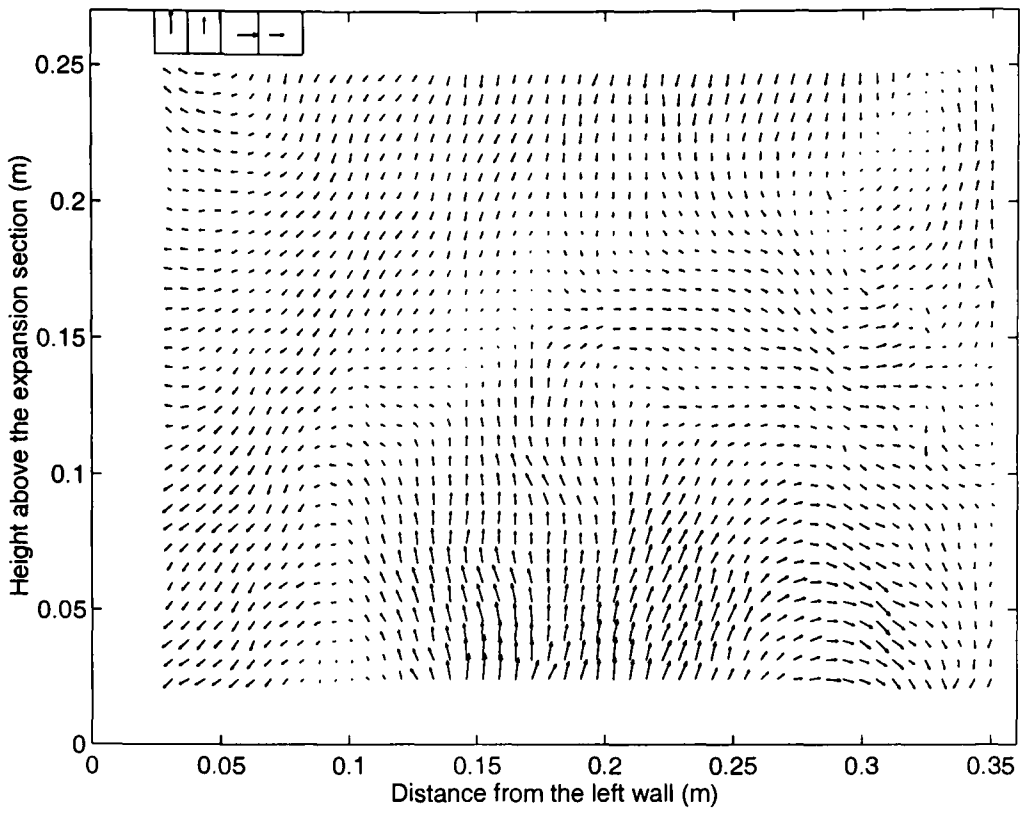

Figure 5.71: Time-averaged vector map over 37 seconds minus the spatial time-averaged velocity (Experiment 1). Velocity vectors in the left upper corner from left to right: 3 cm/s, 2 cm/s, 3 cm/s and 2 cm/s

in the flow, permanent vortices above the bed surface and the expansion region. These recirculation areas are not expected to be seen in instantaneous vector-maps because they are very slow compared with the instantaneous structures. To have an idea of the time scale and stability of these structures the analysis is performed as before but with the time average calculated over 10 seconds, instead of over 37. The whole time interval (37 seconds) is analysed by dividing it into blocks of 10 vector maps, each block overlapping the next one by 5 seconds. The eight different average vector maps obtained in this way are presented in Figure 5.73. The four recirculation areas are masked by the presence of strong turbulent jet-like structures. Looking in turn at each frame of Figure 5.73:

- Frame 1, the two lower recirculation areas are pushed upward by a powerful jet and only a fraction of the upper recirculation areas can be seen at the top corners. The left cell is bigger than the right one. Looking at the individual vector maps used to construct Frame 1 it can be seen that the jets are in general closer to the right than to the left side.

- Frame 2 shows the same kind of behaviour.
- In Frame 3 a powerful jet can be seen close to the centre of the expansion. At the mid-height of the frame the jet has a high horizontal velocity component towards the right, pulling the top recirculation cells into the left corner.
- In Frame 4, the jet is slightly towards the left, making the left lower recirculation area smaller and increasing the size of the lower right cell. Part of the upper recirculation areas can be seen at the top corners.
- In Frame 5 the jet (more powerful than in the previous frame) is on the left hand side resulting in the same behaviour as in Frame 3, but in this case the left cell is smaller and the upper cells are squeezed into the right top corner.
- In Frame 6 there is a big jet on the left, displacing the top left cell. As a consequence a small lower right cell and a large upper right cell are produced.
- Frame 7 shows a jet slightly towards the left, but smaller than in Frames 3, 5 and 6. As a result the recirculation areas are not as distorted as before.
- A very similar pattern to Frame 7 remains in Frame 8.

It can be concluded that the effect of jets on the recirculation cells is as follows:

- When a powerful central jet reaches high into the expanded section the two lower cells are elongated and the top ones are either reduced in size or pushed higher out of the field of view (as can be seen in Frames 1 and 2). This is sketched in Figure 5.74.
- When the jets diverge from the centre line the recirculation areas lose symmetry. When the jet is close to one side, the lower cell on that side is elongated, while the lower cell on the opposite side is flattened. The upper cells are displaced away from the jet. This is sketched in Figure 5.75.

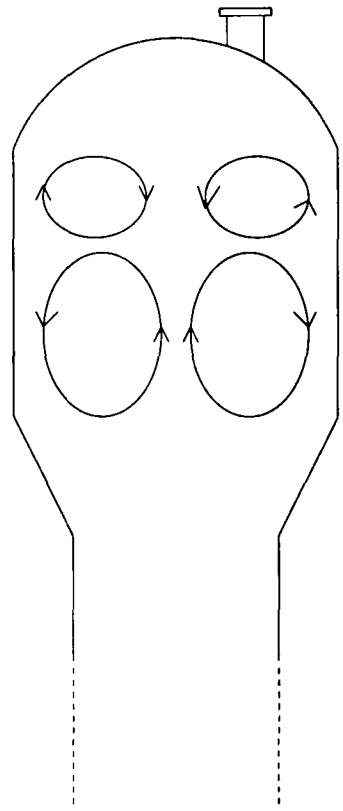

Figure 5.72: Proposed recirculation areas

The time-averaged vector maps over 37 seconds (Figures 5.28 and 5.29) minus the mean spatial time-averaged velocity are presented in Figures 5.76 and 5.77, for Experiments 2 and 3 respectively. They also show four recirculation areas, but are not as symmetric as in the case of Experiment 1. This is logical since in Experiments 2 and 3 the high velocity region is not as central. This effect of a non-central jet can be clearly observed in Figure 5.78 Frame 2 and in Figures 5.79 Frames 5 and 6.

5.4 Conclusions

Enough evidence to propose a mechanism for single bubble eruption has been obtained by injecting single bubbles in an incipiently fluidised bed and analysing the gas above the bed surface using simultaneous image shifting and video recording.

The expansion section of the freeboard could not be analysed because the expansion angle is higher than the seeding particles repose angle. This finding indicates

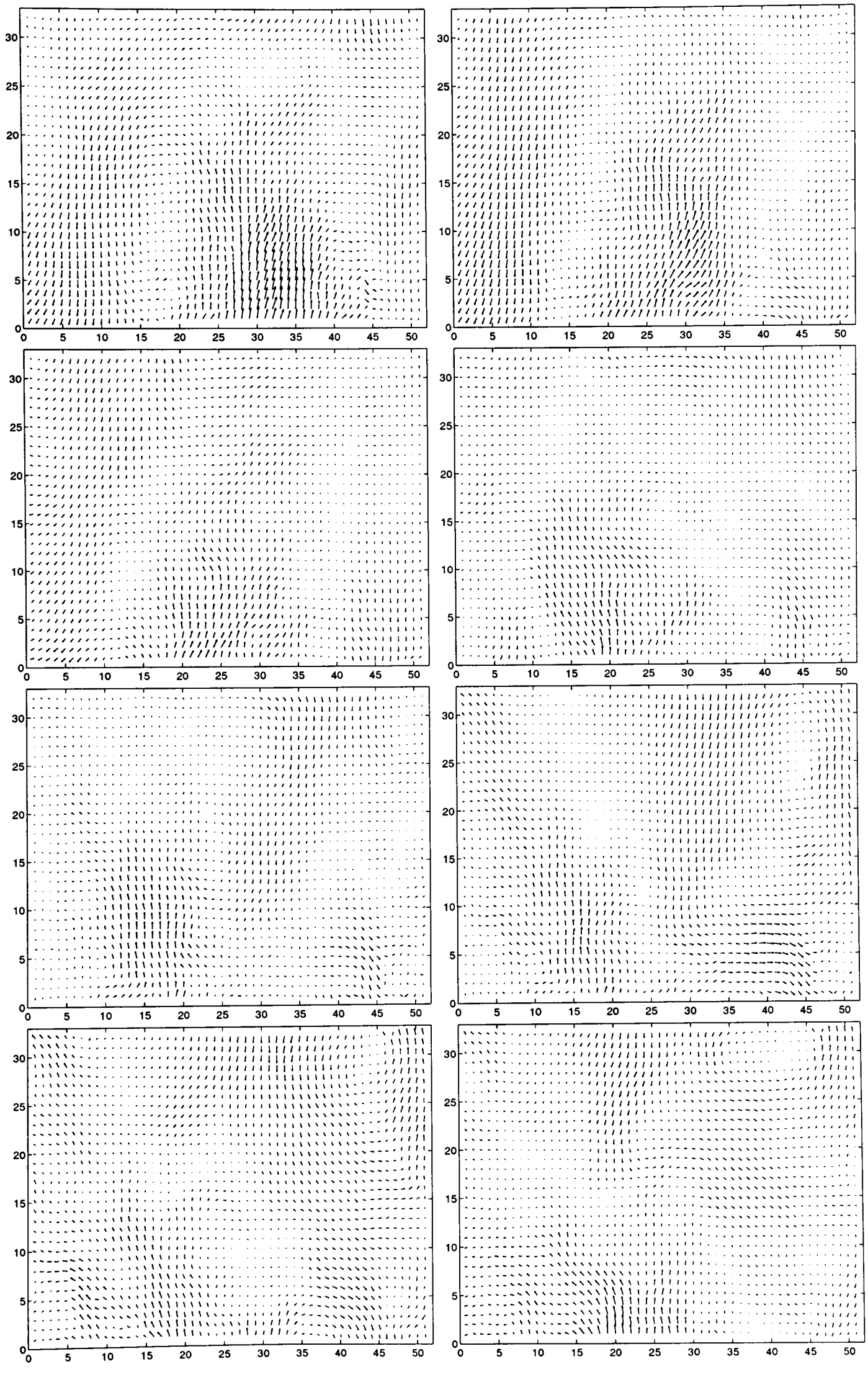

Figure 5.73: Time-averaged vector maps, over 10 seconds, minus the spatial time-averaged velocity (Experiment 1. Frame 1 to 8 are displayed from left to right and from top to bottom)

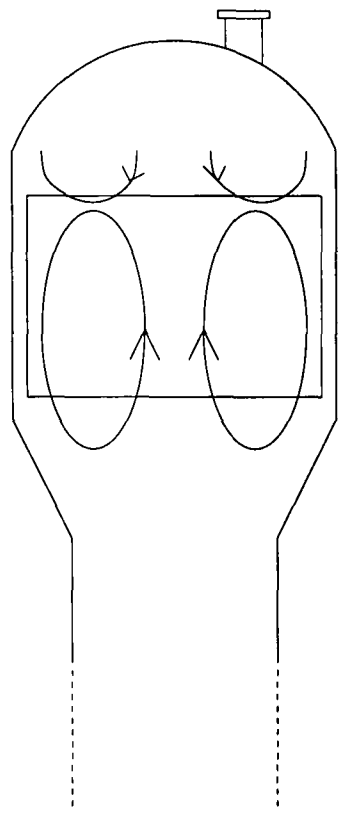

Figure 5.74: Elongated recirculation areas by a central powerful jet

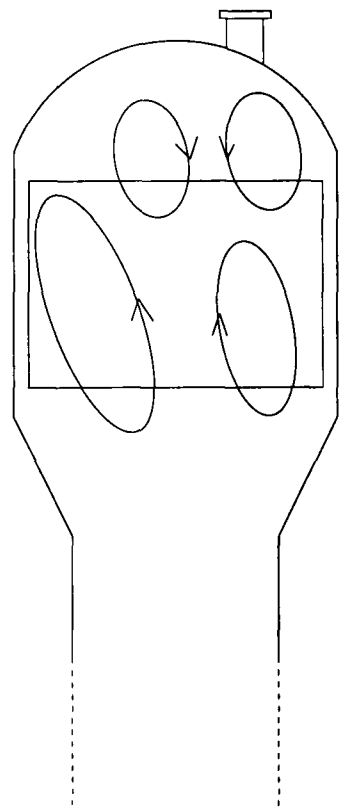

Figure 5.75: Deformation of the recirculation areas by a jet diverging from the centre-line

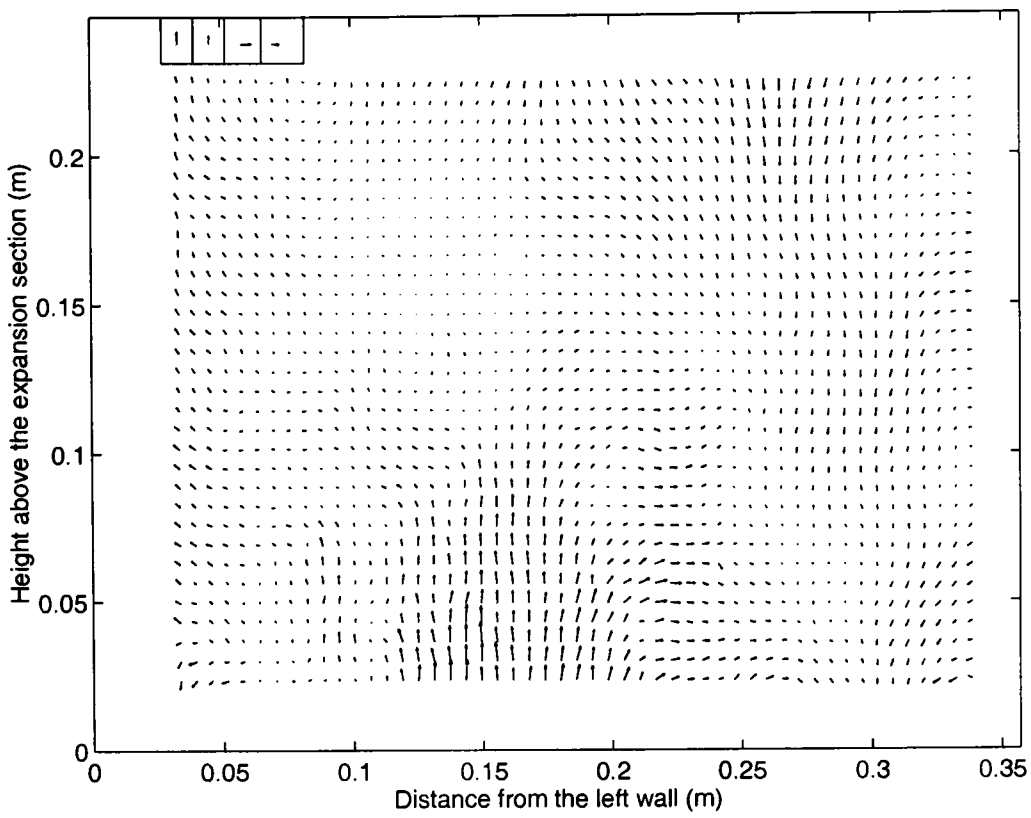

Figure 5.76: Time-averaged vector map over 37 seconds minus the spatial time-averaged velocity (Experiment 2). Velocity vectors in the left upper corner from left to right: 3 cm/s, 2 cm/s, 3 cm/s and 2 cm/s

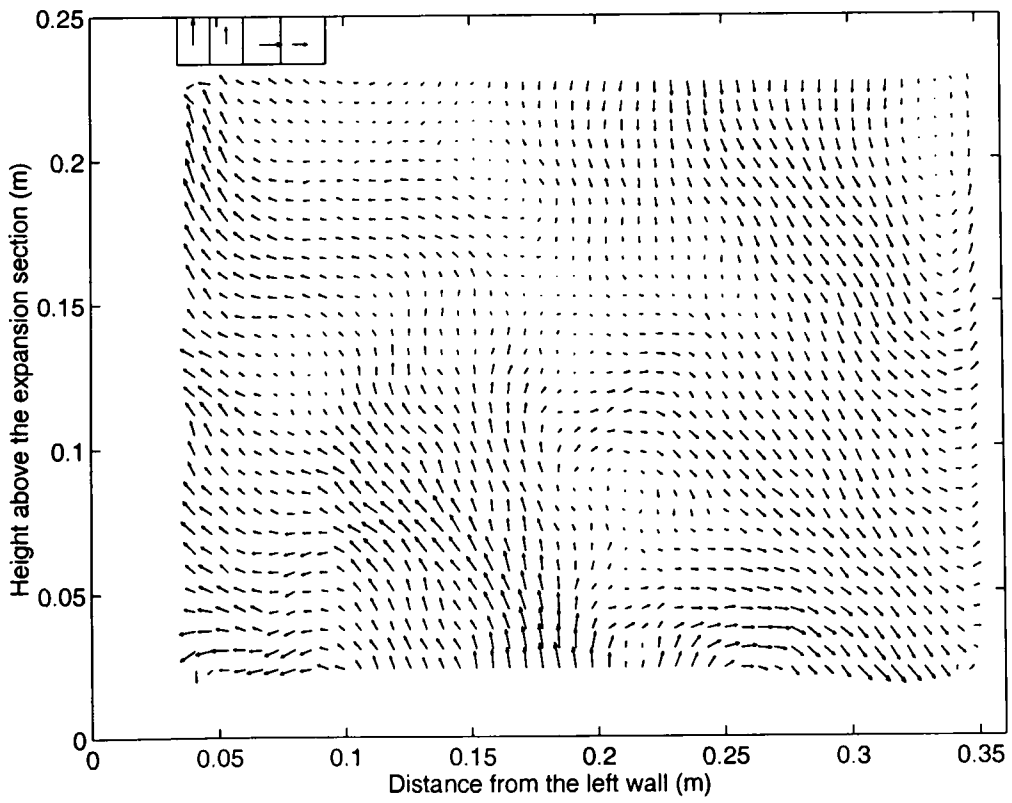

Figure 5.77: Time-averaged vector map over 37 seconds minus the spatial time-averaged velocity (Experiment 3). Velocity vectors in the left upper corner from left to right: 3 cm/s, 2 cm/s, 3 cm/s and 2 cm/s

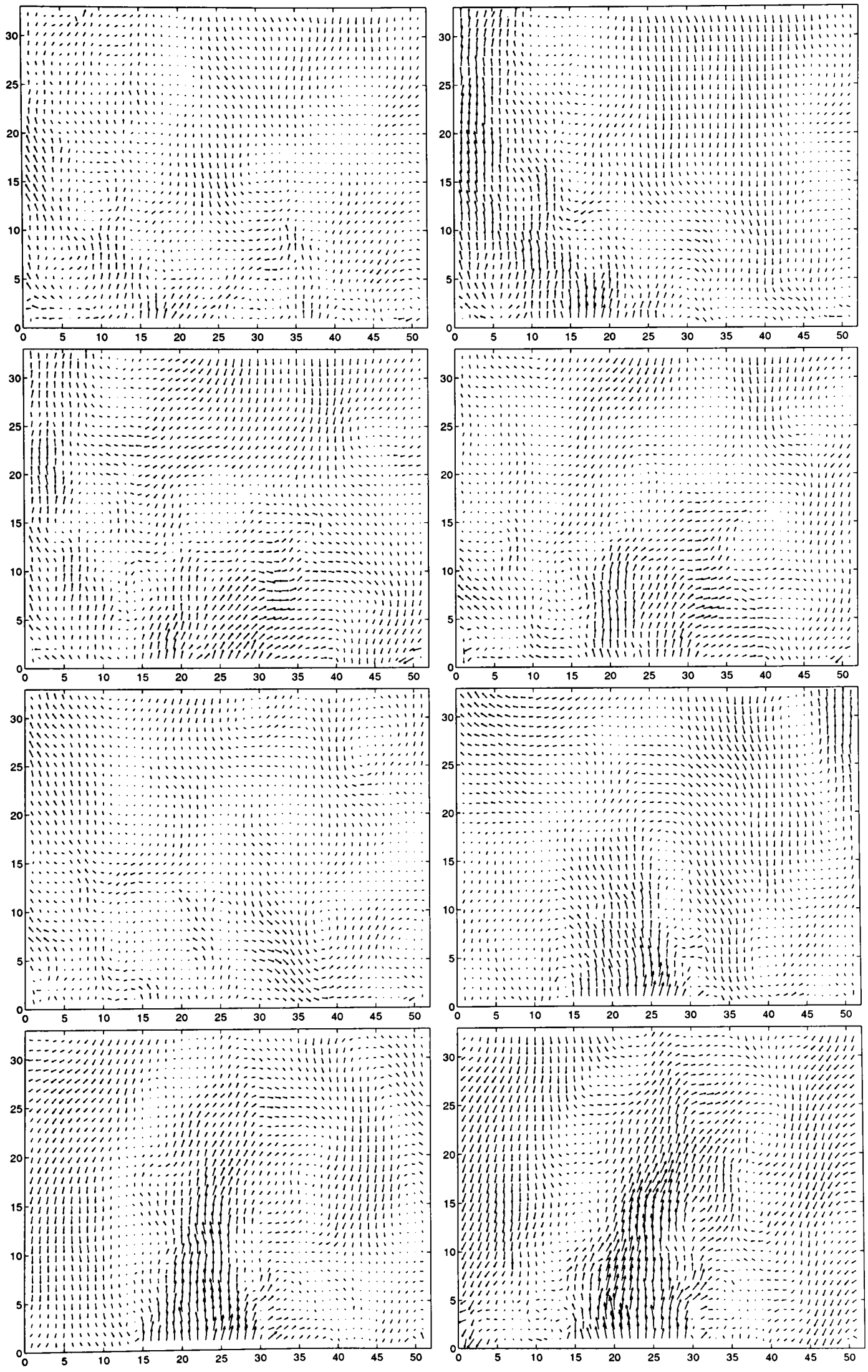

Figure 5.78: Time-averaged vector maps, over 10 seconds, minus the spatial time-averaged velocity (Experiment 2. Frame 1 to 8 are displayed from left to right and from top to bottom)

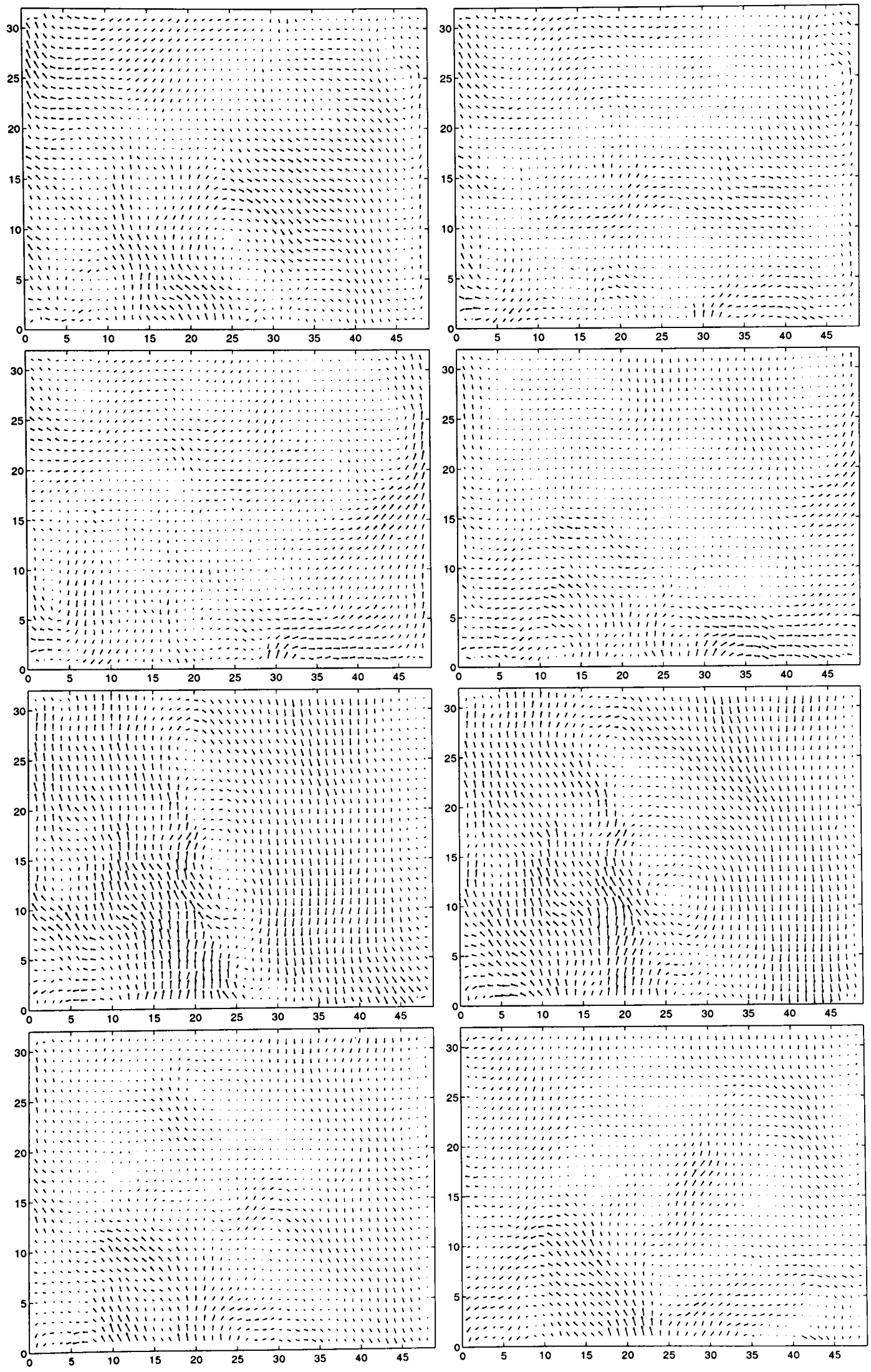

Figure 5.79: Time-averaged vector maps, over 10 seconds, minus the spatial time-averaged velocity (Experiment 3. Frame 1 to 8 are displayed from left to right and from top to bottom)

that the expansion angle may be high enough to permit fibre deposition, promoting fibre growth.

The flow pattern in the expanded section has been analysed by studying instantaneous features of the flow and time-averaged quantities. Instantaneous characteristics indicate the turbulent nature of the flow. Statistical analysis shows that time averaging provides reproducible information. The vertical velocity profile changes with height, having an inverted "U" shape close to the bed surface and a "U" shape at the top of the freeboard. Consequently, the vertical velocity component decreases with height at the bed centre while the opposite occurs near the walls. It is difficult to draw conclusions from the measurements of the horizontal velocity component, since its value is within the experimental error. The flow is characterised by strong fluctuations of the velocity. The spatial correlation coefficients are useful to confirm the nature of the turbulence: non-homogeneous, anisotropic and free-turbulence; they also give an idea of the length scale involved. The average vorticity can be visualised using the vorticity plots. Four recirculation cells have been proposed in this section of the freeboard.

Chapter 6

Investigation of the influence of the superficial gas velocity and geometry of the freeboard on the gas flow pattern

Once the flow pattern in the freeboard was determined at the "working conditions" of the pilot plant (6.3 cm/s superficial velocity, expanded freeboard and off-centre outlet), the influence of different parameters was analysed. Studies using a superficial velocity of 11.5 cm/s, a freeboard without an expansion section (that is, with a straight freeboard) and placing the bed outlet at the centre were carried out to investigate how these factors affect the freeboard flow.

In order to compare the behaviour of gas in the freeboard at the different conditions, instantaneous vector maps will be presented together with the mean velocity profiles and the spatial mean of the time-averaged velocity. Error-bars corresponding to the 95% of confidence have been added to the velocity profiles (calculated using a t-distribution).

6.1 Central outlet

The off-centre outlet was substituted by a central outlet to determine the effect of the outlet location on the gas flow pattern. However, when comparing the two cases, it should be borne in mind that the off-centre outlet was 10 *cm* behind the analysed plane while the central outlet was in the same plane.

6.1.1 Instantaneous flow structures

The instantaneous vector maps showed the same features as the vector maps obtained in the case of the off-centre outlet. Features directly attributable to the location of the outlet were not found.

6.1.2 Statistical description of the flow

Two films of 37 photographs, taken at the same conditions as the off-centre outlet case, were analysed and averaged; they have been labelled as Experiment 4 and Experiment 5 (Table 3.4).

Time-averaged velocity

The time-averaged vector maps corresponding to Experiments 4 and 5 are presented in Figure 6.1 and Figure 6.2, respectively. The vector map corresponding to Experiment 4 displays a central low velocity region, at the top of the freeboard. The average vector map corresponding to Experiment 5 also shows a central low velocity region. This low velocity is as a result of gas travelling fast upwards near the walls. Specially, in Figure 6.2 the velocity is higher on the left hand side than on the right hand side. This behaviour is easily understood when looking at

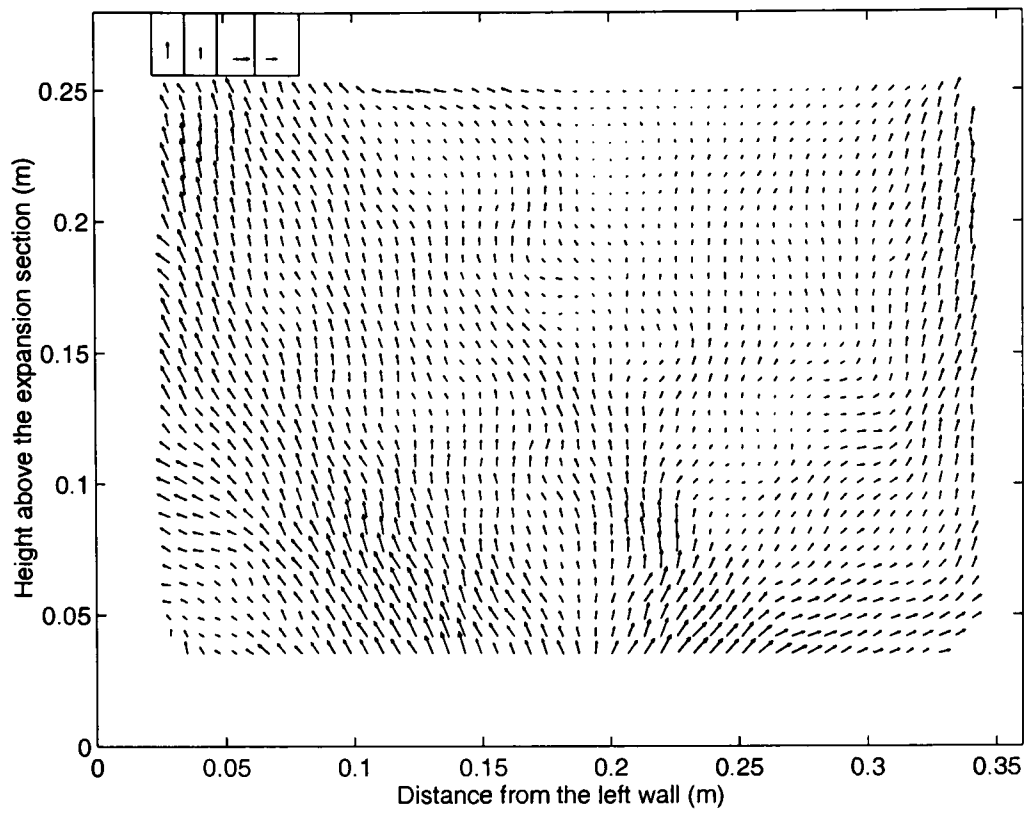

Figure 6.1: Time-averaged vector map over 37 seconds (Experiment 4). Velocity vectors in the left upper corner from left to right: 3 cm/s, 2 cm/s, 3 cm/s and 2 cm/s

the individual vector maps and their circumstances. In Figure 6.3 a large bubble eruption can be seen, ejecting gas towards the left hand side and forcing the gas downwards on the right hand side. This can be seen one second later in Figure 6.4. This eruption was quite powerful (as can be inferred by comparing the magnitude of the velocity vectors with the magnitude of the marker vectors) and influenced the gas flow in the freeboard for a long time (compared to a normal eruption). The influence of the bubble eruption can still be seen five seconds after bubble eruption (Figure 6.5). This violent explosion is consistent with our understanding of the nature of the bubbling phenomenon.

The vertical (v_y) and horizontal (v_x) component of the velocity and the magnitude of the horizontal velocity ($|v_x|$) calculated by spatial averaging over the entire time-averaged vector maps are presented in Table 6.1. The velocities in Experiment 4 are similar to the velocities obtained in the case of the off-centre outlet Table 5.2. However, the velocities in Experiment 5 are lower, perhaps because of the large bubble eruption. It has been observed that a large bubble eruption is followed by very small bubbles. Thirty-seven seconds may not be

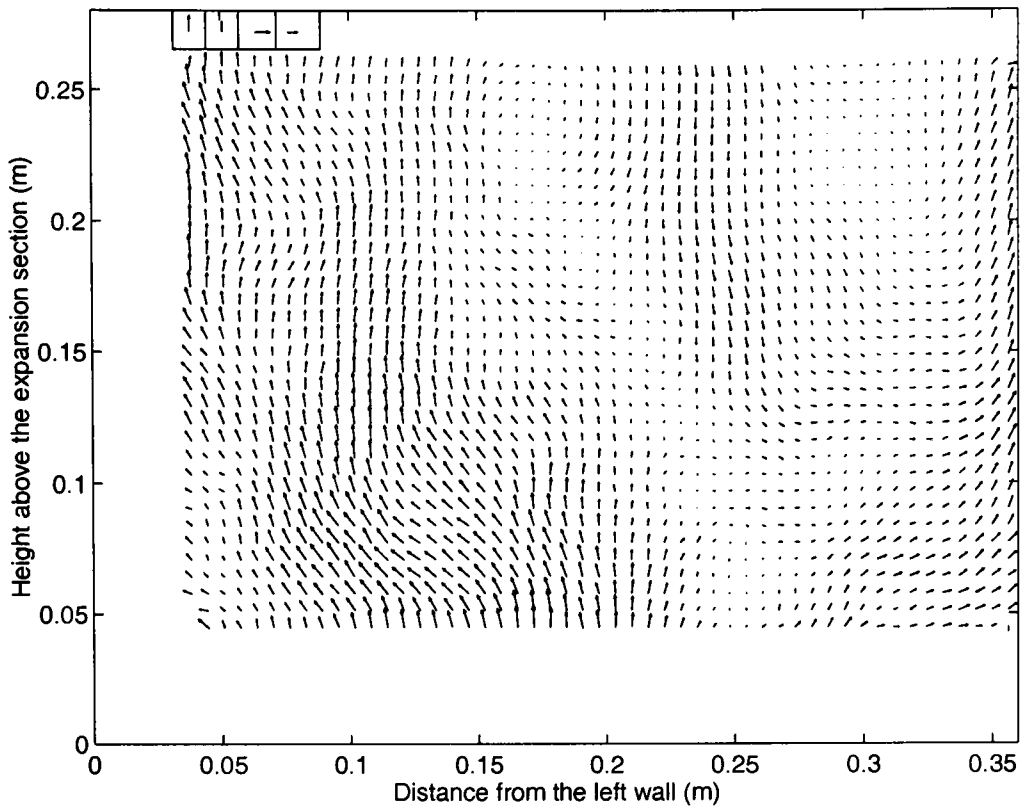

Figure 6.2: Time-averaged vector map over 37 seconds (Experiment 5). Velocity vectors in the left upper corner from left to right: 3 cm/s, 2 cm/s, 3 cm/s and 2 cm/s

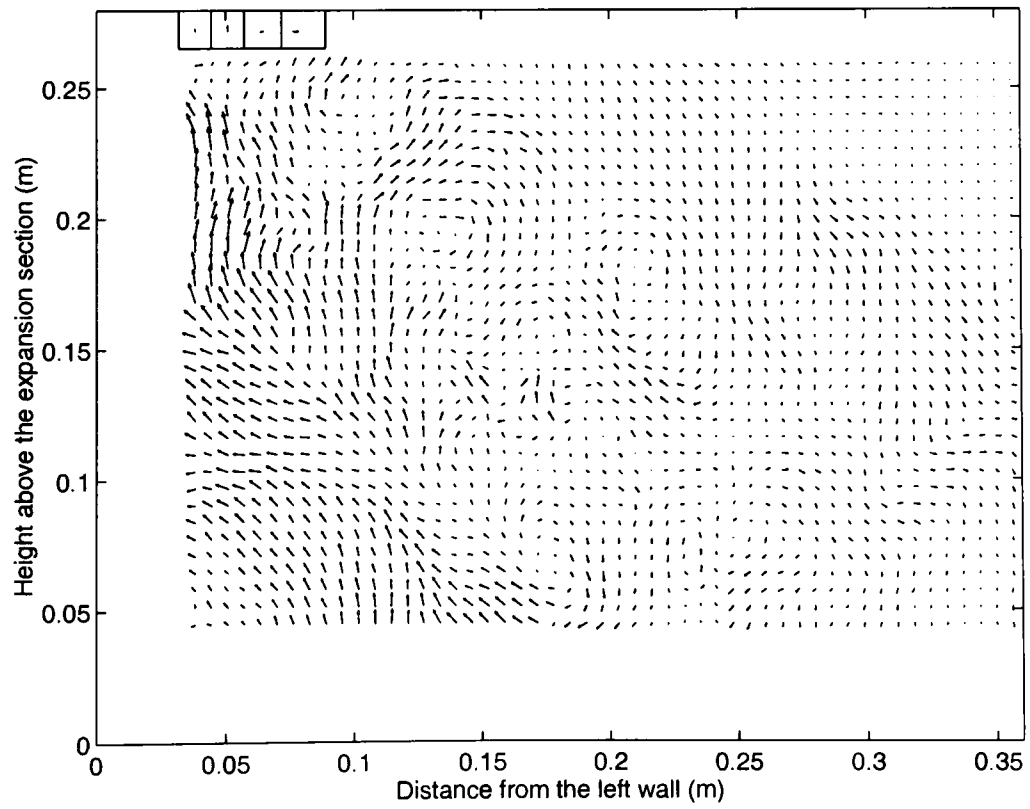

Figure 6.3: Instantaneous vector map (Experiment 5, $t = t_o$ sec). Velocity vectors in the left upper corner from left to right: 4.41 cm/s, 8.82 cm/s, 4.41 cm/s and 8.82 cm/s

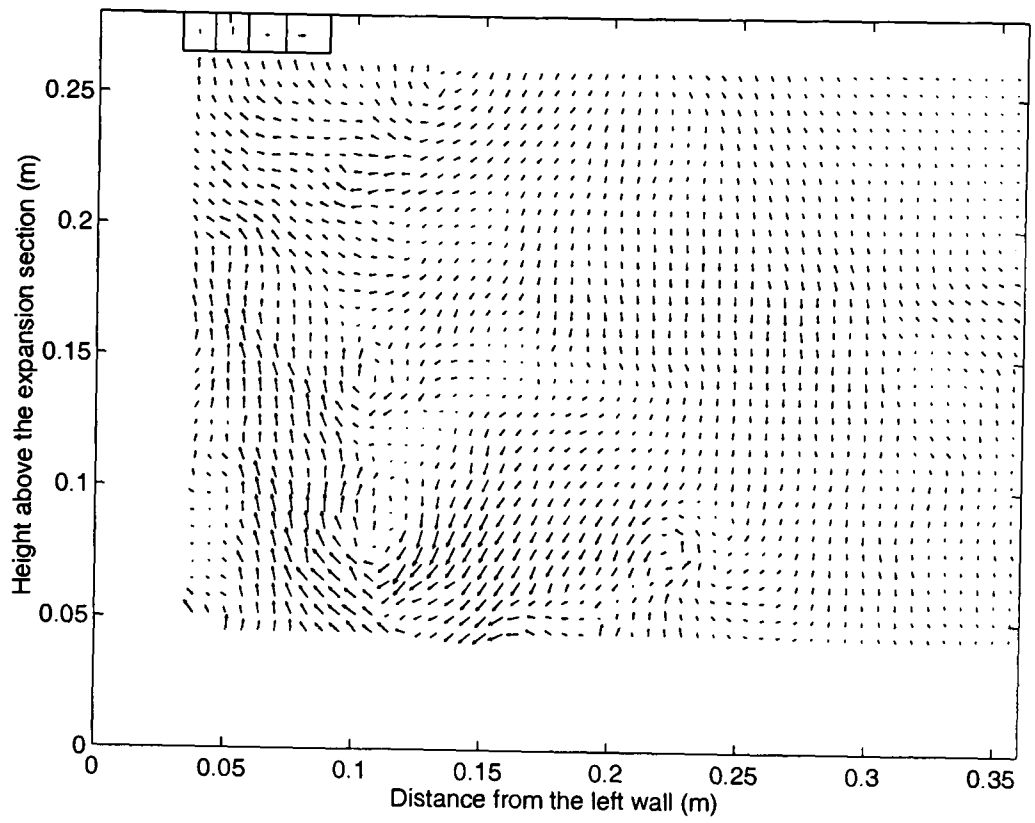

Figure 6.4: Instantaneous vector map (Experiment 5, $t = t_o + 1\ sec$). Velocity vectors in the left upper corner from left to right: 4.41 cm/s, 8.82 cm/s, 4.41 cm/s and 8.82 cm/s

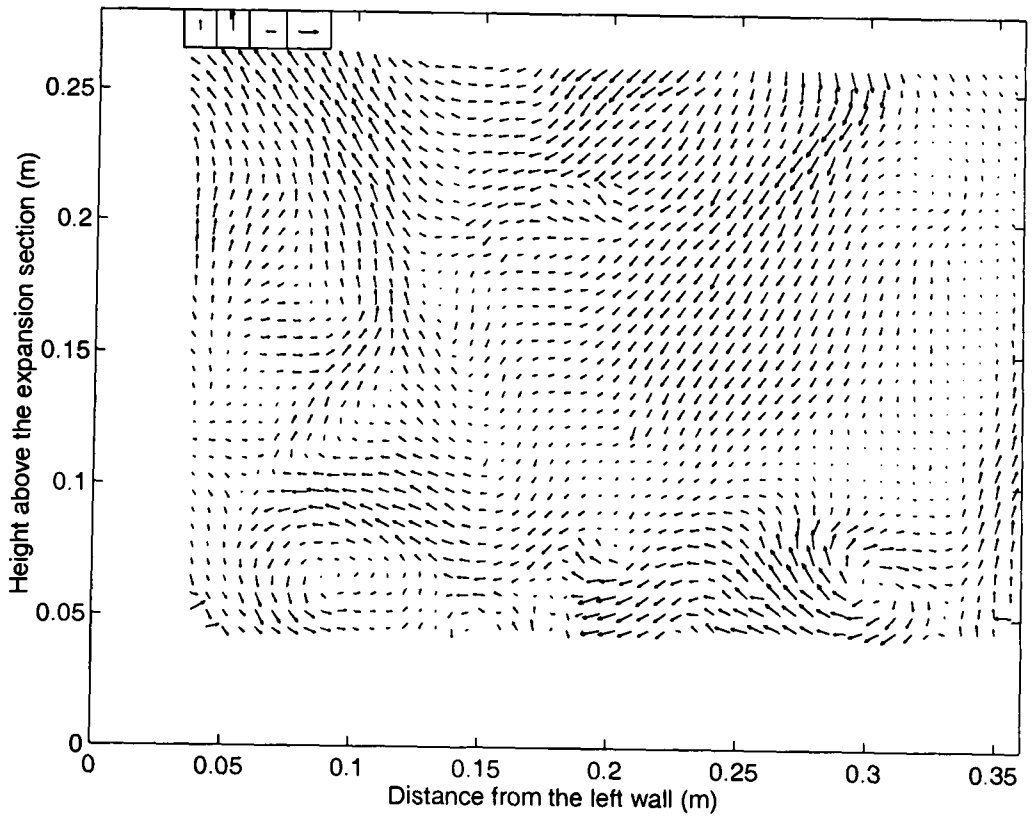

Figure 6.5: Instantaneous vector map (Experiment 5, $t = t_o + 5\ sec$). Velocity vectors in the left upper corner from left to right: 4.41 cm/s, 8.82 cm/s, 4.41 cm/s and 8.82 cm/s

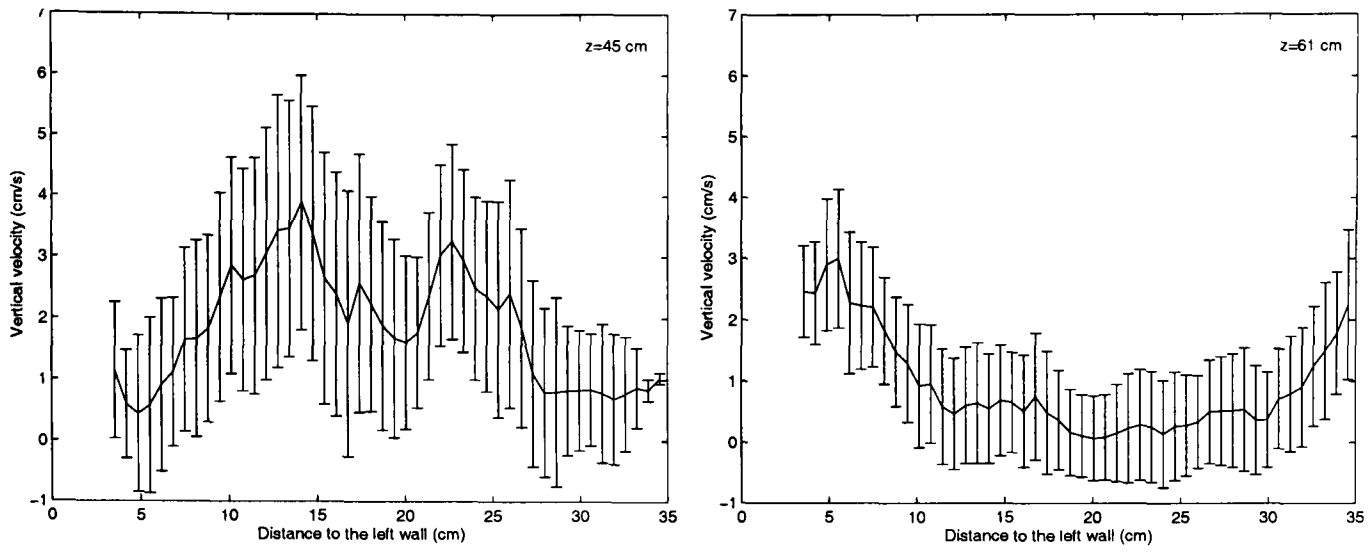

Figure 6.6: Time-averaged vertical velocity profile (Experiment 4)

long enough to average out the effect of the large downward gas movement after bubble eruption.

Experiment number	v_y (cm/s)	Vertical std (cm/s)	v_x (cm/s)	Horizontal std (cm/s)	$\|v_x\|$ (cm/s)
4	1.45	0.25	-0.15	0.13	0.72
5	0.87	0.35	-0.08	0.23	0.60

Table 6.1: Spatial averaged velocity and standard deviation of the time-averaged vector maps

The radial profiles of the time-averaged vertical component of the velocity (Figure 6.6 and 6.7) resemble the profiles obtained for the off-centre outlet (high velocity at the centre of the bed and low velocity near the wall above the bed surface and high velocity near the wall and low velocity at the centre at the top of the expanded region). It was expected that the influence of the central location on the velocity profile close to the outlet ($z = 61\ cm$) would be observed, but no clear indications were found.

The radial profiles of the time-averaged horizontal component of the velocity (Figure 6.8 and 6.9) seem to have central symmetry above the bed surface ($z = 45\ cm$) and they are nearly flat far from the bed surface ($z = 45\ cm$). It should be remembered that the analysed plane is 15 cm below the outlet. Perhaps, this distance is too great to allow for visualisation of any direct influence of the outlet on the flow.

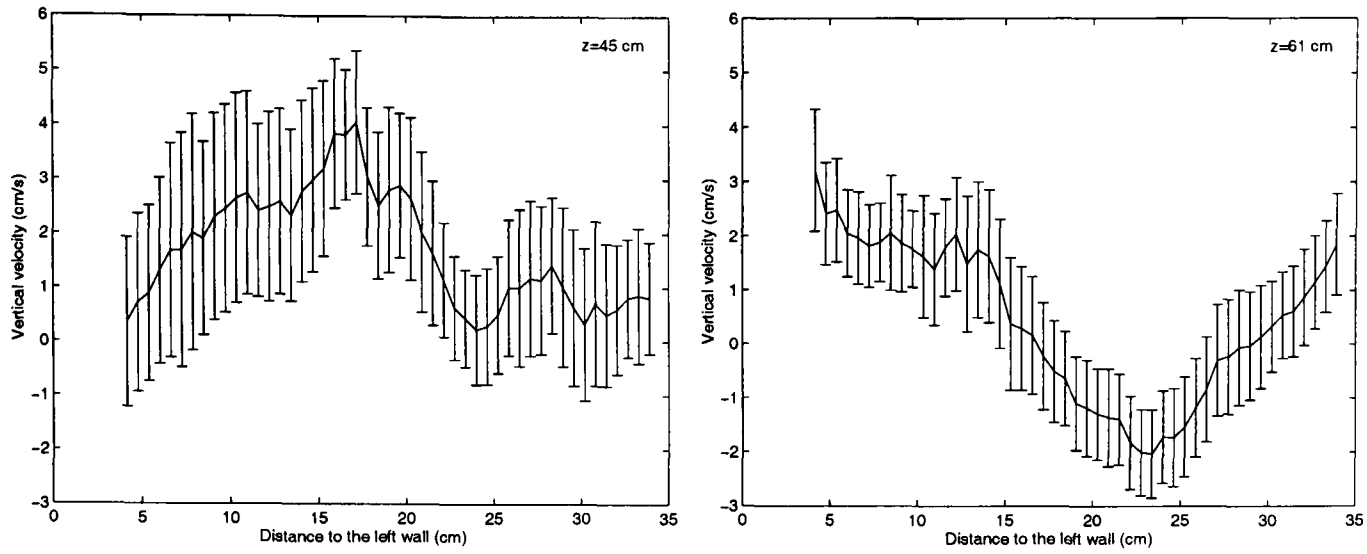

Figure 6.7: Time-averaged vertical velocity profile (Experiment 5)

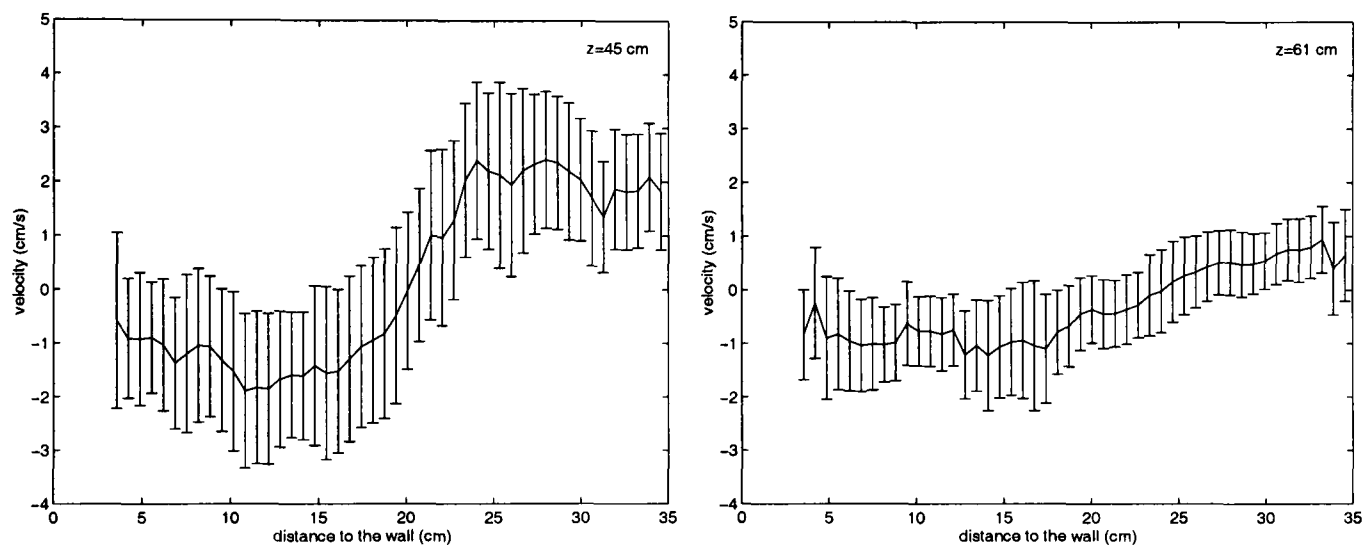

Figure 6.8: Time-averaged horizontal velocity profile (Experiment 4)

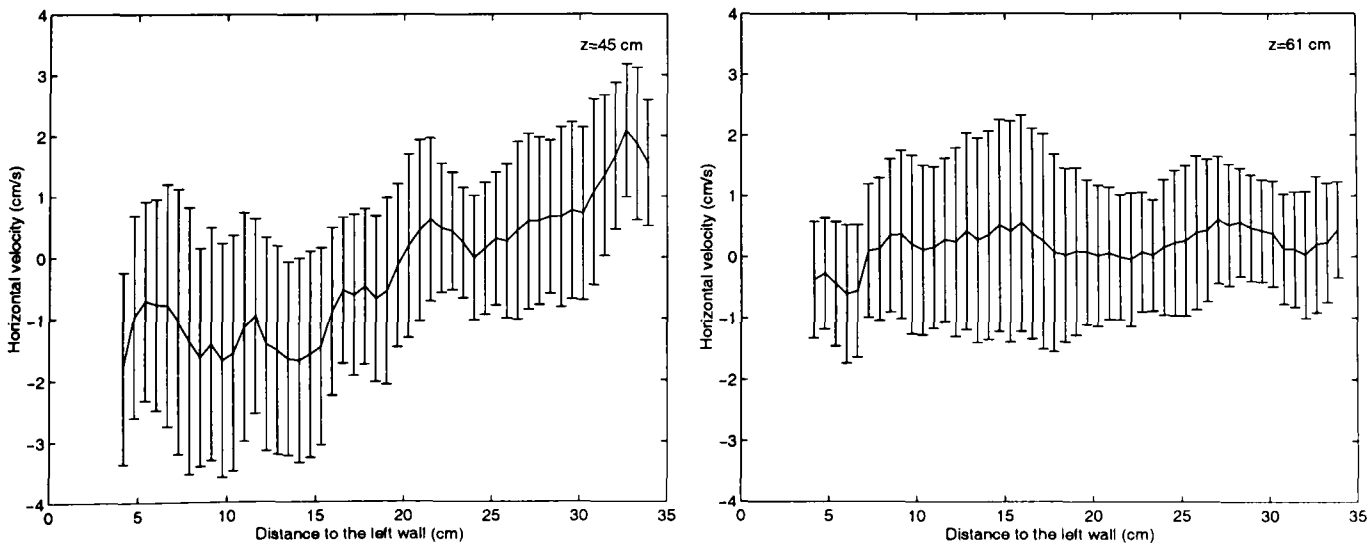

Figure 6.9: Time-averaged horizontal velocity profile (Experiment 5)

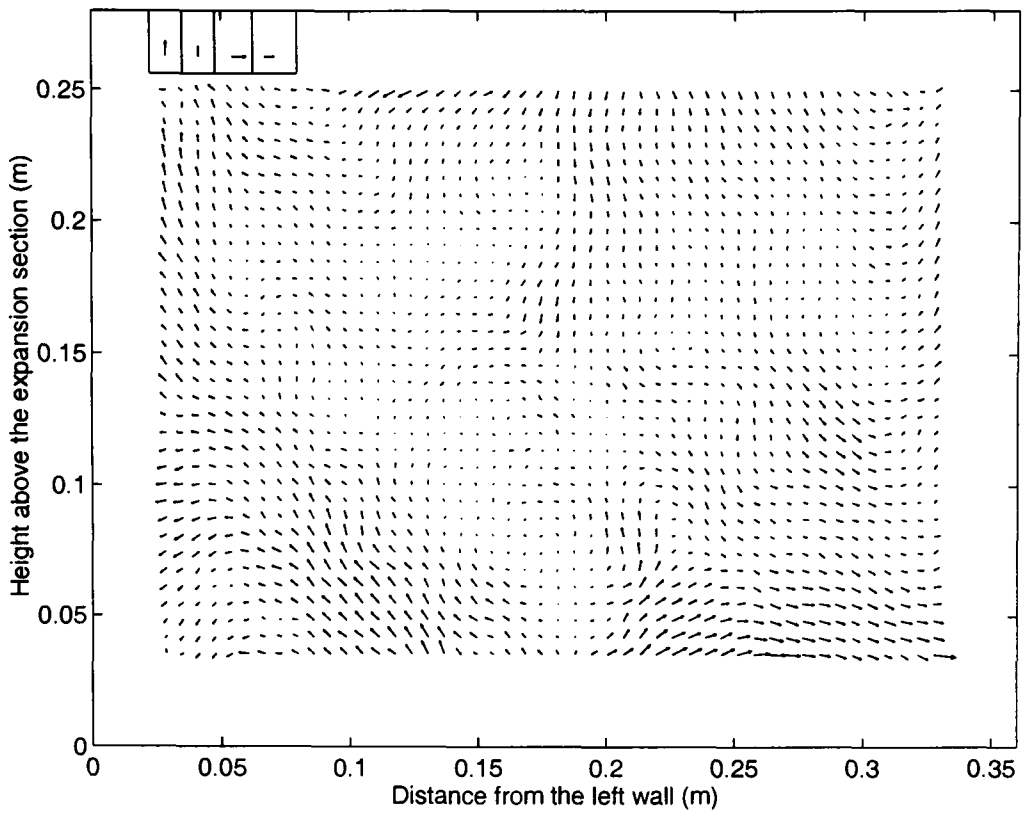

Figure 6.10: Time-averaged vector map over 37 seconds minus the spatial time-averaged velocity (Experiment 4). Velocity vectors in the left upper corner from left to right: 3 cm/s, 2 cm/s, 3 cm/s and 2 cm/s

Secondary structure of the flow

The time-averaged vector maps (Figures 6.1 and 6.2) minus the spatial time-averaged velocity are presented in Figures 6.10 and 6.11, for Experiments 4 and 5, respectively. Four recirculation areas, as in the case of Figures 5.71, 5.76 and 5.77, can be seen. In Figure 6.10 the lower recirculation areas are small. This agrees with the structures presented in the time-averaged vector maps, over 10 seconds, minus the spatial time-averaged velocity, where weak jets are seen (Figure 6.12).

In Figure 6.11 the recirculation areas are distorted due to the presence of powerful jets near the wall (Figure 6.13 Frames 6 and 7).

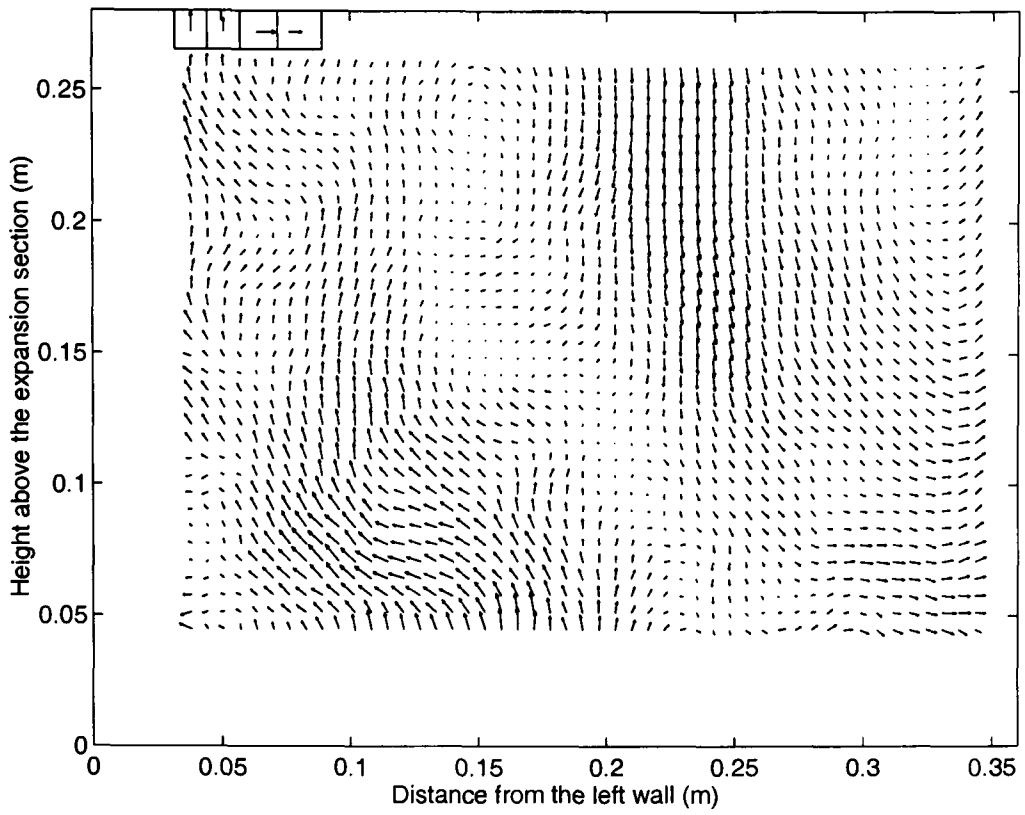

Figure 6.11: Time-averaged vector map over 37 seconds minus the spatial time-averaged velocity (Experiment 5). Velocity vectors in the left upper corner from left to right: 3 cm/s, 2 cm/s, 3 cm/s and 2 cm/s

6.2 Higher gas velocity

An increase of the superficial gas velocity leads to an increase in the size of the bubbles as well as in the bubble velocity and frequency. Consequently, the bubble eruptions are more violent and sand particles are ejected into the freeboard more often than at lower velocity. PIV has the potential to analyse two phase flow. Preliminary studies of two-phase flow were done by Hind *et al.* [126] and McCluskey *et al.* [127]; the two phases were separated and analysed individually. However, more work is required to reduce the cross-talk between the two-phases. Thus, in the present case, the velocity of the sand particles could not be measured.

6.2.1 Instantaneous flow structures

The instantaneous flow structures do not differ qualitatively from the structures found at lower velocity. However, the more violent bubble explosions gave rise

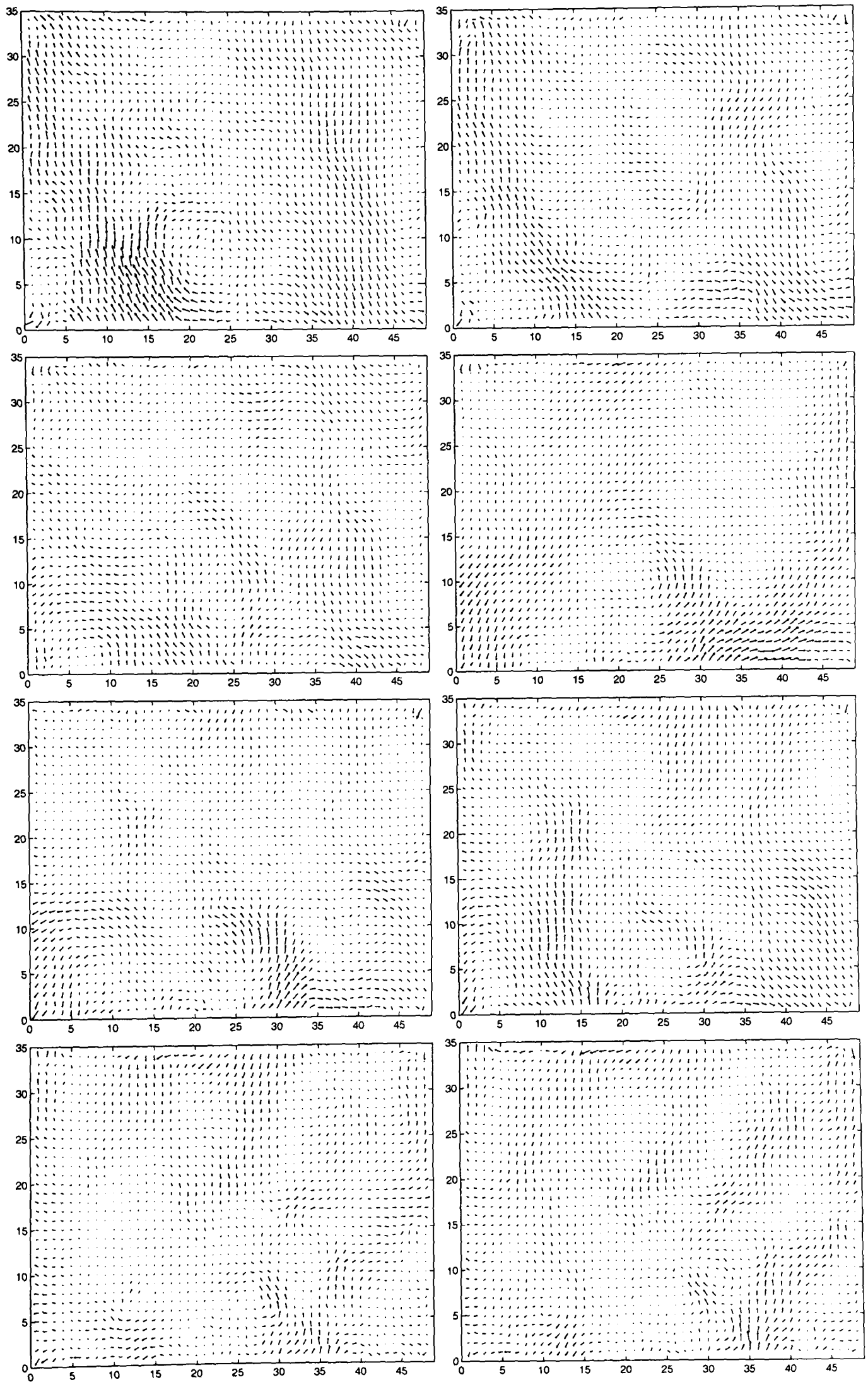

Figure 6.12: Time-averaged vector maps, over 10 seconds, minus the spatial time averaged velocity (Experiment 4. Frame 1 to 8 are displayed from left to right and top to bottom

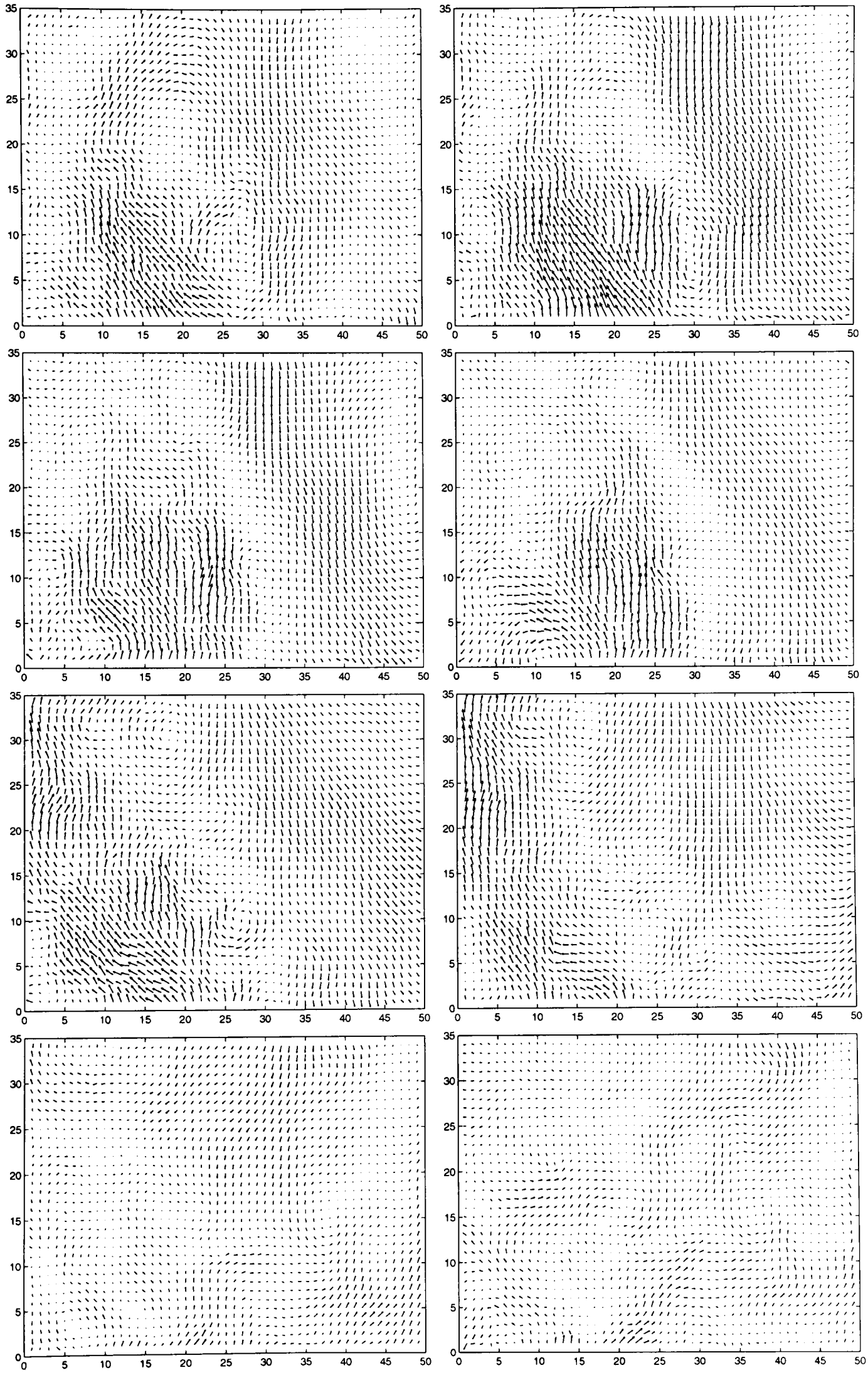

Figure 6.13: Time-averaged vector maps, over 10 seconds, minus the spatial time averaged velocity (Experiment 5. Frame 1 to 8 are displayed from left to right and top to bottom)

to stronger jets and gas velocities and also gave vortices less time to grow in the freeboard. A few vector maps will be presented here to demonstrate the similar behaviour of the gas at the two studied velocities. Figures 6.14 and 6.15 show a central jet, generated by an erupting bubble, with eddies in the interface between the jet and the low velocity region. Figures 6.16 and 6.17 present the ascending gas describing a tortuous path; not even at high velocity does the gas ascend in a straight line. Figures 6.18 and 6.19 display two jets on the right and left hand side, respectively and gas going downwards on the other side. Figure 6.20 corresponds to two jets with a central region of low velocity gas. In Figures 6.21 and 6.22 the gas going downward can be seen interacting with structures remaining from previous eruptions. The gas moves downwards surprisingly fast, because a higher superficial velocity produces larger and faster bubbles, thus the return of the bed surface drags gas faster with it. Figure 6.23 displays downwards gas meeting gas travelling upwards. Figure 6.24 corresponds to a moment after bubble eruption and just before the next bubble arrival, presenting the typical structure remaining after bubble eruption.

Figure 6.25 is an example of a moment when sand was ejected into the freeboard. The sand velocity could not be measured. The left hand side of the vector map is full of spurious vectors due to the presence of sand that has been ejected by a violent erupting bubble. As has been seen in Chapter 4 there are a series of requirements that need to be fulfilled to obtain a successful PIV measurement. Among them are particle light scatter, size, shape and displacement. Since the seeding particles do not have the same features and do not move at the same velocity as the sand, both velocities (sand and gas, representing by seeding particles) could not be measured simultaneously.

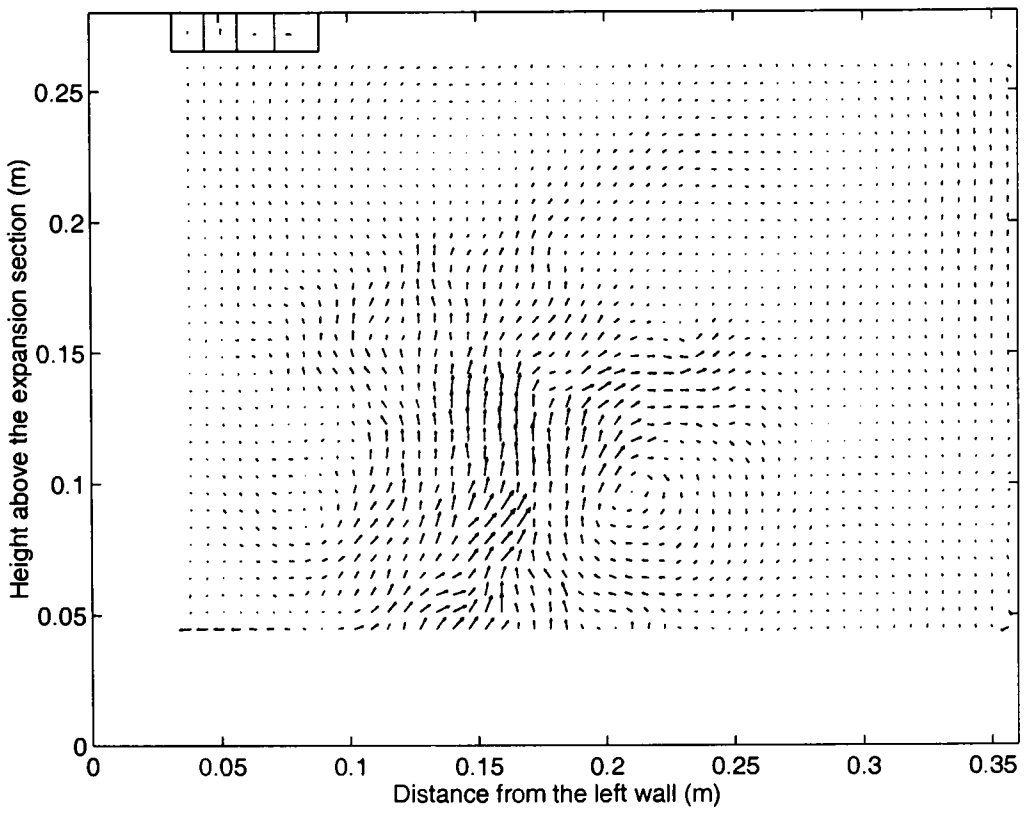

Figure 6.14: Instantaneous vector map. Velocity vectors in the left upper corner from left to right: 4.41 cm/s, 8.82 cm/s, 4.41 cm/s and 8.82 cm/s

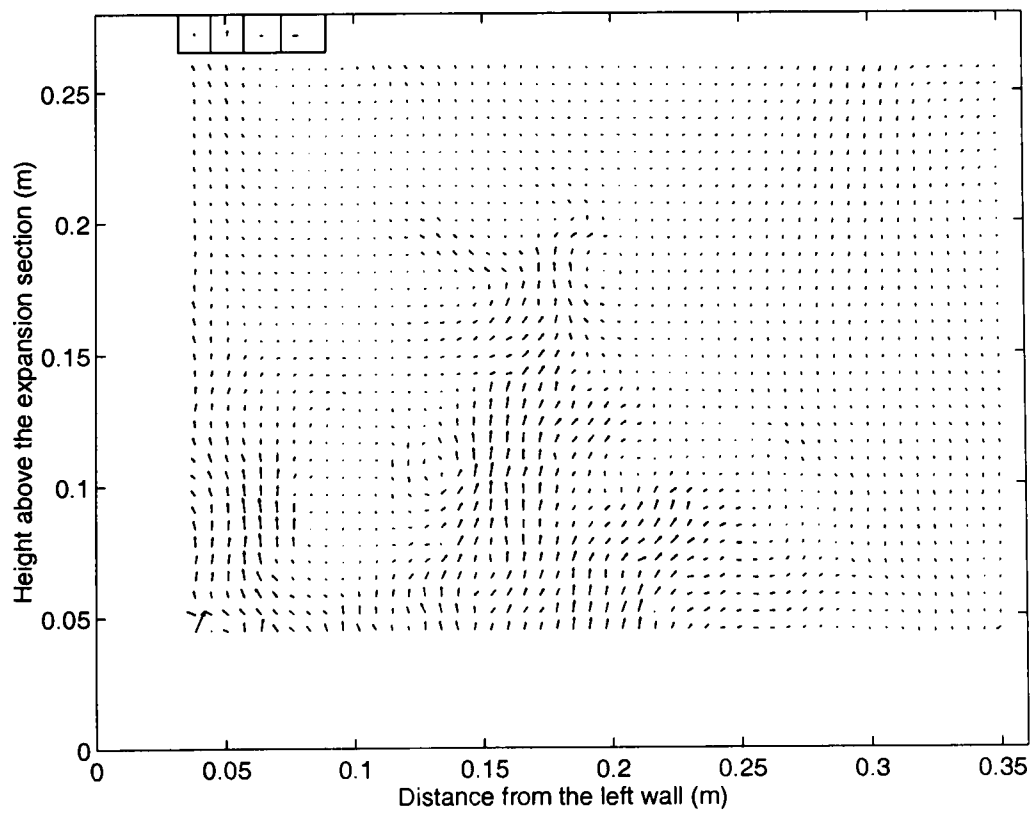

Figure 6.15: Instantaneous vector map. Velocity vectors in the left upper corner from left to right: 4.41 cm/s, 8.82 cm/s, 4.41 cm/s and 8.82 cm/s

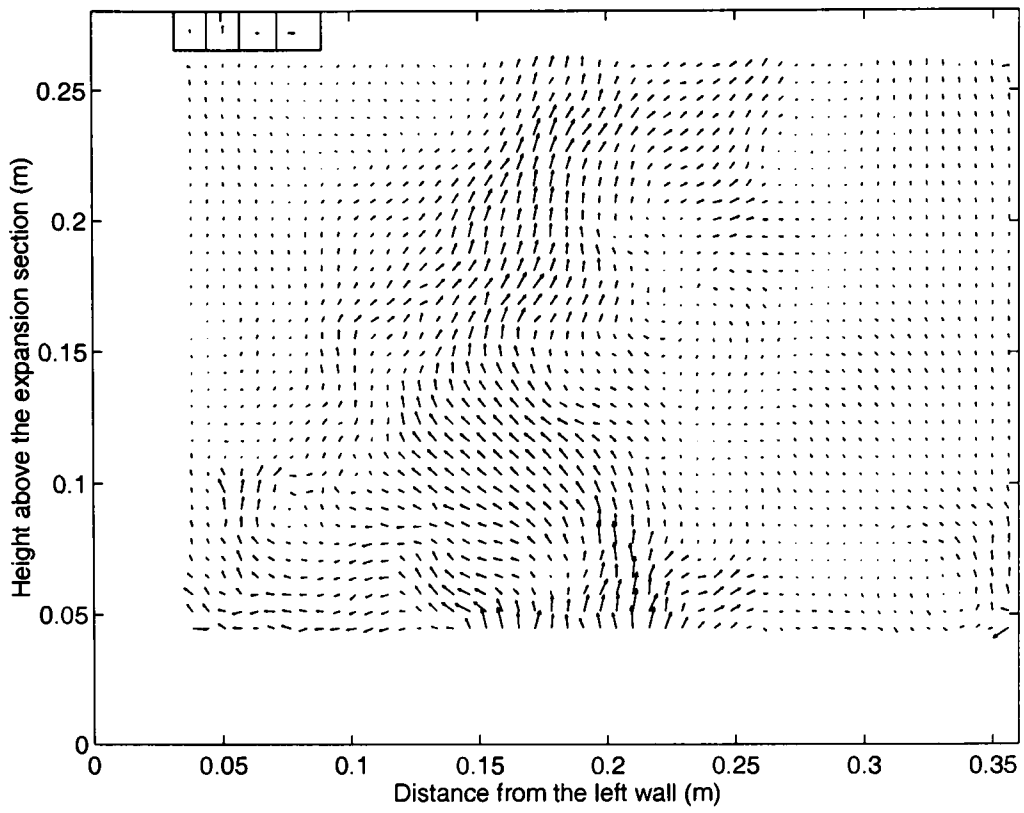

Figure 6.16: Instantaneous vector map. Velocity vectors in the left upper corner from left to right: 4.41 cm/s, 8.82 cm/s, 4.41 cm/s and 8.82 cm/s

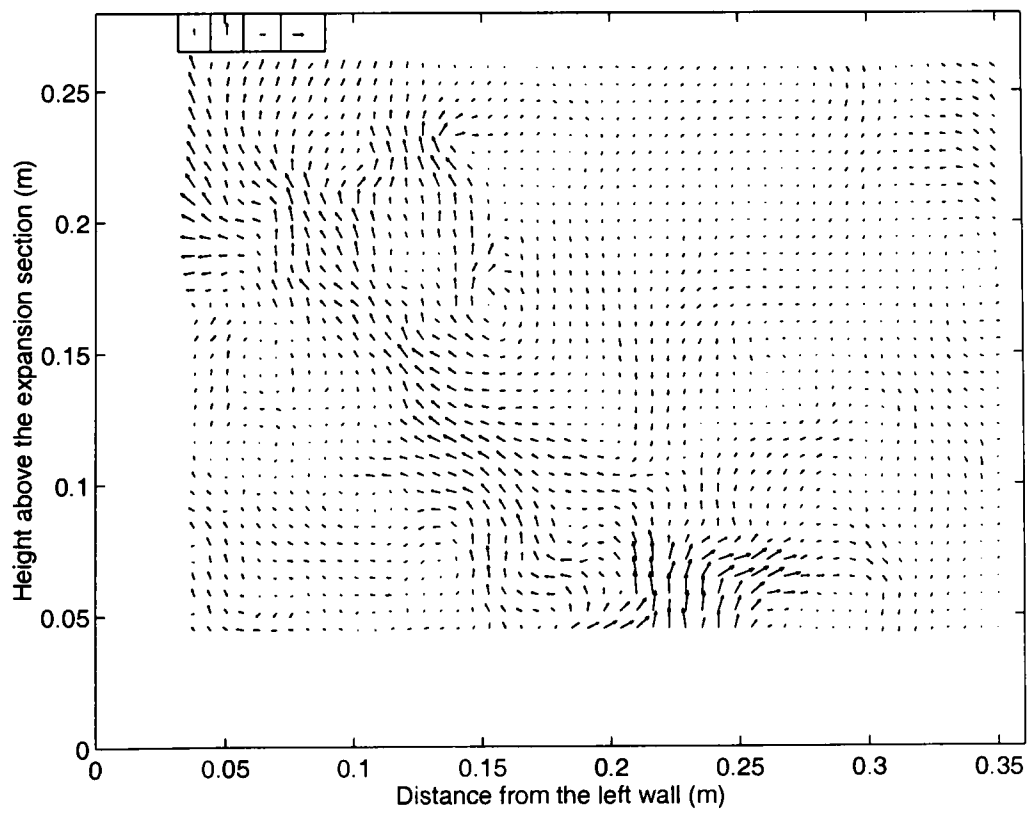

Figure 6.17: Instantaneous vector map. Velocity vectors in the left upper corner from left to right: 4.41 cm/s, 8.82 cm/s, 4.41 cm/s and 8.82 cm/s

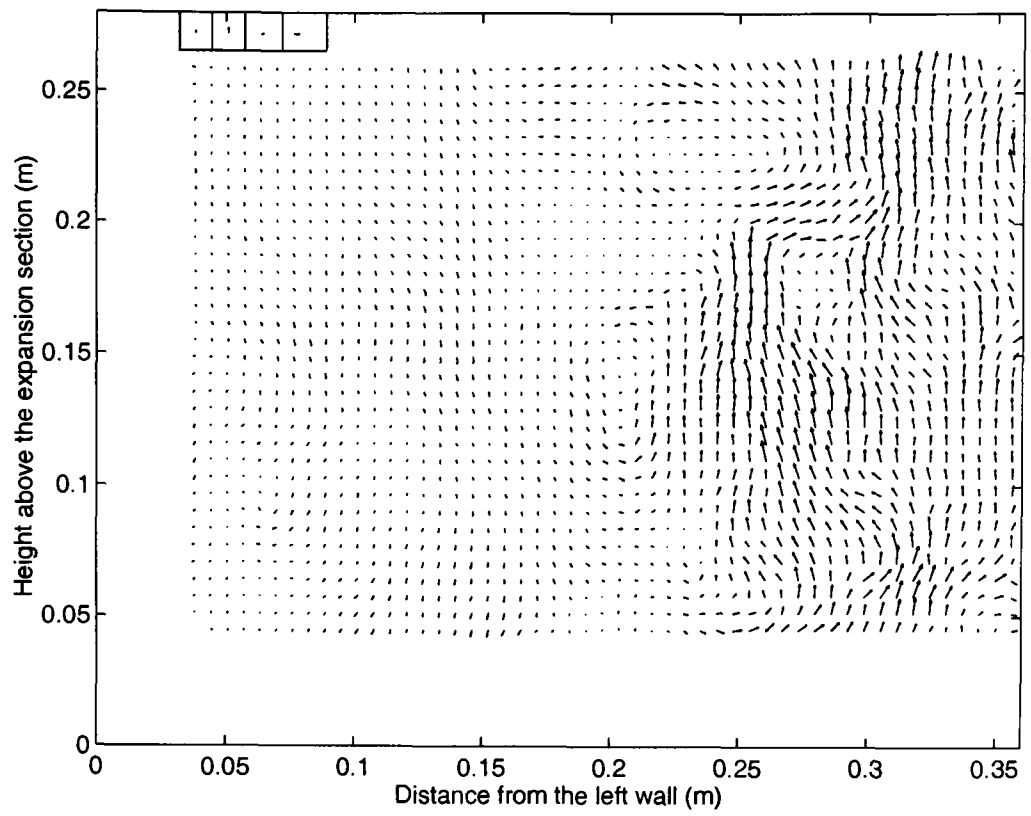

Figure 6.18: Instantaneous vector map. Velocity vectors in the left upper corner from left to right: 4.41 cm/s, 8.82 cm/s, 4.41 cm/s and 8.82 cm/s

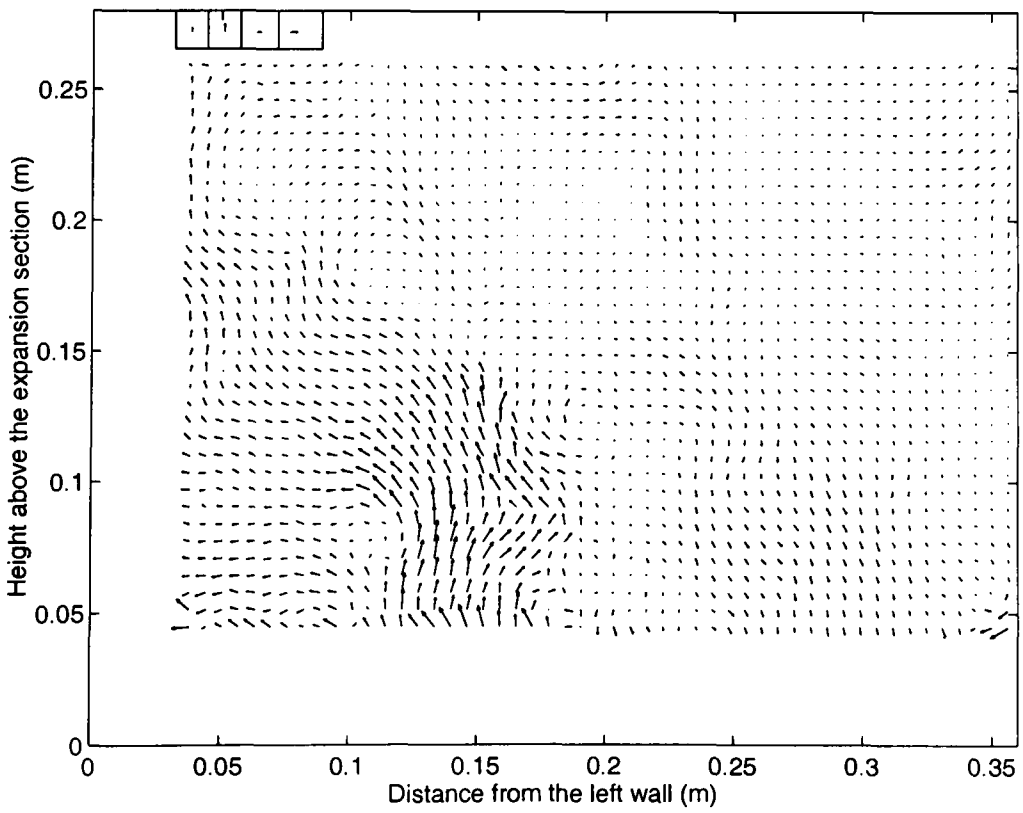

Figure 6.19: Instantaneous vector map. Velocity vectors in the left upper corner from left to right: 4.41 cm/s, 8.82 cm/s, 4.41 cm/s and 8.82 cm/s

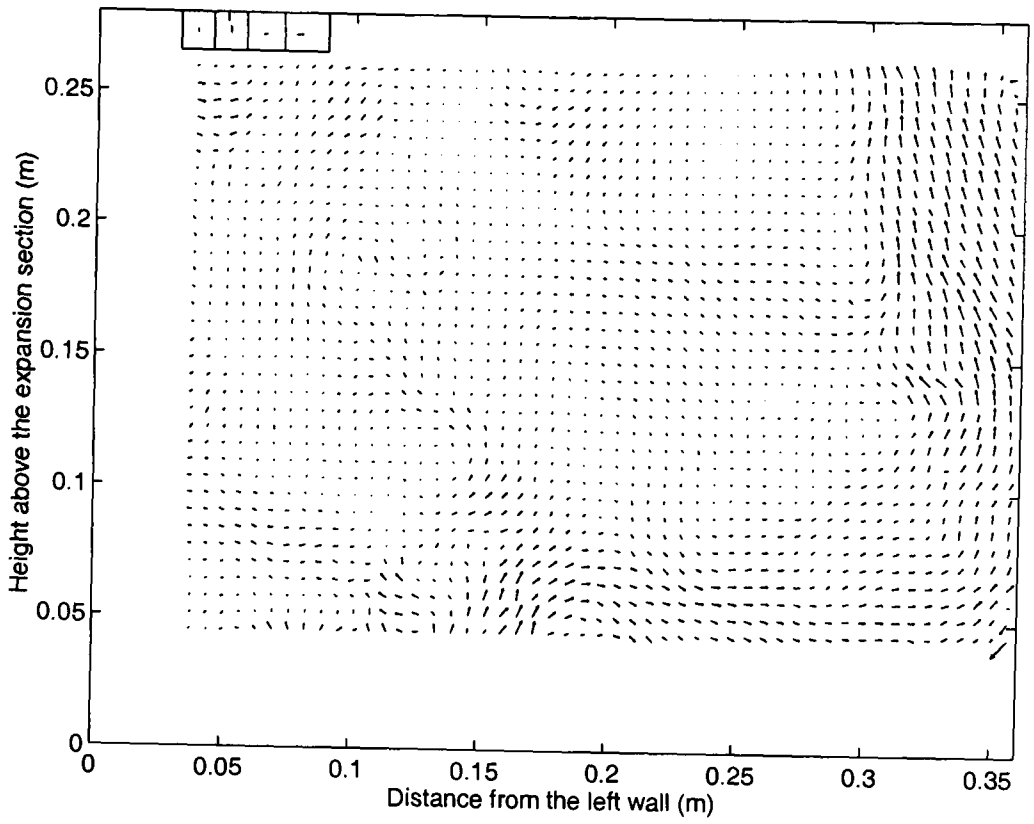

Figure 6.20: Instantaneous vector map. Velocity vectors in the left upper corner from left to right: 4.41 cm/s, 8.82 cm/s, 4.41 cm/s and 8.82 cm/s

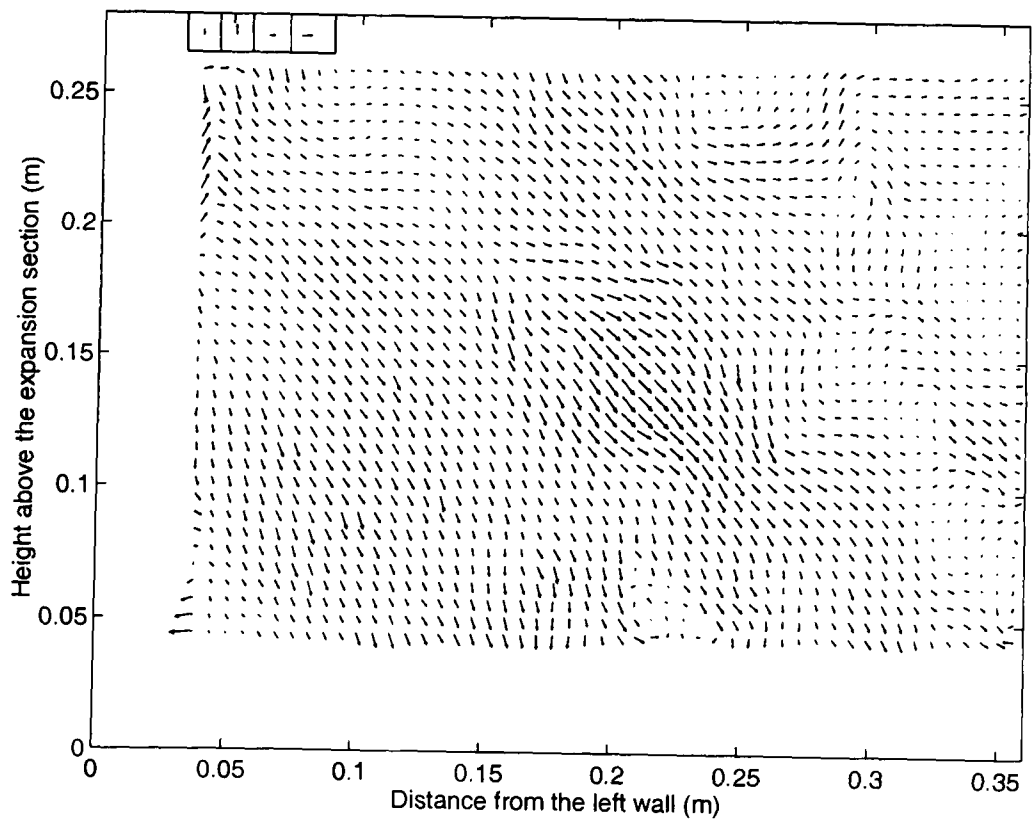

Figure 6.21: Instantaneous vector map. Velocity vectors in the left upper corner from left to right: 4.41 cm/s, 8.82 cm/s, 4.41 cm/s and 8.82 cm/s

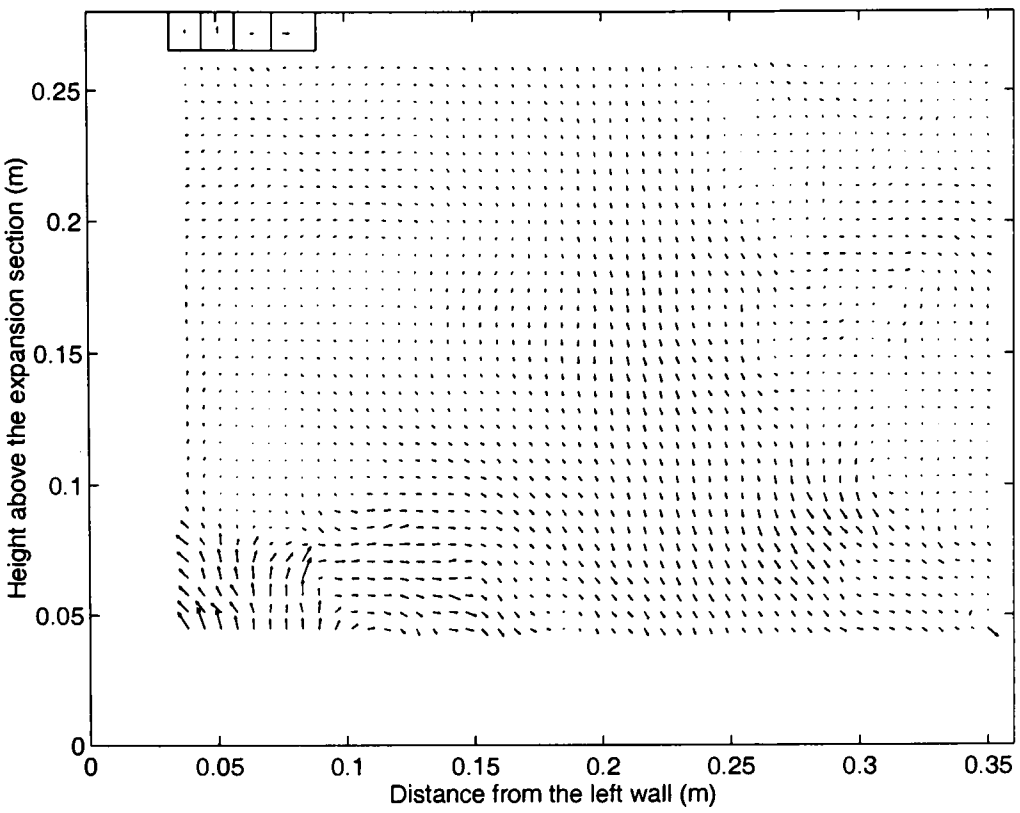

Figure 6.22: Instantaneous vector map. Velocity vectors in the left upper corner from left to right: 4.41 cm/s, 8.82 cm/s, 4.41 cm/s and 8.82 cm/s

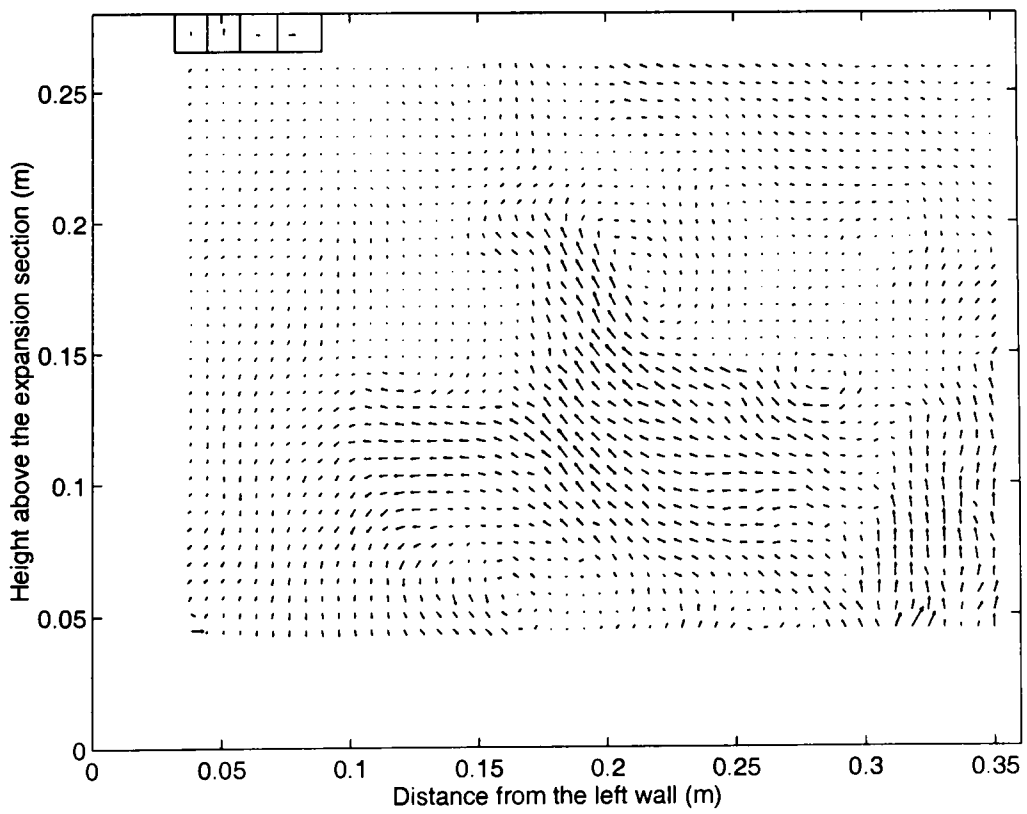

Figure 6.23: Instantaneous vector map. Velocity vectors in the left upper corner from left to right: 4.41 cm/s, 8.82 cm/s, 4.41 cm/s and 8.82 cm/s

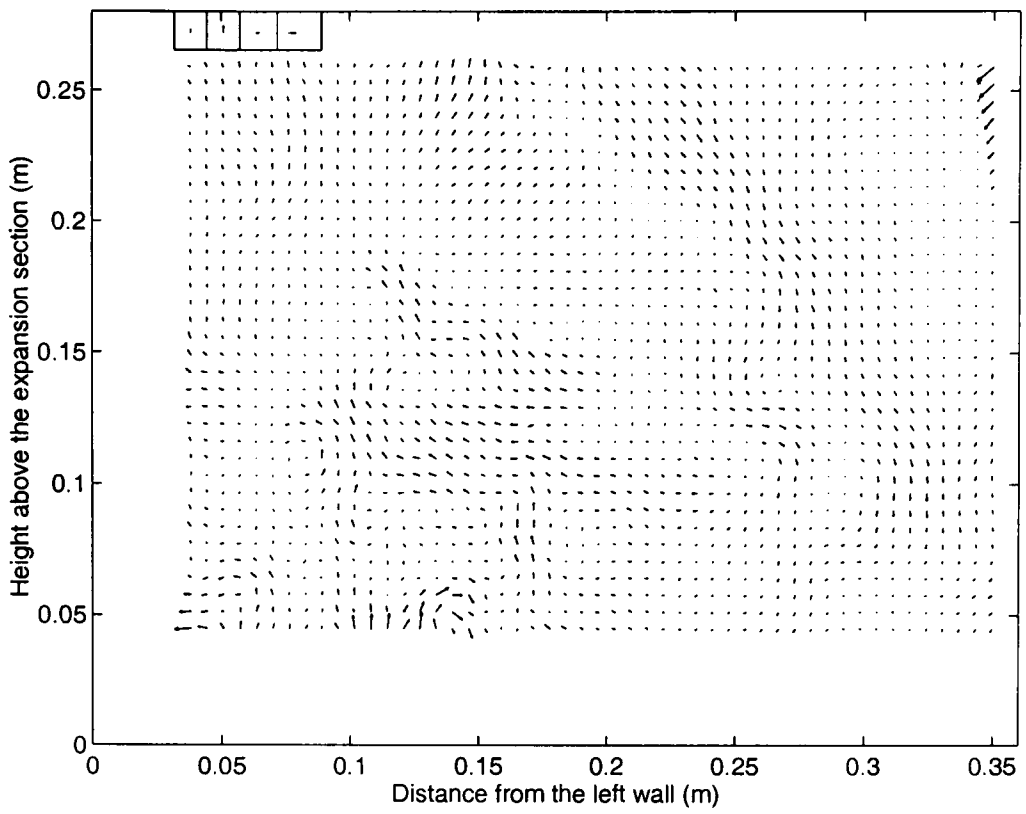

Figure 6.24: Instantaneous vector map. Velocity vectors in the left upper corner from left to right: 4.41 cm/s, 8.82 cm/s, 4.41 cm/s and 8.82 cm/s

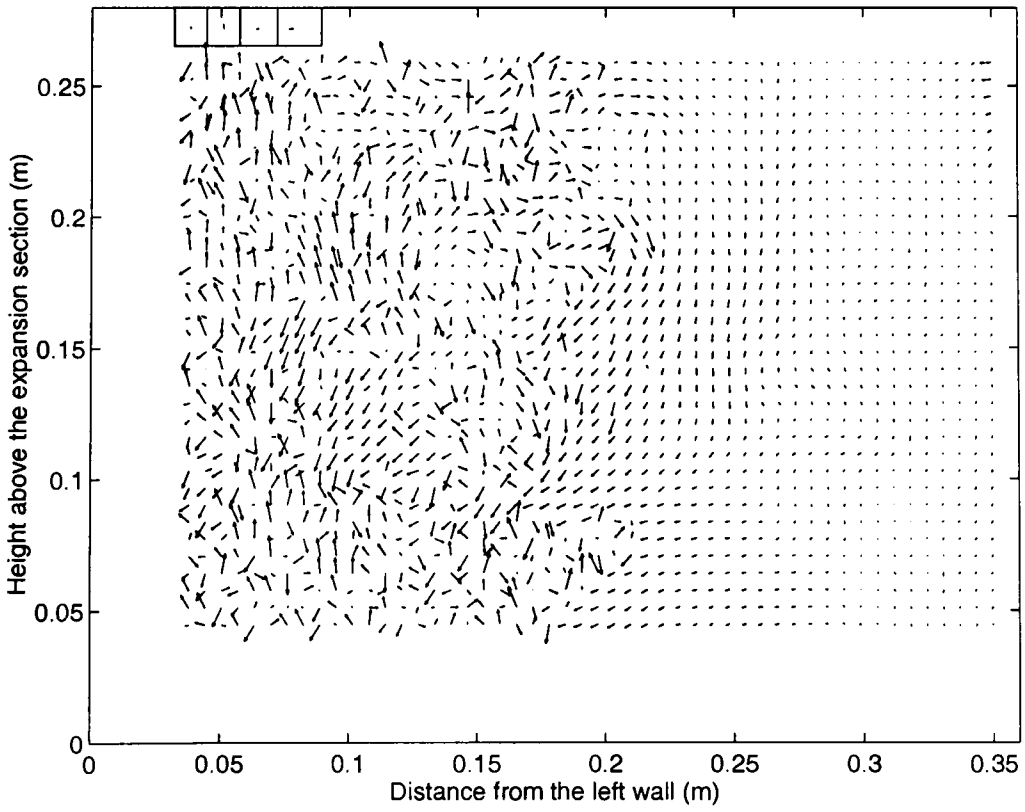

Figure 6.25: Instantaneous vector map. Velocity vectors in the left upper corner from left to right: 4.41 cm/s, 8.82 cm/s, 4.41 cm/s and 8.82 cm/s

6.2.2 Statistical description of the flow

Two experiments were carried out at the same superficial velocity (11.5 cm/s). A central outlet was used in Experiment 6 and an off-centre outlet in Experiment 7; the rest of the conditions were similar for the two cases.

Time-averaged velocity

The gas time-averaged vector maps (Figures 6.26 and 6.27) show a tendency to have a higher velocity near the bed surface. However, there is no clear high velocity region at the centre of the freeboard as in the case of the lower superficial velocity (see Section 5.3.2). The reproducibility of the experiments is not as good as for the lower velocity, due to the nature of the flow rather than the performance of the technique. Figure 6.26 shows a region of low velocity just above the bed surface, on the left hand side. Figures 6.26 and 6.27 have a low velocity region in the centre, slightly towards the right hand side, from the centre of the freeboard to close to the end of the freeboard. They also have high velocity close to the wall; in one case (Figure 6.26) the high velocity is on the right hand side and in the other case on the left hand side (Figure 6.27), indicating that high velocity regions can be either side.

The vertical (v_y) and horizontal (v_x) component of the velocity and the magnitude of horizontal velocity ($|v_x|$) calculated by spatial averaging over the entire time-averaged vector maps are presented in Table 6.2. The values of the two experiments are very close. The vertical component of the velocity is higher than at the working conditions of the pilot plant (See Table 5.2). However, the increase in the vertical velocity component is not directly proportional to the increase of the gas flowrate; the averaged vertical velocity in the freeboard increases less than the superficial gas velocity in the bed. This could be explained by the three-dimensional nature of the flow and the out-of-plane effect. The horizontal

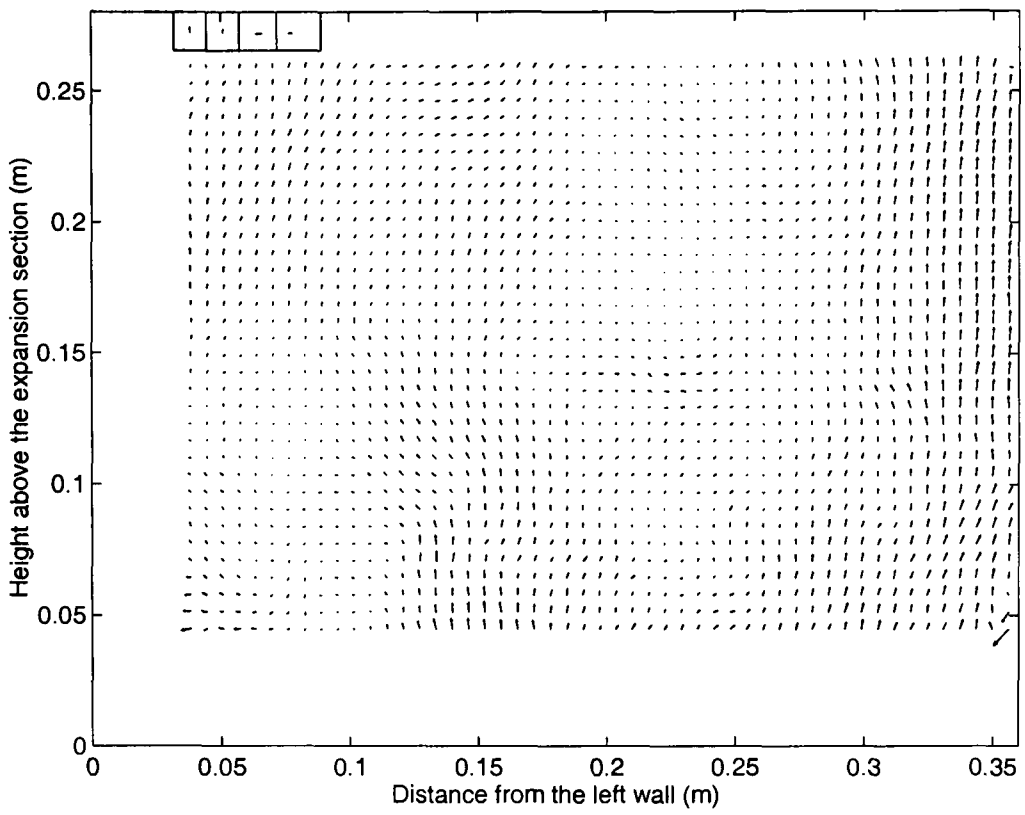

Figure 6.26: Time-averaged vector map over 37 seconds (Experiment 6). Velocity vectors in the left upper corner from left to right: 3 cm/s, 2 cm/s, 3 cm/s and 2 cm/s

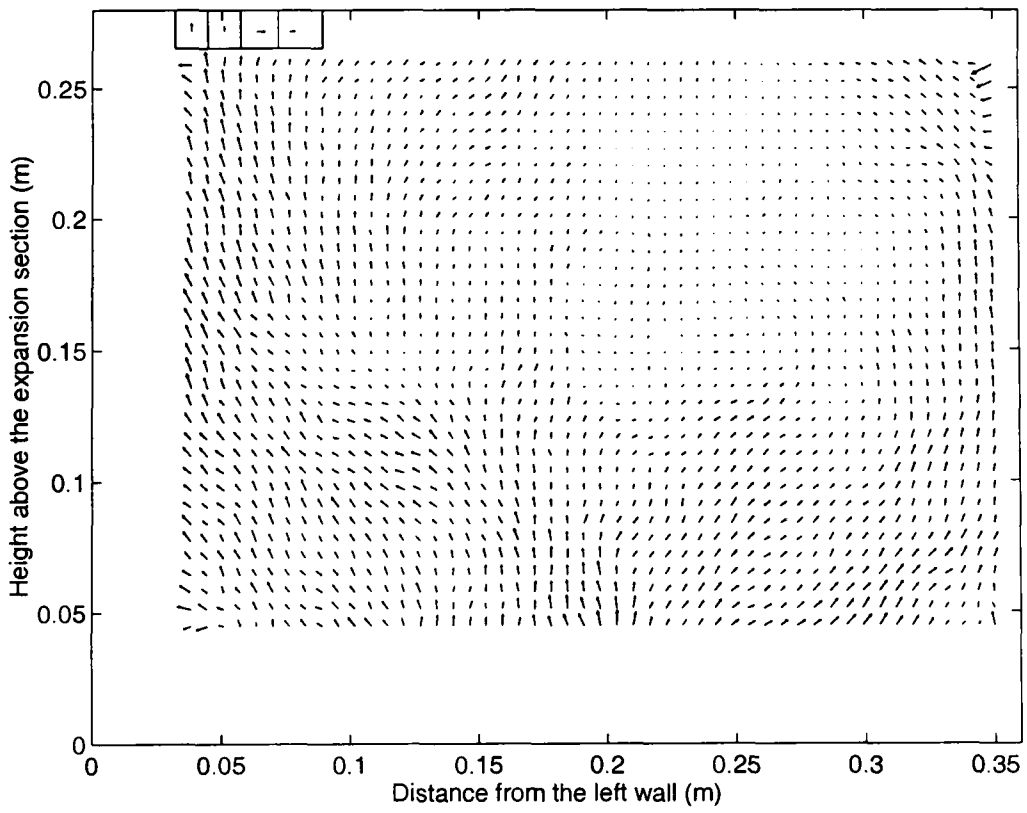

Figure 6.27: Time-averaged vector map over 37 seconds (Experiment 7). Velocity vectors in the left upper corner from left to right: 3 cm/s, 2 cm/s, 3 cm/s and 2 cm/s

component of the velocity seems to be slightly higher than in the case of the working conditions of the pilot plant (See Table 5.2).

Experiment number	v_y (cm/s)	Vertical std (cm/s)	v_x (cm/s)	Horizontal std (cm/s)	$\|v_x\|$ (cm/s)
6	1.80	0.21	0.41	0.24	0.76
7	1.86	0.27	-0.05	0.29	1.05

Table 6.2: Spatial averaged velocity and standard deviation of the time-averaged vector maps

Vertical velocity profiles, with the corresponding 95% confidence error-bars, for two different heights for the two experiments are shown in Figure 6.28 and 6.29. The confidence limits of the velocity are lower than in the previous cases, because some pictures could not be analysed due to the presence of sand in the freeboard, therefore the number of samples decreased and also the confidence limits, which are proportional to the square root of the sample number. The behaviour of the gas at these two heights can be summarised:

- Close to the bed surface, the velocity profile present regions of high velocity at the centre and near the wall and lower velocities between them.
- The velocity profiles present more peaks than at lower velocities, but they may be within the error. More vector maps should be used to smooth the profiles.
- The velocity slightly decreases with height but less than in the case of lower velocity. The high velocity means that the flow does not develop into the "U" shape profile.

The profiles of the horizontal component of the velocity present the following characteristics:

- The highest absolute values are found close to the wall and the minimum values at the the centre.

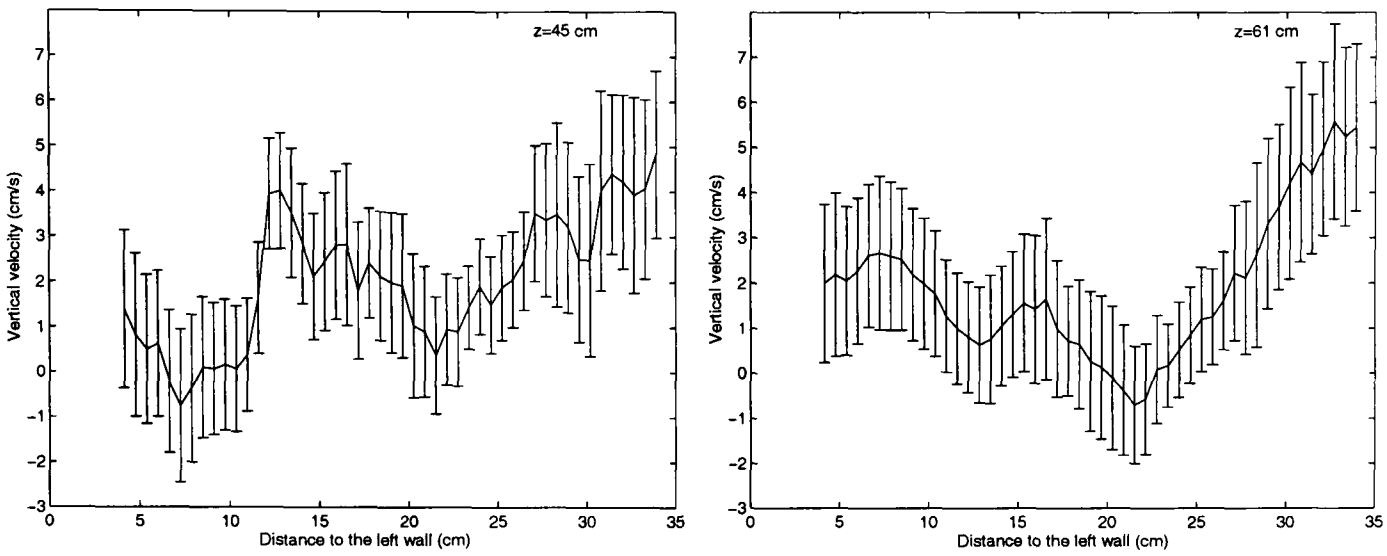

Figure 6.28: Time-averaged vertical velocity profile (Experiment 6)

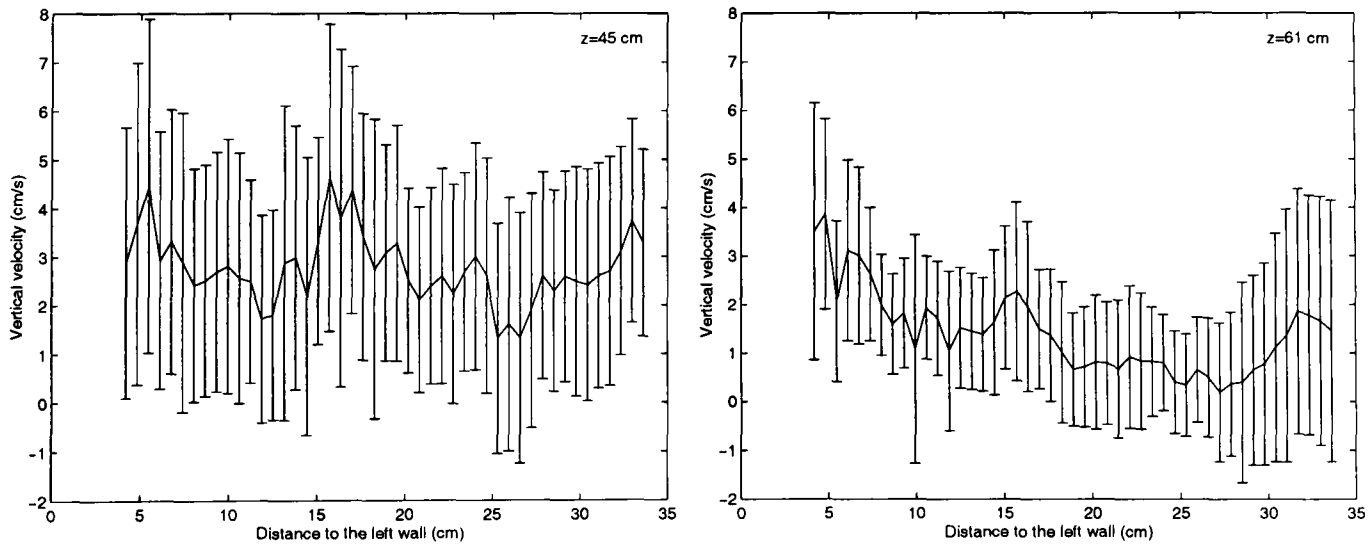

Figure 6.29: Time-averaged vertical velocity profile (Experiment 7)

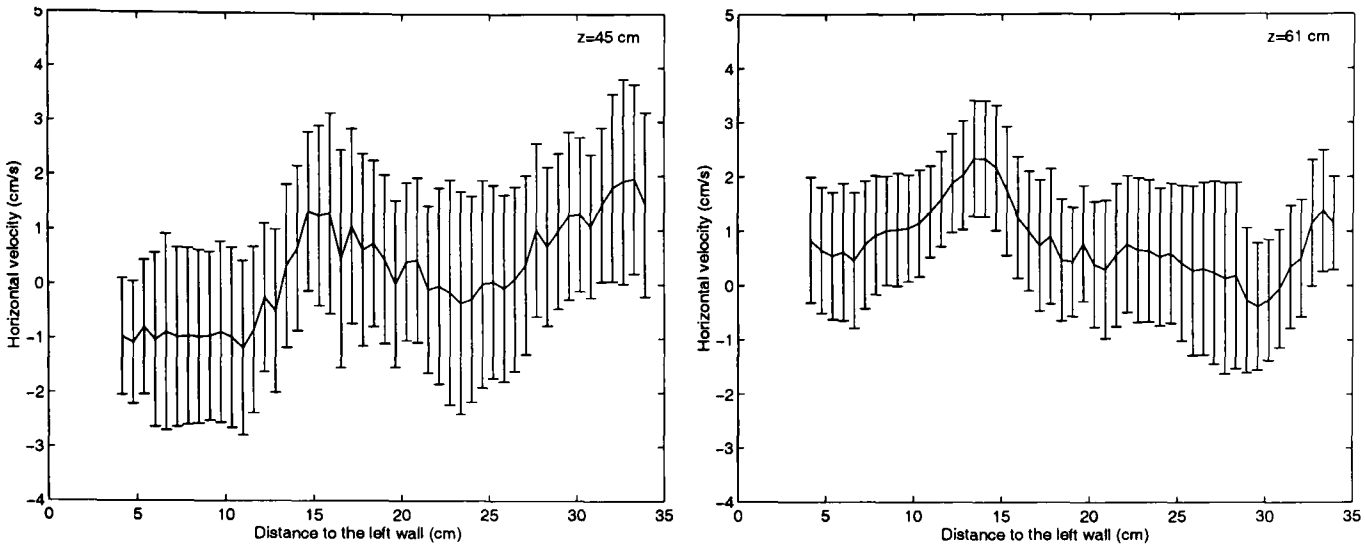

Figure 6.30: Time-averaged horizontal velocity profile (Experiment 6)

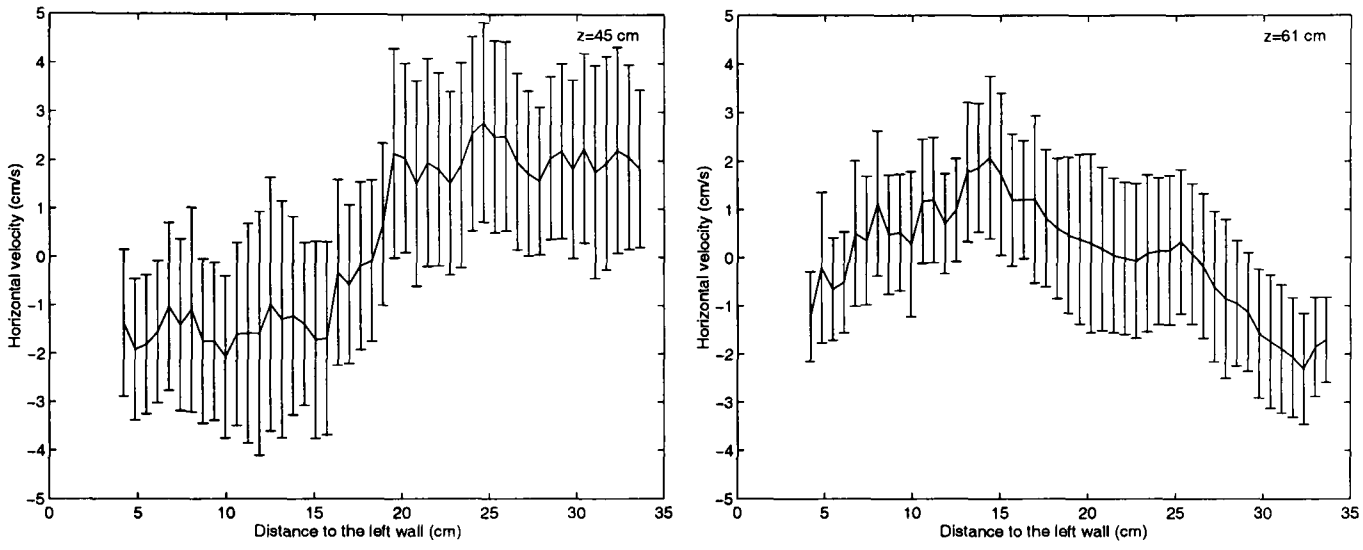

Figure 6.31: Time-averaged horizontal velocity profile (Experiment 7)

- The highest velocities close to the wall swap from one wall to the other with height, implying the presence of some kind of recirculation.
- Figure 6.30 (central outlet) presents more symmetry than Figure 6.31 (off-centre outlet).

Secondary structure of the flow

The time-averaged vector maps (Figures 6.26 and 6.27) minus the spatial time-averaged velocity are presented in Figures 6.32 and 6.33, for Experiments 6 and 7, respectively. There is indication of four recirculation areas, but not as symmetric as in the case of lower velocity (for example Figure 5.71), small vortices can be

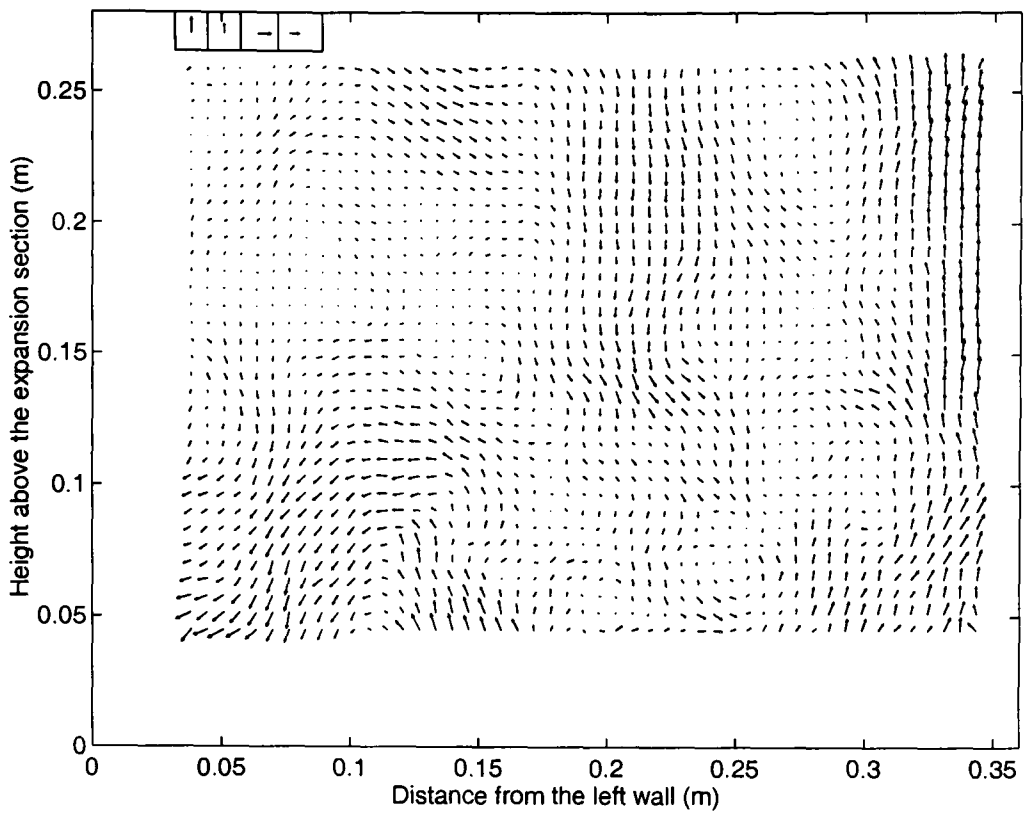

Figure 6.32: Time-averaged vector map over 37 seconds minus the spatial time averaged velocity (Experiment 6). Velocity vectors in the left upper corner from left to right: 3 cm/s, 2 cm/s, 3 cm/s and 2 cm/s

seen outside these recirculation areas. Looking at the time-averaged vector maps, over ten seconds, minus the spatial time averaged (Figures 6.34 and 6.35) it can be seen that the jets are usually close to either wall, as opposed to the centre; as a consequence a downward velocity appears close to the other side, while the intervening region is occupied by small vortices. In Experiment 6, the upward velocity regions are close to the right hand side (Figure 6.34 Frames 3, 4 and 5); this results in asymmetry of the recirculation areas (Figure 6.32). In Experiment 7 the high upward velocity region is close to the left wall (Figure 6.35 Frames 1, 2, 7 and 8) as reflected in Figure 6.33.

6.3 Straight freeboard

The expanded freeboard was substituted by a straight one, with a central outlet, to check the influence of the geometry in the gas flow.

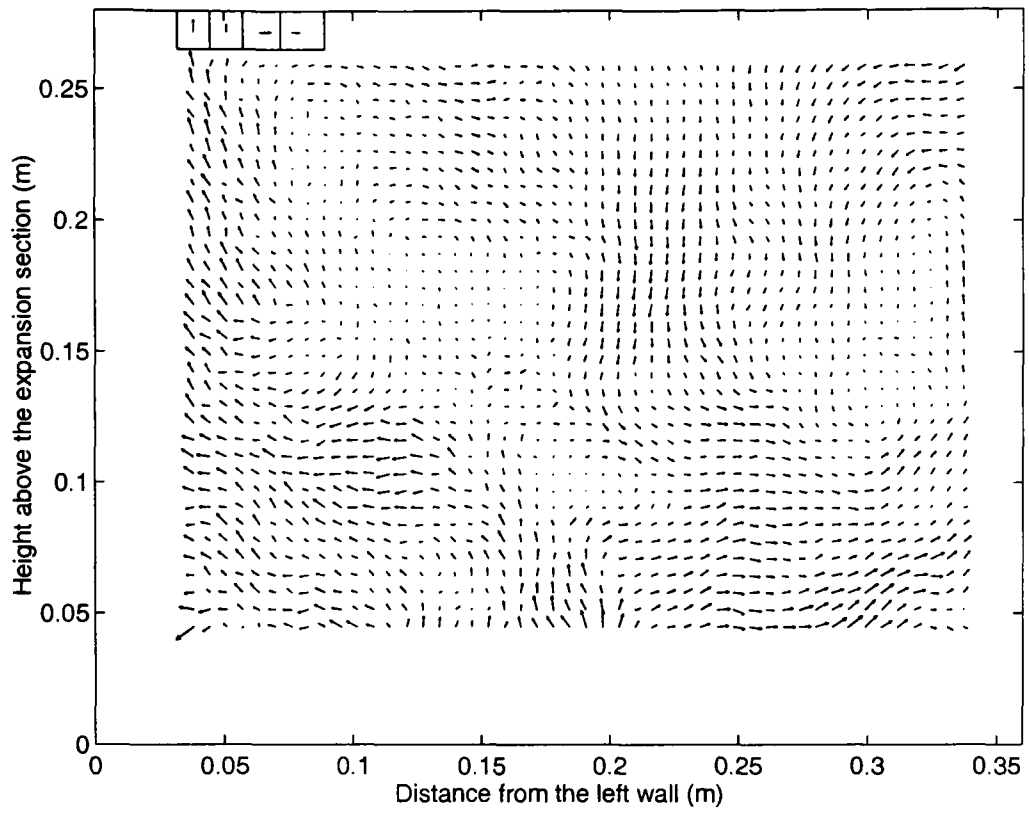

Figure 6.33: Time-averaged vector map over 37 seconds minus the spatial time averaged velocity (Experiment 7). Velocity vectors in the left upper corner from left to right: 3 cm/s, 2 cm/s, 3 cm/s and 2 cm/s

6.3.1 Instantaneous flow structures

The differences between the instantaneous vector maps for the case of expanded freeboard and straight freeboard are:

- Sand, ejected by erupting bubbles, has been found more often in the straight freeboard (approximately in three vector maps out of thirty seven) and the sand particles reached higher velocities in this case than in the case of the expanded one. However, most of the sand particles came back to the bed in both cases.

- No vortices as large as the ones found in the case of the expanded freeboard were found when using the straight freeboard. This indicates that one of the effects of the expansion section is to increase the size and stability of the vortices.

- The gas in the straight section travels faster and with small relative horizontal component than in the expanded section (Figure 6.36 and Figure

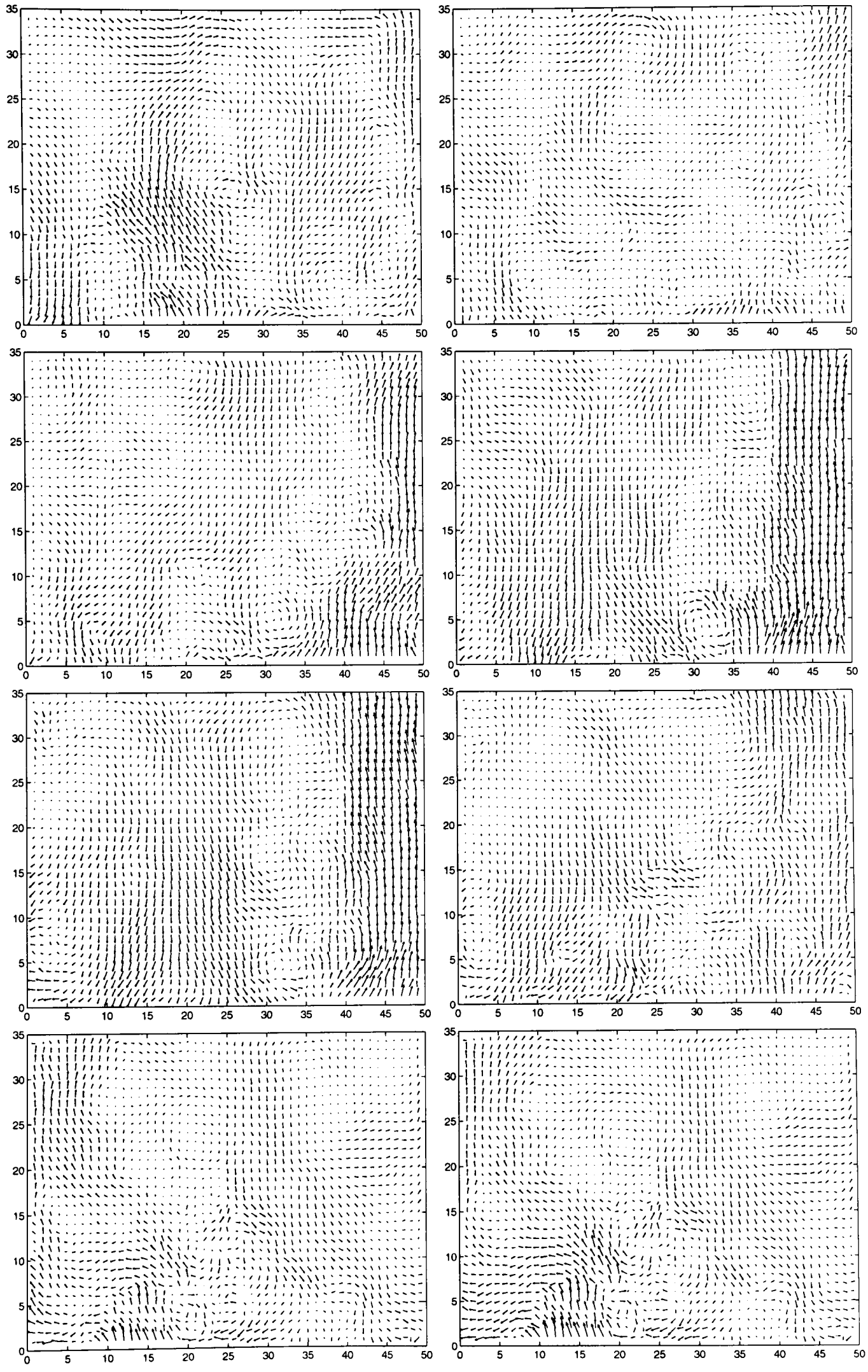

Figure 6.34: Time-averaged vector maps, over 10 seconds, minus the spatial time averaged velocity (Experiment 6. Frames 1 to 8 are displayed from left to right and from top to bottom)

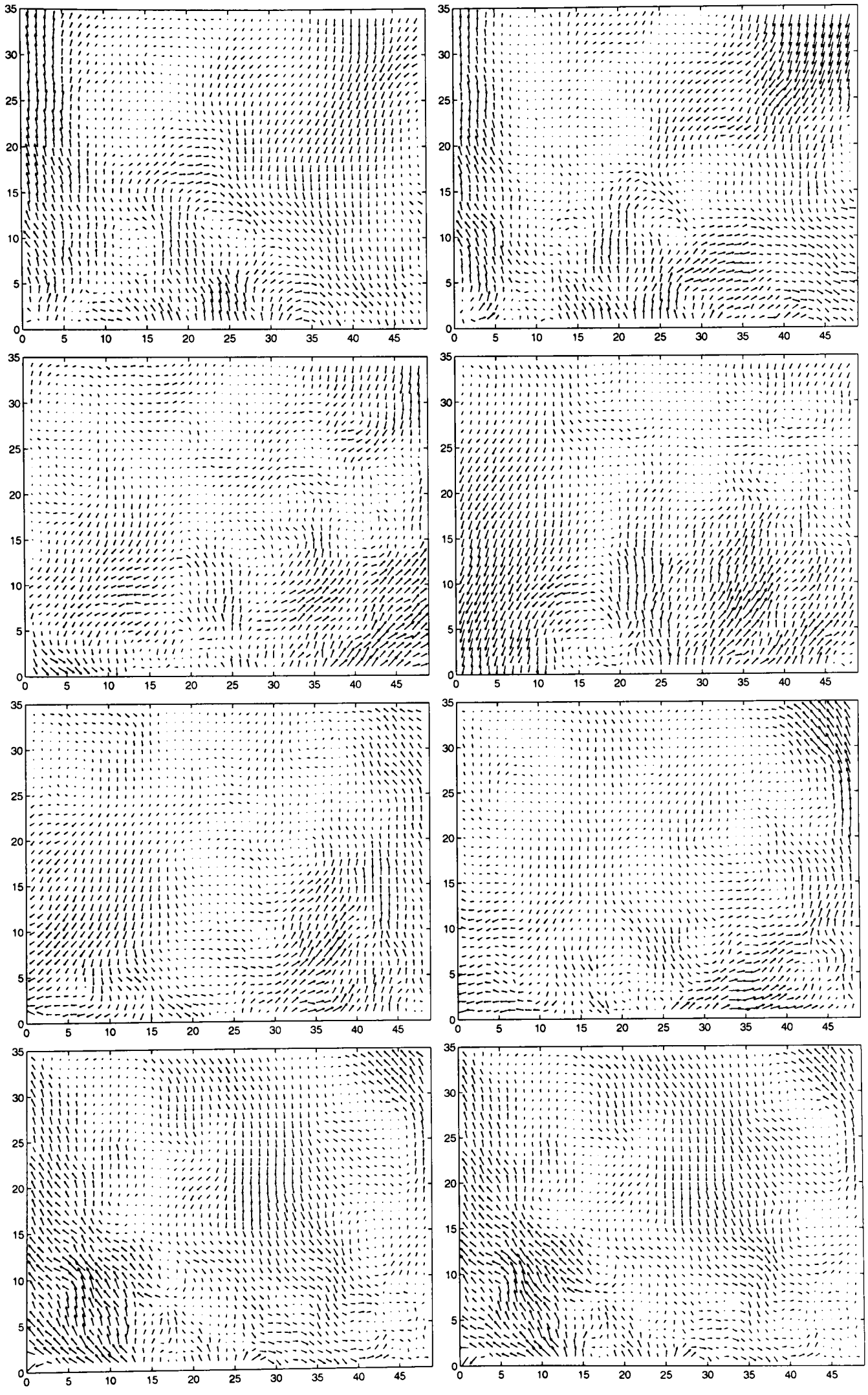

Figure 6.35: Time-averaged vector maps, over 10 seconds, minus the spatial time averaged velocity (Experiment 7. Frames 1 to 8 are displayed from left to right and from top to bottom)

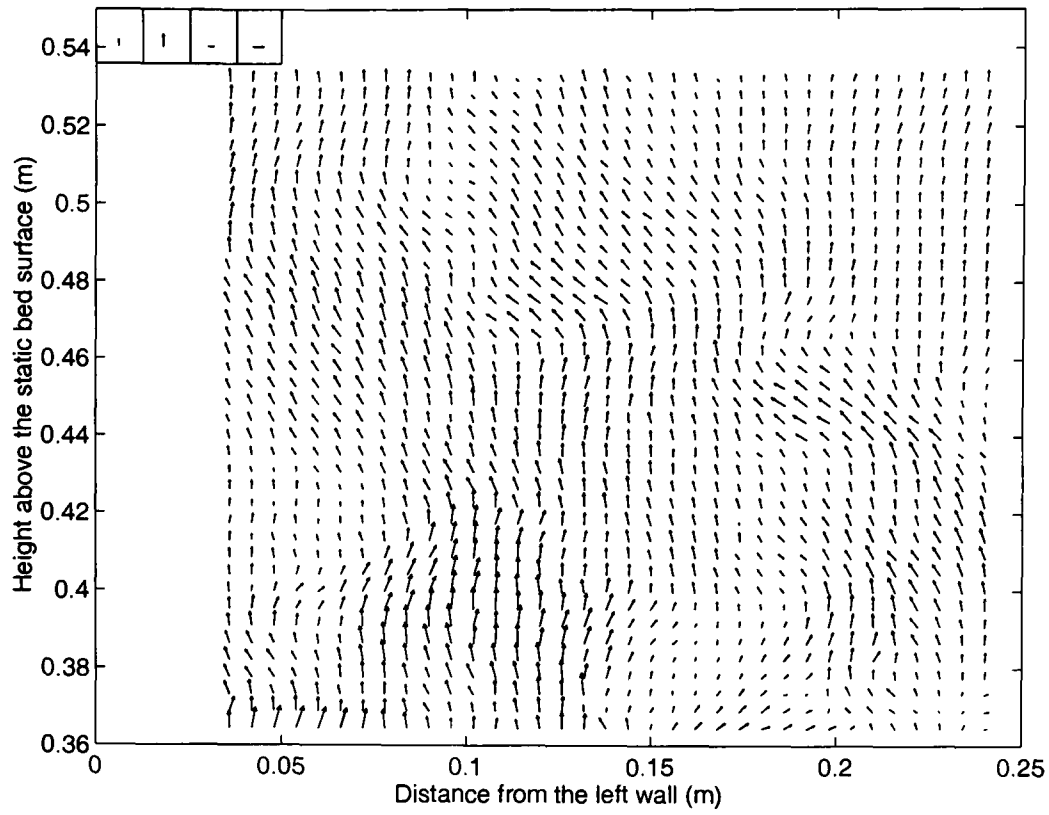

Figure 6.36: Instantaneous vector map. Velocity vectors in the left upper corner from left to right: 4.41 cm/s, 8.82 cm/s, 4.41 cm/s and 8.82 cm/s

6.37).

6.3.2 Statistical description of the flow

The results of two experiments, labelled Experiment 8 and Experiment 9, carried out at the same conditions, are presented here.

Time-averaged velocity

The time-averaged vector maps (Figure 6.38 and Figure 6.39) indicate that the gas follows an almost straight path parallel with the wall. The flow is more homogeneous than the flow found in the case of the expanded freeboard (Figures 5.27, 5.28 and 5.29).

The spatial mean of the time-averaged value of the two components of the velocity are very similar in the case of both experiments (Table 6.3). The vertical velocity

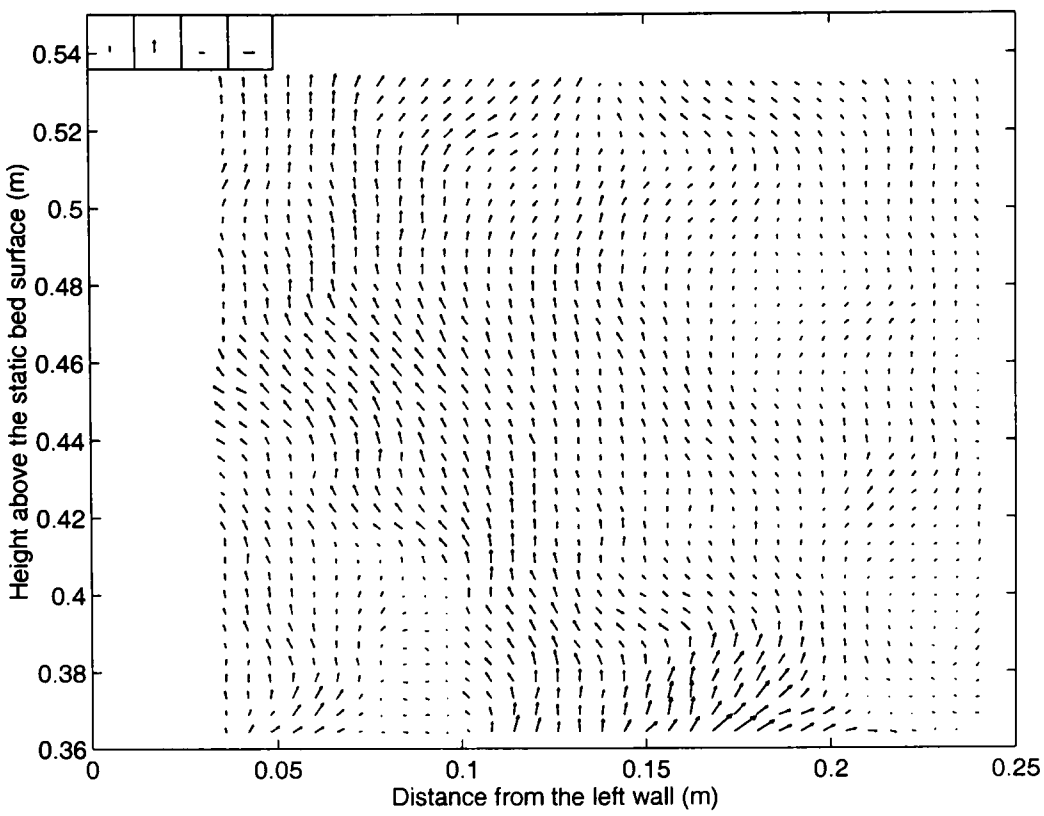

Figure 6.37: Instantaneous vector map. Velocity vectors in the left upper corner from left to right: 4.41 cm/s, 8.82 cm/s, 4.41 cm/s and 8.82 cm/s

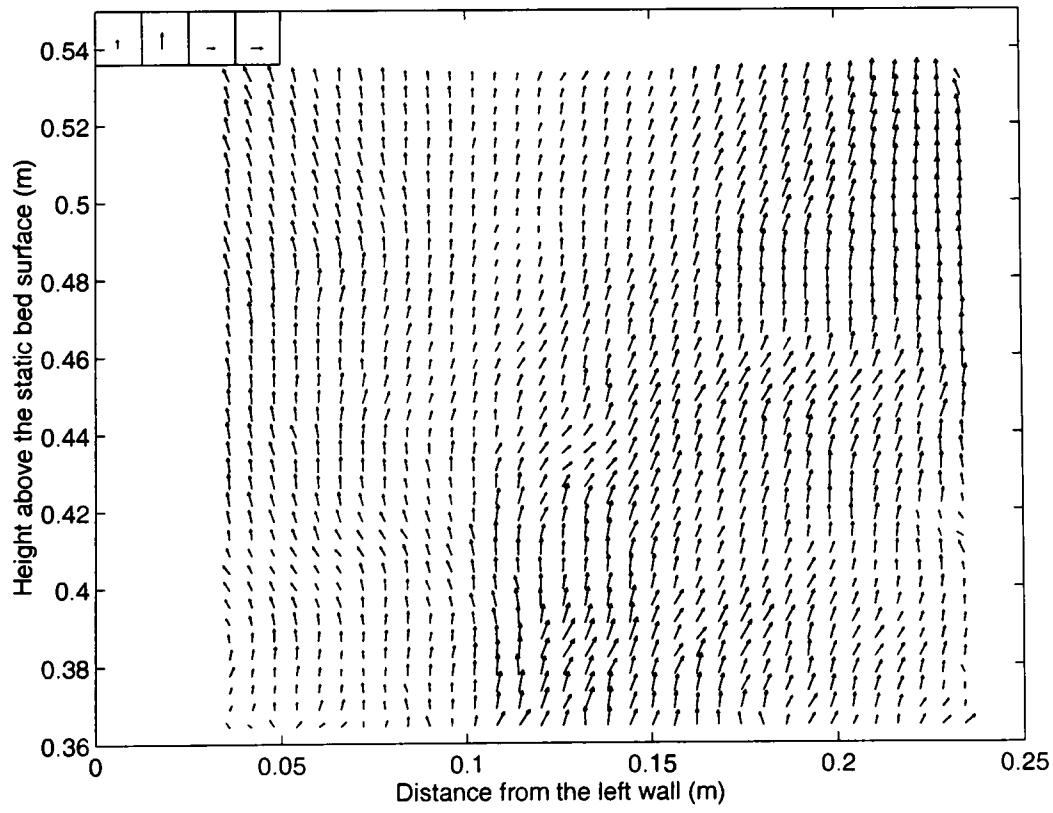

Figure 6.38: Time-averaged vector map over 37 seconds (Experiment 8). Velocity vectors in the left upper corner from left to right: 3 cm/s, 2 cm/s, 3 cm/s and 2 cm/s

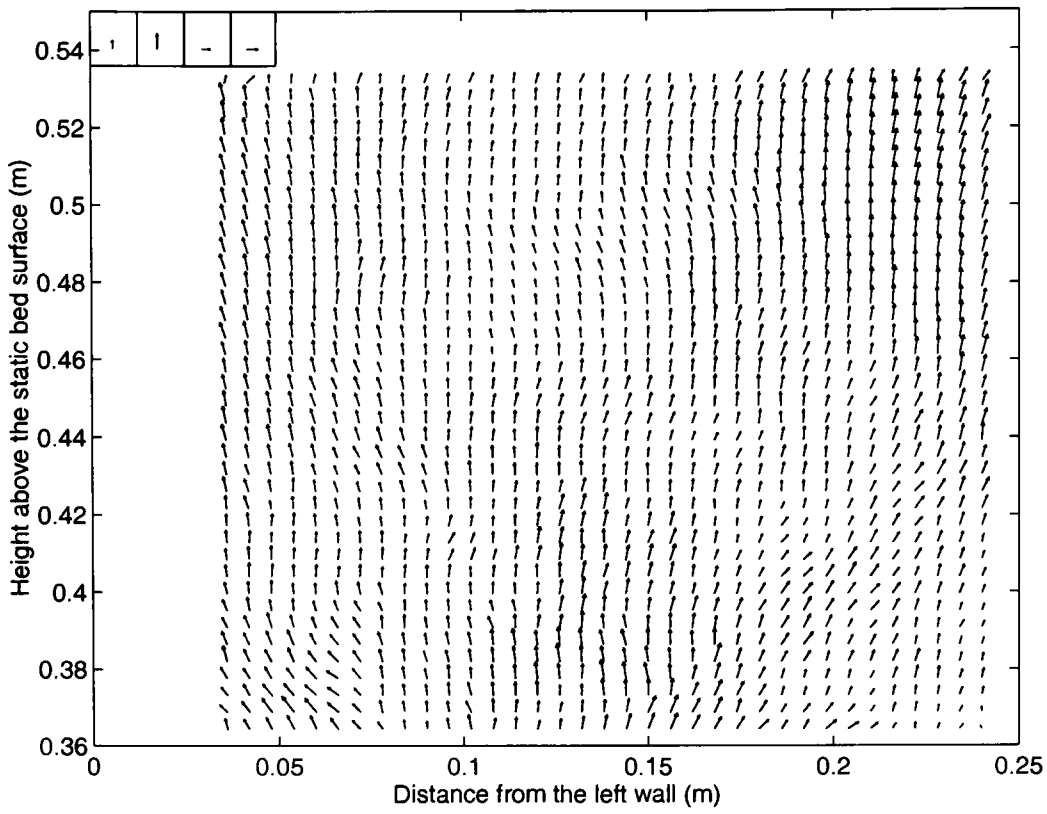

Figure 6.39: Time-averaged vector map over 37 seconds (Experiment 9). Velocity vectors in the left upper corner from left to right: 3 cm/s, 2 cm/s, 3 cm/s and 2 cm/s

(4.4 cm/s) is considerably higher than in the case of the expanded freeboard (1.4 cm/s). This difference cannot be explained by continuity considerations alone, implying that a significant fraction of the flow in the expanded section is not visualised and therefore not included in the averaging. The vertical component of

Experiment number	v_y (cm/s)	Vertical std (cm/s)	v_x (cm/s)	Horizontal std (cm/s)	$\lvert v_x \rvert$ (cm/s)
8	4.36	0.34	0.52	0.08	0.86
9	4.24	0.37	0.14	0.13	0.68

Table 6.3: Spatial average velocity and standard deviation of the time-averaged vector maps

the velocity profiles, with the 95% confidence error-bars, are plotted (Figure 6.40 and Figure 6.41). Only 32 images could be analysed in the case of Experiment 9, resulting in lower confidence limits than in Experiment 8. As in the case of the expanded section, the velocity profile has an inverted "U" shape close to the bed surface and this profile changes with height until it becomes a "U" shape (16 cm later).

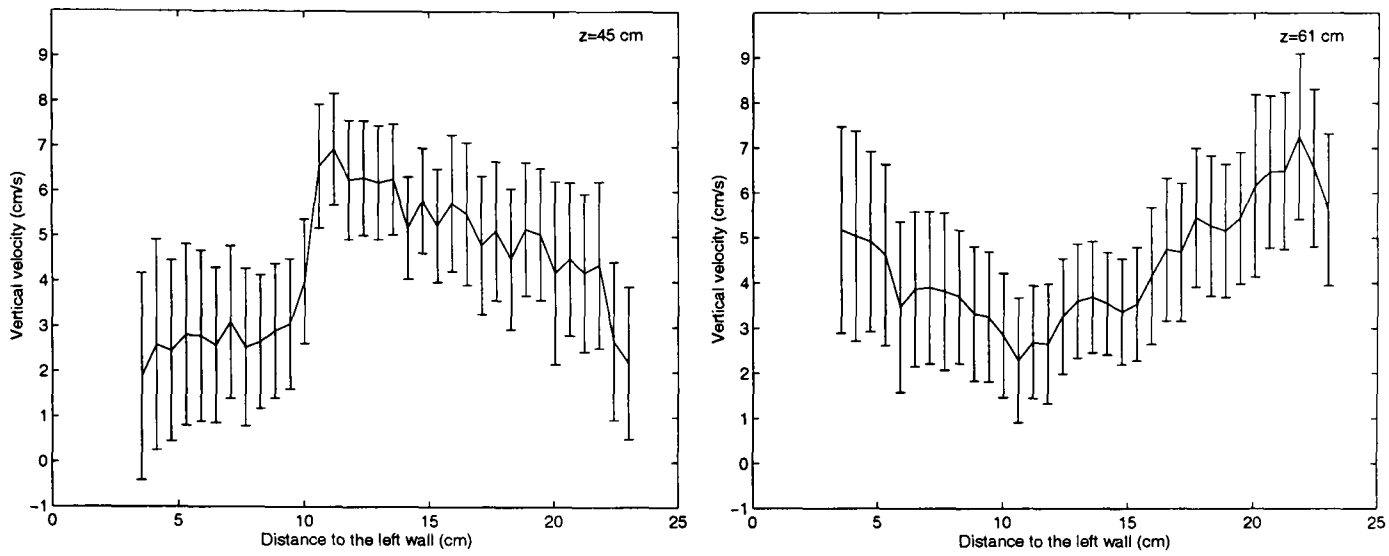

Figure 6.40: Time-averaged vertical velocity profile (Experiment 8)

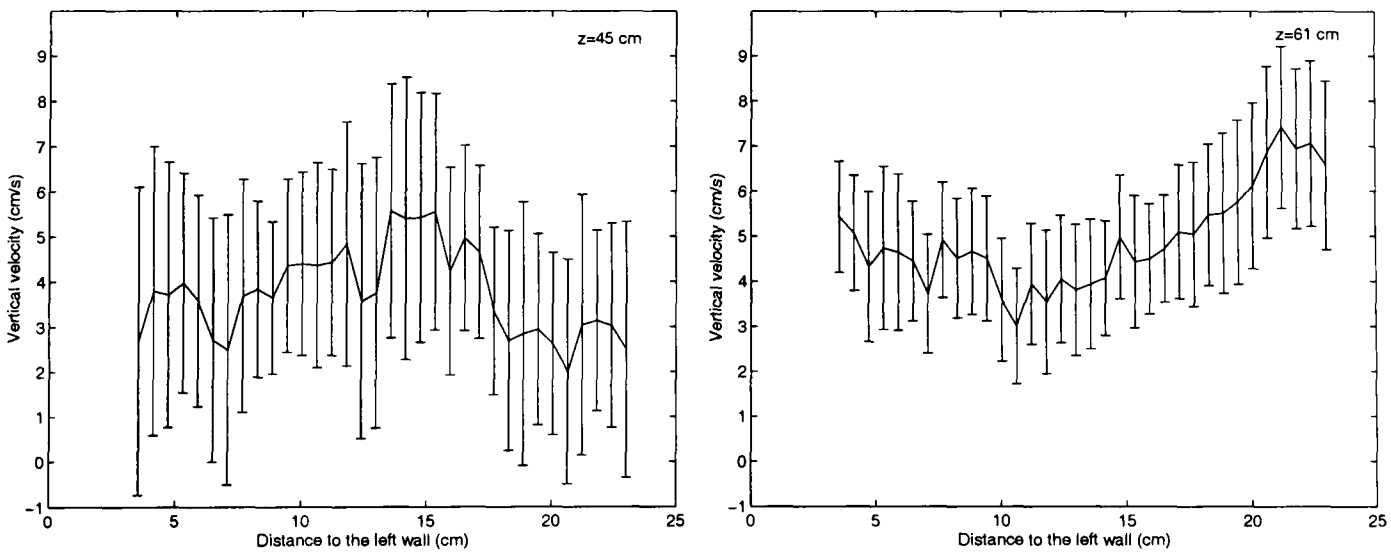

Figure 6.41: Time-averaged vertical velocity profile (Experiment 9)

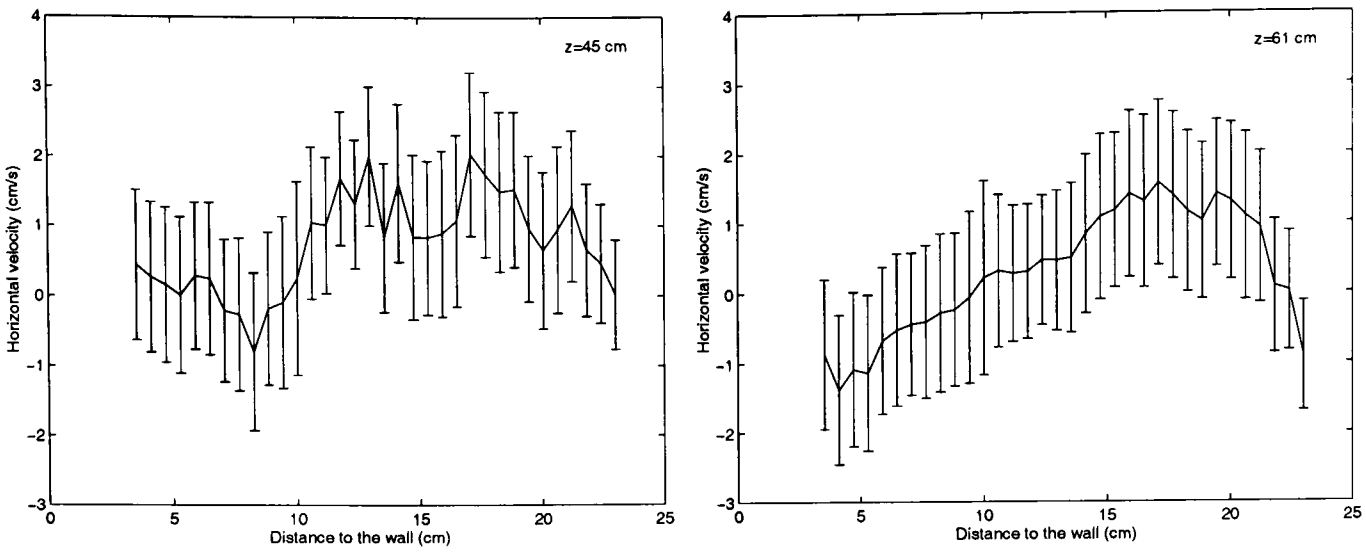

Figure 6.42: Time-averaged horizontal velocity profile (Experiment 8)

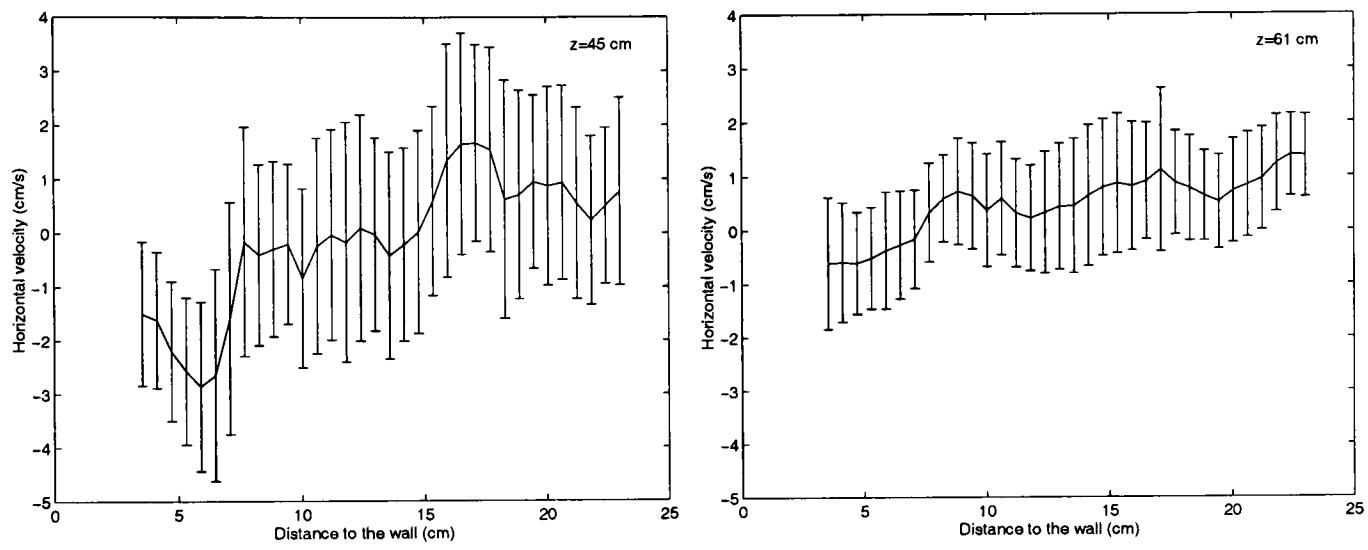

Figure 6.43: Time-averaged horizontal velocity profile (Experiment 9)

The profiles of the horizontal component of the velocity (Figures 6.42 and 6.43) are nearly symmetric.

Secondary structure of the flow

Figures 6.44 and 6.45 show the time-averaged vector maps minus the spatial time-averaged velocity. They show small eddy structures that do not seem to be very stable. The four recirculation areas, as in the case of the expanded freeboard (for example, Figure 5.27) cannot be found in this case. The time-averaged vector maps over 10 seconds, minus the spatial time-averaged velocity (Figures 6.46 and 6.47) confirm the presence of small vortices.

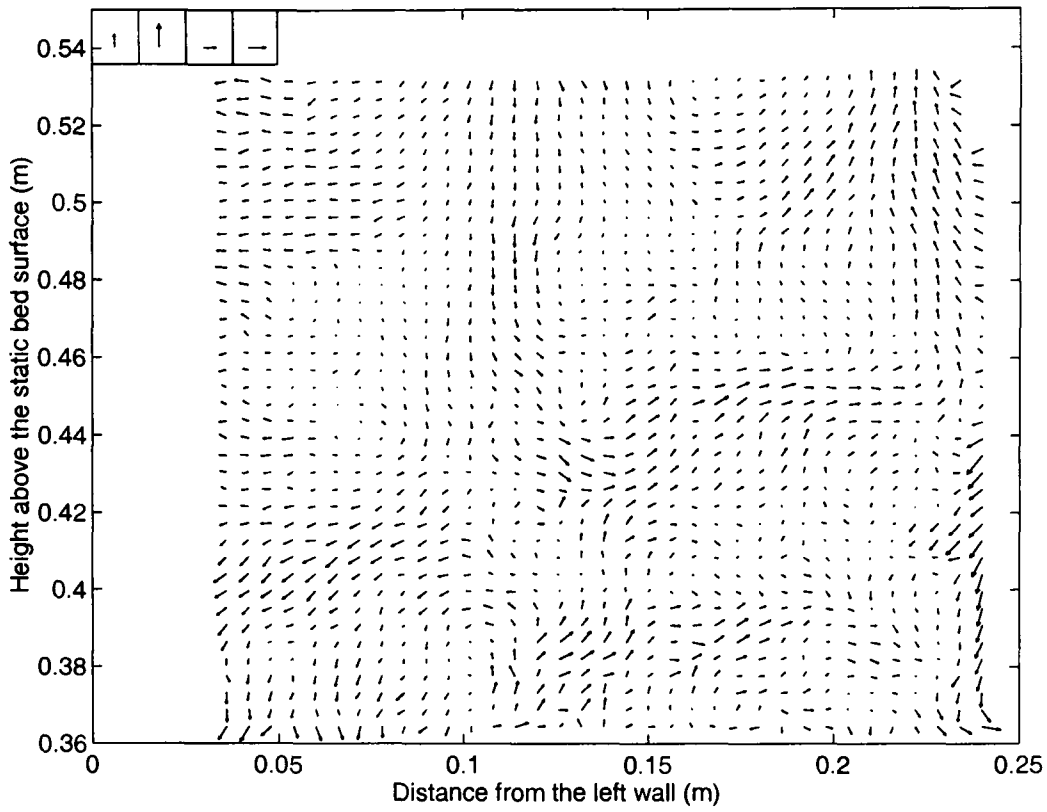

Figure 6.44: Time-averaged vector map over 37 seconds minus the spatial time averaged velocity (Experiment 8). Velocity vectors in the left upper corner from left to right: 3 cm/s, 2 cm/s, 3 cm/s and 2 cm/s

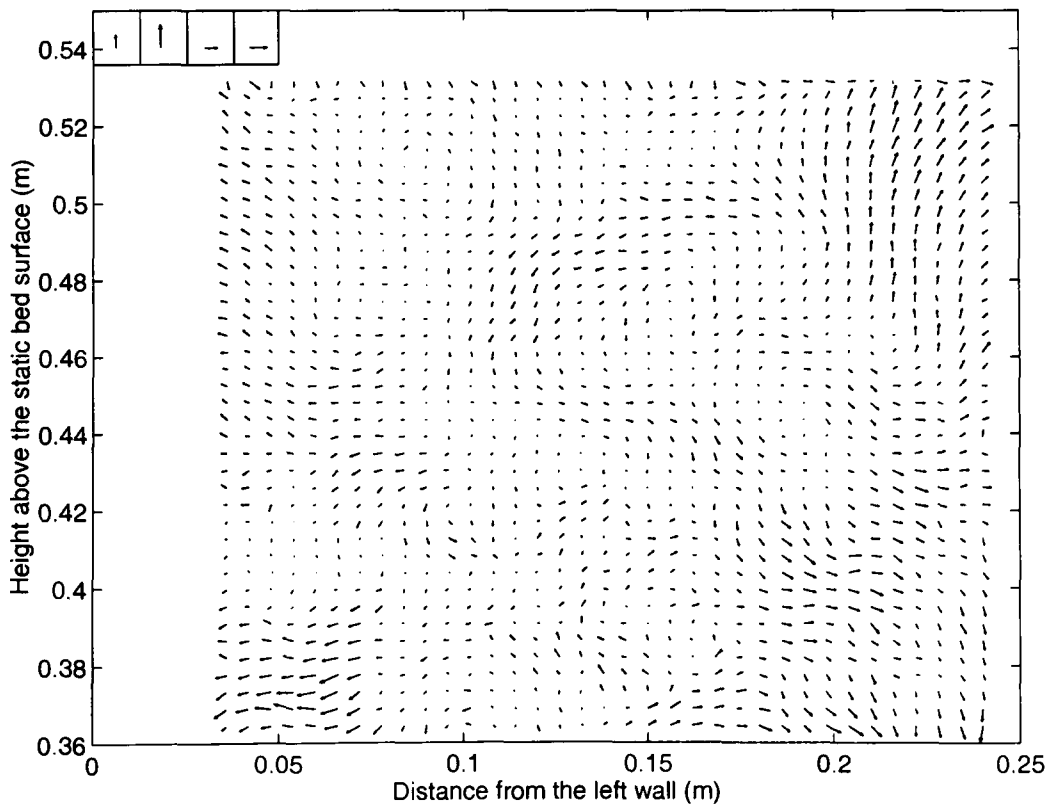

Figure 6.45: Time-averaged vector map over 37 seconds minus the spatial time averaged velocity (Experiment 9). Velocity vectors in the left upper corner from left to right: 3 cm/s, 2 cm/s, 3 cm/s and 2 cm/s

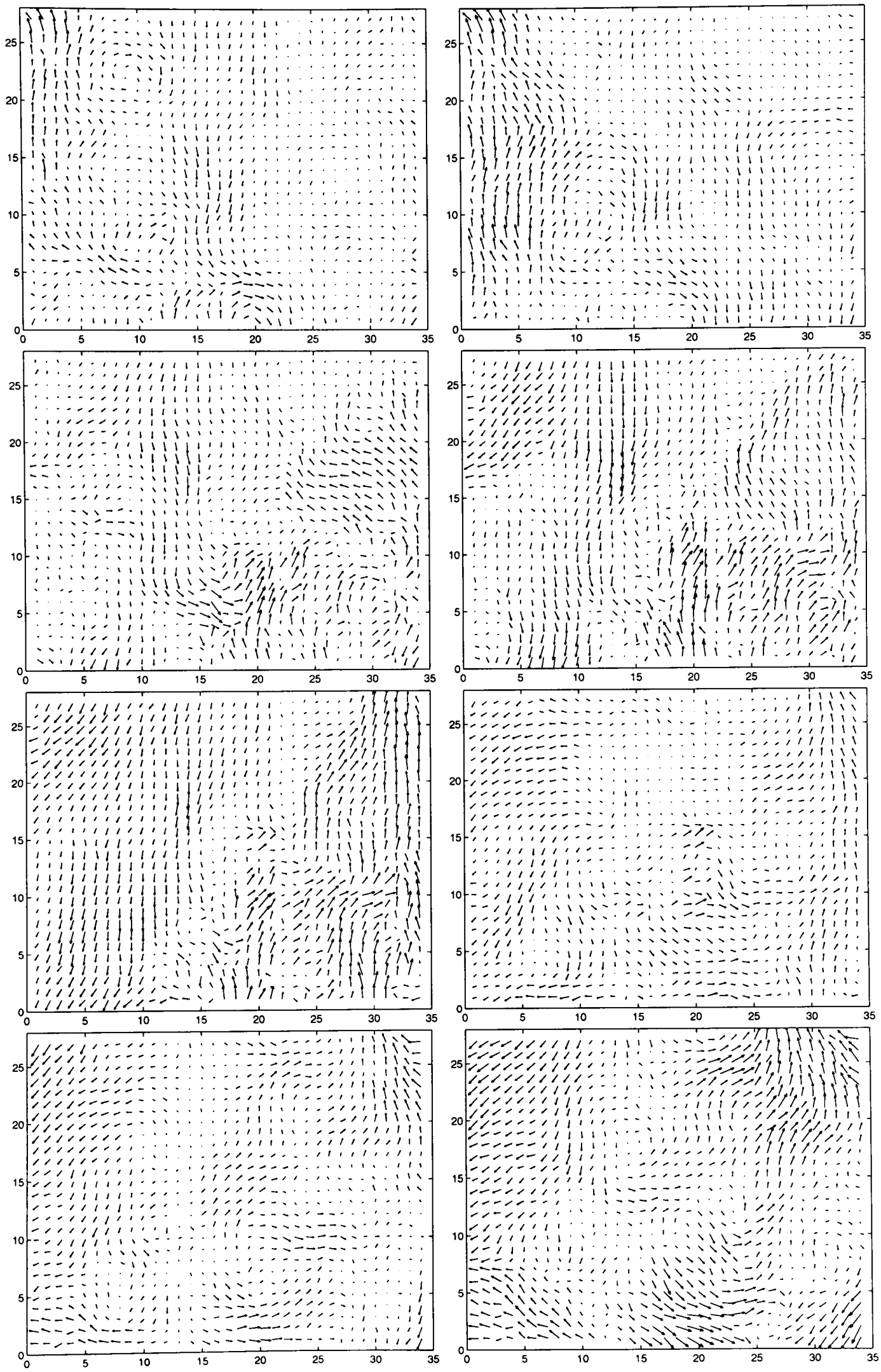

Figure 6.46: Time-averaged vector maps, over 10 seconds, minus the spatial time averaged velocity (Experiment 8. Frames 1 to 8 are displayed from left to right and from top to bottom)

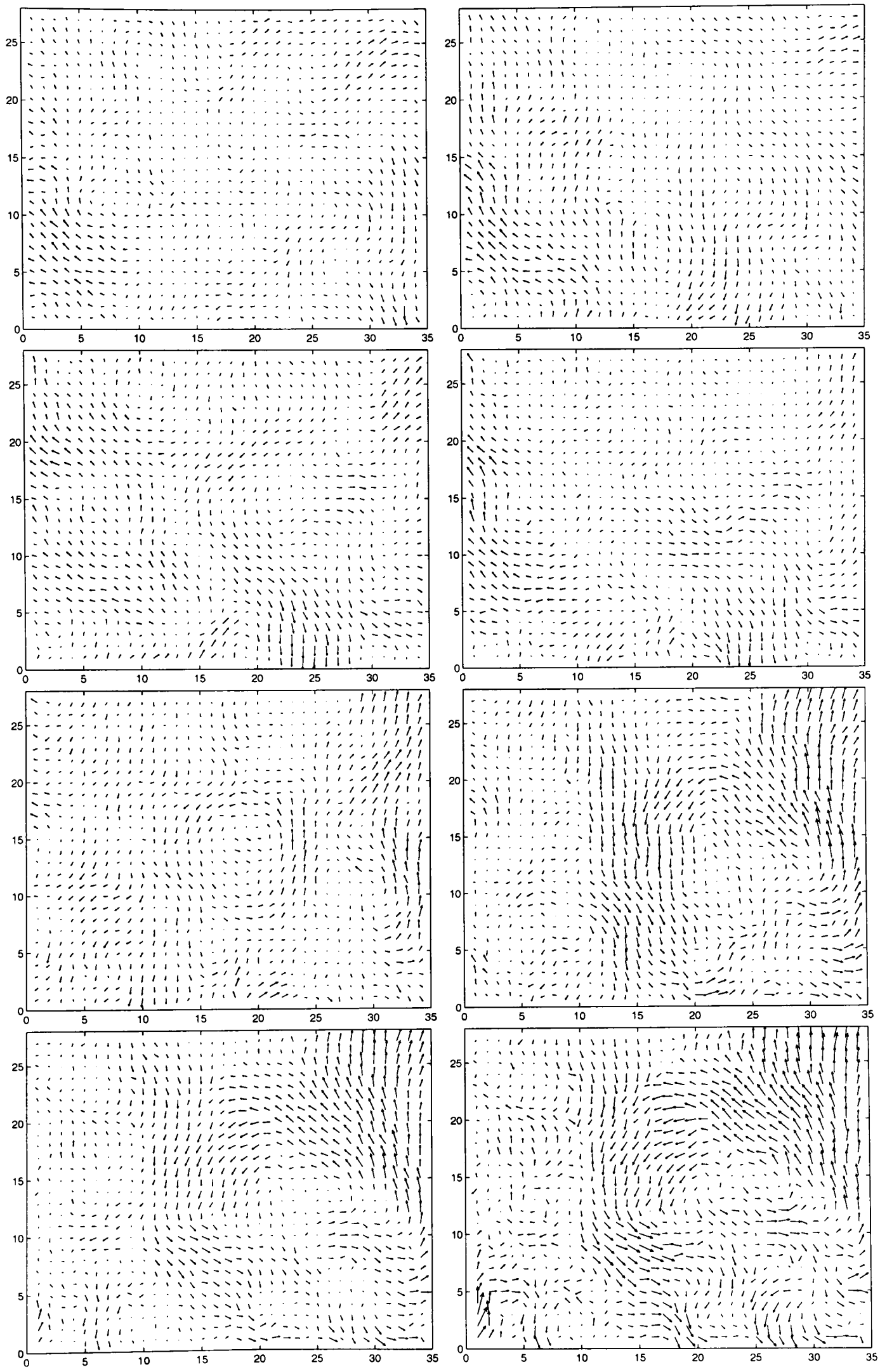

Figure 6.47: Time-averaged vector maps, over 10 seconds, minus the spatial time averaged velocity (Experiment 9. Frames 1 to 8 are displayed from left to right and from top to bottom)

6.4 Conclusions

Firstly, the influence of a central outlet, as opposed to an off-centre one, was studied. The location of the outlet does not seem to influence the vertical velocity component; however it seems to promote a more symmetric horizontal velocity component.

Higher flowrate increases the observed mean velocity, but less so than expected. Higher mean velocity was seen when substituting the expanded freeboard for a straight one. The expanded freeboard seems to promote very large stable recirculation regions. These regions lose stability and symmetry when the gas superficial velocity increases. The straight freeboard precludes the formation of these stable regions but encourages the formation of smaller and more dynamic eddies.

Chapter 7

Discussion

In this chapter, the experimental results obtained for each section of the freeboard are independently analysed, for operating conditions similar to those on the B.P. pilot plant. Furthermore, the experimental results obtained in this study are compared to those obtained from literature in an attempt to gain insights of the freeboard hydrodynamics. The knowledge gained is applied to infer the distribution and residence time of the carbon fibres in the freeboard.

Finally, the results obtained using other operating conditions (bed outlet location, superficial gas velocity and freeboard geometry) are discussed and suggestions are made to improve the freeboard design.

7.1 Flow above the bed surface

7.1.1 Single bubble mechanism

The mechanism of single bubble eruption of a bubble injected into an incipiently fluidised bed has been inferred from gas velocity measurements, using image shifting with simultaneous video visualisation. Figure 7.1 schematically shows the proposed mechanism. The mechanism can be summarised as follows:

a) The bed height increases proportionally to the gas injected.

b) The bed surface starts to bulge as the bubble approaches.

c) From the moment that the bubble nose reaches the bed surface until the bubble reaches its maximum height, gas percolates through the layer of particles above the bubble. The gas velocity is upwards at the bubble centreline and describes a circular movement on the sides of the bubbles, in a manner similar to the flow due to a rising bubble in a fluidised bed. The amount of gas percolating through the bubble is higher than the gas processed by a stationary bubble in a fluidised bed. The bubble decelerates and the voidage of the bulge increases as the bubble rises.

d) When there is no longer sufficient force to support the particles above the bubble, they return coherently to the bed surface, imposing a movement on the gas opposite to the movement induced by a rising bubble.

e) The downward movement of the bulge particles drags gas with it, producing a downward "jet" at the centre of the bed. This jet collides with the bed surface thus imposing a circular movement on the gas, forming side vortices that rotate clockwise on the left and anti-clockwise on the right (the direction of rotation is opposite to the rotation inside a bubble rising in a fluidised bed). If these vortices were in an unbounded medium at

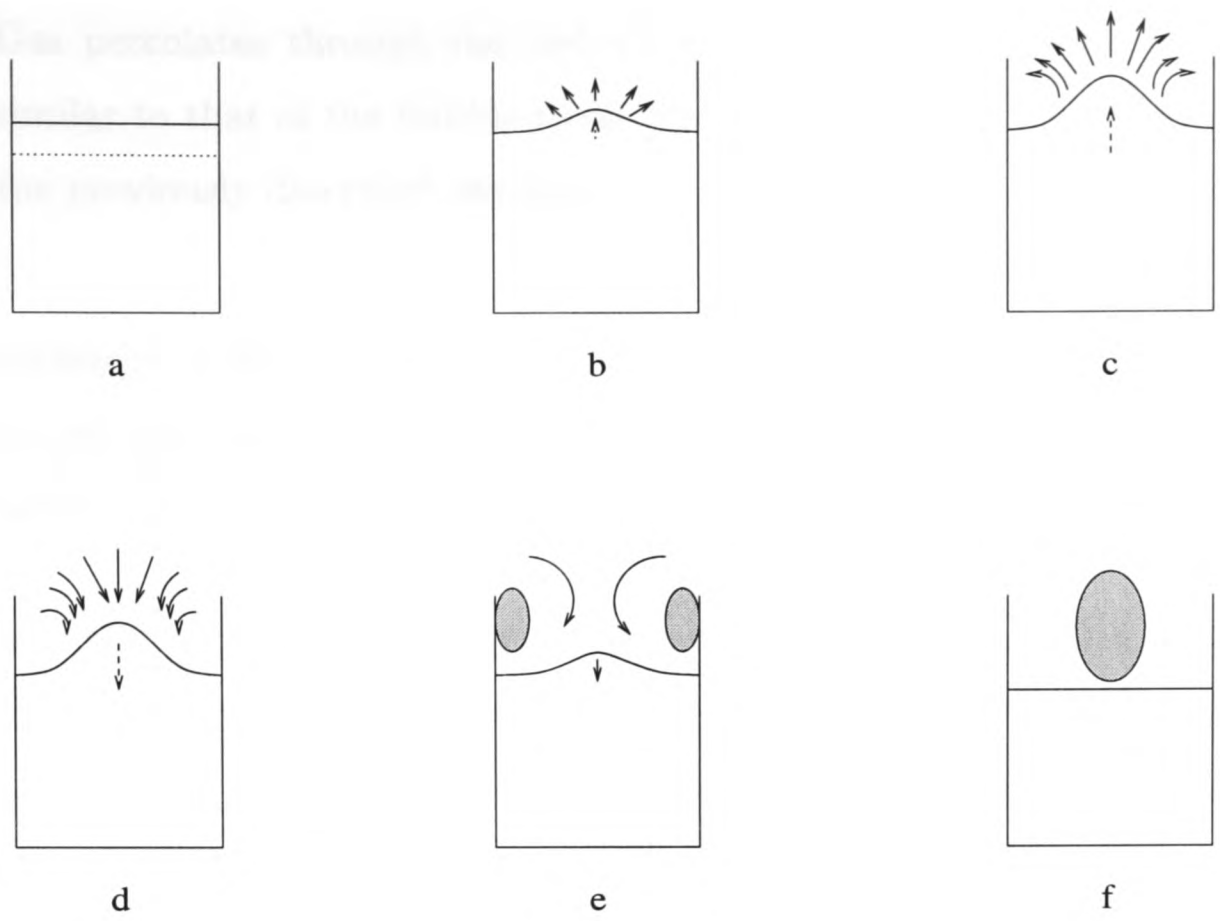

Figure 7.1: Schematic of the cross section of single bubble eruption mechanism

rest they would move downwards; however, the presence of the bed surface precludes this.

f) The vortices expand towards the bed centre until they interact with each other giving rise to a region of high vorticity at the bed centre. This structure moves, expands slowly and eventually dissipates.

In summary, the gas flow pattern above a single erupting bubbles is determined by:

- The movement of the bed surface which is the result of the combination of two effects:
  - Piston-like movement of the bed surface.
  - Time dependent movement of each point at the bed surface (The points at the centre and near the wall are out of phase).

- Gas percolates through the bed surface: it has a circulating movement similar to that of the bubble rising within the bed only during part (c) of the previously described mechanism.

The movement of the bed surface has a greater influence in determining the flow than the gas percolating from inside the bubble. This is expected since the sand momentum is much higher than the gas momentum.

In the sketch of the single bubble eruption shown in Figure 7.1 symmetry is assumed. However, in real conditions it is difficult to achieve this symmetry. Consequently, the two side vortices may have different sizes and strengths giving rise to an asymmetric distribution of the vorticity. It also needs to be considered that in a freely bubbling bed the bubbles rapidly follow each other. Thus, the flow pattern resulting in the freeboard will be a combination of effects arising from each bubble. How these effects combine need to be investigated to gain a deeper insight of the gas behaviour in the freeboard of a bubbling fluidised bed.

In this study the bubble diameter (14 *cm*, as measured at the bed surface) was large compared with the bed diameter (25 *cm*). It would then be expected that the size and strength of the vortex rings are influenced by the presence of the wall. However, it has been demonstrated (Figure 5.10) that a small bubble (7 *cm* diameter) also generated a vortex ring that travelled towards the wall. Afterwards, it had the same behaviour (although not the same strength) as a vortex ring generated after a bigger bubble eruption.

It can be concluded that the flow pattern in the freeboard is mainly determined by bubble eruption and the movement of the bed surface rather than by the continued circulation pattern of bubble gas. These insights into the single bubble eruption mechanism provide new ideas that can be used to model and simulate the flow above a bubble.

7.1.2 Extension of the single bubble mechanism to a bubbling bed

In the bubbling bed, operating at the working conditions scaled down from the pilot plant, approximately 83% of the erupting bubbles at the bed surface were single bubbles. They are expected to have similar behaviour to that found for single injected bubbles. The most striking characteristic above the bubbling bed is the continuous presence of a vortex ring rotating downwards at the centre and upwards near the wall. From the single bubble ejection mechanism proposed here these contra-rotating vortices are generated by the return of the bed surface to its initial height after bubble eruption (the gas is dragged downwards at the centre and pushed upwards near the wall). The rotational direction of the vortices indicates that the most important step in the single bubble ejection mechanism is the return of the bed material to the bed surface (otherwise, the rotational direction of the vortices would be the opposite).

The characteristic bubble frequency is approximately 1.8 sec^{-1} and steps (b) and (c) in Figure 7.1 (when the gas is circulating upwards at the centre and downwards near the wall) only last for less than 0.1 *sec.* Furthermore, the side vortices (e) appear to be stable over such time scale. This explains why vortices rotating downwards at the centre and upwards near the wall are seen continuously. The vortices have a considerable rotational velocity; the vortex cores are devoid of particles because the particles cannot follow the high-curvature streamlines of the vortices (since the response time of the particles is too high compared with the rotational velocity as a consequence of the density difference between the particles and the gas) and the particles are spiralled away from the centre of the vortices. The fibres have a density smaller than the sand and the seeding particles; therefore, they may be entrained and retained in the vortex cores.

If bubbles coalesce just below the bed surface they eject a powerful gas jet. The bed particles are launched higher than the height reached by the bulge of

a single erupting bubble. However, they usually come back to the bed surface before reaching the end of the expansion section. Although only 17% of bubble eruptions involve coalescence this mechanism has a greater effect on the gas flow than single bubble eruption.

7.2 Flow in the expansion section

7.2.1 Theoretical considerations

It is important to consider what happens when a fluid flows through an expansion. As indicated in Section 5.2 an increase in the flow area leads to a drop in the velocity and the pressure rises in the direction of the motion, creating a pressure gradient that is adverse to the flow. The change of flow due to an enlargement region is basically determined by the geometry of the enlargement region and the inlet velocity profile. To study the effect of divergence produced in the flow, laminar and turbulent flow will be reviewed separately.

- Laminar flow.

  The inertia near the wall is very small in comparison with the viscous forces. The adverse pressure can slow the fluid so much that it stagnates. Such a point is termed the *separation point.* Separation occurs when the gradient of the velocity at the boundary is zero. Beyond this point the flow may be reversed (*stalls*), due to the adverse pressure gradient.

  When the velocity, and hence the Reynolds number, is very low, the separation region is small and occurs on both sides of the passage. The fluid re-attaches rapidly and fills the whole section, because the inertial forces are smaller than the viscous forces. This is shown in Figure 7.2 where water flows at $3 - 4\ cm/s$ in a 60 mm diameter horizontal pipe (the Reynolds number is 1.8×10^{-3}) with a 20° diverging angle [128].

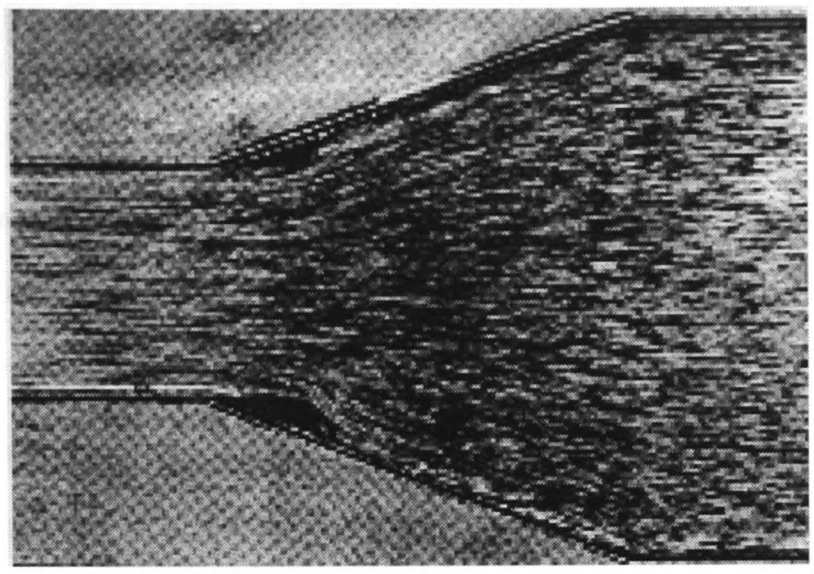

Figure 7.2: Diverging slow laminar flow. From Woods and Clark (1988)

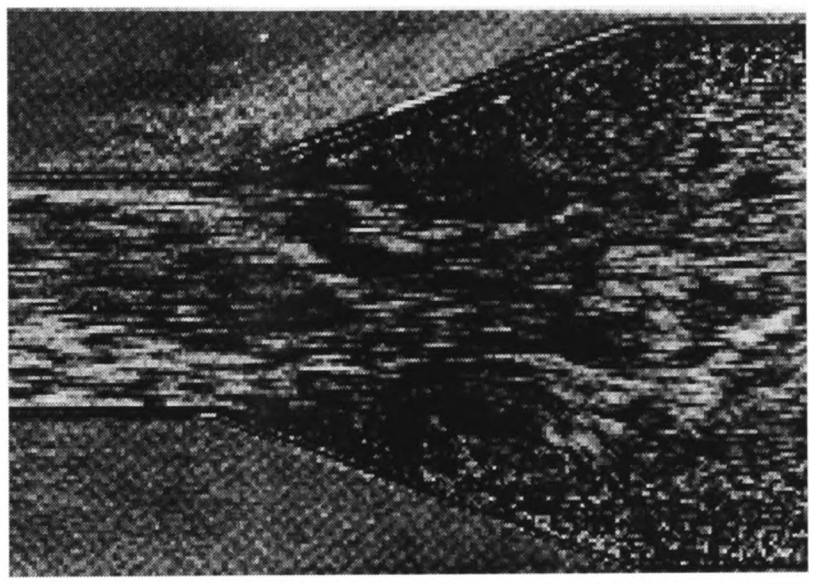

Figure 7.3: Diverging fast laminar flow. From Woods and Clark (1988)

When the velocity is high, and hence the Reynolds number is large (but still laminar), large eddies are formed after the separation point. The boundary layer moves away from the wall, giving rise to a region of slowly moving, eddying flow, as can be seen in Figure 7.3. Figure 7.3 shows water flowing at $15-20\ cm/s$ in a 60 cm diameter horizontal pipe (the Reynolds number is 0.9) with a 20° diverging angle [128].

- Turbulent flow.

Turbulent flow is less likely than laminar flow to suffer separation because of its ability to transfer momentum laterally, which helps the fluid to overcome the adverse gradient of pressure. The non uniformities in the velocity profile at the entrance of the diverging region are maintained or even accentuated as the flow passes this region. The fluctuations increase with distance downstream.

A graph of the different flow regimes that can exist during turbulent flow passing through a diverging area are presented in Figure 7.4. The nomenclature of this graph is shown in Figure 7.5 (the graph was constructed in Stanford University [129]). The different regions were determined by flow visualisation, using either dye injection in a water table or wall tufts during an air test. The flow regimes were classified according to the geometry of the enlargement area. It must be borne in mind that the inlet velocity profile and the Reynolds number have a tremendous effect on the flow regime. Graph 7.4 is valid for Reynolds number above 2×10^3. The different regimes are:

1. Attached flow (region under the curve *aa* in Figure 7.4): the diverging angle is small giving rise to small separation. The velocity and the pressure are symmetric and do not change with the time.

2. Large transitory stall (between the lines *aa* and *bb*): the flow is very erratic with large pressure fluctuations. Eddies are constantly being formed and destroyed. Depending on the geometry the stalls occur i) preferentially on one side ($L/2b_1 \leq 4$), ii) equally often on each side ($4 \leq L/2b_1 \leq 12$) and iii) on both sides simultaneously ($L/2b_1 \geq 16$).

3. Two-dimensional stalls (between the lines *bb* and *dd*, and also between lines *dd* and *cc*): the stall region occurs on a side of the diverging region and the main flow passes along the other side. This pattern is stable and not affected by small disturbances but can be altered by large disturbances which cause a change of the stalls from one wall to the other.

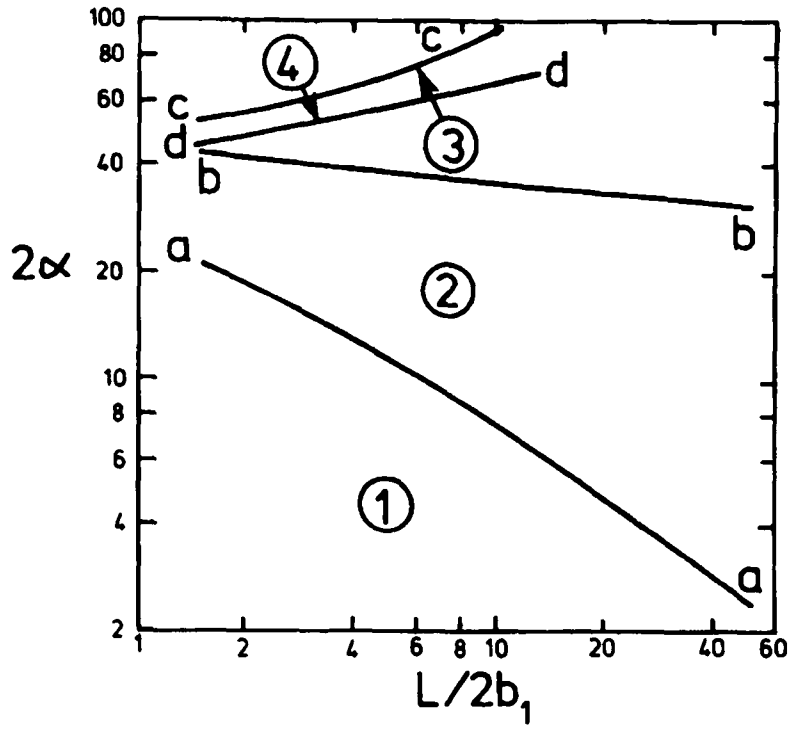

Figure 7.4: Flow regimes in two-dimensional diverging region. From Ward-Smith (1980)

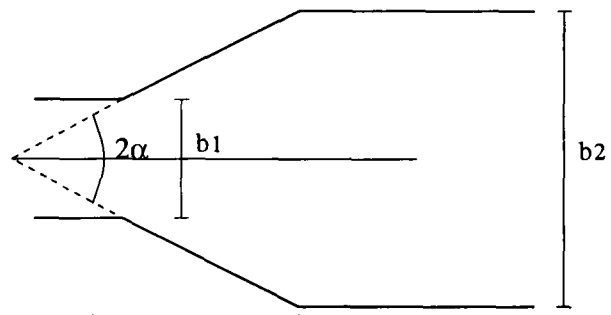

Figure 7.5: Notation for two-dimensional diverging region

4. Jet flow (above the line *cc*; sometimes can also occur in the region between the lines *dd* and *cc*): the flow is symmetric, with large stalls starting at the beginning of the enlargement region.

7.2.2 Practical implications

The flow could not be visualised in the expansion section. Therefore, the available theory is used to make some inferences. Firstly, the flow regime (based on the Reynolds number) needs to be calculated. The flow appears to be turbulent. The fluidised bed has a geometry that resembles a pipe; however, the physical

controlling flow mechanism in a pipe and in the freeboard are different. In a pipe the flow pattern is determined by the friction of the fluid with the wall. This is not the case for the freeboard flow. The most suitable Reynolds number to define here is that based on the bubble properties. The value of the Reynolds number obtained in this way is 6200, indicating that inertial forces predominate over viscous forces. Turbulent flow should, therefore, be expected and is indeed observed.

Graph 7.4 may be used to predict the effect of the enlargement on the flow. However, the geometry of the expansion of the fluidised bed is outside the range of the graph. Consequently, there is not enough information to determine what is happening close to the wall with any degree of certainty.

The angle of the expansion section is higher than the angle of repose of the seeding particles. The carbon fibres are less dense than the seeding particles. Thus, it is expected that fibres may accumulate on the wall. Furthermore, the low velocity close to the wall may make fibre deposition easy. If the adverse pressure gradient close to the wall is large enough, stagnant or recirculating areas may be created causing larger residence times for the fibres.

The expansion section is useful to slow the gas down; this is usually desirable at high fluidising velocity, to avoid particle loss from the the bed. However, in the present case ($u = 2.5 \times u_{mf}$) the particles are not ejected to a significant height. It seems that the main effect of the enlargement area is to slow-down and increase the lifetime of existing vortices as well as create new vortices resulting in a larger residence time of the gas in the freeboard.

7.3 Flow in the expanded section

Traditionally, fluidised bed hydrodynamics have been described in terms of time-averaged properties while the dynamical time dependent behaviour has been neglected. However, knowledge of this behaviour is important for the performance of fluidised beds. More recently, time series have been analysed using chaos theory (due to the irregular non-periodic behaviour of the fluidised bed dynamics) and promising results have been obtained [130, 131, 132, 133]. The present study does not deal with the analysis of time series since the experimental technique was too slow (the average bubble frequency was 0.5 seconds and the closest that two images could be taken was nearly one second). With the available technique and considering the "chaotic" behaviour of a bubbling bed, it seems that the most appropriate way to study the flow is to analyse instantaneous structures together with a statistical analysis of the flow.

7.3.1 Instantaneous flow structures

The gas flow in the expanded region is mainly determined by the flow above the bed surface and slightly modified by the expansion region.

Instantaneous velocity vector maps show that the flow is characterised by the presence of powerful jets, which are much faster than superficial velocity (jets of approximately $7 \times u$ have been found). As a consequence of the interaction of these jets with regions of lower velocity, eddies and vortices are formed. The jets do not ascend following a straight path, due to the fluctuations imposed by the bed surface and the non-uniform pressure distribution in the freeboard. It has been deduced that the location and geometry of the jets is determined by the kind of bubble eruption at the bed surface. A central jet produces eddies on both sides of the jet. A jet near a wall produces eddies only at the bed centre. There is a range of situations between these two extremes.

Although jets generate strong eddies and vortices, they are not the only mechanisms that occur. As found from the single injected bubble eruption mechanism, vortices are also generated by single erupting bubbles that do not give rise to a jet. The vortices that are found near the wall just above the bed surface are stable and have no translational velocity.

Another important finding is that at some instants the flow is downwards at every location in the illuminated plane, demonstrating the large influence of the bed surface on the gas phase. Instantaneous vector maps also show that the nature of the flow is three-dimensional. Regions of converging flow were also observed. No indication of ghost bubble presence has been found. It was demonstrated that if a ghost bubble exists PIV has enough resolution to resolve it.

The observed "turbulent" structures clearly indicate that the turbulence is not wall turbulence (because eddies and vortices do not come from a boundary layer produced by the shear stress between the fluid and the wall) but free-shear turbulence generated by the friction of regions of different velocity. The turbulence is non-homogeneous and anisotropic.

7.3.2 Statistical study of the flow

In this study time-averaged quantities were calculated. In order to evaluate whether inferences can be made of the mean velocity of the system from the mean velocity of the sample it was necessary to resort to statistical procedures. All the classic procedures (as opposed to the non-parametric tests) rely on the following assumptions:

- The sample data are randomly drawn from the population.
- The observations are independent from each other. This can be confirmed looking at consecutive vector maps. They do not have the same features,

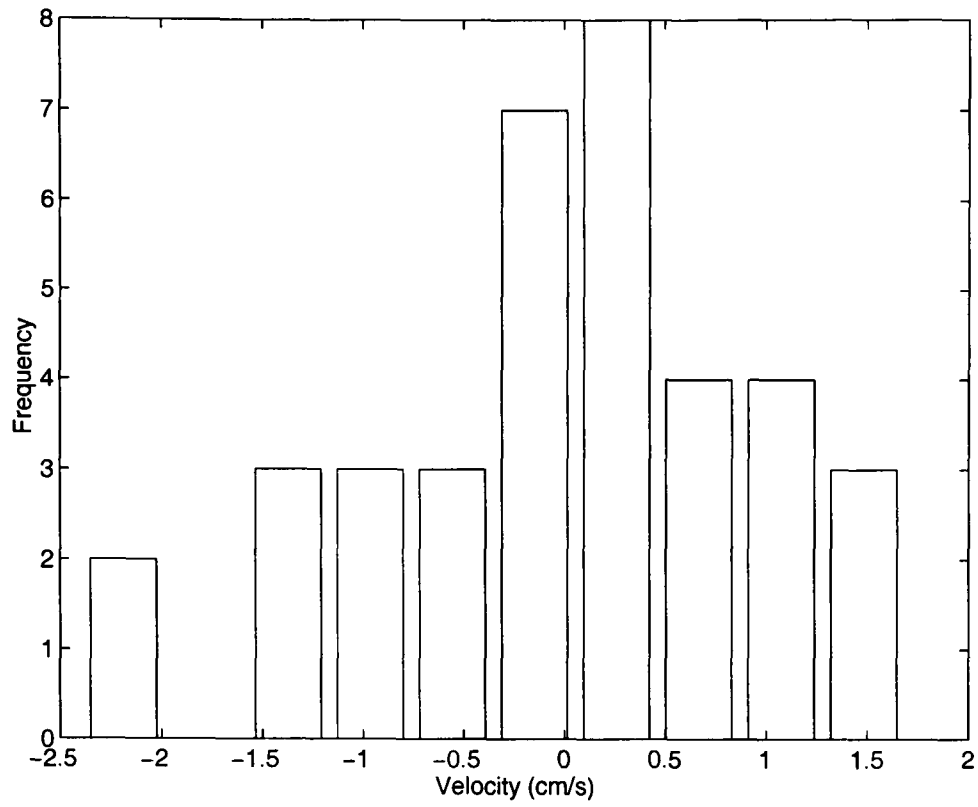

Figure 7.6: Mean vertical velocity component distribution. Experiment 1

since they are too far apart in time, thus they can be considered independent.

- The samples are normally distributed.

From the histograms of the velocity distribution (Figures 7.6 and 7.7) no features that indicate that the samples do not have a normal distribution are found, for example a bimodal distribution. The distributions may have a typical bell-shape if the number of samples were increased. Table 7.1 shows the mean and median values for each experiment. It can be seen that the mean and median values are very close in all cases, indicating a central tendency in the distribution.

The standard deviation of the population is not known, thus the t-distribution has been chosen as a good estimate of the actual sampling distribution. The t-distribution is symmetrical about a zero mean as is the standard normal distribution, but it is more spread out (depending on the degrees of freedom) due to the variation of the sample standard deviation.

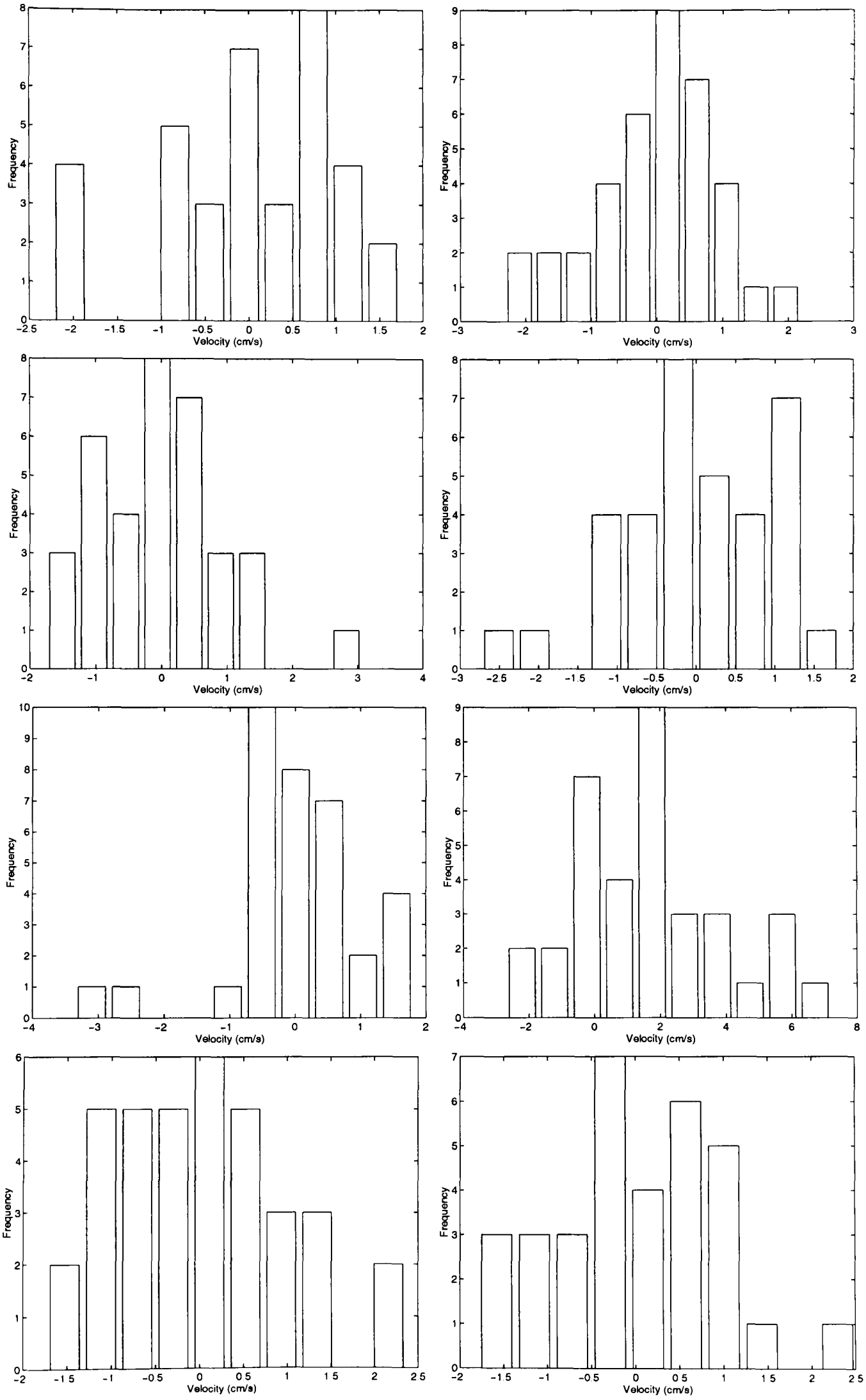

Figure 7.7: Mean vertical velocity component distribution. Experiments 2-9 (from left to right and from top to bottom)

Experiment number	Mean v_y (cm/s)	Median v_y (cm/s)	Mean v_x (cm/s)	Median v_x (cm/s)
1	1.48	1.38	0.47	0.52
2	1.41	1.32	0.28	0.15
3	1.45	1.63	-0.22	-0.01
4	1.45	1.36	-0.15	-0.44
5	0.87	0.66	-0.08	-0.25
6	1.80	1.40	0.41	0.50
7	1.86	1.78	-0.05	0.08
8	4.36	4.40	0.52	0.66
9	4.24	4.14	0.14	0.23

Table 7.1: Mean and median of the time-averaged velocity vector maps for all the experiments

The average vertical velocity component was found to be lower than the superficial velocity. Continuity could not be applied to evaluate the accuracy of the measurements because the investigated plane was parallel to the main direction of flow and not normal to it. The velocity close to the wall could not be measured (due to the inevitable internal laser reflection), but visual observation confirmed the presence of a layer of high upward velocity a few centimeter thick. This could be due to the fact that:

- The voidage is higher close to the wall.
- The particles have a more orderly arrangement close to the wall.

On fluidisation the above flow pattern (a layer of high velocity close to the wall) is rapidly established. This pattern remains after the air was switched off for a few seconds. Particles move upwards near the wall and fall back down at the centre, at velocities higher than their terminal velocities. The same effect was observed by Rix [3].

The radial profile of the vertical velocity component has an inverted "U" shape near the bed surface, a nearly flat profile in the middle of the expanded section and a "U" shape profile close to the top of the expanded region. The calculated profiles

were not completely smooth but show peaks, due to the small number of samples that were used to average. The 95% confidence limits were calculated. From the shape of the radial vertical velocity component profile it is concluded that the velocity decreases with height at the bed centre-line (most of the elutriation models are postulated based on this fact). On the contrary, the velocity increases with height near the wall (this has not been taken into account in the elutriation models).

Hamdullahpur and MacKay [56] observed an inverted "U" shape profile 7.4 cm above the bed surface which changed to a "U" shape profile 12.5 cm above the bed surface. The profile became flat 30 cm above the bed surface. The superficial velocity was 0.20 cm/s. The "U" shape profile was also found by Levy and Lockwood [42] and Lang [59]. Levy and Lockwood took measurements 50 cm above the bed surface, operating at a superficial velocity of $1.7 \times u_{mf}$. Lang studied heights between 90 and 180 cm above the bed surface at superficial velocity of $3.1 \times u_{mf}$ and $4.2 \times u_{mf}$. The horizontal velocity component is higher close to the bed surface, confirming that the horizontal velocity was imposed by erupting bubbles at the bed surface.

The freeboard flow is characterised by high velocity fluctuations. Both velocity components of the rms of the velocity are higher than the corresponding velocity. The fluctuation intensity decays with height.

It is always important in a turbulent flow to know the length- and time-scale characteristics. The time scale could not be calculated because image shifting is slower than the bubble frequency. The spatial correlation coefficients were calculated, confirming that the turbulence is free-shear turbulence, non-homogeneous and anisotropic.

The mean velocity was subtracted from the time-averaged vector map to find the secondary structure of the flow. Four recirculation areas were found, the lower ones rotating downwards at the centre and upwards near the wall. The

upper ones has the opposite rotation direction. These regions were found to have low rotational velocity compared with the vortices formed as a result of bubble eruption. They are easily distorted by the influence of jets ejected form the bed surface.

7.4 Whole picture of the flow

The flow can be described as an instantaneous flow super-imposed on an average flow. The instantaneous features of the flow are determined by bubble eruption. The intermittent movement of the bed surface and the ejection of jets from coalescing bubbles are both of enormous importance. The symmetry of the instantaneous flow is determined by initial jet location. The secondary structures of the flow are depicted in Figure 7.8. The vortices above the bed surface rotate downwards at the bed centre; this is the opposite direction to the ghost bubbles predicted by Pemberton and Davidson [40] and the same as visualised by Levy and Lockwood [42] and Caram *et al.* [41]. These vortices rotate much faster than the other vortices in the freeboard and they do not have any translational movement.

The recirculation areas proposed in the expansion section could not be visualised but they are expected in accordance with the theory. The recirculation areas in the expanded section of the freeboard have been visualised by subtracting the space-time mean velocity from the average vector map. Their rotational velocities are very slow compared with the instantaneous structures (for this reason they cannot be visualised in instantaneous vector maps). The presence of these structures explains the shape of the time-averaged profiles. With this picture in mind and the long residence time of the gas in the freeboard, it is easy to imagine that carbon fibres can be entrained in recirculation areas or instantaneous vortical structures which can give them enough time to grow to undesired length.

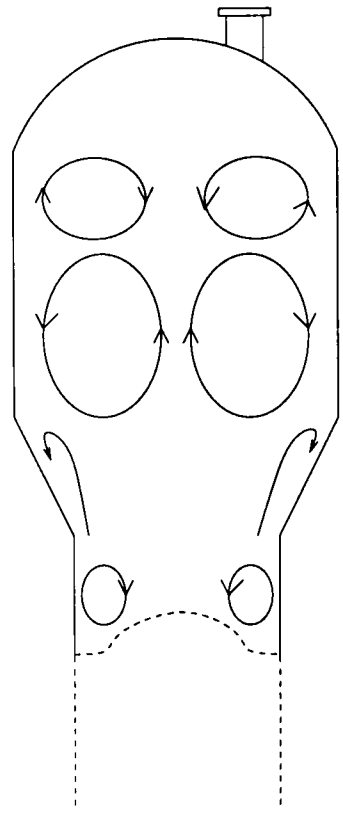

Figure 7.8: Recirculation areas in the freeboard

It has been found that the bed particles do not reach very high into the freeboard, indicating that there is no need to have the expansion to slow down the particles. It seems that the only effect of the expansion is to slow the gas and to stabilise the recirculation regions.

7.5 Comparison with previous models

7.5.1 Single bubble eruption models

In the present study, the side vortices visualised by Levy and Lockwood [42] and Caram *et al.* [41] have also been seen. Caram *et al.* found that the velocity of the vortex rings determined experimentally was proportional to the translation velocity produced by the self-induced motion of a vortex ring, as given by Maxworthy's model [4]. From this work it can be deduced that the vortex rings are ejected at high velocities, the superficial velocity is superimposed on this velocity and the self-induced translational velocity is opposed to the upwards velocity.

This can be written as:

$$U_{meas} \propto U_{eject} + u - U_{vr} \tag{7.1}$$

where U_{meas}, U_{eject}, u and U_{vr} are the measured, the ejection, the superficial and the vortex ring self-induced velocities, respectively.

Pemberton and Davidson [40] proposed that when a single bubble erupts into the upward gas flow above an incipiently fluidised bed a "ghost bubble" is formed, i.e. the gas bubble travels upwards in the freeboard keeping its identity and its circulating gas movement. However, the present results do not support this. If "ghost bubbles" exist they should be readily visible with a technique with as much local resolution as PIV. A "ghost bubble" should be like the vortex ring observed in the expanded freeboard (Figure 5.11) but travelling in the opposite direction. The bubble velocity (66 cm/s) is high compared with the superficial gas velocity (4.7 cm/s). Thus the interstial gas is not expected to mix with the bubble gas, apart from a small recirculation region on both sides of the bubble. Analysing the flow above a single injected bubble, it was found that the gas inside the bubble percolates through the bulge at the bed surface. The gas was not seen to leave the bubble as a coherent entity. A pair of vortices with the same direction as the internal circulation inside the bubble was not seen.

The experimental results qualitatively agree with the theoretical approach of Levy *et al.* [43], where a model for the emulsion phase and the gas of an isolated spherical bubble erupting at the bed surface was proposed. This was based on Davidson's model, for a bubble rising in an infinite three-dimensional medium, modified to include dynamic and kinematic conditions at the bed surface. When the bubble is rising up above the bed surface, the radial profile of the axial velocity shows a peak at the bubble centre line, as can be seen in Figure 7.9. In this figure, the vertical velocity and the radial distance have been made dimensionless using the superficial velocity and the bubble diameter, respectively. These dimensionless results can be directly compared with the results of Levy *et al.* The vertical velocity profile has a characteristic shape: a central core where the gas

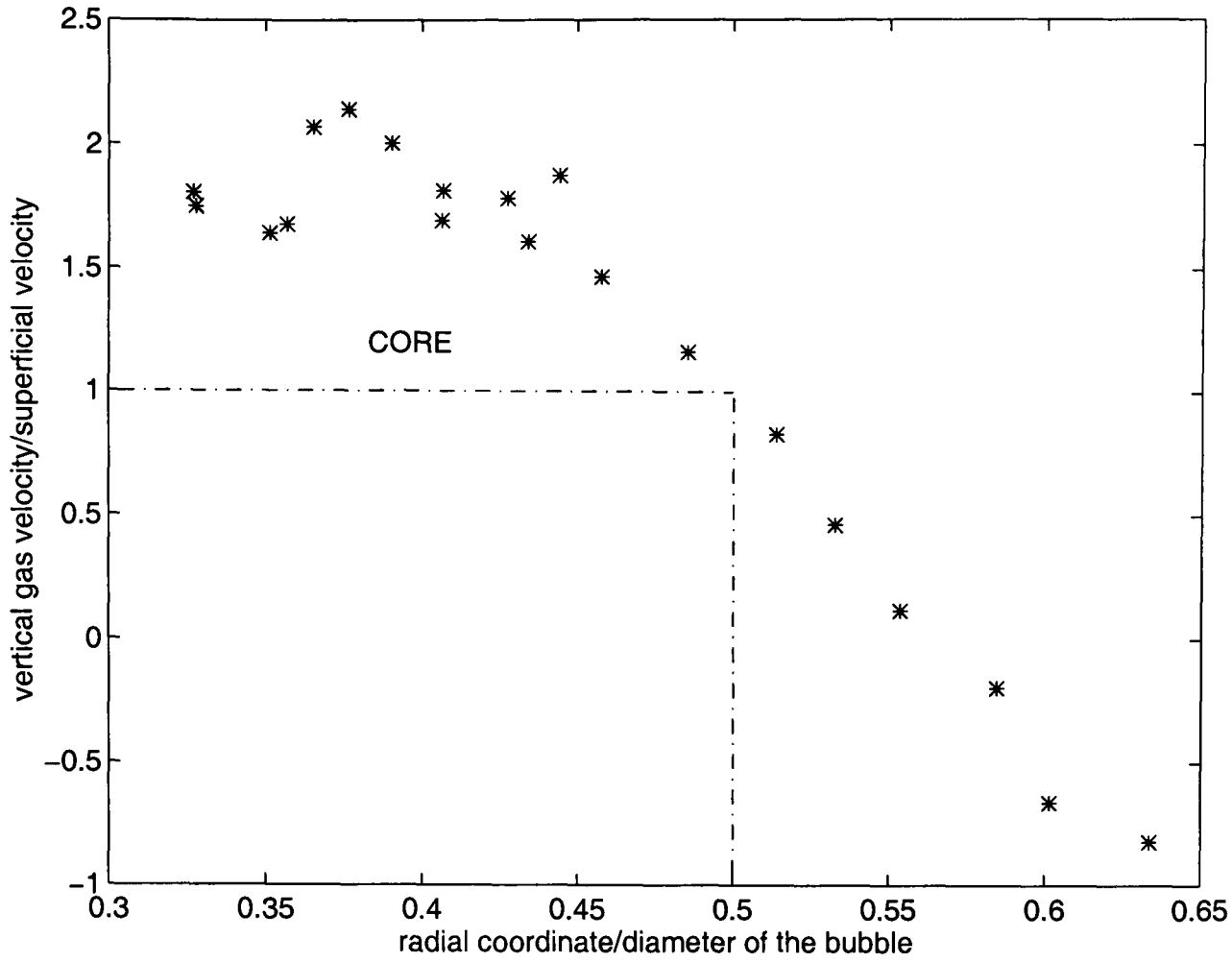

Figure 7.9: Vertical component of the absolute gas velocity above the rising bubble of Figure 5.3

velocity is higher than the superficial gas velocity and an annular region where the velocity is lower than the superficial velocity. Their calculations overpredict by a factor of two, the upward velocity in the core. This may be due to their assumption that the bubble moves upward at a constant velocity. It has been experimentally observed (Table 5.1) that the bubble velocity decreases when the bubble nose reaches the bed surface. They also considered spherical bubbles. A more realistic model should consider spherical cap bubbles.

7.5.2 Gas flow in the freeboard models

Horio *et al.* model

In this model it is postulated that the decay of turbulence in the freeboard is the result of a decay of the velocity pulsation initiated at the bed surface for the erupting bubbles [55]. It was also assumed that the decay of the turbulence is similar to that of a steady free jet. The relationship between the axial velocity and height used was that given by Abramovich in 1963 [134]. This was used with the diameter of the erupting bubble as duct diameter and the fluctuating vertical component of the velocity at the bed surface as initial jet velocity. It was found that the linear relationship between the average of the fluctuating vertical velocity over the horizontal cross-section and the erupting bubble diameter divided by the height is better correlated using empirical parameters than using the Abramovich relationship. The graphs of the fluctuating vertical velocity versus the erupting bubble diameter divided by the height above the bed surface (as in Horio's model) are presented in Figure 7.10 and 7.11. A good fit between the experimental data and the linear regression was found as given by the fit (where r^2 is the correlation coefficient between the dependent and the independent variable) and the residual sum of squares (where s^2 is a measure of the variability of the dependent variable calculated experimentally and given by the linear regression) given in Table 7.2. The experimental data measured at low velocity (Experiments 1-5) fitted better than the corresponding graphs at higher velocity (Experiments 6-9).

Caram *et al.* model

It was postulated that the decay of the turbulence in the freeboard was proportional to the velocity decay of a vortex ring, as given by Maxworthy's theory:

$$\Delta u' \propto t^{-1} \tag{7.2}$$

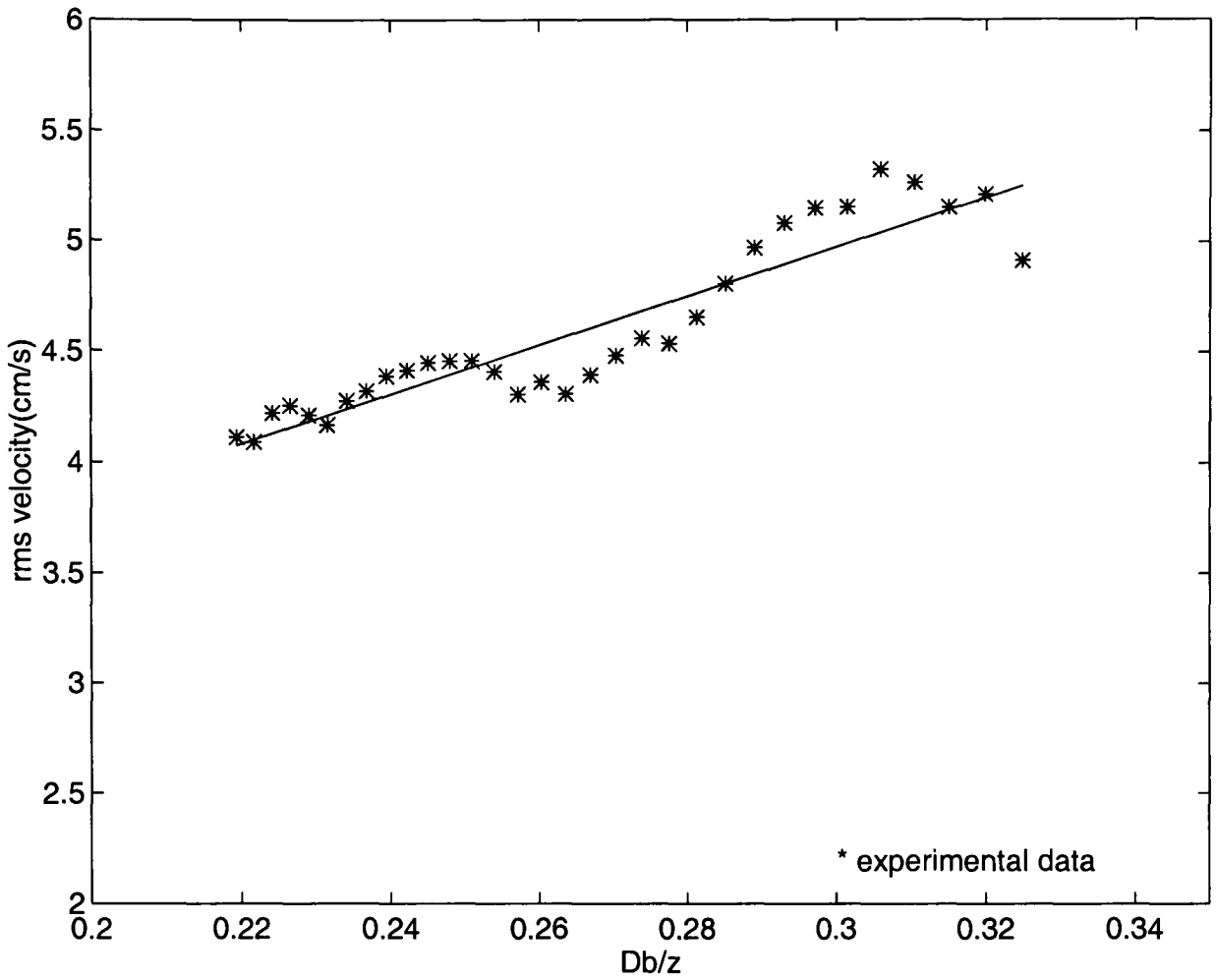

Figure 7.10: Average cross-sectional vertical velocity as function of D_b/z. Experiment 1

Experiment number	r^2	s^2 $(cm/s)^2$
1	99.73	2.08
2	99.84	1.1
3	99.84	1.9
4	99.50	6.7
5	99.83	1.8
6	99.36	9.0
7	99.72	6.6
8	99.28	16.4
9	99.81	6.5

Table 7.2: Percentage fit and residual sum of squares for Figures 7.10 and 7.11

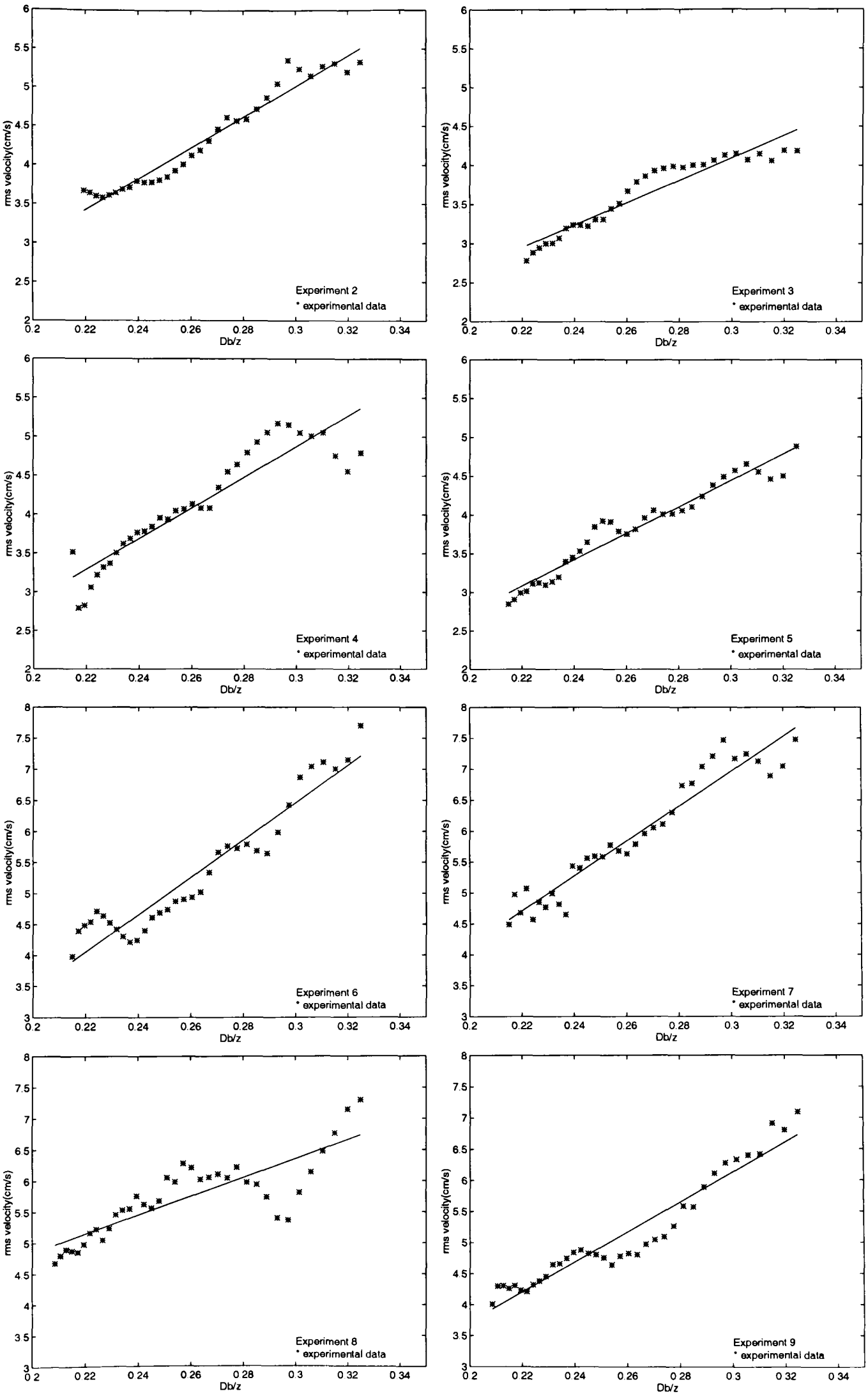

Figure 7.11: Average cross-sectional vertical velocity as function of D_b/z. Exper iments 2-9 (from left to right and from top to bottom)

$\Delta u'$ being the velocity perturbation (i.e: the maximum velocity at the centre-line of the vortex ring). A further assumption was that the vortex ring moves with the gas superficial velocity. From here the following was proposed:

$$\Delta u' \propto \frac{-u}{z} \tag{7.3}$$

This has the same dependence of the fluctuating velocity with height as Horio's correlation. However, there were no experimental data to compare with the theory. Although the correlation found for the fluctuating velocity was the same, this appears to be coincidental since there is no physical analogy between the two models.

Pemberton and Davidson model

It was proposed [40] that the velocity fluctuations in the freeboard were due to the ghost bubbles generated after bubble eruption. Thus, the equation proposed to model the decay of the velocity fluctuations with height was derived from Maxworthy's model for vortex rings and reads:

$$\ln \frac{u_{bo}}{u_r} + \frac{U}{u_{bo}} \left(\frac{u_{bo}}{u} - 1 \right) = \beta z \tag{7.4}$$

where u_r is the bubble velocity relative to the bulk fluid, u_{bo} is the bubble velocity at the bed surface, U is the velocity of the bulk fluid, β is the decay constant and z is the height above the bed surface. When the bulk fluid velocity is 0, Equation 7.4 becomes:

$$u = u_{bo} \exp(-\beta z) \tag{7.5}$$

It was assumed that the amplitude of the turbulence was related to a sequence of ghost bubbles, each one behaving as a single isolated bubble. Thus, the amplitude of the turbulence (u') was proposed to be twice the value of the rms velocity experimentally measured. They plotted Horio's data as well as their own. Horio's data showed the velocity fluctuations averaged over the horizontal cross-section. Their data were measured at the bed centre-line. They assumed that the velocity fluctuations did not vary with radial position. The experimental results of the

Experiment number	β (cm^{-1})	u'_o (cm/s)	r^2	s^2 (cm/s^2)	β_1 (cm^{-1})	u'_{1o} (cm/s)
1	-0.0119	17.32	97.98	0.11	-0.00421	85
2	-0.0227	28.78	96.78	0.12	-0.00421	85
3	-0.0212	22.21	96.90	0.12	-0.00421	85
4	-0.0249	31.34	96.05	0.38	-0.00421	85
5	-0.0228	25.81	96.25	0.10	-0.00421	85
6	-0.0261	43.15	96.25	0.41	-0.00421	100
7	-0.0236	41.95	96.64	0.19	-0.00421	100
8	-0.0128	22.87	97.21	0.33	-0.00421	85
9	-0.0221	34.89	96.16	0.32	-0.00421	85

Table 7.3: Spatial average velocity and standard deviation of the time-averaged vector maps for all the experiments

present work have been plotted in the same manner as Pemberton and Davidson's data. The velocity fluctuations averaged over the horizontal cross-section have been also included (Figures 7.12-7.13). Equation 7.5 has been fitted to the experimental data (assuming that the bulk velocity is low compared with the fluctuations). The experimental values of β and u_o, the correlation coefficients, the residual sum of the squares and the theoretical values of β and u_o are shown in Table 7.3. β_1 and u_{1o} are calculated according with the following equations:

$$\beta_1 = \frac{3\sqrt{\pi \upsilon}}{4 u_0^{'\,1/2} a_0^{3/2}} \tag{7.6}$$

where a_0 is the ghost bubble radius at the bed surface and υ the ghost bubble fluid kinematic viscosity. u'_{1o} is the absolute bubble velocity (as given by [18]) minus minimum fluidisation velocity.

$$u'_{1o} = (u - u_{mf}) + 0.711(g\ D_e)^{1/2} - u_{mf} \tag{7.7}$$

where D_e is the mean experimental diameter of the bubble at the bed surface.

It can be seen in Table 7.3 that β_1 is underestimated by the theory. The theoretical values are one order of magnitude smaller than the experimental one, indicating that the decay is higher than predicted by the vortex ring model. Pemberton and Davidson also found this, suggesting that the ghost bubbles grow faster than expected and the flow within the bubbles may be turbulent. u'_{1o} is

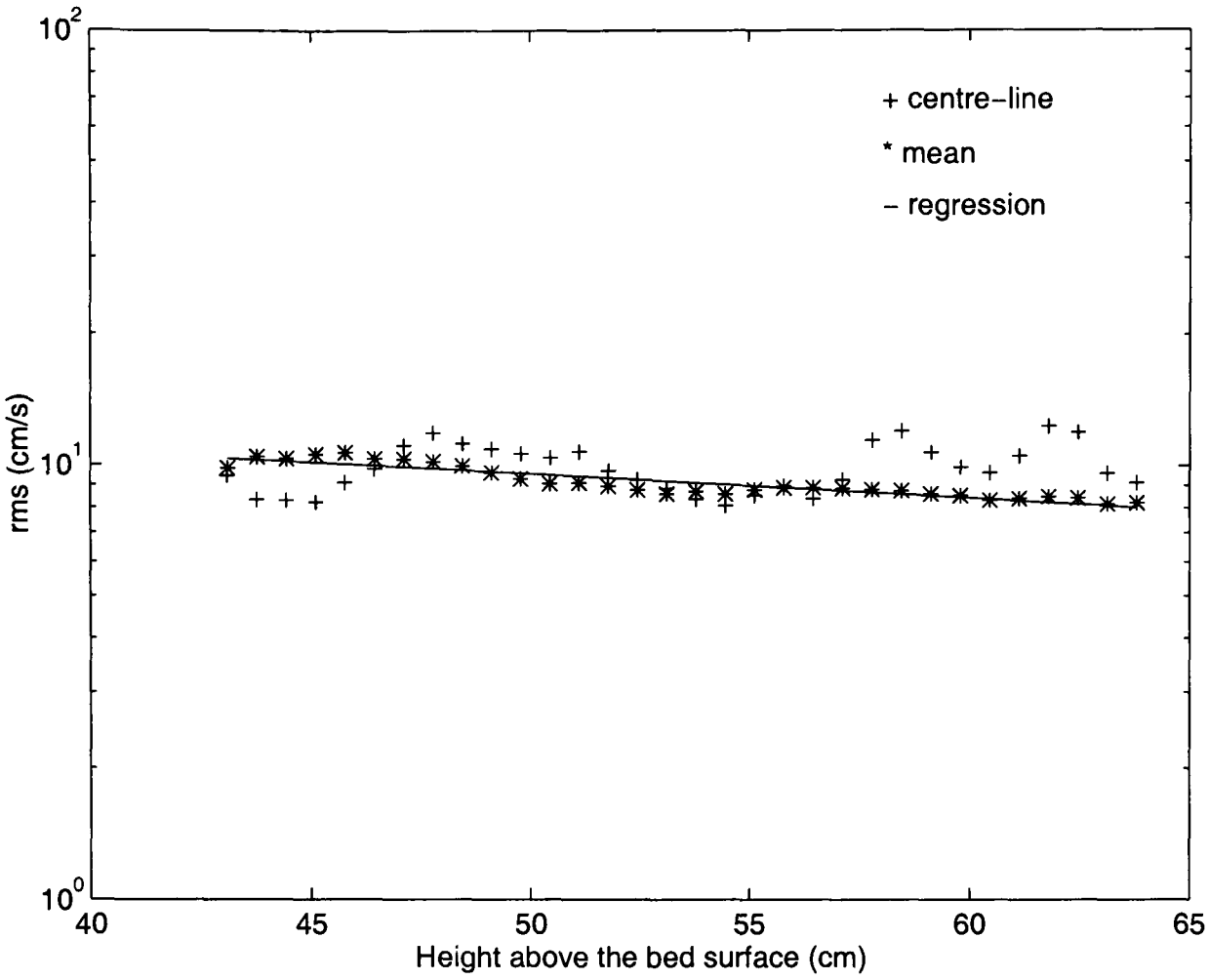

Figure 7.12: Velocity fluctuations against freeboard height. Experiment 1

smaller than u'_o; this could be attributable to the fact that the diameter used in Equation 7.7 (measured at the bed surface) may be bigger than the real bubble diameter. Furthermore, the effect of the velocity reduction due to the expansion has not been considered. The values of u'_o give the right tendency where the highest values correspond to the highest superficial velocity (Experiments 6 and 7 where the superficial velocity was $5 \times u_{mf}$). The values of r^2 and s^2 show that the experimental data fit Equation 7.5 reasonably well.

7.6 Comparison of the flow at the different conditions studied

Firstly, the influence of the outlet location was studied. No clear differences were found in the instantaneous vector maps. The vertical velocity component profiles

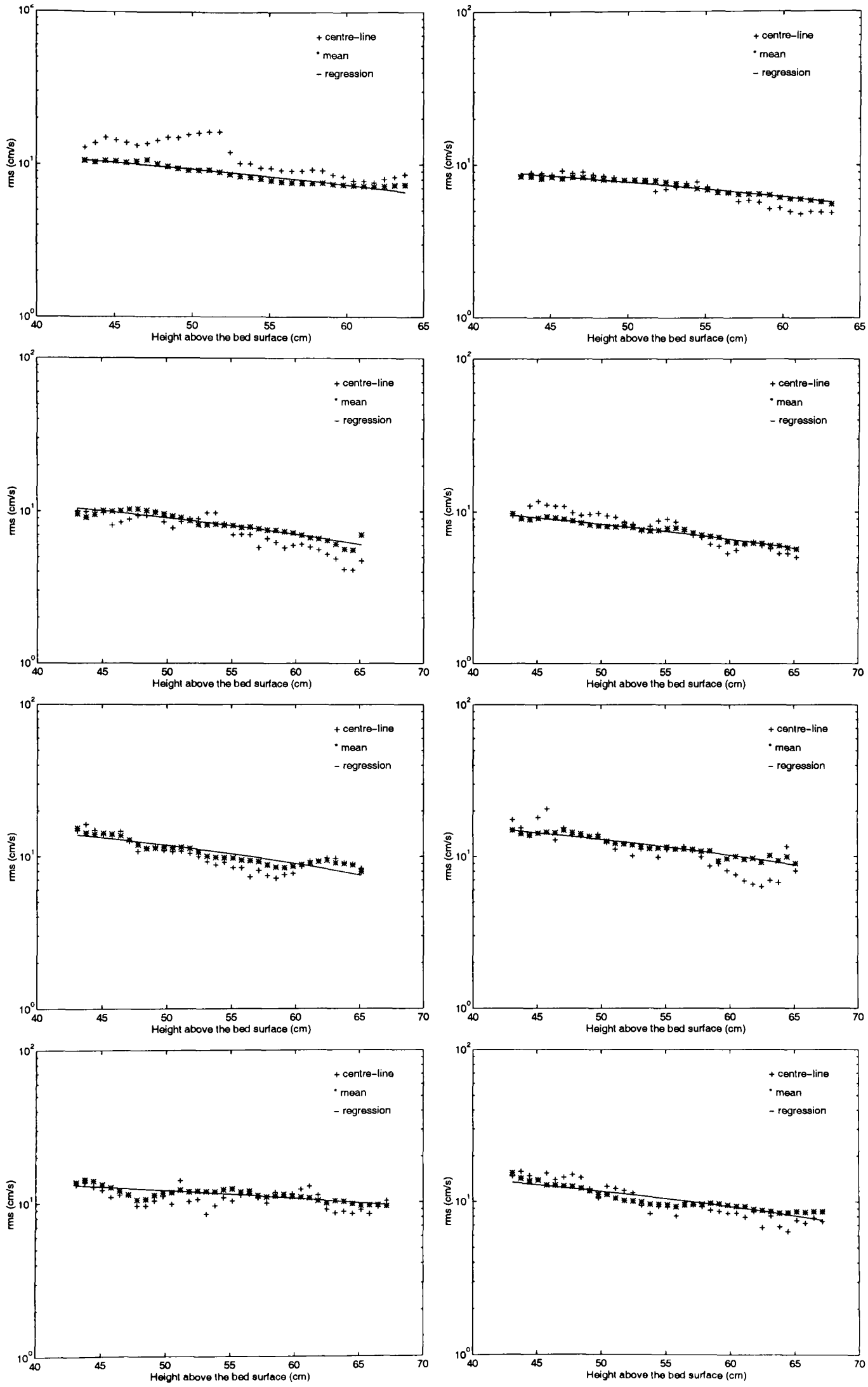

Figure 7.13: Velocity fluctuations against freeboard height. Experiments 2-9 (from left to right and from top to bottom)

were similar to those found in the case of the off-centre outlet. The horizontal velocity component profiles are slightly more symmetric than those calculated for an off-centre outlet. An influence of the location may not have been seen because the analysed plane was 15 *cm* below the outlet and the off-centre outlet was 10 *cm* behind the analysed plane, probably too far to see the direct influence of the outlet.

When the flow was studied at a superficial velocity of 11.5 *cm/sec* it was found that sand particles were ejected more often and more violently into the freeboard. However, the particles were never seen to leave the bed. The vertical velocity component profile does not have a well defined inverted "U" shape as in the case of lower superficial velocity. This is may be because more velocity vector maps are needed to smooth the profile. The vertical velocity component decreases with height, but in the range of heights under consideration the velocity profile did not have enough time to develop into the "U" shape. The secondary structure of the flow shows a tendency to form the four recirculation areas found at lower velocity. However, these recirculation areas are not as well defined and stable as those at lower velocity.

As expected when a straight freeboard was used, more sand particles were seen in the freeboard. However, they returned to the bed. The vertical velocity component profile has the inverted "U" shape found in the expanded section case and the profile changes to a "U" shape with height. The horizontal velocity component profiles are more symmetric than those found in the expanded freeboard with off-centre outlet. The secondary structure of the flow presents small recirculation areas that rotate faster than the four recirculation areas found in the expanded freeboard.

Tables 7.4 and 7.5 contain the experimental conditions (Table 7.4 was presented in Section 3.6 but it is repeated here for ease of reference) and the average velocity for each experiment. The lower average vertical velocity (and hence the longest residence time) obviously corresponds to the case of low superficial velocity and

expanded freeboard. The expanded freeboard slows down the gas and promotes the formation and stability of four slow recirculation areas.

If the superficial velocity is increased the average vertical velocity component increases but less than expected from the increase in superficial velocity. More frequent and violent bubble eruptions take place on the bed surface. The jets ejected from the bubbles destabilise the recirculation cells.

The best way to reduce the residence time in the freeboard is to use a straight freeboard, avoiding the velocity reduction due to the enlargement of the cross-section and avoiding the presence of stable secondary flow structures.

Experiment number	u_s (cm/s)	Freeboard geometry	Outlet location
1	6.3	Expanded	Off-centre
2	6.3	Expanded	Off-centre
3	6.3	Expanded	Off-centre
4	6.3	Expanded	Central
5	6.3	Expanded	Central
6	11.5	Expanded	Central
7	11.5	Expanded	Off-centre
8	6.3	Straight	Central
9	6.3	Straight	Central

Table 7.4: Experimental conditions

Experiment number	v_y (cm/s)	Vertical std (cm/s)	v_x (cm/s)	Horizontal std (cm/s)	$\|v_x\|$ (cm/s)
1	1.48	0.38	0.47	0.15	0.66
2	1.41	0.57	0.28	0.17	0.66
3	1.45	0.27	-0.22	0.05	0.77
4	1.45	0.25	-0.15	0.13	0.72
5	0.87	0.35	-0.08	0.23	0.60
6	1.80	0.21	0.41	0.24	0.76
7	1.86	0.27	-0.05	0.29	1.05
8	4.36	0.34	0.52	0.08	0.86
9	4.24	0.37	0.14	0.13	0.68

Table 7.5: Spatial average velocity and standard deviation of the time-averaged vector maps for all the experiments

Chapter 8

Conclusions and further work

8.1 Conclusions

It has been shown that PIV, implemented by image-shifting, is an excellent technique to study the single phase flow in the freeboard of a fluidised bed. The technique allows flow visualisation and two-dimensional velocity measurements, of an in-flow plane, simultaneously. This complements the traditional techniques relying upon time averaged point measurements.

The gas flow in the expanded freeboard of a fluidised bed (scaled-down from a fluidised bed used in a polymer cracking pilot plant) has been studied to determine the flow pattern and to elucidate why carbon fibres can have enough time in the freeboard to grow to undesirable sizes. Firstly, the gas flow above a single bubble was studied in order to gain insight into the inlet gas flow condition in the freeboard. After this, the flow in the expansion section was considered. Then, the gas flow in the expanded region was measured and analysed in detail. Finally, design parameters such as location of the bed outlet, superficial velocity and a straight freeboard were studied to determine their influence on the flow. The

conclusions obtained from each section of this study are presented individually below.

- **Flow above a single bubble**

  The mechanism for single injected bubble eruption has been determined using velocity vector maps and video recordings. The strong influence of the fluctuating movement of the bed surface on the gas flow in the freeboard has been demonstrated. The present results give enough evidence to refute the ghost bubble theory [40]. The presence of side vortices previously found by Levy and Lockwood [42] and Caram *et al.* [41] has been confirmed. The movement imposed on the gas after the return of the bed surface explains the continuous presence of a vortex ring rotating in an upwards direction at the wall and downwards towards the centre.

- **Flow in the expansion region**

  It has been found that the expansion angle of the freeboard is higher than the deposition angle of the seeding particles, implying that the angle is high enough to allow fibrous carbon deposition. The seeding particles deposited on the expansion wall precluded the analysis of this region. From theoretical considerations, low velocity, and possibly even a separation region, are expected close to the wall, due to the adverse pressure gradient.

- **Flow in the expanded region**

  The flow in the expanded region has been studied by analysing instantaneous flow structures and by performing a statistical analysis. The instantaneous flow pictures are characterised by the presence of powerful jets, ejected from bubbles that coalesce below the bed surface. The interaction of these jets with low velocity regions produces vortical structures. The flow symmetry (or lack of it) is mainly determined by the jet location. Instantaneous vector maps showing a strong downward velocity have been observed, confirming the influence of the bed surface material returning after bubble eruption on the gas flow.

From the instantaneous vector maps it is clear that the freeboard flow is characterised by non-homogeneous, anisotropic, free-shear turbulence.

An inverted "U" shape vertical velocity component profile has been found close to the bed surface. The profile changes with increasing height and eventually becomes a "U" shape. This profile has been reported in the literature before [56], but the mechanism whereby the profile changes was not understood. Subtracting the space-time mean flow velocity from the time-averaged vector map for each experiment clearly indicates the presence of four recirculation areas. These areas explain the change in the velocity profile.

The values of the fluctuations of the velocity measured are higher than the velocity itself. It is clear that the velocity fluctuations come from bubble eruption at the bed surface. The data of the rms of the velocity has the same functional form that the equations proposed by Pemberton and Davidson [40] and Horio [55]. Although Pemberton and Davidson's model is based on the presence of ghost bubbles and we have demonstrated that they do not exist, the model still accounts for a decay of turbulence with height.

The gas flow in the expanded region of the freeboard is the result of strong instantaneous turbulent structures, superimposed on a slow mean velocity with four clear recirculation areas.

The effect of the expansion section on the freeboard flow is: i) to slow down the gas, ii) to create an additional low velocity region close to the wall and iii) to promote and establish the recirculation areas.

- **Influence of bed outlet, superficial velocity and freeboard geometry on the freeboard flow**

  The most effective way to reduce the gas residence time in the freeboard is to use a straight freeboard.

- **Implications on fibre growth**

The present results are useful in predicting if carbon fibres will grow in the freeboard. The fibres can stay in the freeboard for significant times due to the long residence time of the gas. Furthermore, they can be entrained in the vortices produced in the freeboard or in the most stable recirculation areas.

In summary, this work has contributed to a better understanding of the gas flow in the freeboard. The single eruption bubble mechanism is an important contribution from the theoretical point of view and the characterisation of the flow in the expanded section and the influence of different factors in the freeboard flow is important from the practical point of view.

Finally, it must be borne in mind that the considered freeboard is a single phase flow. Predictions cannot be made for a two-phase freeboard where a double-coupling effect (gas interacting with particles and vice-versa) is expected.

8.2 Further work

The main disadvantage of using PIV implemented by image shifting is the slowness of obtaining results. The use of cross-correlation cameras can speed-up the process enormously. Although the resolution is not as good as that of a photographic film, this can be overcome by using more than one camera simultaneously. If cross-correlation cameras are used, not only is the time necessary to obtain a vector map reduced but also the time between images is reduced, allowing one to follow the flow with time. This temporal resolution could help to improve the understanding of the flow considerably.

It would be very interesting to observe the eruption mechanism above single injected bubbles that erupt on one side of the bed (as opposed to a bubble at the bed centre) and also to study injected bubbles that coalesce in different ways

just below the bed surface. The injection of single bubbles in beds of larger diameter should be considered to determine the effect of the bubble diameter to bed diameter ratio on the vortex ring formation.

It would be very useful to study the flow expected due just to the geometry of the freeboard, that is, to study the flow without the presence of the bed material. However, this could not be done with the present equipment because without the bed particles there is not enough pressure drop. To determine the influence of the outlet location it is necessary to build a new freeboard that would allow the analysis of any plane (this was precluded by the available freeboard).

It is also desirable to study internals that may break the recirculation areas found in the freeboard. However, care must be taken in their design, because they could generate new eddies and vortices.

PIV has the potential to be implemented for the study of two-phase flows. This potential should be developed in order to study the gas and particulate phase in the freeboard. This could be very advantageous when proposing entrainment and elutriation models.

Symbols

A	Cross-sectional area of a fluidised bed (m^2)
a	Vortex ring characteristic dimension (m)
C	Fine concentration (%)
C_o	Initial fine concentration (%)
C	Distance between the optical axis of a camera and the image-shifting mirror surface's axis of rotation (m)
C_s	Seeding particle concentration ($particles/m^3$)
$C(s_x, s_x)$	Correlation function at (s_x, s_x) displacement (-)
D_b	Bubble diameter (m)
D_e	Equivalent bubble diameter (m)
D_s	Frontal bubble diameter (m)
d_I	Lenght of an interrogation area (m)
d_i	Particle image diameter (m)
d_p	Particle diameter (m)
d_n	Distributor pitch (^{o})
d_r	Resolution of a recording media (lines/mm)
d_s	Lens point reponse function (-)
d_x	Horizontal displacement (m)
d_y	Vertical displacement (m)
E	Elutriation rate constant (kg/m^2s)
F	The focal length of a camera lens (m)
f	Bubble eruption frequency (s^{-1})
$f^\sharp$	Camera aperture ('f-number') (-)

G_s	Solid flow rate (kg/s)
g	Gravitational constant (m/s^2)
H	Bed height (m)
H_s	Static bed height (m)
I	Vortex ring impulse (m^4/s)
$I(x,y)$	Image intensity at the point (x,y) (-)
K	Vortex ring characteristic circulation (m^2/s)
K_A	Constant in the Abramovich formula (-)
k	Through flow constant (-)
M	Image magnification (-)
m	Through flow coefficient (-)
m	Scaling factor (-)
N	Number of bubble erupting simultaneously (bubbles)
P_n	Distributor orifice diameter (m)
Q	Bubble gas flowrate (m^3/s)
R	Distance between the centre of the mirror and the light sheet (m)
Re	Reynolds number (-)
U_{eject}	Velocity ejection of a vortex ring (m/s)
U_f	Fluid velocity (m/s)
U_{meas}	Velocity measured above a vortex ring (m/s)
U_p	Particle velocity (m/s)
U_{p-f}	Slip velocity (m/s)
U_{vr}	Vortex ring velocity (m/s)
u	Superficial velocity (m/s)
u_b	Bubble rising velocity (m/s)

$u_{b\infty}$ Bubble rising velocity through an infinite medium (m/s)

u_e Gas velocity in the emulsion phase (m/s)

u_r Relative velocity to the bulk fluid (m/s)

u_t Terminal velocity (m/s)

u^* Gas velocity at minimum fluidisation or minimum bubbling velocity (m/s)

u' rms velocity (m/s)

u'_o rms velocity at the bed surface (m/s)

$\tilde{u}'$ mean axial rms (m/s)

$u'_{v\infty}$ rms at fully developed turbulence (m/s)

V Vortex ring volume (m^3)

v_x Space-time mean horizontal velocity (m/s)

v_y Space-time mean vertical velocity (m/s)

w Mirror rotational velocity (rad/s)

z Height above the bed surface (m)

β Ghost bubble decay coefficient (m^{-1})

Δt Time between pulses (s)

Δz Light shee thickness (m)

δ Fraction of surface area occupied by bubbles (-)

δz Depth field of the camera (m)

ε Optical exposure (-)

$\bar{\varepsilon}$ Mean optical exposure (-)

ε_{mf} Minimum fludisation voidage (-)

θ Deviation from single bubble behaviour coefficient (-)

μ Dynamic viscosity (kg/ms)

λ Wave lenght of a light source (μm)

ρ_f Fluid density (kg/m^3)

ρ_p Particle density (kg/m^3)

υ Kinematic viscosity (m^2/s)

Φ_f Bubble flow area shape factor (-)

ϕ Deviation of the visible flow from the two-phase theory (-)

φ Sphericity (-)

Bibliography

[1] M. Gandy. *Recycling and the politics of urban waste.* Earthscan Publication Limited, 1994.

[2] J.R. Fried. *Polymer science and technology.* Prentice Hall PTR, 1995.

[3] S. J. L. Rix. *Particle image velocimetry and its application in the study of gas velocities in the freeboard above bubbling fluidised beds.* PhD thesis, University of Edinburgh, 1998.

[4] T. Maxworthy. The structure and stability of vortex rings. *J. Fluid Mech.*, 51(1):15–32, 1972.

[5] R.D. Toomey and H.F. Johnstone. Gaseous fluidization of solid particles. *Chemical Engineering Progress.*, pages 220–226, 1952.

[6] J.F. Davidson. Symposium on fluidization-discussion. *Trans. Instn. Chem. Engrs.*, 39:230–231, 1961.

[7] R. Clift and J.R. Grace. *In Fluidization.*, chapter 2. Academic Press, London., 1985.

[8] J.R. Grace and J. Clift. On the two-phase theory of fluidization. *Chem. Eng. Sci,*, 29:327–334, 1974.

[9] R.R. Cranfield and D. Geldart. Large particle fluidisation. *Chem. Eng. Sci.*, 29:935–947, 1974.

[10] L. Jones and L.R. Glicksman. An experimental investigation of gas flow in a scale model of a fluidized bed combustor. *Power Technol,*, 45:201–213, 1986.

[11] J.F. Davidson and D. Harrison. The behaviour of a continuously bubbling fluidised bed. *Chem. Eng. Sci,*, 21:731–738, 1966.

[12] M.J. Lockett, J.F. Davidson, and D. Harrison. On the two-phase theory of fluidisation. *Chem. Eng. Sci.*, 21:1059–1065, 1967.

[13] P.N. Rowe, L. Santoro, and J.G. Yates. The division of gas between bubble and interstitial phases in fluidised beds of fine powders. *Chem. Eng. Sci.*, 33:133–140, 1978.

[14] D.L. Pyle and D. Harrison. An experimental investigation of the two-phase theory of fluidization. *Chem. Eng. Sci,*, 33:1199–1207, 1967.

[15] J.G. Yates and D. Cheesman. Voidage variations in the regions surrounding a rising bubble in a fluidized bed. *AIChE Symp. Ser.*, 88(34-39), 1992.

[16] J.G. Yates and D. Cheesman. *AIChE Symp. Ser.*, 88:34–39, 1993.

[17] R. Clift. An occamist review of fluidized bed modelling. *AIChE Symp. Ser.*, 89:1–17, 1993.

[18] J.F. Davidson and D. Harrison. *Fluidised Particles.* 1963.

[19] B.A. Partridge and P.N. Rowe. Analysis of gas flow in a bubbling fluidised bed when cloud formation occurs. *Trans IChemE,*, 44:T349–T358, 1966.

[20] R. Clift, J.R. Grace, L.Y. Cheung, and T.H. Do. Gas and solids motion around deformed and interacting bubbles in fluidized beds. *J. Fluid Mech,*, 51:187–205, 1972.

[21] L.S. Leunh, Nguyen X.T., and F.K. Mak. *AIChE Symp Ser,*, 67:34–47, 1971.

[22] A. Garcia, J.R. Grace, and R. Clift. Behaviour of gas bubbles in fluidized beds. *AIChE Journal,*, 19(2):369–370, 1973.

[23] M. Gautam, J.T. Jurewiez, J.M. Palmer, and R.S. Kate. Fluid flow through bubbles in fluidized beds: Lda measurements in gas-solid flows. *ASME Fed.*, 121:169–175, 1991.

[24] L. Hailu, F. Plaka, R. Clift, and J.F. Davidson. Measurement of gas flow through a two-dimensional bubble in a fluidised bed. *Trans IChemE,*, 71:382–389, 1993.

[25] J.G. Yates, D.J. Cheesman, and Y.A. Sergeev. Experimental observations of voidage distribution around bubbles in a fluidized bed. *Chem. Eng. Sci.*, 49:1885–1895, 1994.

[26] P.N. Rowe. *Experimental properties of bubbles. In Fluidization.*, chapter 4. Academic Press, London., 1971.

[27] A. Hepbasli. Investigation of the bubble behaviour at the free surface of a large three-dimensional gas fluidized bed. *International Journal Of Engineering Research*, 22:885–909, 1998.

[28] R.C. Darton, R.D. LaNauze, J.F. Davidson, and D. Harrison. Bubble growth due to coalescence in fluidised beds. *Trans. IChemE*, 55:274–280, 1977.

[29] C.E.J. Van Lare, H.W. Piepers, J.N. Shoonderbeek, and D. Thoenes. Investigation on bubble characteristics in a gas fluidized bed. *Chem. Eng. Sci.*, 52(5):829–841, 1997.

[30] B.G.M. Van Wachen, J.C. Schouten, R. Krishna, and C.M. Vand den Bleek. Eulerian simulations of bubbling behaviour in gas-solid fluidised beds. *Computers Chem. Eng.*, 22(Suplement):S299–S306, 1998.

[31] R. Krishna, J. Ellenberger, and D.E. Hennephof. Analogous description of the hydrodynamics of gas solid fluidized beds and bubble columns. *Chemical Engineering Journal*, 53:89–101, 1993.

[32] D. Geldart. Types of gas fluidization. *Powder Technology*, 7:285–292, 1973.

[33] M. Horio and A. Nonaka. A genaralized bubble diameter correlation for gas-solid fluidized beds. *AIChE Journal*, 33(11):1865–1872, 1987.

[34] J.F. Davidson, R. Clift, and D. Harrison. *Fluidization.* Academic Press Inc., second edition, 1985.

[35] J. Werther and O. Molerus. The local structure of gas fluidized beds-i. a statistically based measuring system. *Int. J. Multiphase Flow.*, 1:103–122, 1973.

[36] J.S. Lin, M.M. Chen, and B.T. Chao. A novel radioactive particle tracking facility for measurement of solids motion in gas fluidized bed. *AIChE Journal.*, 31:465–472, 1985.

[37] K. Hilligardt and J. Werther. Local bubble gas hold-up and expansion of gas-solid fluidized beds. *Ger. Chem. Engng.*, 9:215–221, 1986.

[38] E.K. Levy, I. Alkan, and H. Caram. Characteristics of erupting bubbles in a three dimensional fluidized bed. *AIChE Symposium Series*, 80(241):1–8, 1984.

[39] W.C. Verloop. *The fluid dynamics of the freeboard in a fluidized bed reactor.* PhD thesis, Delft University of Technology, 1994.

[40] S.T. Pemberton and J.F. Davidson. Turbulence in the freeboard of a gas fluidized bed. the significance of ghost bubbles. *Chem. Eng. Sci.*, 39(5):829–840, 1984.

[41] H.S. Caram, Z. Efes, and E.H. Levy. Gas ans particle motion induced by a bubble eruption at the surface of a gas flidized bed. *AIChE Symposium Series*, 80(234):106–113, 1984.

[42] Y. Levy and F.C. Lockwood. Doppler measurements of flow in the freeboard of a fluidized bed. *AIChE Journal.*, 29:889–895, 1983.

[43] E.K. Levy, H.K. Chen, R. Radcliff, and H.S. Caram. Analysis of gas flow through erupting bubbles in a gas-fluidized bed. *Powder technology*, 54:45–57, 1988.

[44] Y. Levy and F.C. Lockwood. Two phase flow measurements in the freeboard of a fluidized bed using lda. *Israel Journal of Technology*, 18:146–151, 1980.

[45] H. Do, J. Grace, and R. Clift. Particle ejection and entrainment from fluidized beds. *Powder Technology*, 6:195, 1972.

[46] S.C. Saxena and A. Mathur. On the origin of solids projected from the surface of a gas-fluidized bed. *Chem. Eng. Sci.*, 39(5):917–918, 1984.

[47] P.N. Rowe, B.A. Partridge, A.G. Cheney, G.A. Henwood, and E. Lyall. The mechanisms of solids mixing in fluidised beds. *Trans. Instn. Chem. Engrs.*, 43(T271-T286), 1965.

[48] S. George and J. Grace. Entrainment of particles from aggregative fluidized beds. *AIChE Symp. Ser.*, 67(176):74, 1978.

[49] M. Leva and C.Y. Wen. *Fluidisation. Chapter 14.* 1971.

[50] T.P. Chen and S.C. Saxena. *Fluidization.* Cambridge University Press, 1978.

[51] S.C. Saxena and A. Mathur. A model for the projection of solid particles from the surface of a gas fluidized bed. *Chem. Eng. Sci.*, 44(3):774–773, 1989.

[52] H. Hatano and M. Ishida. The entrainment of solid particles from a gas-solid fluidized bed. *Journal of Chemical engineering of Japan*, 14(4):306–311, 1981.

[53] S.T. Pemberton and J.F. Davidson. Elutriation from fluidized beds- i. particle ejection form the dense phase into the freeboard. *Chem. Eng. Sci.*, 41(2):243–251, 1986.

[54] S. Morooka, K. Kawazuishi, and Y. Kato. Holdup and flow pattern of solid particles in freeboard of gas-solid fluidized bed with fines particles. *Powder Technology*, 26:75–82, 1980.

[55] M. Horio, A. Taki, Y.S. Hsieh, and I. Muchi. *Fluidization.* Plenum, 1980.

[56] F. Hamdullahpur and G.D.M. MacKay. Two-phase flow behaviour in the freeboard of a gas fluidized bed. *AIChE Journal*, 32(12):2047–2055, 1986.

[57] K.G. Berkelmann and U. Renz. Gas and solid flow in the freeboard of a fluidized bed combustor. *Powder Technology*, 68(3):183–196, 1991.

[58] J.R. Grace and D. Harrison. The distribution of bubbles within a gas fluidized bed. *Ints. Chem. Eng. Symp. Ser*, 30:105, 1968.

[59] I. Lang. *Structure of flow in the freeboard region of gas solid fluidized bed.* PhD thesis, University of Edinburgh, 1986.

[60] W. Mojtahedi. PhD thesis, University of Edinburgh, 1983.

[61] M. Leva. elutriation of fines from fluidized systems. *Chem. Eng. Prog.*, 47(1):39–45, 1951.

[62] G.L. Osberg and D.H. Charlesworth. Elutriation in a fluidized bed. *Chem. Eng. Progress*, 47:566–570, 1951.

[63] C.Y. Wen and R.F. Hashinger. Elutriation of solid particles form a dense-phase fluidized bed. *AIChE Journal*, 6(2):220–226, 1960.

[64] W.J. Thomas, P.J. Grey, and S.B. Watkins. Effect of particle size distribution in fluidization. *British Chem. Eng.*, 6(2):176–181, 1961.

[65] D. Hanesian and A. Rankell. Elutriation from a multisize particle fluidized bed. *I. and E. C. Fundamentals*, 3:452–458, 1968.

[66] D. Geldart, J. Cullinan, S. Georghiades, D. Gilvray, and D. Pope. *Trans. Inst. Chem. Eng.*, 57:269, 1979.

[67] L. Lin, J.T. Sears, and C.Y. Wen. Elutriation and attrition of char from a large fluidized bed. *Powder Technology*, 27:105–115, 1980.

[68] W.K. Lewis, E.R. Gilliland, and P.M. Lang. Entrainment from fluidized beds. *Chem. Eng. Prog. Symp. Ser.*, 58:65–78, 1962.

[69] D. Kunii and O. Levenspiel. *Fluidization Engineering.* 1969.

[70] D. Merrick and J. Highley. Particle size reduction and elutriation in a fluidized bed process. *AIChE Symp. Ser.*, 70(157):366, 1974.

[71] S.E. George and J.R. Grace. Entrainment of particles from a pilot scale fluidized bed. *Canadian Journal of Chem. Eng.*, 59:279–284, 1981.

[72] C.Y. Wen and L.H. Chen. Fluidized bed freeboard phenomena: entrainment and elutriation. *AIChE Journal*, 28(1):117–128, 1982.

[73] H. Hatano, T. Okuma, and M. Ishida. Bubble eruption model for entrainment phenomena below the tdh for gas solid fluidized bed. *Journal Chem. Eng. of Japan*, 17(5):491–497, 1984.

[74] D. Geldart. *Gas fluidization technology.* Wiley, Chichester, U.K., 1986.

[75] D. Kunii and O. Levenspiel. *Fluidization Engineering.* Butterworth-Heinemann Series in Chemical Engineering, second edition, 1991.

[76] F.E. Milioli and P.J. Foster. Entrainment and elutriation modelling in bubbling fluidized beds. *Powder Technology*, 83:233–243, 1995.

[77] F.A. Zenz and N.A. Weil. A theoretical-empirical approach to the mechanism of particle entrainment from fluidized beds. *AIChE Journal*, 4(4):472–479, 1958.

[78] S.T. Pemberton and J.F. Davidson. Elutriation from fluidized beds- ii. disengagement of particles from gas in the freeboard. *Chem. Eng. Sci.*, 41(2):253–262, 1986.

[79] L.R. Glicksman and T. Yule. Prediction of the particle flow condictions in the freeboard of a freely fluidized bed. *Chem. Eng. Sci.*, 50(1):69–79, 1995.

[80] J. Corella, R. Bilbao, and M.P. Aznar. Improvements in the fluidized beds. bubble diameter and type of the solid flow with internals and with an enlargement in the upper zone of the bed. In *World congress of chemical engineering (Procedings of the second edition)*, volume 3, pages 36–40, 1981.

[81] J. Corella and R. Bilbao. Fluid dynamic study of a new type of solid gas contactor: Fluidized/fixed or fluidized bed. *Ind. end. Chem. Process Des. Dev.*, 21:545–550, 1982.

[82] J. Corella, R. Biblbao, J. Lezaun, and A. Monzon. Effect of some internals on the solid flow in a continuous fluidized bed with an increase of cross section. *Fluidization IV, International Conference on Fluidization. Kashikojim, Japan*, pages 211–18, 1983.

[83] J. Corella and R. Bilbao. Increase of the gas conversion in a fluidized bed by enlarging the cross section of the upper zone of the bed. *Ind. Eng. Chem. Process Des. Dev.*, 22:329–334, 1983.

[84] J. Corella and R. Bilbao. Model for the gas flow in a fluidized bed with increase of the cross section in its upper zone. *Ind. Eng. Chem. Process Des. Dev.*, 22:334–339, 1983.

[85] J. Corella, R. Biblbao, A. Monzon, J. Lezaun, and F. Fernandez. Flow model for the solid in a continuos fluidized bed with increase of the cross section in its upper zone. *Ind. Eng. Chem. Process Des. Dev.*, 25:188–197, 1986.

[86] S.M. Tasirin and D. Geldart. Entrainment of fines from fluidized beds with an expanded freeboard. *Chem. Eng. Comm.*, 166:217–230, 1998.

[87] L.R. Glicksman. Scaling relationships for fluidized beds. *Chem. Eng. Sci.*, 39(9):1373–1379, 1984.

[88] M.T. Nicastro and L.R. Glicksman. Experimental verification of scaling relationships for fluidized bed. *Chem. Eng. Sci.*, 39(9):1381–1391, 1984.

[89] L.R. Glicksman. Scaling relationships for fluidized beds. *Chem. Eng. Sci.*, 43(6):1419–1421, 1988.

[90] M. Horio, A. Nonaka, Y. Sawa, and I. Muchi. A new similarity rule for fluidized bed scale-up. *AIChE Journal*, 32(9):1466–1482, 1986.

[91] T.J. Fitzgerald and S.D. Crane. Conference on fluidized bed combustion. 1980.

[92] L.R. Glicksman, M.R. Hyre, and P.A. Farrell. Dynamic sumilarity in fluidization. *Int. J. Multiphase Flow*, 20:331–386, 1994.

[93] M. Horio, T. Shibata, and I. Muchi. Proc. fourth international conference. In D. Kunii and R. Toei, editors, *Fluidization*. Engineering Foundation, 1984.

[94] R.C. Weast, editor. *Handbook of chemistry and physic.* CRC Press, 1982.

[95] G.F. Kinney. *Engineering propierties and applications of plastics.* John Wiley and Sons, 1957.

[96] J.C. Dainty. Some statistical properties of random speckle patterns in coherent and partially coherent illumination. *Optica Acta*, 17(10):761–772, 1970.

[97] I. Grant. Particle image velocimetry: a review. *Proc. Instn. Mech. Engrs*, 211(Part C):55–76, 1997.

[98] W. Lauterborn and A. Vogel. Modern optical techniques in fluid mechanics. *Ann. Rev. Fluid Mech.*, 16:223–244, 1984.

[99] R.J. Adrian. Multi-point optical measurements of simultaneous vectros in unsteady flow - a review. *Int. J. Heat and Fluid Flow*, 7(2):127–145, 1986.

[100] R.J. Adrian. Particle-imaging techniques for experimental fluid mechanics. *Ann. Rev. Fluid Mech.*, 23:261–304, 1991.

[101] T.D. Dudderar, R. Meynart, and P.G. Simpkins. Full-field methodology for fluid velocity measurements. *Optics and Laser in Engineering*, 9:163–199, 1988.

[102] I. Grant and G.H. Smith. Modern developments in particle image velocimetry. *Optics and Laser in Engineering*, 9:245–264, 1988.

[103] L. Hesselink. Digital image processing in flow visualization. *Ann. Rev. Fluid Mech.*, 20:421–485, 1988.

[104] P. Buchhave. Particle image velocimetry - status and trends. *Experimental Thermal and Fluid Science*, 5:586–604, 1992.

[105] C. J. Ague and J. Jimenez. On the performance of particle tracking. *J. Fluid Mech.*, 185:447–468, 1987.

[106] A. Melling. Seeding gas flow for laser anemometry. In *Advanced instrumentation for aero-engine components*, Propulsion and energetics panel, 67th symposium, pages 8–1–8–11, Philadelphia, May 1986.

[107] C. Gray. *The development of particle image velocimetry for water wave studies.* PhD thesis, University of Edinburgh, 1989.

[108] A.J. Martin. *Laboratory simulation and numerical modelling of the kinematics of oceanic internal waves.* PhD thesis, Universtity of Edinburgh.

[109] R.J. Adrian and C.S. Yao. Pulsed laser technique application to liquid and gaseous flows and the scattering power of seed materials. *Applied Optics*, 24:44–52, 1986.

[110] T. Bruce, W.J. Eason, C. Gray, D.R. Greated, D.R. McCluskey, and D.J. Skyner. Particle image velocimetry- a practical course., 1993.

[111] L.C. Liu, C.C. Landreth, R.J. Adrian, and T.J. Hanratty. High-resolution measurement of turbulent structure in a channel with piv. *Exp. Fluids.*, 10:301–312, 1991.

[112] R. J. Adrian. Image technique shifting to resolve directional ambiguity in double-pulsed velocimetry. *Appl. Opt.*, 26:3855–3858, 1986.

[113] I. Grant and A. Liu. Directional ambiguity resolution in piv by pulse tagging. *Exp. Fluids.*, 10:71–76, 1990.

[114] R. D. Keane and R.J. Adrian. Optimization of particle image velocimetry. part 1: Double pulsed systems. *Meas. Sci. Technol.*, 1:1202–1215, 1990.

[115] C.E. Willert and M. Gharib. Digital particle image velocimetry. *Exp. Fluids*, 10:181–193, 1991.

[116] T. Utami and Blackwelder R.F. A cross-correlation technique for velocity field extraction from particulate visualization. *Exp. Fluids.*, 10:213–223, 1991.

[117] M. Raffel and J.Q. Kompenhas. Theoretical and experimental aspects of image-shifting by means of a rotating mirror system for particle image velocimetry. *Meas. Sci. Technol.*, 6(6):795–808, 1995.

[118] I.G. Morrison. *The hydrodynamic performance of an oscillating water column wave.* PhD thesis, Edinburgh University, 1996.

[119] T.S. Durrani and C.A. Greated. *Laser systems in flow measurement.* Plenun. New York, 1977.

[120] G.B. Wallis. *One-dimensional two-phase flow.* MacGraw-Hill, 1969.

[121] P.N. Rowe and R. Matsuno. Single bubbles injected into a gas fluidised bed and observed by x-rays. *Chem. Eng. Sci.*, 26:923–935, 1971.

[122] H.S. Mickley, K.A. Smith, and E.I. Korchak. Fluid flow in packed beds. *Chem. Eng. Sci.*, 20:237–246, 1965.

[123] D. J. Tritton. *Physical fluid dynamics.* Oxford Science Publications, second edition, 1988.

[124] A.A. Townsend. *The structure of turbulent shear flow.* Cambridge University Press, second edition, 1973.

[125] A.K. Hind. *An investigation into the flow fields around bluff bodies and artificial heart valves.* PhD thesis, University of Edinburgh, 1998.

[126] A.K. Hind, D.R. McCluskey, J.R.E. Christy, W.J. Easson, C.A. Greated, and D.H. Glass. Piv analysis of two-phase air particle flows. In The Institution of Mechanical Engineers, editor, *In Optical Methods and Data Processing in Heat and Fluid Flow*, City University. London, 2-3 April 1992.

[127] D.R. MacCluskey, A.K. Hind, S.L.J. Rix, M.L. Jacobsen, J.R.E. Christy, W.J. Easson, D.H. Glass, and C.A. Greated. Development and application of a simultaneous two-phase piv system for the analysis of air-particle flow fields. In *In Optical Methods and Data Processing in Heat and Fluid Flow II*, City University. London, April 1994.

[128] W.A. Woods and D.G. Clark. *Visualized flow.* Pergamon Press, 1988.

[129] A.J. Ward-Smith. *Internal fluid flow.* Clarendon Press, 1980.

[130] M.L.M Vander Stappen. *Chaotic hydrodynamics of fluidized beds.* PhD thesis, Delft University of technology, 1996.

[131] M. Van den Bleek and J.C. Schouten. Deterministic chaos: a new tool in fluidized bed design and operation. *The Chemcial Engineering Journal*, 53:75–87, 1993.

[132] J.C. Schouten, M.L.M. Vander Stappen, and C.M. Van Den Bleek. Scale-up of chaotic fluidized bed hydrodynamics. *Chem. Eng. Sci.*, 51(10):1991 - 200, 1996.

[133] J. Stringer. Is a fluidized bed a chaotic dynamic system? In *Proc. 10th Int. Conf. on Fluidized bed combustion*, pages 265–272, San Francisco, 1989.

[134] G. N. Abramovich. *The theory of turbulent jets.* M.I.T. Press, Cambridge, Massachusetts., second edition, 1963.